Development of Next Generation Photoelectrochemical and Polymer Transistor Devices

by

Pegah Ghamari

Department of Electrical and Computer Engineering

Faculty of Engineering, McGill University

Montréal, August 2022

A thesis submitted to McGill University in partial fulfillment

of the requirements of the degree of Doctor of Philosophy

Research Supervisors:

Prof. Dmytro Perepichka

Prof. Odile Liboiron-Ladouceur

Acknowledgements

I would begin by expressing my sincere gratitude to my supervisor Prof. Dmytro Perepichka, for his continuous support, encouragement, and patience during this long Ph.D. journey. He taught me how to grow as a researcher, through his outstanding guidance on considering all hidden angels of any matter. It is such an honor to work with him at the prestigious McGill university. My earnest thanks to my co-supervisor Prof. Odile Liboiron-Ladouceur for her support and great help during my Ph.D. I thank my co-workers Dr. Dadvand, Dr. Niazi, and all lab members of Perepichka's lab for their great help, discussions, suggestions, and collaboration, it was a pleasure working with such talented people. My special thanks to the Chemistry department's technical research personnels, Dr. Stein, Dr. Ramkaran, and Dr. Titi, who provided their knowledge and expertise on characterization techniques.

I would particularly like to thank Prof. Zetian Mi for his guidance and help specially in beginning years of my Ph.D. I had a great time and gained a lot of experience working in McGill Nanotools Microfab cleanroom for two years and I'd like to express my gratitude to my former colleagues at this lab.

I thank to the McGill Engineering Doctoral Awards (MEDA) program for the financial support. I also acknowledge the research support by The Fonds de recherche du Québec – Nature et technologies (FRQNT) and Natural Sciences and Engineering Research Council of Canada (NSERC).

I would like to express my deepest appreciation and love to my family, especially to my dear parents, Ghamar Allipour and Abdolhossein Ghamari, for their support throughout my life and during my Ph.D. studies from a long distance.

Last but by no means least, I would like to express my heartfelt gratitude to my husband Dr. Amir Afshani, for standing by my side and providing unconditional love, encouragement, and support in all aspects of my life.

Abstract

This research thesis focuses on two main studies involving micro/nano structural engineering of organic/inorganic semiconductor devices for development of next generation high performance and stable electronics. In the first project, we have explored the potential of GaN-based nanocrystals for the development of artificial photosynthesis devices for the conversion of CO_2 to syngas, a mixture of CO and H_2, and one of the promising future solar fuels. By integrating the Pt/TiO_2 cocatalyst with the strong light harvesting of p-n Si junction and efficient electron extraction effect of GaN nanowires, we demonstrated an efficient and stable photoelectrochemical (PEC) reduction of CO_2 into syngas product with controlled composition. It was found that the metal/oxide interface provides multifunctional catalytic sites that are inaccessible with the individual components, which structurally and electronically facilitate CO_2 conversion into CO. As a result, a record solar-to-syngas (STS) efficiency of 0.87 % and a benchmark turnover number (TON) of 24800 are achieved. In addition, we developed a decoupling strategy involving Au-Pt dual cocatalysts to achieve high energy conversion efficiency with controlled syngas composition. By integrating spatially separated a CO-generating catalyst (Au) and an H_2-generating catalyst (Pt) with GaN nanowires on planar Si photocathode, we achieved a record photon-to-current efficiency of 1.88 % and controllable syngas product with tunable CO/H_2 ratio (0–10) under one-sun illumination. Our designed PEC system exhibited highly stable syngas production in the 10 h duration test.

In the second project we investigated the improvement of organic field-effect transistors (OFETs) performance and stability using doping strategy. OFETs are emerging as promising building blocks for large-area printable and flexible electronics. However, they have yet to be implemented in practical applications due to operational challenges such as low mobility and device instability, both of which are linked to charge carrier trapping phenomena. Intentional molecular doping has been found to be an effective approach for mitigating trap states and enhancing the charge transport. However, unresolved issues such as unwanted off current and limited library of applicable molecular dopants have limited the effectiveness of the doping technique in addressing OFETs operational challenge. Here, we have introduced nitrofluorene (NF) acceptors as novel p-dopants for polymer OFETs due to superior solubility, air stability, and ease of energy level tunability. The addition of NFs to a standard commercial diketopyrrolopyrrole-thienothiophene

(DPP-DTT) polymer showed outstanding device performance, including an ~5-fold enhancement in the saturation field-effect mobility (up to ~8 $cm^2V^{-1}s^{-1}$), lowering threshold voltage, and one order of magnitude decrease in contact resistance. The NF-doping mechanism was investigated via spectroscopic, microscopic, and electrical characterization, which revealed the synergetic effect of filling deep traps and modified microstructure on significantly improved performance OFETs. In continue, we evaluated the environmental and operational stability of pristine and doped transistors. By exploring the impact of air exposure on pristine OFET performance, we found that suppression of electron-induced traps by oxygen doping, as well as diffusion of water molecules to semiconductor networks, lead to device environmental instability. We demonstrate that TeNF doping suppresses both effects, resulting in environmentally independent performance and good long-term stability of unencapsulated devices in ambient air (10% deterioration after 4 months storage). The doped OFETs also show significantly reduced bias stress effect and hysteresis. Such improvement of the environmental and operational stabilities is achieved by suppressing the majority-carrier traps (including electron-induced deep traps), and better microstructural order in TeNF doped polymer films.

Résumé

Cette thèse de recherche se concentre sur deux études principales impliquant l'ingénierie structurale micro/nano de dispositifs semi-conducteurs organiques/inorganiques pour le développement de l'électronique haute performance et stable de prochaine génération. Dans le premier projet, nous avons exploré le potentiel des nanocristaux à base de GaN pour le développement de dispositifs de photosynthèse artificielle pour la conversion du CO_2 en gaz de synthèse, un mélange de CO et H_2, et l'un des futurs carburants solaires prometteurs. En intégrant le cocatalyseur Pt/TiO_2 avec la forte collecte de lumière de la jonction p-n Si et l'effet d'extraction d'électrons efficace des nanofils de GaN, nous avons démontré une réduction photoélectrochimique (PEC) efficace et stable du CO_2 en produit de gaz de synthèse avec une composition contrôlée. Il a été constaté que l'interface métal/oxyde fournit des sites catalytiques multifonctionnels inaccessibles avec les composants individuels, qui facilitent structurellement et électroniquement la conversion du CO_2 en CO. un chiffre d'affaires de référence (TON) de 24800 est atteint. De plus, nous avons développé une stratégie de découplage impliquant des cocatalyseurs doubles Au-Pt pour atteindre une efficacité de conversion d'énergie élevée avec une composition de gaz de synthèse contrôlée. En intégrant spatialement séparés un catalyseur générateur de CO (Au) et un catalyseur générateur de H_2 (Pt) avec des nanofils de GaN sur une photocathode plane en Si, nous avons atteint un rendement photon-courant record de 1,88 % et un produit de gaz de synthèse contrôlable avec CO/accordable. Rapport H_2 (0–10) sous un éclairage solaire. Notre système PEC conçu a présenté une production de gaz de synthèse très stable dans le test de durée de 10 h.

Dans le deuxième projet, nous avons étudié l'amélioration des performances et de la stabilité des transistors à effet de champ organique (OFET) en utilisant une stratégie de dopage. Les OFET apparaissent comme des blocs de construction prometteurs pour l'électronique imprimable et flexible à grande surface. Cependant, ils doivent encore être mis en œuvre dans des applications pratiques en raison de défis opérationnels tels que la faible mobilité et l'instabilité du dispositif, qui sont tous deux liés aux phénomènes de piégeage des porteurs de charge. Le dopage moléculaire intentionnel s'est avéré être une approche efficace pour atténuer les états de piège et améliorer le transport de charge. Cependant, des problèmes non résolus tels qu'une bibliothèque hors tension indésirable et limitée de dopants moléculaires applicables a limité l'efficacité de la technique de

dopage pour relever le défi opérationnel des OFET. Ici, nous avons introduit des accepteurs de nitrofluorène (NF) en tant que nouveaux dopants p pour les OFET polymères en raison de leur solubilité supérieure, de leur stabilité à l'air et de leur facilité de réglage du niveau d'énergie. L'ajout de NF à un polymère DPP-DTT commercial standard a montré des performances de dispositif exceptionnelles, y compris une amélioration de ~5 fois de la mobilité à effet de champ de saturation (jusqu'à ~8 $cm^2V^{-1}s^{-1}$), une tension de seuil abaissée et un ordre diminution de l'ampleur de la résistance de contact. Le mécanisme de dopage NF a été étudié via une caractérisation spectroscopique, microscopique et électrique, qui a révélé l'effet synergique du remplissage des pièges profonds et de la microstructure modifiée sur des OFET aux performances considérablement améliorées. En continu, nous avons évalué la stabilité environnementale et opérationnelle de transistors vierges et dopés. En explorant l'impact de l'exposition à l'air sur les performances parfaites de l'OFET, nous avons constaté que la suppression des pièges induits par les électrons par dopage à l'oxygène, ainsi que la diffusion des molécules d'eau sur les réseaux de semi-conducteurs, entraînaient une instabilité environnementale de l'appareil. Nous démontrons que le dopage au TeNF supprime les deux effets, ce qui se traduit par des performances indépendantes de l'environnement et une bonne stabilité à long terme des dispositifs non encapsulés dans l'air ambiant (détérioration de 10 % après 4 mois de stockage). Les OFET dopés présentent également un effet de contrainte de polarisation et une hystérésis considérablement réduite. Une telle amélioration des stabilités environnementales et opérationnelles est obtenue en supprimant les pièges à porteurs majoritaires (compris les pièges profonds induits par les électrons) et un meilleur ordre microstructural dans les films polymères dopés au TeNF.

TABLE OF CONTENTS

List of Figures

List of Abbreviations

AFM	Atomic Force Microscopy
CE	Counter Electrode
CO	Carbon Monoxide
CO_2	Carbon Dioxide
COF	Covalent Organic Framework
ETL	Electron Transport Layer
FET	Field Effect Transistor
FWHM	Full Width at Half Maximum
GaN	Gallium Nitride
GC	Gas Chromatograph
GIWAXS	Grazing-Incidence Wide-Angle X-ray Scattering
GHC	Green House Gas
HOMO	Highest Occupied Molecular Orbital
HTL	Hole Transport Layer
HECs	Hydrogen Evolution Catalysts
HER	Hydrogen Evolution Reaction
HF	Hydrofluoric Acid
HRTEM	High Resolution Transmission Electron Microscopy
InGaN	Indium Gallium Nitride
InGaP	Indium Gallium Phosphide
InN	Indium Nitride
$KHCO_3$	Potassium Bicarbonate
LED	Light Emitting Diode

LUMO	Lowest Unoccupied Molecular Orbital
MBE	Molecular Beam Epitaxy
MOSFET	Metal Oxide Semiconductor Field Effect Transistor
MOFs	Metal-organic frameworks
NW	Nanowire
OFET	Organic Field-Effect Transistors
OLEDs	Organic Light Emitling Diodes
OPVs	Organic Photovoltaics
OSCs	Organic Semiconductors
OTS	Octadecyltrichlorosilane
PC	Photocatalytic or Photochemical
PEC	Photoelectrochemical
RHE	Reversible Hydrogen Electrode
RE	Reference Electrode
SAM	Self-Assembled Monolayers
SEM	Scanning Electron Microscopy
STS	Solar-to-Syngas
TEM	Transmission Electron Microscopy
TGA	Thermal Gravimetric Analysis
TON	Turnover Number
WE	Working Electrode
XPS	X-ray Photoelectron Spectroscopy
XRD	X-Ray Diffraction

Chapter 1 : Introduction

Semiconductors are a critical component of electronic technology and modern life, allowing breakthroughs in communications, computing, healthcare, clean energy, transportation, space exploration, and a variety of other real-life applications. Semiconductors are materials with finite band gap (E_g) between the occupied valence and empty conductance bands that can display electronic conductivity under certain conditions.[1,2] The band gap is the key feature of semiconductors that determines their electrical and optical properties, and it enables the development of electronic components such as transistors or photovoltaic cells, the output of which can be controlled by external stimuli such as light, temperature, electrical fields, etc.

Semiconductors are categorized as inorganics or organics based on their building blocks. Based on the differences in their electrical, chemical, and mechanical properties, each category provides distinct advantages and disadvantages for use in a wide variety of electronic applications and modern technologies. Inorganic semiconductors are composed of solid-state structures of group III, IV, and V elements (i.e., Si, Ge, GaN, GaAs) and metal oxides/chalcogenides (i.e., TiO_2, V_2O_5, CdS, ZnSe).[2,3] Because of their covalently bonded structures, most inorganic semiconductor materials offer more efficient charge transport properties, better structural rigidity, and stability compared to typical organic semiconductors, making them an excellent choice for high frequency or high power applications.[3] However, their low solubility, high temperature processing, and high manufacturing costs are significant drawbacks that limit their usage in many important applications.[3] Organic semiconductors, on the other hand, are carbon-based molecules or polymers with p-conjugated structures, bound together in solid state by relatively weak van der Waals forces.[4] Although the weaker intermolecular interactions, and lower degree of order limit the charge transport in OSCs, their exotic properties such as flexibility, low cost and low temperature fabrication, as well as solution processability make them ideal choices for flexible and printable electronics on large area surfaces (Figure 1.1). [4,5]

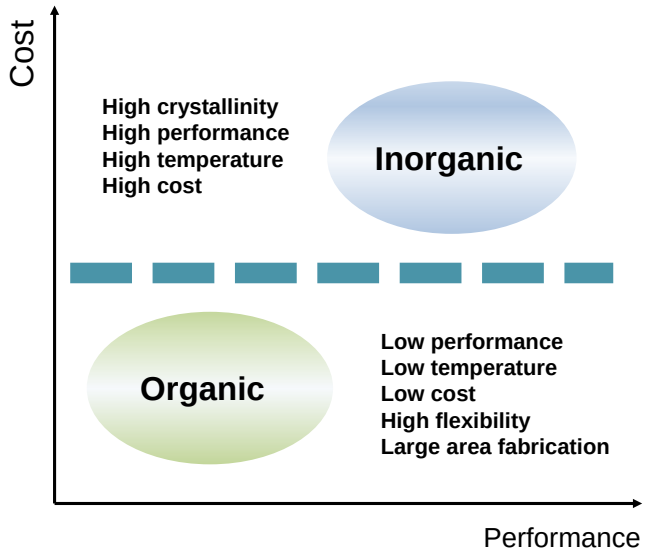

Figure 1.1: Comparing performance versus processing cost of organic and inorganic semiconductors.[6]

As the building blocks of modern technology, advancements in semiconductor technology have changed many parts of our life (communications, healthcare, energy, and so on), and the greatest potential still lies ahead. In this way, synthesis of new semiconductors or innovative hybridization of existing materials to provide desired properties for modern applications, advancements in processing and device fabrication, designing novel architectures and surface/interface engineering all play major role in the development of next generation high performance-stable semiconductor technology.

In this thesis, we have shed light on the process-structure-property-performance relationship in the development of high performance and stable electronic devices in two directions, inorganic and organic semiconductors. To achieve this goal, we have focused our efforts on two major global technological challenges: (I) The production of clean and affordable energy. (II) Development of low-cost, flexible microelectronics.

In the first project, we have demonstrated a novel photocathode based on III-nitrides inorganic semiconductors to address current challenges for high efficiency and robust systems for converting greenhouse gases (CO_2 in this case) to value-added fuels using sustainable solar energy. In the second project, carried out in Prof. D. F. Perepichka's lab we have studied the impacts of doping on the performance and stability of organic field effect transistors (OFETs), a key component of

flexible microelectronics. We introduced nitrofluorene as a new p-dopant family for OFETs and established its effectiveness in addressing the OFET commercialization bottlenecks by enhancing device figures of merit and operational/environmental stability. In the following sections, we will discuss the motivation, the current literature, and challenges for these two projects.

1.1 Motivation for CO_2 reduction into chemical fuels

Currently, the production of energy including heating and electricity relies mostly on non-sustainable fuels such as oils, coal, and natural gas. Consumption of such fossil fuels is the primary cause of global greenhouse gas emissions (GHG) and the climate changing crisis. The rising levels of carbon dioxide (CO_2) is recognized as the main contributor to the GHG emission (~79%) (Figure 1.2).[7] Substantial efforts have been made over the past two decades to control GHG emissions. On the other hand, a large portion of the world's population (3 billion) lacks access to affordable fuel for basic needs and over 10% still do not have access to electricity. The Sustainable Development Goals (SDG) of the United Nations aim to provide everyone with affordable, reliable, and sustainable energy, by 2030.[8] Therefore, development of an alternative clean fuel that is affordable for the whole population has become a global goal.

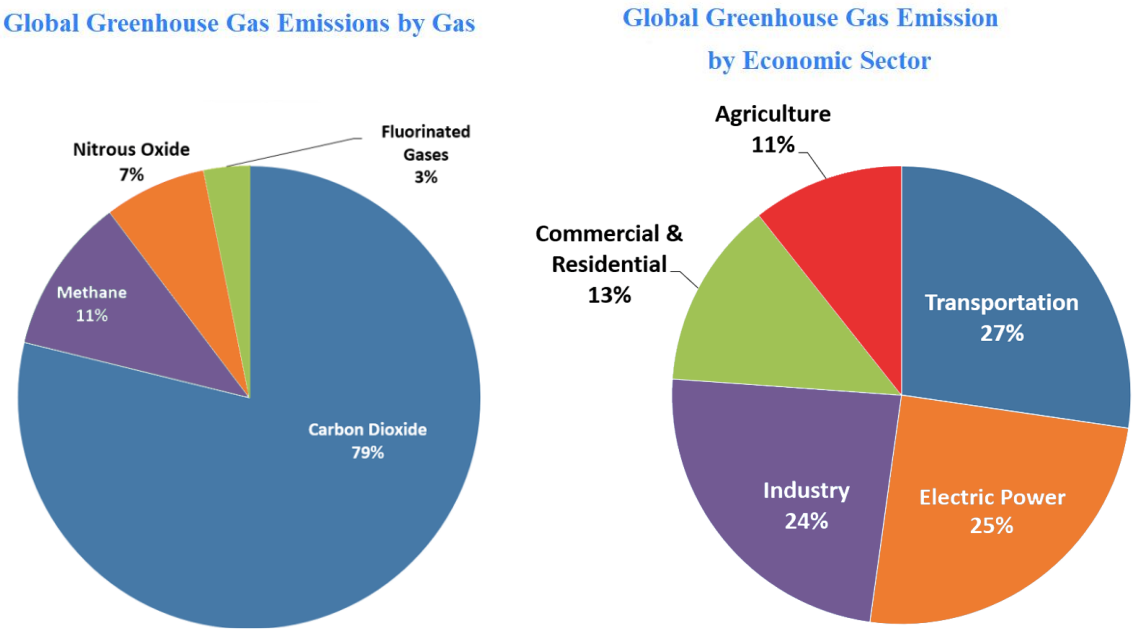

Figure 1.2: Global GHG emission produced by human activities in 2020 categorized based on the economic sectors that lead to their production. (Reproduced with permission from ref 7)

To achieve this goal, the scientific community is exploring several solutions for lowering CO_2 emissions or recycling it. Producing energy from renewable sources or consuming fuels with lower carbon levels than fossil fuels are among such solutions.[9] In particular, converting CO_2 into storable fuels (such as CH_3OH or CH_4) with the use of a sustainable energy would be an economic and less environmentally destructive strategy for addressing the CO_2 emission crisis.[9,10] The CO_2 could also be converted into valuable chemical products such as CO or HCOOH which would reduce the need of petroleum feedstock for chemical industry, while further mitigating the greenhouse gas emission. However, CO_2 is a thermodynamically stable molecule, and its reduction requires substantial amounts of energy or extremely reactive reagents.[11] In this context, photocatalytic (PC) and photoelectrochemical (PEC) approaches have been explored for CO_2 reduction. The former imitates the natural photosynthesis process by using solar energy to convert CO_2 into value-added chemicals.[12,13]

The first demonstration of photoelectrochemical and photocatalytic CO_2 reduction using semiconductor photocatalyst were reported by Halmann in (1978) and Inoue in (1979), respectively.[14,15] Since then, the majority of reported PEC and PC CO_2 reduction systems have relied on metal oxide photocatalysts such as TiO_2, ZnO, WO_3, and $SrTiO_3$, which generally are only active under UV irradiation (only 4% of the solar spectrum).[16] On the other hand, other photocatalysts such as CdS, ZnS, and SiC, have an appropriate bandgap for photocatalytic reactions in visible light (about 43% of the solar spectrum), but they are highly photodegradable.[17]

In this regard, development of photocatalysts that are both efficient and stable under visible light remains challenging.[18] III-nitride semiconductors (GaN, InN, and their ternary alloys) with a direct and narrow band gap for absorbing visible light and crossing the CO_2 reduction potential would be promising photocatalyst candidates.[19] In this research we have developed a novel photocatalyst based on III-nitride nanostructures for highly efficient and stable CO_2 reduction into fuel. We demonstrated high solar-to-syngas efficiency photoelectrochemical cell with tunable CO/H_2 ration by designing and synthesis metal/oxide cocatalyst (TiO_2-Pt) and dual metal cocatalyst (Au-Pt) integrated with GaN nanowires and Si solar cell platform.[20,21]

1.2 Motivation for development of organic field effect transistor

Digital technology has revolutionized our daily life, and it is difficult to imagine life without ubiquitous electronic devices that surround us, such as giant screens, personal computers,

smartphones, smart tags and sensors. The field-effect transistor (FET) is a fundamental building block of integrated circuits which is used as a switch or to amplify signals.[22] Thin film transistors based on inorganic semiconductors have dominated the microelectronics industry for more than 50 years. This first bipolar junction transistor (BJT) was fabricated based on germanium in 1947 at Bell Labs in New Jersey, by John Bardeen, Walter Brattain, and William Shockley, who won the Nobel Prize in Physics in 1956 for discovering the transistor effect.[23] In 1954, the first silicon transistor was demonstrated at Bell Labs by doping silicon single-crystals to control the conductivity, and it quickly replaced geranium transistors due to easier fabrication procedure.[24] Since then, numerous efforts have been made to decrease the size and fabrication costs of semiconductor devices while enhancing lifetime and reliability, which sparked the development of digital microelectronics and catapulted humanity into the Information era.

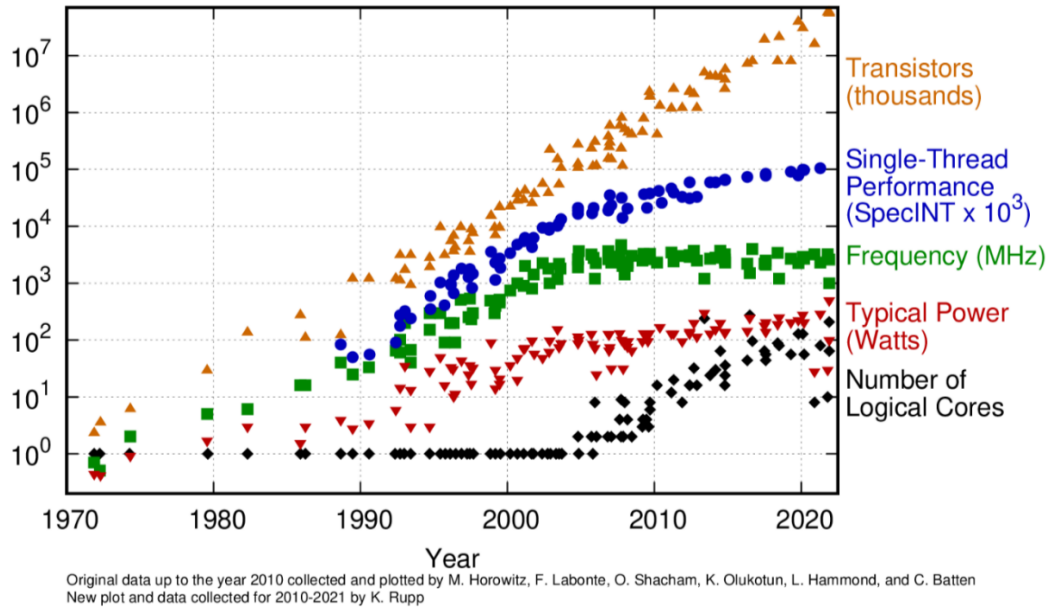

Figure 1.3: The evolution of Moore's law in past five decades. (Reproduced with permission from ref 25)

Gordon Moore published a paper in 1965, later termed Moore's law, in which he predicted that the size of transistors would decrease and the number of transistors on an integrated circuit would double every ~two years.[26] The Figure 1.3 highlights the evolution of Moore's law in past five decades.[25] Due to considerable breakthroughs in semiconductor technology and transistor miniaturisation over the past decades, the state-of-the-art integrated circuits include billions of silicon transistors.[27] On the other hand, electronic devices made of inorganic materials such as

silicon or III-V compounds are manufactured using a complex, non-ecofriendly, and expensive fabrication process that is relied on rigid substrates. Besides that, the needs of many next generation electronic applications such as flexible and foldable displays, wearable electronics, and stretchable sensors cannot be accomodated by silicon technology.

Consequently, other classes of semiconductor materials such as metal oxides, perovskites, quantum dots and organic semiconductors have attracted a lot of interest by microelectronics community. Organic materials drawn great attention in 1977, when Heeger and his coworkers discovered the semiconducting nature of plastics.[28] Since then organic semiconductors (OSCs) have been extensively studied in microelectronics, because of their exceptional properties such as flexibility and stretchability, low cost fabrication, and roll-to-roll printability on large area devices.[29,30] Many breakthroughs in organic material design, processing processes, and device engineering over the last few decades have resulted in substantial development in organic electronic devices such as organic light emitting diodes (OLED),[31,32] organic photovoltaic (OPV),[33,34] and organic field-effect transistors (OFET).[35,36] Between them OLEDs have had a tremendous impact on the technology market, and they are now widely available in many commercial products such as mobile phone displays, televisions, smart watches, and other portable digital devices (Figure 1.4).

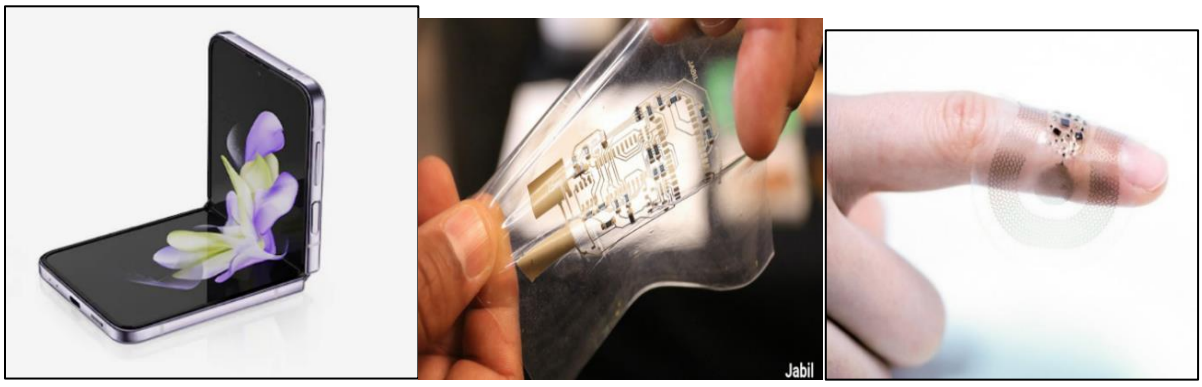

Figure 1.4: Implementation of flexible and stretchable organic electronic devices. (Reproduced with permission from ref 37)

OFET was introduced by Koezuka et al. in 1987 using polythiophene as the semiconductor component.[38] Since then, tremendous efforts have been made to develop high performance OFETs for use in various electronic and optoelectronic applications such as bioelectronics sensing devices, electronic tags, memory devices, or employing in the active-matrix backplane in optical displays.

Despite their promising mechanical properties, OSCs have lower mobilities as compared to inorganic semiconducting materials such as metal oxides and silicon.[29,30] Figure 1.5 compares the mobility of OFETs to other FET technologies with respect to processing temperature. Different technologies offer different benefits and drawbacks. Although OFETs have lower mobility than other competitors, their low temperature solution processability allows for low-cost fabrication on large area flexible substrates. While metal-oxide based FETs (> 10 $cm^2V^{-1}s^{-1}$), which are currently utilized as backplane in OLED displays, require high temperature (> 250°C) and highly cost manufacturing process.[39]

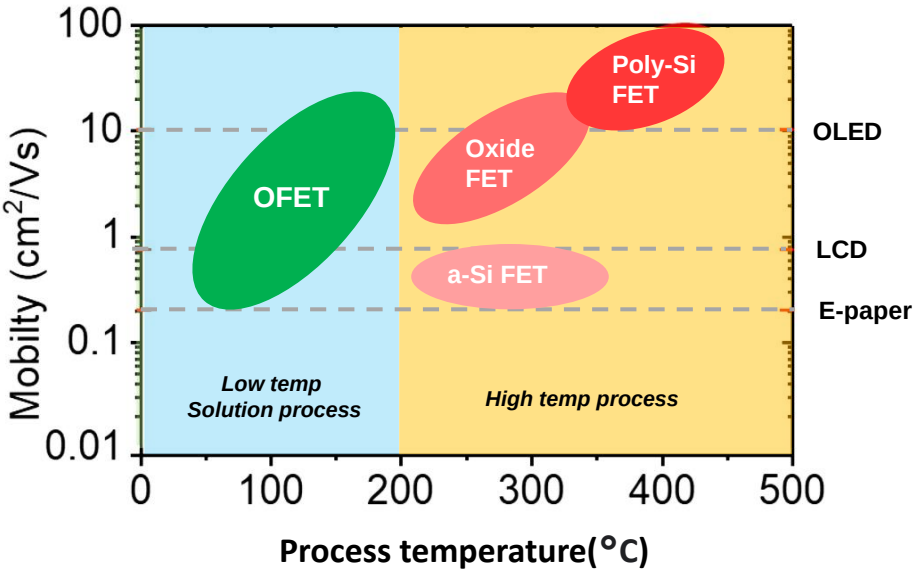

Figure 1.5: Mobility and processing temperature comparison in various FET technologies. (Reproduced with permission from ref 40)

The primary focus of OFET research in recent years has been on increasing the field effect mobilities, resulting in $\mu > 10$ $cm^2V^{-1}s^{-1}$. Despite significant advancements in OFET mobility, they have yet to be employed in practical applications due to insufficient operational and environmental stability.[29,41,42] In this research, we investigate OFET doping as an alternative approach to address OFET operational challenges. We introduce nitrofluorenone acceptors as promising p-dopants for polymer OFETs and demonstrate their effects on performance and stability of DPP-DTT polymer transistors.[43]

1.3 Organization of thesis

This research thesis focuses on two main studies involving micro/nano structural engineering of organic/inorganic semiconductors for development of next generation high performance and stable photoelectrochemical and polymer transistor devices.

Chapter 1 outlines a general introduction, the motivations and objectives for these studies and the contribution of research findings to original knowledge.

Chapter 2 provides an overview on fundamental backgrounds, a detailed literature review on state-of-the-art, the current challenges and the possible solutions for both PEC and OFET devices.

Chapter 3 introduces a novel photocathode based on GaN nanowires and metal-oxide (Pt-TiO_2) interface as cocatalysts for high efficiency photoelectrochemical reduction of CO_2 to syngas fuels.

Chapter 4 presents an efficient and stable PEC CO_2 reduction system for syngas production with controllable composition using Au-Pt dual cocatalysts.

Chapter 5 demonstrates the impact of novel nitrofluorenone (NF) p-type dopants on improving the performance of DPP-DTT polymer OFETs.

Chapter 6 evaluates the impact of NF doping on environmental and operational stability of DPP-DTT polymer OFETs.

Chapter 7 provides a conclusion to this thesis study and suggest future research opportunities.

1.4 Contribution to Original Knowledge

In this thesis, we have established the role of process-structure-property-performance relationship in the development of next generation high performance-stable semiconductor technology with two key objectives: (1) production of sustainable energy by implementation of novel III-nitrides base photocathode for PEC reduction of CO_2 into storable syngas fuels and (2) development of flexible microelectronics by addressing the operational challenges of polymer OFETs using doping approach

In ***Chapter 3***, we design and implement a novel TiO_2-Pt/GaN/Si photocathode for high efficiency PEC CO_2 reduction to syngas fuels. We demonstrate that incorporation of metal-oxide (Pt-TiO_2) interface as co-catalyst with efficient electron extraction of GaN nanowires and strong light harvesting of Si solar cell and, resulting in a benchmarking solar-to-syngas efficiency of 0.87%,

CO faradic efficiency of 78%, and desirable high stability of 10 h. We further show that CO/H_2 ratios of produced syngas could be tuned in a wide range between 4:1 and 1:6 at varied applied potentials. The findings of this study are published as "Photoelectrochemical CO_2 Reduction into Syngas with the Metal/Oxide Interface, Chu, S.[*] Ou, P.[*] Ghamari, P.[*] Vanka, S. Zhou, B. Shih, I. Song, J, Mi, Z, *J. Am. Chem. Soc*. 2018, *140*, 7869-7877. [[*] Authors contributed equally to this work]."

In ***Chapter 4***, we introduce Au-Pt dual co-catalyst to increase conversion efficiency and enhance the controllability of PEC CO_2 reduction to syngas fuels. We demonstrate $AuPt_{0.2}$/GaN/Si photocathode results in a record solar-to syngas efficiency of 1.88%, CO faradic efficiency of 90%, photostability of 10 h and a benchmark turnover number (TON) of ~60000. The spatially separated H_2 evolution and CO evolution catalytic cities lead to superior tunability of CO/H_2 ratios product from 1:99 and 10:1, by simply varying the composition of dual cocatalysts. The results of this study are published as "Decoupling Strategy for Enhanced Syngas Generation from Photoelectrochemical CO_2 Reduction, S. Chu* P. Ou*, R Rashid*, P. Ghamari*, R. Wang, N. Tran, S. Zhao, H. Zhang, J. Song, Z. Mi, *iScience*, 2020, *23*, 101390. [* These authors contributed equally to this work]."

In ***Chapter 5***, we introduce nitrofluorenone derivatives as novel p-dopants for polymer OFETs and demonstrate its effectiveness on enhancing the DPP-DTT based OFETs figures of merit, including an ~5-fold enhancement in field-effect mobility (up to ~8 $cm^2V^{-1}s^{-1}$), lowering threshold voltage, and one order of magnitude decrease in contact resistance. The spectroscopic and microscopic characterization reveal that the synergetic effect of filling deep traps and modified microstructure lead to significantly improved performance of OFETs. The findings of Chapter 5 are published as "Controlling Structural and Energetic Disorder in High-Mobility Polymer Semiconductors via Doping with Nitroaromatics, P. Ghamari, M. R. Niazi and D. F. Perepichka, *Chem. Mater*. 2021, *33*, 2937-2947."

In ***Chapter 6***, we evaluate the impact of NF doping on environmental and operational stability of transistors. We demonstrate that air exposure of pristine DPP-DTT OFET leads to suppression of electron-induced traps by oxygen doping in the short term, and diffusion of water molecules to semiconductor networks in the long term which resulting in environmental instability of devices. TeNF doping suppresses both effects, resulting in environmentally independent performance and

4 months long-term stability of unencapsulated devices in ambient air. TeNF-doped OFETs also exhibit much lower hysteresis and bias stress impact. The enhanced stability of TeNF doped OFETs is achieved by suppressing majority-carrier traps (including electron-induced deep traps) and improving microstructural order in TeNF doped polymer films. Chapter 6 is based on a manuscript under preparation: Improved environmental and operational stability of polymer field-effect transistors via doping with tetranitrofluorenone. Ghamari, P.; Niazi, M. N.; Perepichka, D. F. *to be submitted*, 2022.

1.5 Contribution of Authors

This dissertation includes the contribution from the candidate and other individuals. The majority of this PhD research was carried out in chemistry department of McGill University under supervision of Prof. Dmytro Perepichka. He provided funding and research objectives for OFET projects, and intellectual guidance for preparing the entire PhD thesis. The CO_2 reduction projects were done under supervision of Prof. Zetian Mi in the electrical engineering department and McGill Nanotools Microfab lab. The contribution of individuals to the works presented from chapter 3 to chapter 6 is described as follows:

Chapter 3: Candidate, Dr. Chu and Prof. Zetian Mi conceived the ideas and worked together on results analysis and discussions. Candidate performed all the cleanroom work for fabrication of Si solar cell bases (HF etching, p-n doping and annealing, and PV analysing). The GaN nanowire growth was done by Dr. Vanka. All the PEC experiments were done by candidate including designing and optimizing the photocathodes (synthesizing Pt particles and TiO_2 nanosheets) and conducting the PEC measurements and analysis. The structural characterizations (TEM, SEM) were performed by Dr. Chu. Dr. The computational analysis was done by Dr. Ou and Prof. Song.

Chapter 4: Dr. Candidate conceived the initial ideas and developed the strategies with help of Dr. Chu and Prof. Zetian Mi. Candidate performed all the cleanroom work for fabrication of Si solar cell bases (HF etching, p-n doping and annealing, and PV analysing). The GaN nanowire growth was done by Dr. Rashid, Dr. Wang, and Dr. Hong. All the PEC experiments were done by candidate including designing and optimizing the photocathodes (synthesizing Pt-Au particle) and conducting the PEC measurements. Dr. Rashid participated in the final step of the PEC experiments and performed some control experiments. Structural characterizations (TEM, SEM) were done by Dr. Chu and Dr. Rashid. Dr. Ou and Prof. Song did computational analysis.

Chapter 5: Candidate conceived the initial ideas and develop the strategies with help of Prof. Perepichka. All the OFET fabrications electrical characterizations were done by candidate herself. Candidate performed all the morphology and microstructural analysis (AFM, GIWAXS). Dr. Hatem Titi helped with GIWAXS characterization. All the spectroscopic analysis including UV-Vis, PYSA and EPR analysis were done by candidate herself. Dr. Stein guided the candidate for EPR characterizations. Candidate analysed the results and provided discussions with help of Prof. Perepichka and Dr. Niazi. Prof. Igor F. Perepichka from Northwestern Polytechnical University provided dopants compounds.

Chapter 6: Candidate conceived the initial ideas and develop the strategies with help of Prof. Perepichka. All the OFET fabrications and characterizations were done by candidate herself. The OFET environmental characterization setup was prepared by candidate with help of Dr. Dadvand. The morphology and microstructural analysis (AFM, GIWAXS) were done by candidate herself. Candidate performed temperature dependent EPR analysis with guidance of Dr. Stein. Candidate analysed the results and provided discussions with the help of Prof. Perepichka and Dr. Niazi. Prof. Igor F. Perepichka from Northwestern Polytechnical University provided dopants compounds.

1.6 References

1. Kittel, C. *Introduction to Solid State Physics*; John Wiley & Sons: New York, **2005**.
2. Schroder, D. K. *Semiconductor Material and Device Characterization*, 3rd ed.; John Wiley & Sons: New York, **2006.**
3. Grundmann, M. *The Physics of Semiconductors: An Introduction Including Nanophysics and Applications*; Springer-Verlag: Berlin, **2010**.
4. Brütting, W. *Physics of Organic Semiconductors*; WILEY-VCH Verlag: Weinheim, Germany, **2004**.
5. Qian, Y.; Zhang, X. W.; Xie, L. H.; Qi, D. P.; Chandran, B. K.; Chen, X. D.; Huang, W. Stretchable Organic Semiconductor Devices. *Adv. Mater.* **2016**, *28*, 9243−9265.
6. Kumar, B.; Kaushik, B. K.; Negi, Y. S. Organic Thin Film Transistors: Structures, Models, Materials, Fabrication, and Applications: A Review. *Polym. Rev.* **2014**, *54*, 33−111.
7. U.S. Environmental Protection Agency. https://www.epa.gov/ghgemissions/overview-greenhouse-gases. Accessed 1 August **2022**.
8. United nations. https://sdgs.un.org/goals. Accessed 10 August **2022**.

9. Hernandez, S.; Farkhondehfal, M. A.; Sastre, F.; Makkee, M.; Saracco, G.; Russo, N. Syngas Production from Electrochemical Reduction of CO_2: Current Status and Prospective Implementation. *Green Chem*. **2017**, *19*, 2326−2346.
10. Roy, S. C.; Varghese, O. K.; Paulose, M.; Grimes, C. A. Toward Solar Fuels: Photocatalytic Conversion of Carbon Dioxide to Hydrocarbons. *ACS Nano* **2010**, *4*, 1259-1278.
11. Chu, S.; Kong, X.; Vanka, S.; Guo, H.; Mi, Z. Artificial Photosynthesis on III-nitride Nanowire Arrays. *Semicond. Semimetals* **2017**, *97*, 223−255..
12. Wu, J.; Huang, Y.; Ye, W.; Li, Y. CO_2 Reduction: From the Electrochemical to Photochemical Approach. *Adv. Sci*. **2017**, *4*, 1700194.
13. Olah, G. A.; Goeppert, A.; Prakash, G. K. S. Chemical Recycling of Carbon Dioxide to Methanol and Dimethyl Ether: From Greenhouse Gas to Renewable, Environmentally Carbon Neutral Fuels and Synthetic Hydrocarbons. *J. Org. Chem*. **2009**, *74*, 487–498.
14. Halmann, M. Photoelectrochemical Reduction of Aqueous Carbon-Dioxide on p-Type Gallium-Phosphide in Liquid Junction Solar-Cells. *Nature* **1978**, *275*, 115–116.
15. Inoue, T.; Fujishima, A.; Konishi, S.; Honda, K. Photoelectrocatalytic Reduction of Carbon-Dioxide in Aqueous Suspensions of Semiconductor Powders. *Nature* **1979**, *277*, 637–638.
16. Abe, R. Recent Progress on Photocatalytic and Photoelectrochemical Water Splitting under Visible Light Irradiation. *J. Photochem. Photobiol., C* **2010**, *11*, 179−209.
17. Kudo, A.; Miseki, Y. Heterogeneous Photocatalyst Materials for Water Splitting. *Chem. Soc. Rev*. **2009**, *38*, 253−278.
18. Mao, J.; Li, K.; Peng, T. Y. *Catal. Sci. Technol*. **2013**, *3*, 2481− 2498.
19. Kibria, M. G.; Mi, Z. Artificial photosynthesis using metal/ nonmetal-nitride semiconductors: current status, prospects, and challenges. *J. Mater. Chem. A* **2016**, *4*, 2801−2820.
20. Chu, S.; Ou, P.; Ghamari, P.; Vanka, S.; Zhou, B.; Shih, I.; Song, J.; Mi, Z. Photoelectrochemical CO_2 reduction into syngas with the metal/oxide interface. *J. Am. Chem. Soc*. **2018**, *140*, 7869− 7877.
21. Chu, S.; Ou, P.; Rashid, R. T.; Ghamari, P.; Wang, R.; Tran, H. N.; Zhao, S.; Zhang, H.; Song, J.; Mi, Z. Decoupling Strategy for Enhanced Syngas Generation from Photoelectrochemical CO_2 Reduction. *iScience* **2020**, *23*, 101390.
22. Sirringhaus, H. Device Physics of Solution-Processed Organic Field-Effect Transistors. *Adv. Mater.* **2005**, *17*, 2411–2425.

23. Shockley, William B., John B.; Walter H. B. *Nobel prize in physics 1956-presentation speech*.
24. Riordan, M. The Lost History of the Transistor, *IEEE Spectrum*, **2004**, 48-49.
25. https://github.com/karlrupp/microprocessor-trend-data. Accessed 5 August **2022**.
26. Moore, GE. Cramming more components onto integrated circuits, *Electronics*, **1965**, *86*, 114.
27. https://www.ibm.com/thought-leadership/innovation-explanations/mukesh-khare-on-smaller-transistors-analytics/ Accessed 1 Jun **2022**.
28. Chiang, C.K.; Fincher Jr, C.R.; Park, Y.W.; Heeger, A.J.; Shirakawa, H.; Louis, E.J.; Gau, S.C.; MacDiarmid, A. G. Electrical conductivity in doped polyacetylene. *Physical review letters*, **1977**, *39*, 1098.
29. Sirringhaus, H. 25th Anniversary Article: Organic Field-Effect Transistors: The Path Beyond Amorphous Silicon. *Advanced Materials*. **2014**; *26*, 1319-1335.
30. Dong, H.; Fu, X.; Liu, J.; Wang, Z.; Hu, W. 25th Anniversary Article: Key Points for HighMobility Organic Field-Effect Transistors. *Advanced Materials*. **2013**, *25*, 6158-6182.
31. Cicoira, F.; Santato, C. Organic Light Emitting Field Effect Transistors: Advances and Perspectives. *Advanced Functional Materials*. **2007**, *17*, 3421-3434.
32. Murawski, C.; Leo, K.; Gather, M. C. Efficiency Roll-Off in Organic Light-Emitting Diodes. *Advanced Materials.* **2013**, *25*, 6801-6827.
33. Mishra, A.; Bäuerle, P. Small Molecule Organic Semiconductors on the Move: Promises for Future Solar Energy Technology. *Angew. Chemie Int. Ed*. **2012**, *51*, 2020– 2067.
34. Leo, K. Organic photovoltaics. *Nature Reviews Materials*, **2016**, *1*, 16056.
35. Ward, J. W.; Lamport, Z. A.; Jurchescu, O. D. Versatile organic transistors by solution processing. *ChemPhysChem*, **2015**, *16*, 1118–1132.
36. Reese, C.; Bao, Z. Organic single-crystal field-effect transistors. *Mater. Today*, **2007**, *10*, 20.
37. (a) https://www.samsung.com/ca/smartphones/galaxy-z-flip4/buy/ Accessed 10 August **2022**. (b) https://www.semi.org/en/communities/flextech/what-are-flexible-electronics. 10 August **2022**. (c) https://www.nature.com/articles/d41586-021-00739-z, Accessed 10 August **2022**.
38. Koezuka, H.; Tsumura, A.; Ando, T. Field-effect transistor with polythiophene thin film. *Synthetic Metals.* **1987**, *18*, 699-704.
39. Zhu, H.; Shin, E. S.; Liu, A.; Ji, D.; Xu, Y.; Noh, Y. Y. Printable semiconductors for backplane TFTs of flexible OLED displays. *Adv. Funct. Mater.* **2020**, *30*, 1904588.
40. https://www.azom.com/article.aspx?ArticleID=9210. Accessed 17 August **2022**.

41. Paterson, A. F.; Tsetseris, L.; Li, R.; Basu, A.; Faber, H.; Emwas, A. H.; Panidi, J.; Fei, Z.; Niazi, M. R.; Anjum, D. H.; Heeney, M.; Anthopoulos, T. D. Addition of the Lewis Acid $Zn(C_6F_5)_2$ Enables Organic Transistors with a Maximum Hole Mobility in Excess of 20 cm(2) V(-1) s(-1). *Adv Mater.* **2019**, *31*, 1900871.
42. Uemura, T.; Rolin, C.; Ke, T. H.; Fesenko, P.; Genoe, J.; Heremans, P.; Takeya, J. On the Extraction of Charge Carrier Mobility in High-Mobility Organic Transistors. *Adv. Mater.* **2016**, *28*, 151−155.
43. Ghamari, P.; Niazi, M. R.; Perepichka, D. F. Controlling Structural and Energetic Disorder in High-Mobility Polymer Semiconductors via Doping with Nitroaromatics. *Chem. Mater.* **2021**, *33*, 2937−2947.

Chapter 2 : Fundamental Background and Literature Review

This chapter provides an overview of fundamental principles, current state-of-the-art, existing challenges, and possible solutions in two research areas of this thesis: (1) photoelectrochemical CO_2 reduction to syngas based on III-nitrides nanowires and (2) doping strategy for improving the performance of organic field effect transistors.

2.1 CO_2 reduction to syngas based on III-nitride nanostructures

2.1.1 Photoelectrochemical and photochemical CO_2 reduction

CO_2 reduction is a promising route for reducing the planetary greenhouse effect and converting it into valuable chemicals and storable sustainable fuels.[1,2] However, CO_2 is a thermodynamically stable molecule, therefore its reduction requires substantial amounts of energy.[3] In this regard, the photoelectrochemical (PEC) and photocatalytic (PC) conversions are two sustainable approaches using solar energy and proper photocatalysts for efficient CO_2 reduction. A PEC cell consists of a photoactive semiconductor as the working electrode (WE), a counter electrode (CE) which is usually Pt, a reference electrode (RE) such as single-junction Ag/AgCl, and appropriate electrolyte such as $KHCO_3$.[4,5]

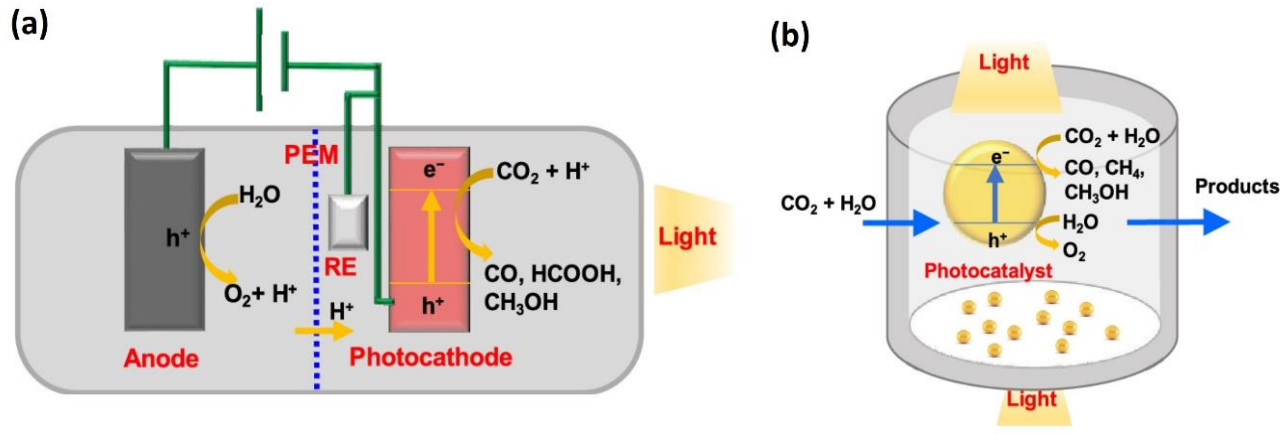

Figure 2.1: (a) Photoelectrochemical and (b) photochemical reaction cell.[6]

In a PEC cell, the CO_2 reduction happens in the cathode and water oxidation occurs in the anode. A PEC cell combines light absorption, charge generation and separation, hole, electron, ionic and molecular transport functions in a single device (Figure 2.1a).[6] In the photochemical (PC)

technique, CO_2 reduction occurs directly through light absorption, charge carrier separation, and catalytic reactions in an integrated system. (Figure 2.1 b).[6] PC CO_2 reduction is a wireless approach that requires no external bias. This results in less control over the reaction and, in most cases, lower efficiency, but it makes the system simpler and more cost effective.[6,7]

2.1.2 Photoelectrochemical CO_2 reduction to syngas

Syngas is a CO and H_2 mixture that serves as a crucial feedstock to produce various liquid fuels such as methanol. It is currently produced by a steam reforming of methane (a non-renewable fossil fuel) but could in principle be made by reduction of CO_2 and H_2O. CO_2 reduction requires efficient catalysts and sufficient energy input to active linear CO_2 molecule.[3] PEC and PC CO_2 reduction suffer from poor performance, due to competing reaction pathways and diverse reduction products including carbon monoxide (CO), formic acid (HCOOH), methane (CH_4), ethylene (C_2H_4). Moreover, the hydrogen evolution reaction (HER) is kinetically favored over the CO_2 reduction reaction (CO_2RR).[1] Therefore, CO_2 reduction to syngas, which combines both CO_2RR and HER, would be a more efficient photocatalytic reaction (Table 2.1).

Table 2.1: Standard electrochemical potentials for CO_2 reduction reactions (standard Nernst potentials (E°) at 25 °C, 1 bar and pH = 7).[1]

Reaction	E^o (V vs. NHE)
Potential of CO_2 reduction reactions	
$CO_2 + 2H^+ + 2e^- \rightarrow CO + H_2O$	−0.53
$CO_2 + 2H^+ + 2e^- \rightarrow HCOOH$	−0.61
$CO_2 + 4H^+ + 2e^- \rightarrow H_2CO + H_2O$	−0.48
$CO_2 + 8H^+ + 8e^- \rightarrow CH_4 + H_2O$	−0.38
$CO_2 + 6H^+ + 2e^- \rightarrow CH_3OH + H_2O$	−0.24
$CO_2 + e^- \rightarrow CO_2^{\cdot -}$	−1.9
Oxidation Potential of H_2O	
$2H_2O \rightarrow O_2 + 4H^+ + 4e^-$	+0.82

Various semiconductor photocathodes, including p-Si, ZnTe, CdTe, p-InP, p-GaP, p-GaN, p-NiO Cu_2ZnSnS_4, Cu-based photocathodes (e.g., CuO, Cu_2O, $CuBi_2O_4$, and $CuFe_2O_4$), and some phosphorus compounds have been investigated for PEC CO_2 reduction into CO,[8-16] usually in conjunction with a molecular metal-complex or metal co-catalyst (e.g., Au, Ag, and derivatives) to realize selective CO production. However, it remains challenging to develop efficient and stable PEC catalytic system that can activate inert CO_2 molecule at a low overpotential, and selectively produce syngas with controlled composition in a wide range required for synthesis of different downstream products (i.e., methanol).[3,17]

Numerous novel photocatalysts have been designed and studied in order to achieve this goal. Chu et al. demonstrated highly efficient PEC CO_2 reduction to syngas system using ZnO-Cu/GaN/Si photocathode. A high Faradaic efficiency of 70% for CO was obtained at a low onset potential of 0.07 V vs. RHE, and stability of 10 h. However, the CO/H_2 ratio in the products was 1:2, which is proper ratio for only few downstream such as methanol.[18] A wafer-scale nanoconed Si arrays substrate decorated with Au and Cu nanoparticles has been found to achieve $CO:H_2$ ratio from 1:2 to 1:6. The use of Cu co-catalyst resulted in a CO Faradaic efficiency of 15% and a total efficiency of 44% into syngas, at an applied potential of –1.6 V vs. Ag/AgCl.[19] An artificial photosynthetic system using an N-TiO_2 photoanode that converts CO_2 into syngas with a conversion efficiency of 14% and a Faradaic efficiency of 80%. The system is tunable with a wide range of $CO:H_2$ ratio between 1:2 and 5:1.[20] Palladium nanomeshes (Pd-NMs) constructed with branch-like Pd nanoparticles demonstrated a low onset potential of –0.4 V vs. RHE, the efficient CO_2 into syngas reduction with a Faradaic efficiency of 90% (at applied –0.6 V vs. RHE) and a wide range of CO/H_2 ratios.[21] It has been demonstrated that using a photoelectrode-photovoltaic tandem system with two absorbers for PEC CO_2 reduction is an alternative strategy to achieve high conversion efficiency. Tandem PV-PEC cells with a triple-layered ZnO@ZnTe@CdTe core-shell photocathode decorated with gold nanoparticles and a $CH_3NH_3PbI_3$ perovskite solar cell resulted in 80% CO Faradaic efficiency and solar-to-CO conversion efficiency over 0.35% and solar to fuel efficiency of 0.43%.[22] On the other hand, integration of $CH_3NH_3PbI_3$ perovskite solar cell with PEC cell using IrO_2 as an anode and oxidized Au as a cathode led to achieving solar-to-CO efficiency of 6.5% and solar to fuel of 7%.[23]

2.1.3 III-nitride materials as photocatalyst

III-nitride semiconductor materials, such as GaN, InN, and their ternary alloys have attracted a lot of research interest in optoelectronics due to their exceptional electrical, optical, and structural properties. As shown in figure 2.2, the band gape of III-nitrides can be tuned from 0.7 eV (InN) to 6 eV (AlN) by varying In and Al composition in ternary alloys.[24] Covering the entire solar spectrum and having high absorption coefficient makes III-nitrides promising choice for solar energy harvesting systems such as water splitting or CO_2 reduction.[25,26] Furthermore, high charge carrier mobility due to near defect-free structure, resulting in excellent charge carrier extraction for efficient solar-fuel conversion. The high crystallinity and N-terminated surface of III-nitrides also result in superior photo stability, making them outstanding choices for photoanodes and photocathodes.[17,25]

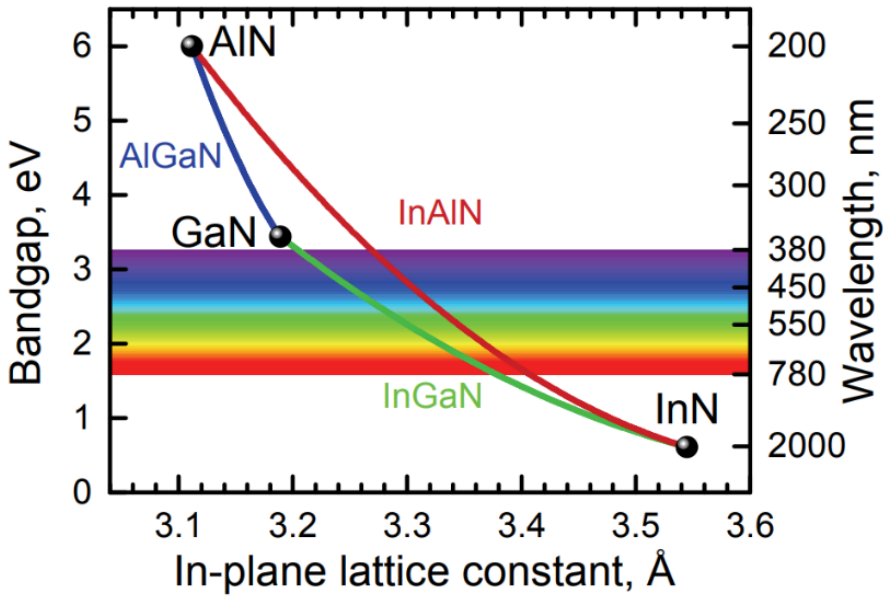

Figure 2.2: Bandgaps of wurtzite GaN, AlN and InN and their alloy (Reproduced with permission from ref 34).

Figure 2.3 compares band-edge positions of $In_xGa_{1-x}N$ photocatalysts with conventional semiconductor photocatalysts vs. RHE. By varying In composition, the bandgap of $In_xGa_{1-x}N$ can be tuned from 0.64 to 3.4 eV, which is narrower than of most metal oxide materials but still large enough to cover the redox potentials of CO_2 reduction and water splitting in a large range of pH

solutions.[17] The conduction band edge of GaN is more negative than of most metal oxides (1.2 V versus NHE at pH 0), providing a large potential difference for the reduction of CO_2 molecules.[3,17]

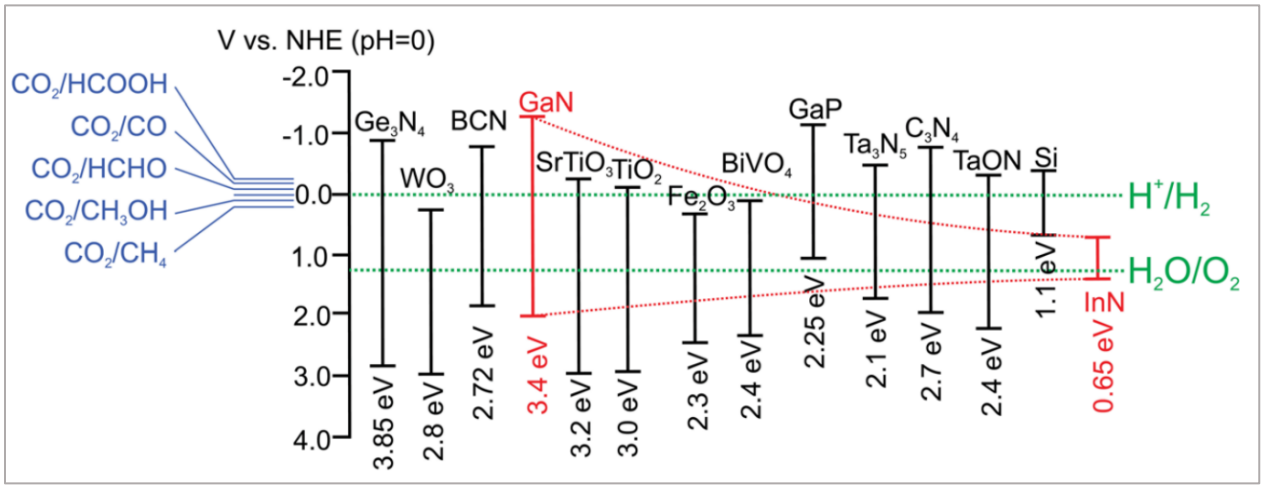

Figure 2.3: Band-edge positions of III-nitride photocatalysts compared with that of other conventional semiconductor photocatalysts. Red dotted lines show band-edge positions of $In_xGa_{1-x}N$, in which x represent In compositions and increases from left to right (0-1). Green dotted lines show the oxidation and reduction potentials of water. Blue lines show the reduction potentials of CO_2 to various to other carbon-based chemicals (Reproduced with permission from ref 17).

2.1.4 III-nitride nanostructures

The near dislocation free nature of III-nitrides nanowires (NWs) provides substantial advantages over the thin film semiconductors for photocatalytic applications. The lower density of lattice dislocation in III-nitride nanowires results in fewer nonradiative recombination sites for carriers as compared to planar III-nitride devices.[27] The array of nanowires provides a large surface area for reaction site and loading co-catalyst for photocatalytic applications.[28] Furthermore, nanowire arrays dramatically boost light absorption due to light trapping and scattering effects. The reflection in 1D nanostructures is substantially lower than in 2D grown films.[29] Based on the unique properties of III-nitride and 1D nanowires (NWs), such as strong light absorption, rapid electron-hole separation, negligible carrier recombination, and large surface area for catalytic reactions, InGaN and GaN NWs offer a suitable platform for high solar-to-fuel conversion (Figure 2.4).[17]

In this study, III-nitrides nanowires (GaN NWs) were grown using plasma-assisted molecular-beam epitaxy (MBE), which is a proper method for the defect-free growth of high quality crystalline planar and nanowire semiconductors.[3,17]

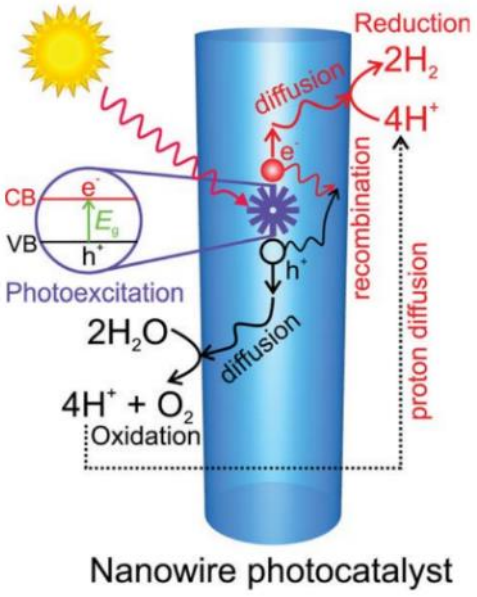

Figure 2.4: Schematic of artificial photosynthesis process on surface of nanowire photocatalysts including photoexcitation, carrier generation, diffusion, recombination, and oxidation-reduction in water splitting. (Reproduced with permission from ref 17).

2.1.5 CO_2 reduction using GaN nanowires

The first demonstration of GaN nanowire arrays for direct photochemical reduction of CO_2 into CH_4 and CO was reported by Al Otaibi et al. in 2015.[30] The bare GaN nanowires were found to have higher photoactivity for CO production than CH_4, with evolution rates of 47 and 1.3 μmol g^{-1} h^{-1}, respectively. It was demonstrated that the use of Rh/Cr_2O_3 core/shell or Pt nanoparticles on GaN NW walls significantly improves the selectivity for CH_4 formation over CO.[30] Applying Rh/Cr_2O_3 core/shell cocatalyst results in an increase in CH_4 formation rate up to 3.5 μmol g^{-1} h^{-1} with one order of magnitude lower CO formation rate. On the other hand, introduction of Pt nanoparticles increases the CH_4 evolution rate to 14.8 μmol g^{-1} h^{-1}, while no change on CO formation. This study demonstrates the potential of GaN NW for selective CO_2 reduction (Figure 2.5).

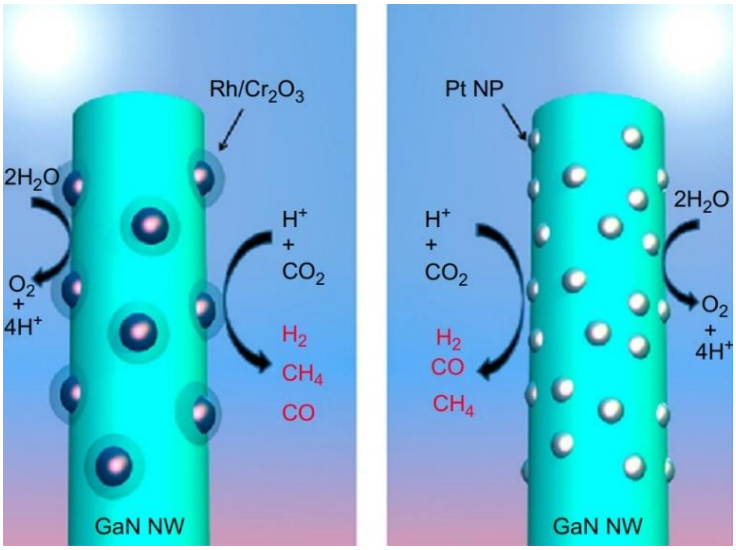

Figure 2.5: Schematic of the photoreduction processes of CO_2 on Rh/Cr_2O_3 and Pt-decorated GaN nanowires. (Reproduced with permission from ref 30).

The impact of NW band gap engineering on photocatalytic activity has been investigated, by using GaN/InGaN NWs for CO_2 reduction under visible light. Alloying GaN with Indium results in InGaN NW with a 50% In composition and a band gap of 1.7eV, which is still acceptable for CO_2 reduction and water oxidation.

By decorating GaN/InGaN with Pt nanoparticles, Al Otaibi et al. demonstrate high CO_2 conversion to CH_3OH with an evolution rate of rate of 0.5 mmol g^{-1} h^{-1} under visible light irradiation and in the presence of H_2 reagent (Figure 2.6a).[31] It is also demonstrated that the surface properties of the nanowire may be precisely modified using an intentional doping strategy. The incorporation of Mg dopant increases the photocatalytic activity of CO_2 reduction by 50-fold due to a reduced surface potential barrier and increased CO_2 molecule adsorption.[31]

The integration of GaN nanowires with a p-n junction modified with a Cu cocatalyst resulted in a Cu/GaN/Si photocathode that enables for highly selective CO_2 reduction to CH_4 (Figure 2.6b). This integrated structure combines strong light harvesting of Si p-n junction and efficient electron extraction effect of GaN nanowire arrays. With copper as the cocatalyst, the device demonstrated a 30 times greater Faradaic efficiency of 19% for CO_2 to CH_4 compared to 0.6% for CO_2 to CO.[32]

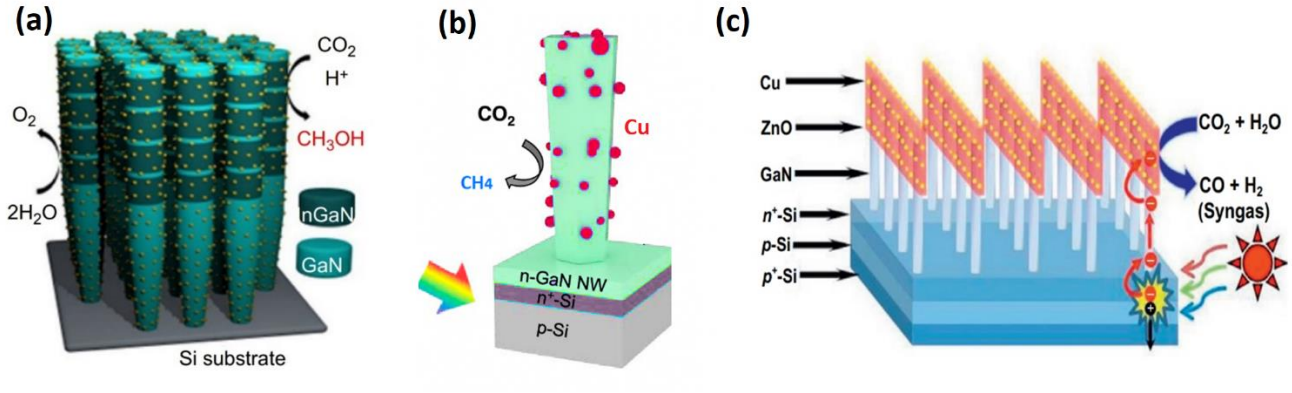

Figure 2.6: Schematic of (a) p-InGaN/GaN NW photocatalyst decorated with Pt nanoparticles (b) Cu/GaN/n^+-p Si photocathode (c) Cu–ZnO/GaN/n^+-p Si photocathode. (Reproduced with permission from ref 18,31,32)

Chu et al, demonstrated highly efficient PEC CO_2 reduction to syngas system, using ZnO-Cu/GaN/Si photocathode (Figure 2.6c). A high Faradaic efficiency of 70% for CO was obtained at an underpotential of 180 mV because of the joint impact of strong light harvesting of p-n junction Si, rapid electron extraction of GaN NWs, and fast surface reaction kinetics of Cu-ZnO cocatalysts.[18] The CO/H_2 ratio in the products was 1:2, which is an ideal mixture for industrial methanol production. It is suggested that employing Cu-ZnO cocatalysts offers synergistically absorption and activation of CO_2 on ZnO and protons/electrons transferring reactions on Cu. This work piqued our interest in conducting more investigation on III-nitrides cocatalysts for CO_2 reduction into syngas.

2.2 Development of high performance and stable OFETs using doping strategy

2.2.1 Organic semiconductors

Organic semiconductors (OSCs) are carbon-based materials with conjugated double bonds where the π-π interactions enable charge transport. The properties of OSC, such as electrical and mechanical properties or solubility, can be tailored by modifying the structure of the molecule or adding different side groups.[33] Organic semiconductors, like inorganic semiconductors, can be classified as p-type or n-type depending on the main charge transporting carriers. A p-type semiconductor is a hole-transport material with low ionization potential (IP) while an n-type semiconductor is an electron-transporting material, possessing a high electron affinity (EA).[34,35]

Organic semiconductors derived from conjugated molecules and side groups are generally categorized into two groups of small molecules such as pentacene and rubrene, and polymers such as P3HT and DPP-DTT.[36]

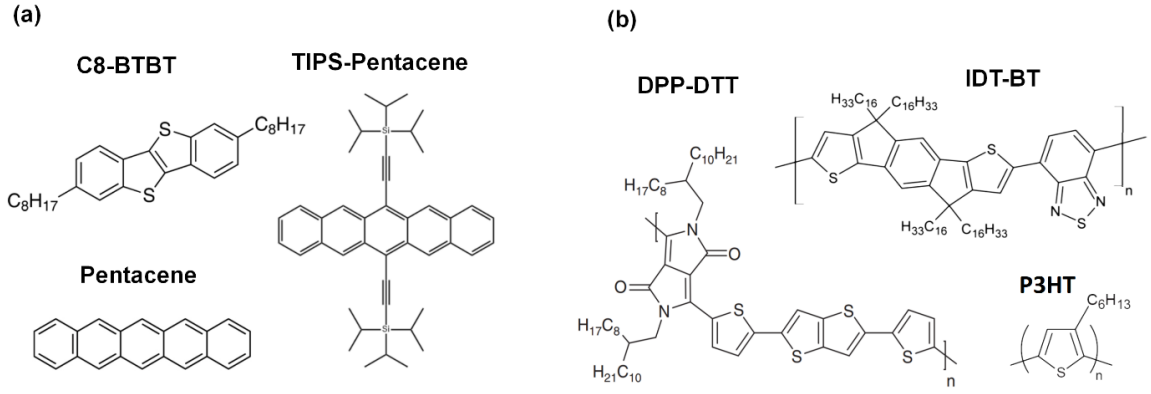

Figure 2.7: Chemical structure of some well-known (a) small molecules, (b) polymers.

Small molecule semiconductors are conjugated polycyclic compounds with low molecular weight that can pack into well-organized polycrystalline films. This packing results in superior intermolecular charge transfer and higher mobility than polymer semiconductors. Small molecules, on the other hand, are typically more difficult to process from solution compared to polymers, and vacuum deposition is the most common method of film deposition.[37] Typical examples of small-molecule OSCs are linear fused-ring aromatic molecules (e.g., pentacene and rubrene), heteroaromatic oligomers (e.g., oligothiophenes) and two-dimensional fused ring compounds (e.g., porphyrine and phthalocyanine derivatives). Figure 2.7 depicts some common organic small molecule and polymer OSC. Pentacene is one the most studied OSCs consisting of five linearly fused benzene rings and showed OFET mobility up to 3 $cm^2\ V^{-1}s^{-1}$ in polycrystalline thin film and even higher mobility of 35 $cm^2\ V^{-1}s^{-1}$ were reported based on space-charge limited current measurements in single crystals.[38] However, due to poor solubility of pentacene in common hydrocarbon solvents, it isn't usable for low-cost large area solution processible OFET fabrication. Attaching bulky groups of triisopropyl-silylethynyl (TIPS) to pentacene, Anthony et al. developed a soluble derivative 6,12-bis(tri-*iso*-propylsilylethynyl)pentacene, known as TIPS-pentacene. The attached side chains are not only act as solubilizing groups, but also force the conjugated rings to stack in a two-dimensional bricklayer arrangement improving the π–π orbital overlap in the crystal. This enabled solution processable OFETs with high field effect mobilities in the range of 1-11

$cm^2V^{-1}s^{-1}$.[39,40] Cn-BTBTs are another family of small molecules with high solubility due to their alkyl chains; among them, the C8-BTBT has shown remarkable OFETs performance with reported mobility above 10 $cm^2V^{-1}s^{-1}$ in single components and up to 20 $cm^2V^{-1}s^{-1}$ in polymer blend systems (Figure 2.7a).[41,42]

Polymers are made up of repeated molecular subunits that together form very large molecules with covalently bound carbon backbones. The covalent polymer chains are held together in solids by weak van der Waals forces, and often have spaghetti-like microstructures, which gives polymers their unique flexibility.[38] It also leads to amorphous or semicrystalline microstructures with low long-range order which limits charge transport. Poly(3-hexylthiophene) known as P3HT is one of the very first solution-processed polymer used as active layer in p-type OFETs.[43] It has been demonstrated that head-to-tail self-orientation of P3HT provides a well-ordered lamellar structure with a preferable edge-on orientation of the thiophene rings to the substrate results in mobility ranging 0.05-0.2 $cm^2V^{-1}s^{-1}$.[44]

Donor-acceptor (D-A) polymers with an alternating array of donor and acceptor moieties are one of the recently developed polymers with narrow band gaps and strong intramolecular charge transport which have demonstrated to be promising OSCs for high performance OFETs.[45] The key feature that enables high performance D–A polymers is tailoring the microstructure and electronic structure through the appropriate choice of donor or acceptor units. The majority of reported high mobility OFETs based on p-type D-A polymers contain diketopyrrolopyrrole (DPP), isoindigo (IIG), and benzothiadiazole (BT)-based acceptors, have planar structure, rigid backbone, and strong intermolecular interaction.[46]

BT-based polymers are one of the most extensively researched D-A polymers in OFETs. It's reported that copolymerizing BT with IDT donor unit, indacenodithiophene-co-benzothiadiazole (IDT-BT), resulted in OFET mobility about 1 $cm^2V^{-1}s^{-1}$, despite having a near-amorphous structure.[46,47] The relatively high mobility of IDT-BT is attributed to the planar and torsional-free conformation of IDT-BT polymers, which results in a low energetic disorder (24 meV).[48] Increasing the molecular weight of IDT-BT or blending it with small molecules increased OFET mobility to 4 and 13 $cm^2V^{-1}s^{-1}$, respectively.[25,49] Copolymerization of the BT acceptor unit with another extended fused aromatic building unit, indacenodithieno[3,2-b]thiophene (IDTT), resulted in a high degree of backbone planarity and an increase in hole mobility up to 8 $cm^2V^{-1}s^{-1}$.[50]

CDT-based polymers are another class of high-performance D-A polymer. The CDT donor unit lowers the reorganization energy, which significantly enhances intermolecular interactions and improve OFETs performance. It has been reported that copolymerizing CDT and BT, cyclopentadithiophene-benzothiadiazole (CDT-BT), resulted in a high mobility exceeding 10 $cm^2V^{-1}s^{-1}$.[51,52]

The DPP unit is one of the most promising acceptor units in high-performance D-A polymers owing to its great planarity and a strong electron deficiency. Since the invention of DPP-based D-A polymers, numerous high-performance DPP-based OFETs have been reported, among which copolymerizing with thienothiophene (TT) and (E)-1,2-di(2-thienyl)ethene (TVT) donor units are the best performing OFETs with mobility up to 10 and 18 $cm^2V^{-1}s^{-1}$respectivly.[53,54] Although numerous advancements in molecular design of D-A polymers and processing strategies lead to significant improvement in OFET performance and reporting mobilities exceeding 20 $cm^2\ V^{-1}\ s^{-1}$ for p-type D–A polymer, the nonlinearity of OFET transfer curves caused by carrier trapping at bulk OSC and OFETs interfaces led to significant overestimation in most of the reported mobilities.[55,56] To avoid such overestimations, Choi et al, has proposed to calculate effective mobility (μ_{eff}) for OFETs that exhibit nonideal behaviour, instead of saturation mobility (μ_{sat}).[57] We calculated the effective mobility for high mobility p-type OFETs reported in the last ten years using recent reviews and the proposed method (Equations 2.6 and 2.7 below).[46,57-59]

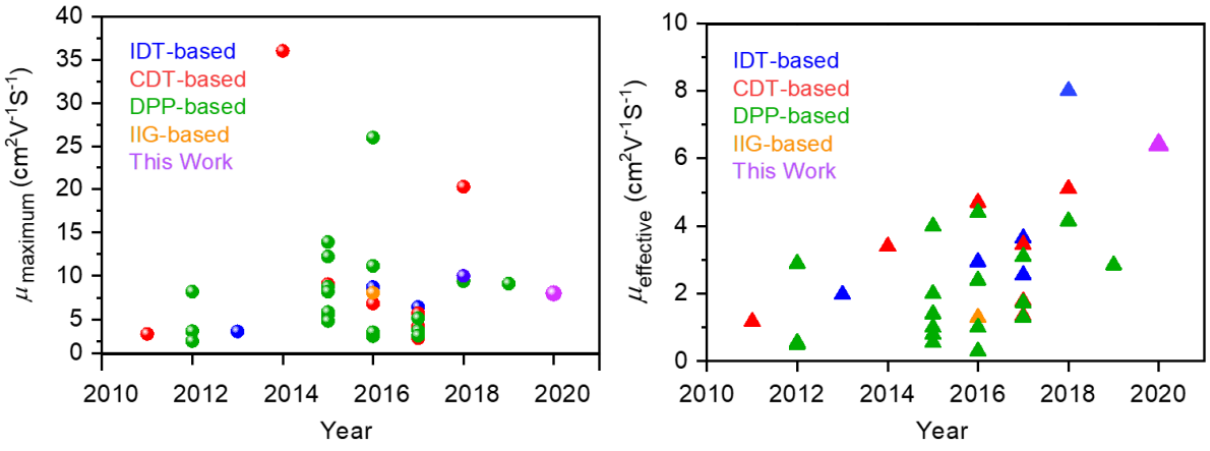

Figure 2.8: Comparison between the maximum and the effective hole mobility of reported high-performance polymer semiconductor OFETs. (left) The maximum reported saturation hole mobility of high-performance polymer OFETs; only data for polymer OFETs with μ_{sat}>2.5 $cm^2V^{-1}\ S^{-1}$ are selected. (right) Calculated reliability factors and effective mobility of the same OFETs.[46,58]

As shown in Figure 2.8, from all state-of-art polymer OFETs reported in the last decade, only a few examples have the effective mobility of 5-10 $cm^2V^{-1}s^{-1}$.

2.2.2 The charge transport in organic semiconductors

In the context of solid-state physics, conjugated polymers can be described as a disordered net of conduction routes in which charge carriers are delocalized within a conjugated segments and "hop" to neighboring segments. Therefore, the charge transport mechanism through disordered polymers is known as the hopping mechanism.[60,61] In contrast, for highly ordered and defect free organic crystals, charge carriers are thought to be delocalized throughout the bands that extend the entire crystal. So, charge transport in highly ordered periodic crystals is best described by band-like transport.[62] In practice, a hybrid model that incorporates extended states in bands and localized states in the bandgap is more realistic model for the vast majority of disordered high-mobility organic materials. This model is known as multiple trapping and release (MTR) and was developed by Le Comber and Spear for amorphous silicon (Figure 2.9).[60-62]

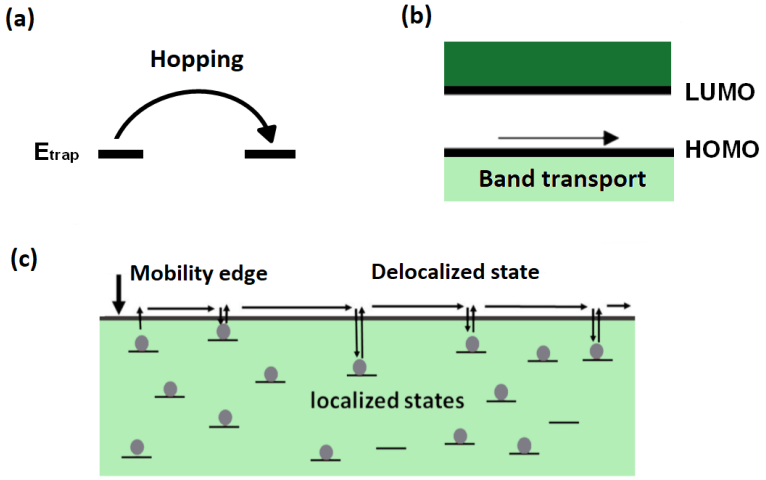

Figure 2.9: Charge transport models. (a) Hopping between localized states, (b) band-like charge transport, (c) multiple trapping and release (MTR) model that combines trap states with band-like charge transport.[63]

The free carrier that are captured by localized states, known as traps, wouldn't contribute to electrical current, hence the overall conductivity in MTR model is dominated by the localized trap states that lie next to the band edge (HOMO/LUMO for p-type/n-type materials). Figure 2.10 depicts the density of states (DOS) for an organic semiconductor based on the MTR model. Highly

disordered systems show broad DOS, but more ordered systems have considerably narrower DOS.[64] Based on the relative position of trap states to the band-edge, they are categorized into two types:

(i) Localized states within few k_BT of the band-edge are termed shallow traps, and charge carriers can be thermally excited into/relaxed from extended band states.

(ii) Traps that positioned much further than k_BT from the band-edge are deep traps which have a negligible probability of being thermally excited.

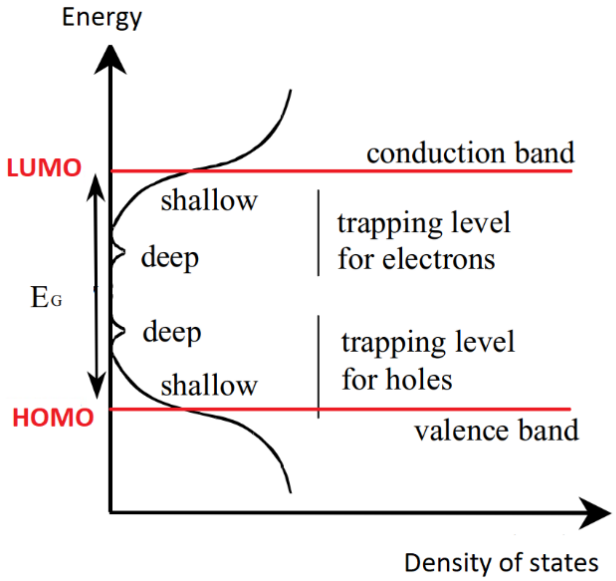

Figure 2.10: Density of states for multiple trapping and release model.[65]

2.2.3 The origin of trap states in organic semiconductors

OSC trap states can originate from either intrinsic or extrinsic factors. Static disorder caused by chemical impurities or structural defects that form during or after film (or crystal) formation is the primary cause of intrinsic traps in OSCs. Structural defects in polycrystalline small molecules are mostly caused by displacement or misorientation of molecules from their equilibrium positions or intramolecular distortion. In polymers, twisted chains and entanglements, or boundaries at crystalized domain are few causes of structural defects.[66] Extrinsic traps can be introduced from surrounding environment (such as oxygen or water), through intentional doping, or via contact with other materials such as metals, dielectrics, or other OSCs.[66,67] Figure 2.11 shows different sources of trap states in OSCs.

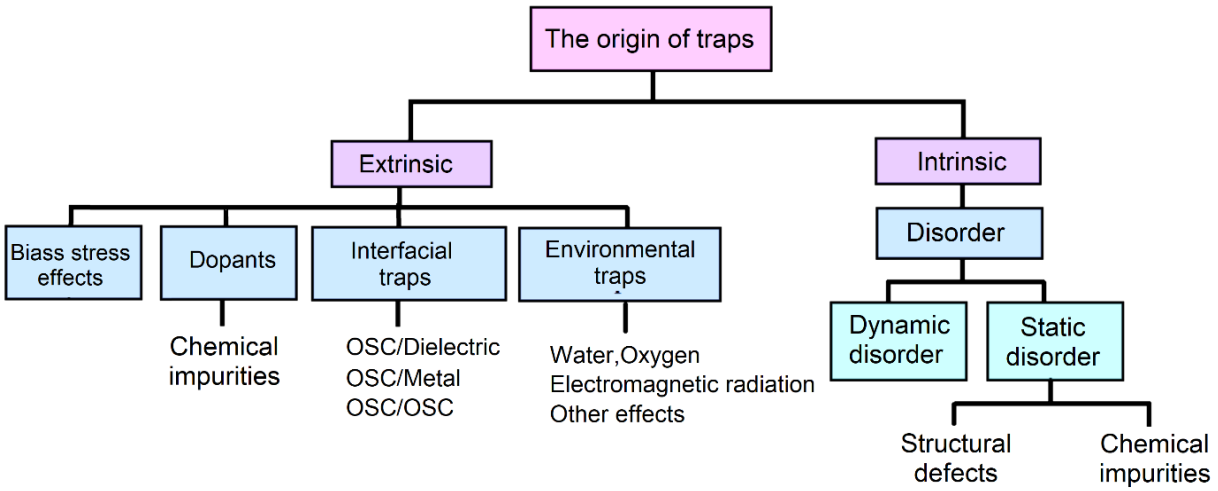

Figure 2.11: Origin of f charge carrier traps in OSCs. (Reproduced with permission from ref 67)

2.2.4 Organic Field-effect transistors

2.2.4.1 The operation principle

OFETs are three-therminal devices built on a metal-insulator-semiconductor (MIS) capacitor with a gate electrode in direct contact with dielectric and two metallic electrodes in direct contact with the OSC known as source and drain gate electrodes(Figure 2.12). When external electric field is the applied between gate and source electrodes (V_{GS}), the charges accumulate at the interface between the OSC and the dielectric, with the charge polarity opposite to that applied voltage.

The accumulated charge forms a conductive pathway at the OSC/dielectric interface, known as a channel, allowing charge carriers to flow through it by applying a constant voltage between drain and source (V_{DS}). V_{DS} acts as a driving force for charge movement, V_{GS} determines the size of the active channel (charge carrier density in the accumulated layer) and the flow of charges through the channel is defined as (I_{DS}).[68,69]

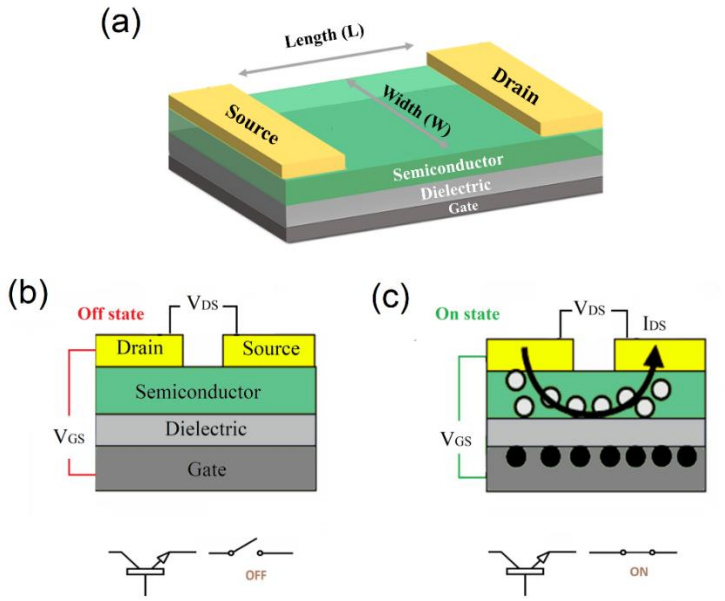

Figure 2.12: (a) OFET architecture, (b) OFET schematic in off-state (c) OFET schematic in on-state.

Depending on the sequence in which the drain/source and gate contacts are deposited relative to the OSC and dielectric layers, OFETs are commonly fabricated in one of the following four configurations: bottom-gate top-contact (BG-TC), bottom-gate bottom-contact (BG-BC), top-gate bottom-contact (TG-BC) and top-gate-top-contacts (TG-TC) as shown in Figure 2.13.

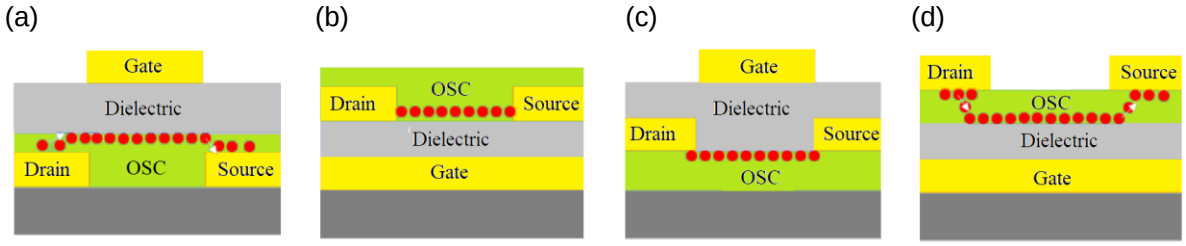

Figure 2.13: (a) Top gate bottom contact, TG-TC. (b) Bottom gate bottom contact, BG-BC. (c) Top gate top contact, TG-TC. (d) Bottom gate top contact, BG-TC.

Top-contact transistors usually show higher field effect mobility due to better microstructural order/morphology of OSC film formed on a smooth dielectric surface, as compared to that in vicinity of metal electrodes in bottom-contact devices. On the other hand, top-contact OFET manufacturing and downsizing of top-contact devices are limited by metal contact deposition (usually by evaporation through a shadow mask). The top-gate configuration often involves the

deposition of polymer dielectric, which could increase the complexity of device manufacture while also preventing the deterioration of the underlying OSC by the ambient environment.[70]

2.2.4.2 Extraction of OFETs parameters

The electrical performance of OFETs can be determined by two types of current-voltage characteristics, known as the transfer and output characteristics (Figure 2.14). Transfer curves represent the measured I_{DS} at sweeping V_{GS} under a constant V_{DS} and are used for extraction of the field effect mobility (μ), the threshold voltage (V_{th}) and the subthreshold swing (SS), the on-state I_{DS}, the off-state I_{DS}, and their ratio (I_{ON}/I_{OFF}).

Output characteristics consist in measuring I_{DS} while sweeping the V_{DS} at constant V_{GS}. These characteristics exhibit two regimes: 1) linear and 2) saturation regime. In the linear regime ($V_{DS} < V_{GS}-V_{th}$), I_{DS} increases linearly with V_{DS} due to accumulation of charges at OSC/dielectric, increasing the conductivity of OSC at interface. On the other hand, the magnitude of I_{DS} becomes independent of V_{DS} in the saturation regime ($V_{DS} > V_{GS}-V_{th}$). Accumulated charges in the channel are depleted at the drain electrode when $V_{DS} >> V_{GS}-V_{th}$, resulting in a channel pinch-off and I_{DS} becoming constant. Output curves can be used to determine the contact resistance (see below).[71,72]

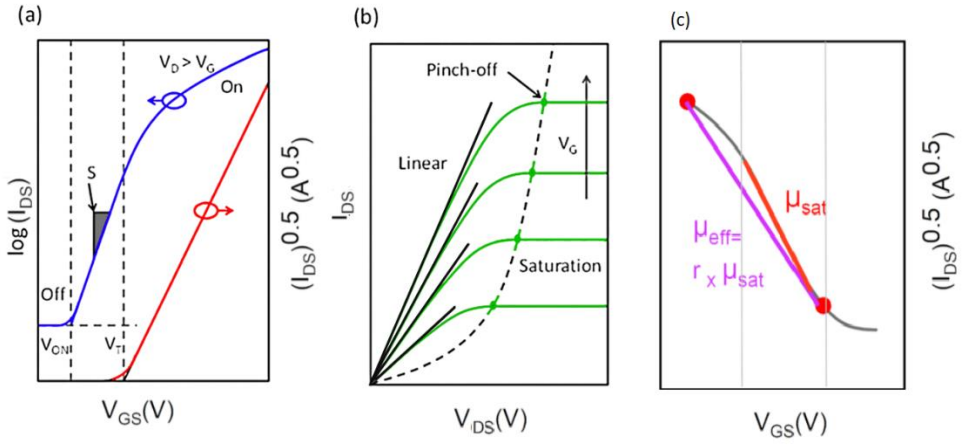

Figure 2.14: (a) Transfer and (b) Output characteristics (c) Effective vs saturation mobility.

The transistor I_{DS} in the linear and saturation regimes can be estimated using conventional MOSFET equations established using the gradual channel approximation.[56] This model is based on the assumption that $V_{GS} > V_{DS}$, and mobility is not dependent on charge carrier density in the channel. The IDS in accumulation mode is described by equation 2.1.

$$I_{DS} = \frac{WC_i}{L}\mu[(V_{GS} - V_{th})]V_{DS} - \frac{1}{2}{V_{DS}}^2 \quad (2.1)$$

where, W and L are the width and the length of the channel, Ci is the gate dielectric capacitance per unit area, and μ is the field effect mobility (hole or electron).

In the linear regime ($V_{DS} << V_{GS}-V_{th}$), equation 2.1 is written as equation 2.2

$$I_{DS}(lin) = \frac{WC_i}{L}\mu_{lin}[(V_{GS} - V_{th})]V_{DS} \quad (2.2)$$

The linear mobility (μ_{lin}) can be extracted from equation 2.2. μ_{lin} is obtained by differentiating I_{DS} with respect to V_{GS}:

$$\mu_{lin} = \frac{L}{WC_iV_{DS}}\frac{\partial I_{DS}lin}{\partial V_{GS}} \quad (2.3)$$

The $\frac{\partial I_{DS}lin}{\partial V_{GS}}$ will be determined from the slope of the transfer characteristics in the linear regime. In the saturation regime ($V_{DS} >> V_{GS}-V_{th}$), equation 2.1 is modified to equation 2.4.

$$I_{DS}(sat) = \frac{WC_i}{2L}\mu_{sat}[(V_{GS} - V_{th})]^2 \quad (2.4)$$

The saturation mobility (μ_{sat}) can then be calculated using equation 2.5:

$$\mu_{sat} = \frac{2L}{WC_i}\frac{\partial^2 I_{DS}sat}{\partial {V_{GS}}^2} \quad (2.5)$$

The $\frac{\partial^2 I_{DS}sat}{\partial {V_{GS}}^2}$ can be extracted from the slope of the transfer characteristics ($I_{DS}^{0.5}$ vs V_{GS}) measured in the saturation regime, as shown in Figure 2.14. For the OFETs with V_{GS}-dependent mobility, the effective mobility (μ_{eff}) is calculated using equation 2.6:

$$\mu_{eff} = r_{sat} \times \mu_{sat} \quad (2.6)$$

In which r_{sat} is reliability factor, and it is defined as the ratio of the maximum channel conductivity experimentally achieved in a FET at the maximum gate-source voltage to the maximum channel conductivity expected in a correctly functioning ideal FET with the claimed carrier mobility μ_{sat}

and identical other device parameters at the same maximum gate-source voltage (Figure 2.14c). The reliability factor is calculated using equation 2.7:

$$r_{sat} = \left(\frac{\sqrt{|I_{DS}|^{\max}} - \sqrt{|I_{DS}|^{0}}}{|V_{GS}|^{\max}} \right)^2 \Big/ \left(\frac{\mathrm{WCi}}{2L} \mu_{sat} \right) \qquad (2.7)$$

Other figures of merit such as V_{th}, I_{ON}/I_{OFF}, and SS can be extracted the transfer characteristics on a logarithmic scale (log I_{DS} vs V_{GS}) and as $I_{DS}^{0.5}$ vs V_{GS}. OFET switching grade is determined by the ratio of maximum and minimum I_{DS} values (I_{ON}/I_{OFF}) from the transfer curve. V_{th} can be extracted by liners extrapolating of transfer curves to the V_{GS} axis, as shown in Figure 2.14. **2.2.4.3 Contact resistance**

The energy difference between the work function (φ_m) of metal and the HOMO (LUMO) of the p-type (n-type) semiconductor causes a potential barrier for charge injection at the metal/semiconductor interface known as a Schottky barrier (see Figure 2.15).[72,73] Contact resistance is the result of a potential barrier existing at the contact and it can significantly reduce the performance of OFETs due to the drain voltage drop at the contact, resulting in lower charge mobilities in the channel. To decrease the contact resistance in OTFTs, the height of the φ_B can be reduced by choosing a metal with a suitable φ_m for the HOMO (LUMO) of the OSC.[73,74] However the limitation of metals with high enough work function for p-type OSCs (φ_m > 5 eV) and instability concerns with proper metals for n-type OSCs (φ_m < 4 eV) confine the library of proper metals for OFETs contacts. Employing the appropriate OFET architecture is another approach for reducing contact resistance.

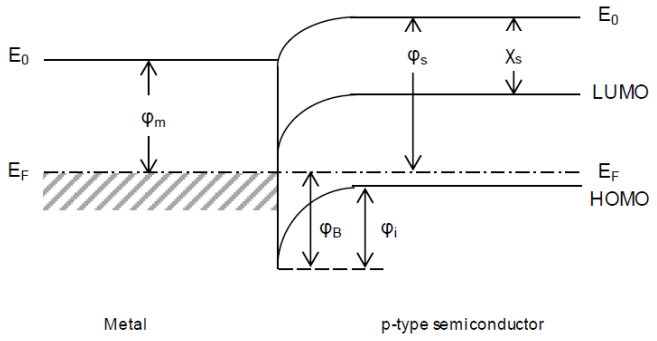

Figure 2.15: Energy diagram depicting Schottky barrier at metal/OSC interface.

It is frequently emphasised that OFETs with bottom contact configuration exhibit higher contact resistance due to poor microstructural properties of growth film near the metal contacts. Use of a

self-assembled monolayer (SAM) that intentionally induces a dipole at the metal surface could change the actual work function of the source and drain electrodes and modify the potential barrier. Reducing contact resistance using OSC doping is an alternate strategy that is widely used in the inorganic semiconductor devices and could be an effective technique to offer efficient charge injection.[75-77] (The effect of doping on contact resistance in OFET is discussed further in session 2.2.10). Output curves are used to determine the contact resistance of OFET devices via the transmission line method (TLM).[74] This method determines output curves (I_{DS} vs V_{DS}) for OFETs with varying channel lengths. The total resistance is calculated using equation 2.8:

$$R_{ON} = \frac{\partial V_{DS}}{\partial I_{DS}} = R_{ch} + 2R_C \qquad (2.8)$$

Where, R_{ON} is total resistance, R_{ch} is channel resistance R_C is contact resistance. The $\frac{\partial V_{DS}}{\partial I_{DS}}$ can be extracted from the slope of output characteristics in the linear regime as shown in Figure 2.16. The R_{ON} is plotted as a function of channel lengths for various V_{GS}, and extrapolation of this curve to channel length (L) = 0 provides $2R_C$, as shown in Figure 2.16.

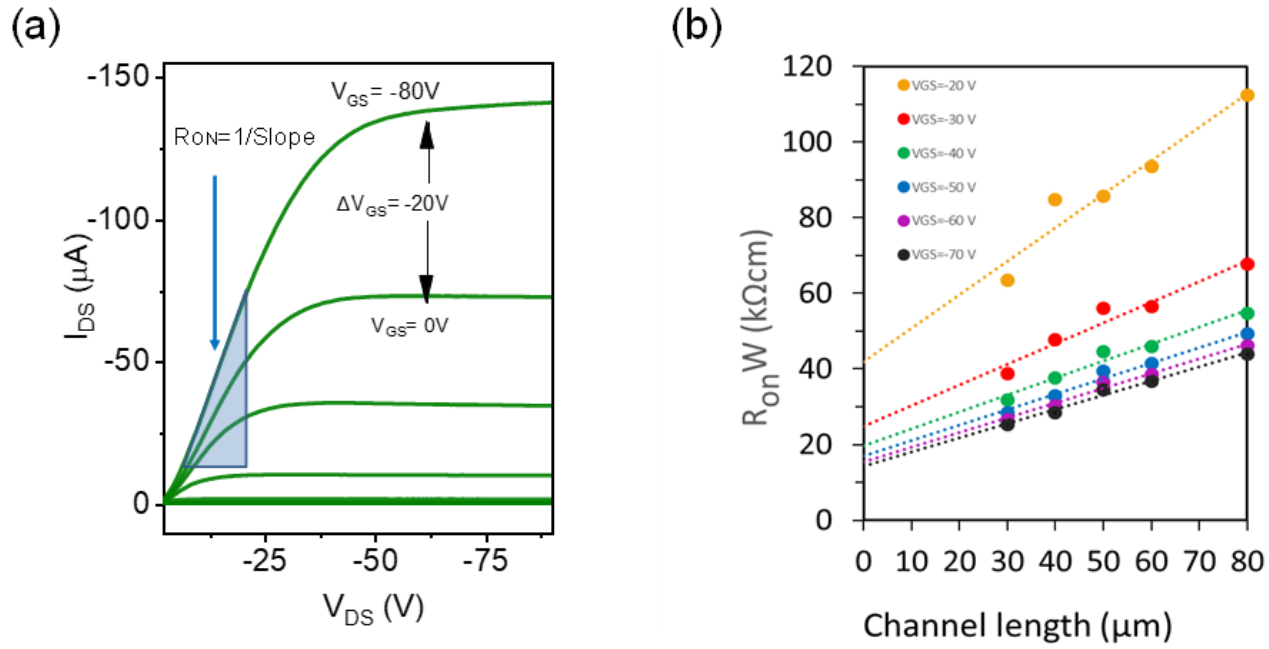

Figure 2.16: Output characteristics of an OFET showing the determination of R_{ON} in the linear regime (b) R_{ON} plotted as a function of channel length for various V_{GS}, for extraction of R_C.

2.2.4.4 OFETs operational challenges

As previously noted, despite substantial advances in material and device architectural design to increase charge transport properties, OFETs have yet to be used in real-word applications.[78] The main bottlenecks are operational and environmental instability, which refer to OFET performance variation due to charge carrier trapping under different environmental conditions or electrical operating stress.[79-81] Such instabilities lead to threshold voltage (V_{th}) shift, decrease of μ and on/off current ratio, hysteresis of current-voltage characteristics, and in the case of irreversible trapping, lead to shortening of operational lifetime.[67,69-84]

Environmental stability

The detrimental effect of ambient air on the performance of n-type OFETs is commonly highlighted in the literature, and it is recognized to be associated with electron trapping by O_2 and H_2O.[85] However, the impact of ambient air exposure on p-type OFETs performance are less concrete. In principle, oxygen can behave as a p-dopant for OSC by forming an OSC-oxygen charge transfer complex, which is expected to increase off-current rather than carrier mobility. Nevertheless, several studies have indeed shown mobility improvement of OFET in ambient air.[86-88] On the other hand, numerous studies have linked the OFETs' performance degradation with water-induced traps upon exposure to the air. Water molecules can interact with the charge carriers (polarons) in the semiconductor because of its strong dipole moment, producing energy-stabilized "trap" states.[80,89,90] The water molecules that are physically absorbed at dielectric interface or confined in nanovoids could interact with dielectric functional groups, resulting in charge carrier trapping.[91,92]

Operational stability

Operational instability is another hindrance to developing stable OFETs is which refers to degrading or altering the OFETs performance during or after device operation. It manifests as hysteresis or V_{th} shift during cyclic V_{GS} sweeping or I_{DS} drop under gate bias stressing (figure 2.17). Operational instability generally caused by charge carrier trapping at the semiconductor/dielectric interface, at grain boundaries or within the bulk semiconductor.[93,94]

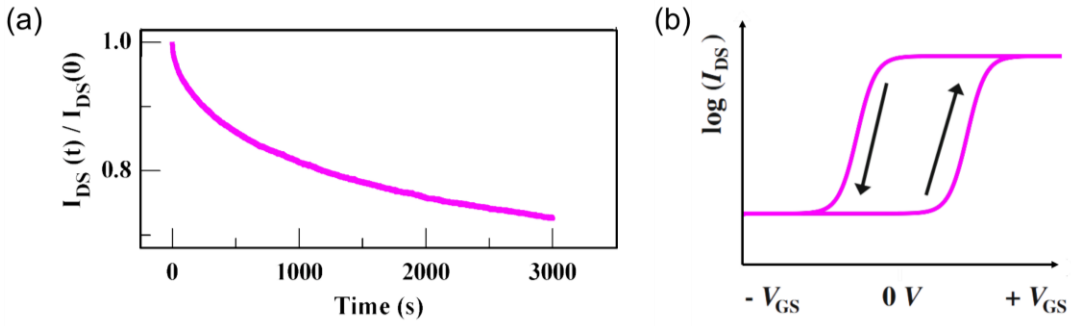

Figure 2.17: (a) I_{DS} under continuous gate bias stress (b) cyclic transfer characteristics of OFET with hysteresis

2.2.4.5 Towards stable and high performance OFETs

Significant efforts have been made in material design (i.e., varying substituents and heteroatoms, donor-acceptor copolymers, improved backbone planarity, etc.) and processing techniques to enhance charge transport and overcome OFET instabilities problems. Over the years, OFET studies were mostly focused on improving OFET mobility rather than addressing stability challenges. Reducing structural defects by aligning the polymer backbone chains in the OFET channel direction (by nano-grooving, blade coating, etc.),[95,96] post-treatment approaches (thermal and solvent vapor annealing), using additives (solvents or ionic additives),[90,97] blending techniques (with insulating or semiconducting materials)[98] are just a few of the strategies being investigated to improve OFET figures of merit. It is worth mentioning that improving charge transfer through trap mitigation may also improve operational and environmental stability.

Improving OFET stability received increased attention throughout the last decade. Passivation of dielectric surfaces using hydrophobic SAMs has been proven to improve OFET performance and ambient stability. However, it does not eliminate all surface traps, also may introduce more surface traps due to chemical and physical instability.[91,99] Polymer dielectrics used as an ad-layer on SiO_2 or in combination with OSC can reduce trap density at the interface and increase OFET stability.[100-102] Flame annealing the SiO_2 surface prior to the semiconductor film coating has been recently shown as another effective method in reducing the water-induced traps at the OSC/dielectric interface.[103] Addition of solvents and molecular additives to the OSC matrix have also been shown to reduce water-induced traps in polymer OFETs by filling the nanocavities in the polymer film.[77]

Doping is an ultimate way to improve the charge transport in OSC by increasing the conductivity or passivation of the charge carrier trap. As a result, it could be a potential method for enhancing the OFET's figure of merit and addressing stability issues.[104,105] Doping played an important role in the development of efficient optoelectronic devices such as OLEDs, where p-doped hole transport layers resulted in much lower operating voltages. Doping of organic transistors is lagging behind those of OLEDs and OPVs due to serious concerns about rising off-current and a lack of feasible dopants for OFET application However, in recent years, promising demonstrations of OFET doping have been reported, indicating improvements in transistor characteristics such as mobility, threshold voltage, contact resistance and stability.[103,106-108]

2.2.5 Organic semiconductors doping

The vast majority of molecular dopants are neutral compounds that only exchange electrons with the OSC without undergoing any chemical reactions. The electron transfer is thought to occur via interaction of OSC with dopant molecules, which results in formation of ion-pair (full electron transfer) or charge-transfer complex (CTC) which results in redistribution of charge density from donor to acceptor.

Ion-pair formation

The primary doping mechanism in organic semiconductors proceeds via an electron transfer process from the OSC to the dopant (p-type doping) or from the dopant to the OSC (n-type doping). In the case of p-type doping, electrons are transferred from the highest occupied molecular orbital (HOMO) of the semiconductor to the lowest unoccupied molecular orbital (LUMO) of the dopant. In the case of n-type doping the opposite occurs, electrons are transferred from the HOMO of the dopant to the LUMO of the OSC (Figure 2.18).[103,109] This electron transfer results in the formation of a localised charges on the dopant and a mobile charge carrier in the OSC. The increased concentration of holes (p doping) or electrons (n doping) shifts the Fermi level towards the transport band.[110]

Charge transfer complex formation

Another mechanism for OSC doping involves the formation of charge transfer complex (CTCs). The frontier orbitals of OSC and dopant undergo hybridization to form a new set of occupied ($HOMO_{CTC}$) bonding and unoccupied ($LUMO_{CTC}$) antibonding orbitals. In contrast with the IP

doping, CTC formation can also occur in systems having EA $_{dopant}$ << $HOMO_{OSC}$ (for p-type doping) and EA $_{dopant}$ >> $HOMO_{OSC}$ (for n-type doping). The degree of hybridization and energy level splitting are linked to the extent of orbital overlap and the energy level mismatch between OSC and dopant.[103,104]

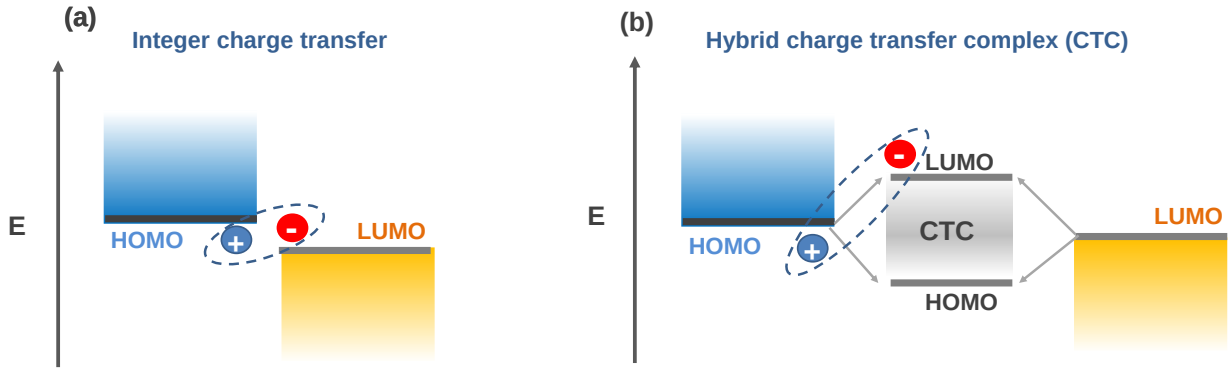

Figure 2.18: Schematic of (a) ion-pair formation and (b) charge transfer complex.

2.2.6 Dopant materials

To dope organic semiconductors, a wide range of chemical species have been used as additives. This section classifies the most important examples of p-dopants for organic semiconductors based on structural and mechanistic properties.

2.2.6.1 Elemental dopants

The earliest example of organic semiconductor doping is the use of diatomic halogens such as bromine (Br_2) and iodine (I_2) for doping of polyacetylene. Iodine, in particular, has been extensively used for p-doping of organic semiconductors such as pentacene, phthalocyanines, and polythiophenes. Oxygen can also cause p-doping of organic semiconductors with low IE, such as polythiophenes.[111,112]

2.2.6.2 Inorganic dopants

Metal oxides like MoO_3, WO_3, V_2O_5 and Fe_3O_4 have been commonly employed for contact doping of p-type OFET, particularly for those OSCs with a high IP (Figure 2.19). However, their low stability and high deposition temperature limit their use as prospective dopants. MoO_3 is the most commonly used dopant among all metal oxides due to its low temperature deposition temperature (~400 °C).[113,114]

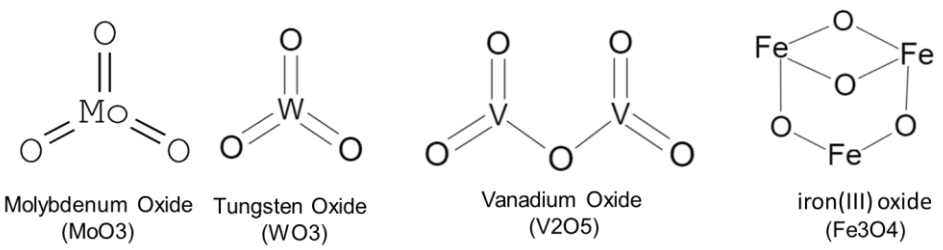

Figure 2.19: Structures of metal oxide p-dopants

2.2.6.3 Molecular dopants

Molecular dopants have advantages over elemental dopants owing to their potential of properties modification, less diffusion into the organic active layer (causing device degradation) and higher stability.

TCNQ derivatives: Tetracyanoquinodimethane (TCNQ) with EA=4.2 eV and its derivatives are the most often utilized molecular p-dopants for OSCs (Figure 2.20). F4-TCNQ is a strong electron acceptor with EA= 5.2 eV which is extensively applied as a p-type dopant for a wide range of OSC. Substitution of two fluorine with electron withdrawing CN group in F2HCNQ, results in even stronger electron affinity of 5.4 eV. Although TCNQs are less volatile than elemental dopants, they are relatively small molecules and may still exhibit significant dopant diffusion or uncontrolled dedoping due to their volatility.[115] Increasing molecular weight by extending the aromatic core (i.e., F6-TCNNQ, EA=5.3 eV), or substitution with a bulky group (i.e., F3-TCNQ-Ad1, EA=5.2 eV) limit the diffusivity while improve solution processability.[116-118]

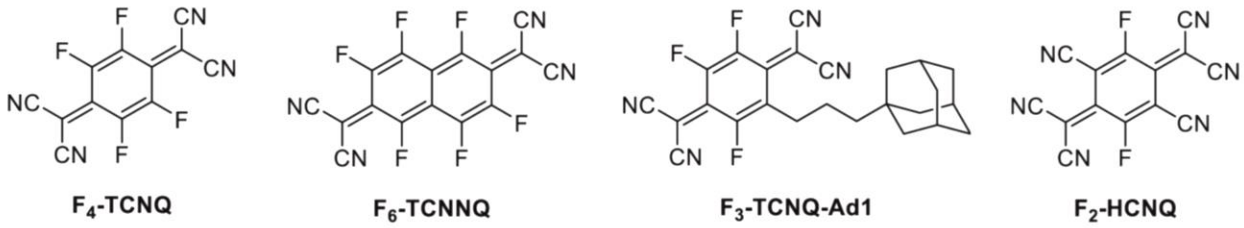

Figure 2.20: Structures of TCNQ-based molecular p-dopants.

Radialene-based dopants: Radialene are cyclic compounds containing cross-conjugated exocyclic double bonds. CN6-CP is a radialene-based dopant with EA of 5.87 eV which makes it an efficient p-dopant for hole transporting materials. However, the low solubility limits its

applicability for blend doping. Other derivatives such as CN6-CP•−/TBA+ and TMCN3-CP are shown to have better solubility but with lower EA (5.1 and 5.5 eV respectively) and demonstrate to be effective p-dopant for polymers such as P3HT and DPP copolymers (Figure 2.21).[119-121]

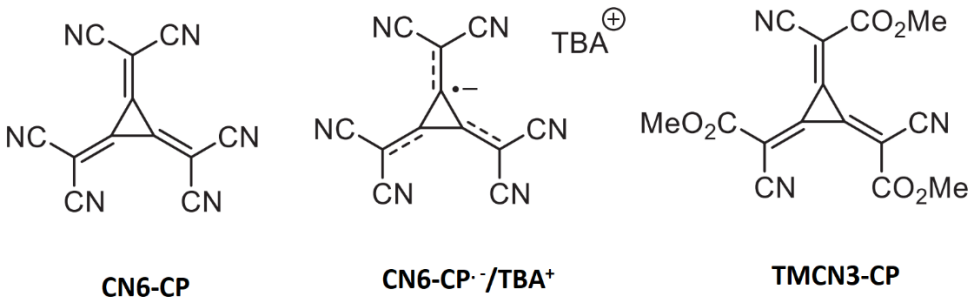

Figure 2.21: Structures of radialene-based dopants

Fullerene dopants: Fluorinated organic molecules based on fullerene are another class of molecular p-dopants (Figure 2.22). The two most commonly used dopants of this family are $C_{60}F_{36}$ and $C_{60}F_{48}$, which have much lower LUMO levels than C_{60} (EA=4.2 eV). $C_{60}F_{36}$ with EA=5.4 eV is reported to have a doping efficiency comparable to F4-TCNQ, but with lower volatility and better deposition control. $C_{60}F_{48}$ is very strong p-dopant (EA=5.85 eV) which has shown promising results in the doping of OFET, OPV, and thermoelectric devices. The bulky nature of fullerene derivatives results in lower diffusivity and enhanced thermal and morphological stability of doped devices.[122-124]

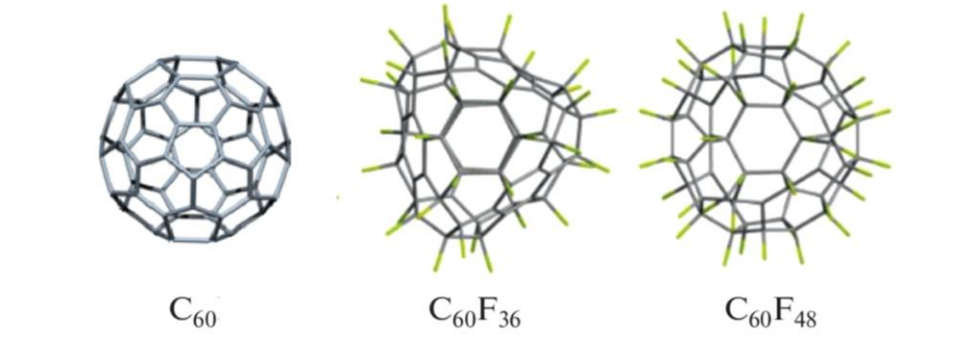

Figure 2.22: Structures of Fullerene molecular p-dopants.

Organometallics: Organometallic dopants are introduced as both p- and n-type doping. Molybdenum tris[1,2-bis(trifluoromethyl)ethane-1,2-dithiolene] $Mo(tfd)_3$, is a strong dopant that

can be an alternative for F4-TCNQ with less volatility and diffusivity issues. To avoid the precipitation problem of $Mo(tfd)_3$ doping, $Mo(tfd\text{-}CO_2Me)_3$ and $Mo(tfd\text{-}COCF_3)_3$ are the preferred solution-processable derivatives (Figure 2.23).[125-127] Other examples of organometallic dopants that can be used as n-type materials are $Cr_2(hpp)_4$, $W2(hpp)_4$, $Ru(terpy)_2$, and $Ru(t\text{-}but\text{-}terpy)_2$. However, they have poor air stability.

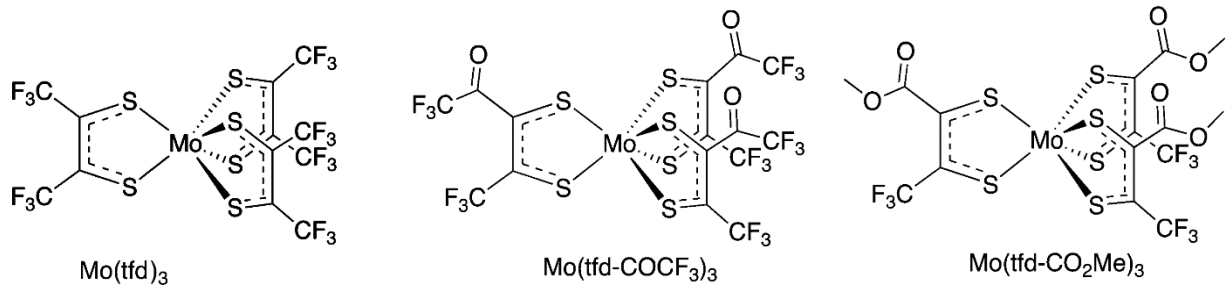

Figure 2.23: Structures of Organometallics molecular p-dopants.

2.2.6.4 Bronsted and Lewis Acids

Most common inorganic Brønsted acids can act as p-dopants, especially for polyanilines and polypyrroles polymers, where doping occurs via proton transfer processes. Some examples of Bronsted acid doping systems are the doping of polythiophenes with tridecafluoro1,1,2,2-tetrahydrooctyl trichlorosilane (FTS) and the interface doping of pentacene OFETs with acidic monolayers.[128,129] Oxidizing Lewis acids such as $FeCl_3$, $SbCl_5$ or $AsCl_5$, have been found to be effective p-dopants for organic semiconductors, where doping occurs by electron transfer reactions. They are, nevertheless, highly sensitive to humidity and show formation of side products (Such as HCl). FeCl3 is the most common Lewis acid dopant which is used to dope carbon nanotubes (CNTs), and N,N′-diphenyl-N,N′-bis(3-methylphenyl)-1,1′-biphenyl-4,4′-diamine (TPD). Another examples are Bismuth carboxylates and Lithium bis (trifluoromethyl sulfonyl) imide (Li TFSI), the latter of which is frequently used to p-dope and increase the conductivity of 2,2′,7,7′- tetrakis (N,N-di-p-methoxyphenyl-amine)-9,9′-spiro-bifluorene (spiro-MeO-TAD), however the actual dopant spiro-MeO-TAD-TFSI is probably generated from molecular oxygen.[130-132]. Boron trifluoride (BF_3), a nonoxidizing Lewis acid, was initially used as a dopant for PPV polymer in 1995 by Utley et al. However, its chemically reactive to water and oxygen. Tris(pentafluorophenyl)borane (BCF) is the favored Lewis acid dopant over BF_3 due to its high Lewis acidity and the superior water and oxygen endurance. It's been reported to enhance solar

cell performance by p-doping of hole transport layers (HTLs). The bis(pentafluorophenyl)zinc [$Zn(C_6F_5)_2$] is an alternative Lewis acid dopant that has been reported to remarkably increase the hole mobility of C_8-BTBT:C_{16}IDT-BT blends from ≈2 to 21 $cm^2 V^{-1} s^{-1}$. [42,133,134]

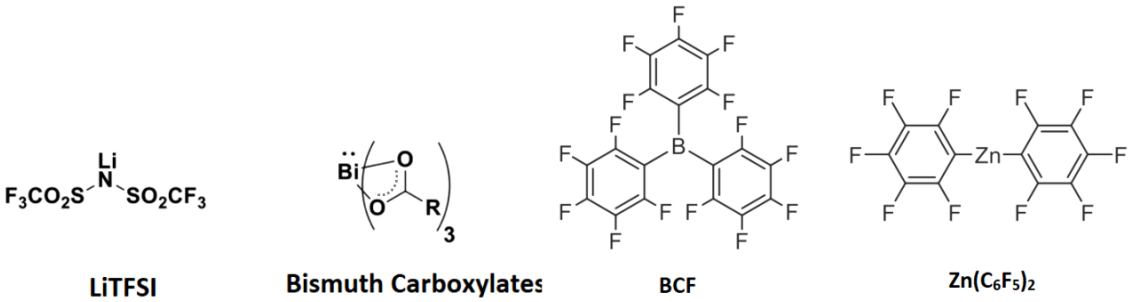

Figure 2.24: Structures of Bronsted and Lewis Acids p-dopants.

2.2.7 Doping in OFETs

Despite the success of the doping technique in optoelectronics such as OLEDs and OPVs through improved charge injection by doping of HTL and ETL, doping has been less explored in OFET applications due to major concerns regarding uncontrollable increases in off current. Also, the library of practical dopants for OFETs applications is limited due to the solubility, energy level matching and stability.[104,105] Despite these challenges, the use of dopants, whether as part of an injection layer or for bulk doping of semiconductor channel, has sparked a lot of research interest in recent years (See Figure 2.25). Here we discuss the influence of two key transistor doping approaches, channel doping and contact doping, on device figure of merits, as well as how this strategy may improve OFET performance and stability.

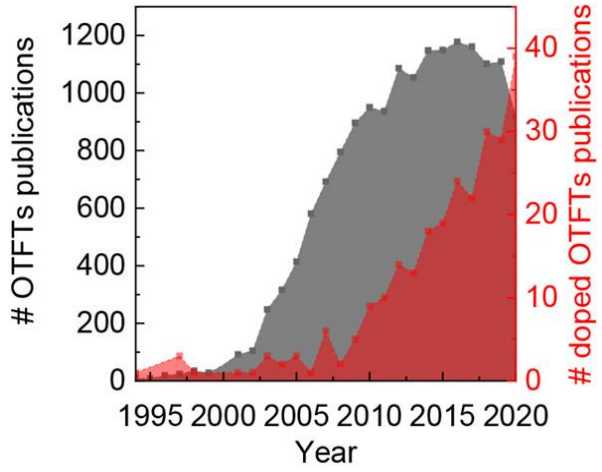

Figure 2.25: The number of publications per year (from ISI Web of Science) involving OTFTs (gray) and doped OTFTs (red). (Represented with permission from ref 92)

2.2.8 Impact of molecular doping on OFETs performance

Molecular doping could affect the energetic configuration of the semiconductor network and, consequently, the general characteristics of the transistor. The degree of this impact is highly dependent on doping concentration. It has been demonstrated that using low doping concentrations (molar concentrations $<10^{-3}$) can fill trap states leading to a shift in Vth toward zero and, lower SS, along with enhanced linearity in the I_{DS} 0.5 vs V_{GS} plot (Figure 2.26 b, c). Passivation of traps improves charge transport, resulting in increased mobility (Figure 2.26 a).[135-137] On the other hand, if the dopant concentration is too high, it may generate excess charges in the bulk of the semiconductor and result in an increased off-current (Figure 2.26d). The higher dopant concentration may increase energetic disorder and induced more traps which lead to shift of threshold voltage toward higher potentials, a decreased on current, and lower μ (Figure 2.26 d).[105]

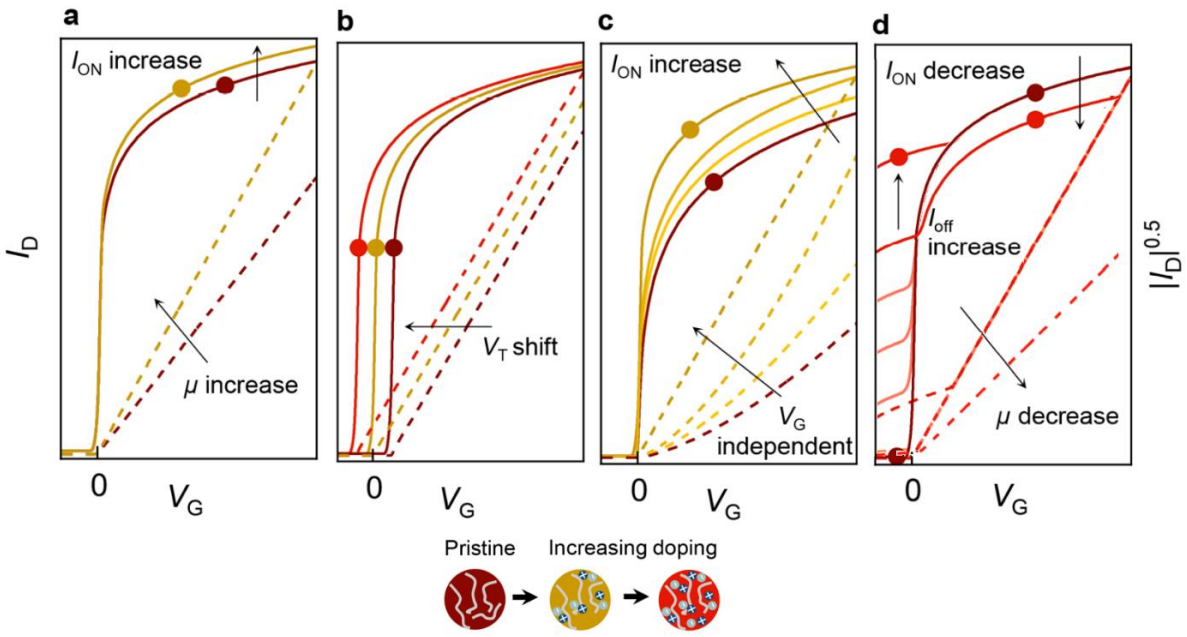

Figure 2.26: The impact of doping concentration on OFETs. (a) mobility, (b) threshold voltage, (c) V_{GS} dependence mobility. (d) I_{on}/I_{off} current. (The solid lines represent I_{DS}-V_{GS} curves, and dotted lines represent $I_{DS}^{0.5}$-V_{GS} curves. Pristine, low concentration, and high concentration doped OFETs characteristics are shown, respectively by dark red, yellow, and light red lines.)[92]

Despite the aforementioned expected impact of doping on OFET performance, the relationship between doping and transistor performance is more complex and uncertain. Introducing dopants into host semiconductors results in a complex energetics-doping-microstructure interrelationship. Doping can cause structural ordering of the OSC host and the formation of larger crystallites in

some instances (Figure 2.27b), whereas it can also induce future distortion and structural disruption (Figure 1.27c).[138-140] Therefore, the structural impacts of doping on the host OSC may outweigh the intended electrical doping.

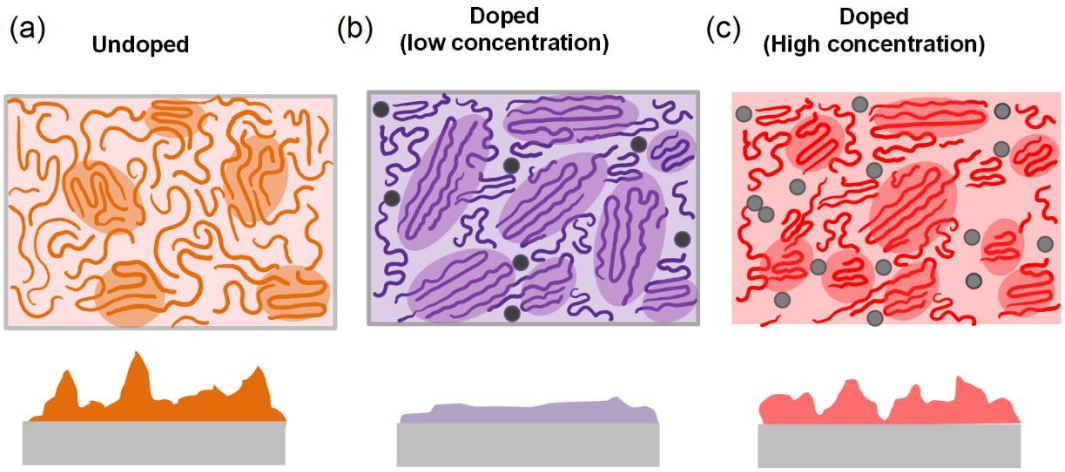

Figure 2.27: The possible impact of doping concentration on polymer film microstructure

2.2.9 Channel doping

Channel doping has been investigated from the early days of OFETs. Jarret et al in 1995 demonstrated how the charge-carrier mobility of amorphous *poly(dodecyloxyterthiophene)* (polyDOT3) increased via doping with 2,3-dichloro-5,6-dicyano1,4-benzoquinone (DDQ).[141] However, early studies revealed that enhanced charge transfer of doped OFETs is accompanied by undesired rise of OFET off-current, lowering the research interest to OFET doping.[109,142]

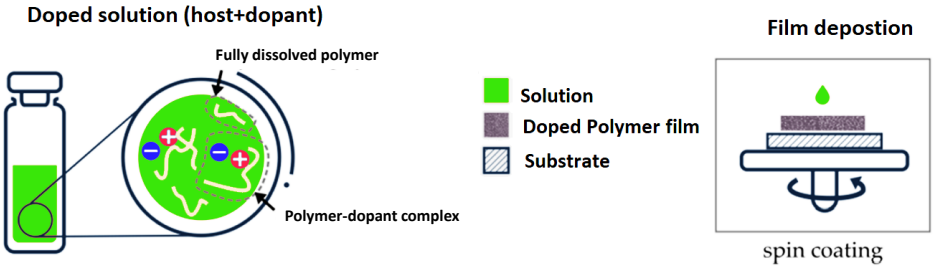

Figure 2.28: coprocessing the OSC: dopant blend from solution

Channel doping can be accomplished through the deposition of a thin dopant layer directly onto the OSC, co-evaporation of two materials, or coprocessing the OSC: dopant blend from solution, which is the most commonly used processing route (see Figure 2.28). The latter has been used for a variety of doped OFETs, such as F4-TCNQ: DPP-BTz, pyronin B: DPPTTT, TFP and OFN with P3HT, FTCS: TIPS-pentacene, BCF with different polymers, small molecules, and polymer: small molecules blends.[143-146] Panidi et al. demonstrated how BCF doping leads to considerable improvements in a wide range of OFETs, highlighting the importance of microstructure and morphology in device performance.[147] Doping of OCSs blends such as small molecules: polymer blend doping (ternary blend) shows very promising impact on OFETs performance, attributed to both electronic and structural effects induced upon doping. In small molecule: polymer blends, the polymer acts both a binder, which aids film formation, and as a charge-transport medium, which enhances the connection between high mobility small molecule crystallites. The ultimate example of a polymer: small-molecules: dopant system is blending of polymer C_{16}-IDTBT and small molecule C_8-BTBT doped with $C_{60}F_{48}$, BCF, and ZnCF, which achieved record mobility of 20 $cm^2 V^{-1} s^{-1}$ and enhanced overall OFET performance.[42,147,148] It is worth noting that the most important accomplishments in doping strategies to improve OFETs have been based on small molecule semiconductors, with only a few articles reporting significant enhancements in charge mobility in polymer-based OFETs. For example, TCNQ derivatives, the most common molecular p-dopants, have been shown to enhance the hole mobility of diketopyrrolopyrrole-thienothiophene polymer (DPP-DTT) from 1.03 to 1.2 $cm^2V^{-1}s^{-1}$.[90,149] Doping of the indenopyrazine-thiophene polymer with $B(C_6F_5)_3$ Lewis acid increased its hole mobility from 0.08 to 0.6 $cm^2V^{-1}s^{-1}$. An even more pronounced mobility enhancement in DPP-DTT OFETs, from 0.6 to 3.5 $cm^2V^{-1}s^{-1}$, was reported using pyronin B dye (3,6-bis(diethylamino)xanthylium tetrachloroferrate).[150]

2.2.10 Contact doping

Reducing contact resistance to enhance charge carrier injection is a key requirement for developing high-performance OTFTs. Bulk doping itself can enhance charge injection from metal to OSC by lowering interfacial trap density and modifying the depletion width at the metal/OSC interface due to enhanced bulk conductivity. However, as noted previously, bulk doping may affect the channel microstructure, and increase the off current.[72,109] On the other hand, in contact doping, the dopant is confined close to the contacts and the channel remains unaffected. Contact doping can be

accomplished through the use of SAM layers, or via vapor or solution deposition methods in different configurations, as illustrated in Figure 2.29.[151]

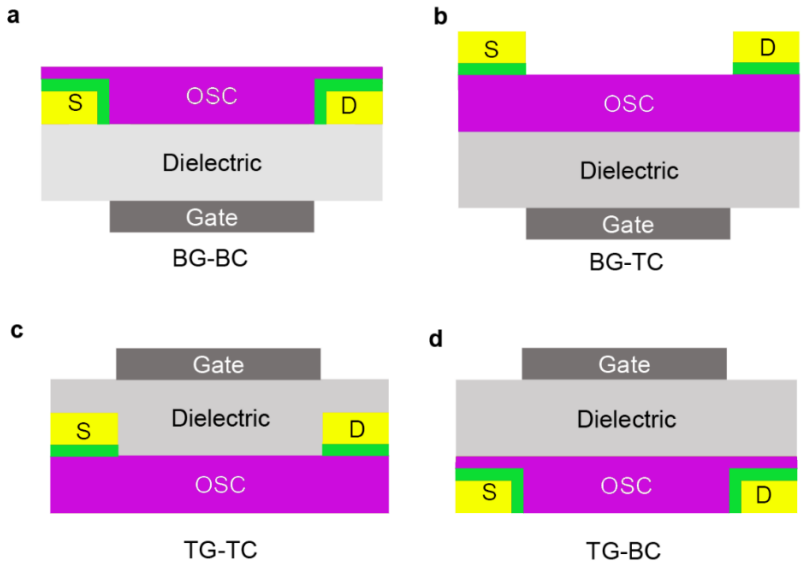

Figure 2.29: Different configurations of contact doping.

Many conventional p-dopants such as, F_4-TCNQ, F_6-TCNNQ, $C_{60}F_{36}$, $C_{60}F_{48}$, as well as n-dopants such as Pyronin B, lithium benzoate, $W_2(hpp)_4$, have been used for contact doping with vapor deposition technique.[124,151-154] Contact doping with the mentioned dopants reduces contact resistance and improves OFET performance by increasing mobility, controlling the threshold voltage, and improving environmental and operational stability.[151,152,154,155] Nonetheless, contact doping may result in an increase in off current due to dopant molecules diffusion into the channel. Diffusion of dopant molecules are suggested to be limited by using dopant-blockade molecules, argon plasma etching of contacts, or inject-printing of electrodes using of F4-TCNQ doped Ag nanoparticle ink.[156,157]

2.3 References

1. Hernandez, S.; Farkhondehfal, M. A.; Sastre, F.; Makkee, M.; Saracco, G.; Russo, N. Syngas Production from Electrochemical Reduction of CO_2: Current Status and Prospective Implementation. *Green Chem.* **2017**, *19*, 2326−2346.
2. Roy, S. C.; Varghese, O. K.; Paulose, M.; Grimes, C. A. Toward Solar Fuels: Photocatalytic Conversion of Carbon Dioxide to Hydrocarbons. *ACS Nano* **2010**, *4*, 1259−1278.

3. Chu, S.; Kong, X.; Vanka, S.; Guo, H.; Mi, Z. Artificial Photosynthesis on III-Nitride Nanowire Arrays. *Semicond. Semimetals* **2017**, *97*, 223−255.
4. Wu, J.; Huang, Y.; Ye, W.; Li, Y. CO_2 Reduction: From the Electrochemical to Photochemical Approach. *Adv. Sci*. **2017**, *4*, 1700194.
5. Olah, G. A.; Goeppert, A.; Prakash, G. K. S. Chemical Recycling of Carbon Dioxide to Methanol and Dimethyl Ether: From Greenhouse Gas to Renewable, Environmentally Carbon Neutral Fuels and Synthetic Hydrocarbons. *J. Org. Chem*. **2009**, *74*, 487–498.
6. He, J.; Janáky, C. Recent Advances in Solar-Driven Carbon Dioxide Conversion: Expectations versus Reality. *ACS Energy Lett*. **2020**, *5*, 1996−2014.
7. Ali, S.; Flores, M. C.; Razzaq, A.; Sorcar, S.; Hiragond, C. B.; Kim, H. R.; Park, Y. H.; Hwang, Y.; Kim, H. S.; Kim, H.; Gong, E. H.; Lee, J.; Kim, D.; In, S. Gas Phase Photocatalytic CO_2 Reduction, "A Brief Overview for Benchmarking. *Catalysts* **2019**, *9*, 727.
8. Song, J. T.; Ryoo, H.; Cho, M.; Kim, J.; Kim, J. G.; Chung, S. Y.; Oh, J. Nanoporous Au thin films on Si photoelectrodes for selective and efficient photoelectrochemical CO_2 reduction. *Adv. Energy Mater*. **2017,** *7*, 1601103.
9. Jang, Y. J.; Jeong, I.; Lee, J.; Lee, J.; Ko, M. J.; Lee, J. S. Unbiased sunlight-driven artificial photosynthesis of carbon monoxide from CO_2 using a ZnTe-based photocathode and a perovskite solar cell in tandem. *ACS Nano* **2016**, *10*, 6980−6987.
10. Barton, E. E.; Rampulla, D. M.; Bocarsly, A. B. Selective solardriven reduction of CO_2 to methanol using a catalyzed p-GaP based photoelectrochemical cell. *J. Am. Chem. Soc.* **2008**, *130*, 6342−6344.
11. DuChene, J. S.; Sweeny, B. C.; Johnston-Peck, A. C.; Su, D.; Stach, E. A.; Wei, W. D., Hot Hole Collection and Photoelectrochemical CO_2 Reduction with Plasmonic Au/p-GaN Photocathodes, Nano Lett. **2018**, *18*, 2545-2550.
12. Kamimura, S.; Sasaki, Y.; Kanaya, M.; Tsubota, T.; Ohno, T. Improvement of Selectivity for CO_2 Reduction by Using Cu2ZnSnS4 Electrodes Modified with Different Buffer Layers (CdS and In2S3) under Visible Light Irradiation. *RSC Adv*. **2016**, *6*, 112594−112601.
13. Sahara, G.; Abe, R.; Higashi, M.; Morikawa, T.; Maeda, K.; Ueda, Y.; Ishitani, O. Chem. Commun., Photoelectrochemical CO_2 reduction using a Ru(ii)–Re(i) multinuclear metal complex on a p-type semiconducting NiO electrode, *Chem. Commun*. **2015**, *51*, 10722-10725.

14. Arai, T.; Tajima, S.; Sato, S.; Uemura, K.; Morikawa, T.; Kajino, T, Selective CO_2 conversion to formate in water using a CZTS photocathode modified with a ruthenium complex polymer, *Chem. Commun*. **2011**, *47*, 2664-12666
15. Schreier, M.; Luo, J. S.; Gao, P.; Moehl, T.; Mayer, M. T.; Gratzel, M., Covalent Immobilization of a Molecular Catalyst on Cu2O Photocathodes for CO_2 Reduction, *J. Am. Chem. Soc.* **2016**, *138*, 1938-1946.
16. Wang, Z.; Zhang, L.; Schülli, T. U.; Bai, Y.; Monny, S. A.; Du, A.; Wang, L. Identifying copper vacancies and their role in the CuO based photocathode for water splitting. *Angew. Chem*. **2019**, *131*, 17768−17773.
17. Kibria, M. G.; Mi, Z. Artificial photosynthesis using metal/ nonmetal-nitride semiconductors: current status, prospects, and challenges. *J. Mater. Chem. A* **2016**, 4, 2801−2820.
18. Chu, S.; Fan, S.; Wang, Y.; Rossouw, D.; Wang, Y.; Botton, G. A.; Mi, Z. Tunable syngas production from CO_2 and H_2O in an aqueous photoelectrochemical cell. *Angew. Chem., Int. Ed.* **2016**, *55*, 14262−14266.
19. Pang, H.; Yang, G. L.; Li, P.; Huang, H.; Ichihara, F.; Takei, T.; Ye, J. H. Wafer-scale Si nanoconed arrays induced syngas in the photoelectrochemical CO_2 reduction. *Catal. Today* **2020**, *339*, 321− 327.
20. Long, J.; Zhang, H.; Ming, J.; Zhao, J.; Gu, Q.; Xu, C.; Ding, Z.; Yuan, R.; Zhang, Z.; Lin, H.; Wang, X. High-rate, tunable syngas production with artificial photosynthetic cells. *Angew. Chem., Int. Ed.* **2019**, *58*, 7718−7722.
21. Wu, J.; Xie, Y.; Ren, Z.; Du, S.; Meng, H.; Zhao, L.; Wang, X.; Wang, G.; Fu, H. Porous palladium nanomeshes with enhanced electrochemical CO_2-into-syngas conversion over a wider applied potential. *ChemSusChem*, **2019**, *12*, 3304−3311.
22. Jang, Y. J.; Jeong, I.; Lee, J.; Lee, J.; Ko, M. J.; Lee, J. S. Unbiased sunlight-driven artificial photosynthesis of carbon monoxide from CO_2 using a ZnTe-based photocathode and a perovskite solar cell in tandem. *ACS Nano,* **2016**, *10*, 6980−6987
23. Schreier, M.; Curvat, L.; Giordano, F.; Steier, L.; Abate, A.; Zakeeruddin, S. M.; Luo, J.; Mayer, M. T.; Gratzel, M. Efficient photosynthesis of carbon monoxide from CO_2 using perovskite photovoltaics. *Nat. Commun*. **2015**, *6*, 1-6.

24. Arteev, D.S.; Sakharov, A.V.; Zavarin, E.E.; Lundin, W.V.; Smirnov, A.N.; Davydov, V.Y.; Yagovkina, M.A.; Usov, S.O.; Tsatsulnikov, A.F. Investigation of Statistical Broadening in InGaN Alloys. *J. Phys. Conf. Ser*. **2018**, 1135, 012050
25. Jung, H. S.; Hong, Y. J.; Li, Y.; Cho, J.; Kim, Y. J.; Yi, G. C. Photocatalysis Using GaN Nanowires, *ACS Nano.* **2008**, *2*, 637−642.
26. Osterloh, F. E. Inorganic Nanostructures for Photoelectrochemical and Photocatalytic Water Splitting. *Chem. Soc. Rev.* **2013**, *42*, 2294−2320.
27. Kudo, A.; Miseki, Y. Heterogeneous Photocatalyst Materials for Water Splitting. *Chem. Soc. Rev*. **2009**, *38*, 253−78.
28. Deng, J.; Su, Y.; Liu, D.; Yang, P.; Liu, B.; Liu, C. Nanowire Photoelectrochemistry. *Chem. Rev*. **2019**, *119*, 9221−9259.
29. Liu, C.; Dasgupta, N. P.; Yang, P. Semiconductor Nanowires for Artificial Photosynthesis. *Chem. Mater*. **2014**, *26*, 415−422.
30. Alotaibi, B.; Fan, S.; Wang, D.; Ye, J.; Mi, Z. Wafer-Level Artificial Photosynthesis for CO_2 Reduction into CH4 and CO Using GaN Nanowires. *ACS Catal*. **2015**, *5*, 5342−5348.
31. AlOtaibi, B.; Kong, X.; Vanka, S.; Woo, S. Y.; Pofelski, A.; Oudjedi, F.; Fan, S.; Kibria, M. G.; Botton, G. A.; Ji, W.; Guo, H.; Mi, Z. Photochemical carbon dioxide reduction on Mg-doped Ga (In) N nanowire arrays under visible light irradiation, ACS Energy Lett. 2016, 1, 246-252.
32. Wang, Y.; Fan, S.; AlOtaibi, B.; Wang, Y.; Li, L.; Mi, Z. A monolithically integrated gallium nitride nanowire/silicon solar cell photocathode for selective carbon dioxide reduction to methane. *Chem. - Eur. J*. **2016**, *22*, 8809−8813
33. Köhler, A.; Bässler, H. *Electronic processes in organic semiconductors: An introduction*. John Wiley & Sons, **2015**.
34. Brütting, W. *Physics of Organic Semiconductors*; WILEY-VCH Verlag: Weinheim, Germany, **2004**.
35. Qian, Y.; Zhang, X. W.; Xie, L. H.; Qi, D. P.; Chandran, B. K.; Chen, X. D.; Huang, W. Stretchable Organic Semiconductor Devices. *Adv. Mater.* **2016**, *28*, 9243−9265.
36. Facchetti, A. Semiconductors for organic transistors. *Materials Today*. **2007**, *10*, 28-37.

37. Zhengran, H.; Zhang, Z.; Bi, S.; Chen, J.; Li, D. Conjugated polymer controlled morphology and charge transport of small-molecule organic semiconductors, *Scientific Reports*, **2020**, *1*, 1-9.
38. Jurchescu, O. D., Baas, J. & Palstra, T. T. M. Effect of impurities on the mobility of single crystal pentacene. *Appl. Phys. Lett*. **2004**, *84*, 3061–3063.
39. Sheraw, C. D., Jackson, T. N., Eaton, D. L. & Anthony, J. E. Functionalized Pentacene Active Layer Organic Thin-Film Transistors. *Adv. Mater*. **2003**, *15*, 2009–2011.
40. Yao, Z.-F.; Wang, J.-Y.; Pei, J. Control of π-π Stacking via Crystal Engineering in Organic Conjugated Small Molecule Crystals. *Cryst. Growth Des*. **2018**, *18*, 7−15.
41. Ebata, H. et al. Highly Soluble [1]Benzothieno[3,2- b]benzothiophene (BTBT) Derivatives for High-Performance, Solution-Processed Organic Field-Effect Transistors. *J. Am. Chem. Soc*. **2007,** *129*, 15732–15733.
42. Paterson, A. F.; Tsetseris, L.; Li, R.; Basu, A.; Faber, H.; Emwas, A. H.; Panidi, J.; Fei, Z.; Niazi, M. R.; Anjum, D. H.; Heeney, M.; Anthopoulos, T. D. Addition of the Lewis Acid Zn(C6 F5)2 Enables Organic Transistors with a Maximum Hole Mobility in Excess of 20 cm(2) V(-1) s(-1). *Adv Mater*. **2019**, *31*, 190087.
43. Sirringhaus, H.; Brown, P. J.; Friend, R. H.; Nielsen, M. M.; Bechgaard, K.; Langeveld-Voss, B. M. W.; Spiering, A. J. H.; Janssen, R. A. J.; Meijer, E. W.; Herwig, P.; de Leeuw, D. M., Two-dimensional charge transport in self-organized, high-mobility conjugated polymers. *Nature* **1999**, *401*, 685-688.
44. Chang, 1. F.; Sun, B. Q.; Breiby, D. W.; Nielsen, M. M.; SolIing, T. I.; Giles, M.; McCulloch, 1.; Sirringhaus, H., Enhanced mobility of poly(3-hexylthiophene) transistors by spin-coating from high-boiling-point solvents. *Chem Mater* **2004**, *16*, 4772-4776.
45. Müllen, K.; Pisula, W. Donor-Acceptor polymers, *J. Am. Chem. Soc.* **2015**, *137*, 9503-9505.
46. Kim, M.; Ryu, S. U.; Park, S. A.; Choi, K.; Kim, T.; Chung, D.; Park. T. Donor−Acceptor-Conjugated Polymer for High-Performance Organic Field-Effect Transistors: A Progress Report. *Adv. Funct. Mater*. **2019**, *30*, 1904545.
47. Bronstein, H.; Leem, D. S.; Hamilton, R.; Woebkenberg, P.; King, S.; Zhang, W.; Ashraf, R. S.; Heeney, M.; Anthopoulos, T. D.; Mello, J. d.; McCulloch, I. Indacenodithiopheneco-Benzothiadiazole copolymers for high performance solar cells or transistors via alkyl chain optimization. *Macromolecules* **2011**, *44*, 6649–6652

48. Venkateshvaran, D.; Nikolka, M.; Sadhanala, A.; Lemaur, V.; Zelazny, M.; Kepa, M.; Hurhangee, M.; Kronemeijer, A. J.; Pecunia, V.; Nasrallah, I.; et al. Approaching Disorder-Free Transport in HighMobility Conjugated Polymers. *Nature* **2014**, *515*, 384−388.
49. Zhang, X.; Bronstein, H.; Kronemeijer, A. J.; Smith, J.; Kim, Y.; Kline, R. J.; Richter, L. J.; Anthopoulos, T. D.; Sirringhaus, H.; Song, K.; et al. Molecular Origin of High Field-Effect Mobility in an Indacenodithiophene-Benzothiadiazole Copolymer. *Nat. Commun*. **2013**, *4*, 1-9.
50. Zhang, W. M.; Han, Y.; Zhu, X. X.; Fei, Z. P.; Feng, Y.; Treat, N. D.; Faber, H.; Stingelin, N.; McCulloch, I.; Anthopoulos, T. D.; et al. A Novel Alkylated Indacenodithieno[3,2-b] thiophene-Based Polymer for High-Performance Field-Effect Transistors. *Adv. Mater*. **2016**, *28*, 3922−3927.
51. Coppo, P.; Turner, M. L. Cyclopentadithiophene based electroactive materials. *J. Mater. Chem.* **2005**, *15*, 1123–1133.
52. Yamashita, Y.; Hinkel, F.; Marszalek, T.; Zajaczkowski, W.; Pisula, W.; Baumgarten, M.; Matsui, H.; Müllen, K.; Takeya, J. Mobility Exceeding 10 $cm^2V^{-1}s^{-1}$ in Donor-Acceptor Polymer Transistors with Band-like Charge Transport. *Chem. Mater.* **2016**, *28*, 420-424.
53. Back, J. Y.; Yu, H.; Song, I.; Kang, I.; Ahn, H.; Shin, T. J.; Kwon, S.-K.; Oh, J. H.; Kim, Y.-H. Investigation of Structure−Property Relationships in Diketopyrrolopyrrole-Based Polymer Semiconductors via Side-Chain Engineering. *Chem. Mater*. **2015**, *27*, 1732−1739.
54. Ma, J.; Liu, Z.; Wang, Z.; Yang, Y.; Zhang, G.; Zhang, X.; Zhang, D. Charge Mobility Enhancement for Diketopyrrolopyrrole-Based Conjugated Polymers by Partial Replacement of Branching Alkyl Chains with Linear Ones. Mater. *Chem. Front.* **2017**, *1*, 2547−2553.
55. Phan, H.; Ford, M. J.; Lill, A. T.; Wang, M.; Bazan, G. C.; Nguyen, T.-Q. Electrical Double-Slope Nonideality in Organic Field-Effect Transistors. *Adv. Funct. Mater*. **2018,** *28*, 1707221.
56. Uemura, T.; Rolin, C.; Ke, T. H.; Fesenko, P.; Genoe, J.; Heremans, P.; Takeya, J. On the Extraction of Charge Carrier Mobility in High-Mobility Organic Transistors. *Adv. Mater.* **2016**, *28*, 151-155.
57. Choi, H. H.; Cho, K.; Frisbie, C. D.; Sirringhaus, H.; Podzorov, V. Critical assessment of charge mobility extraction in FETs. *Nat. Mater*. **2017**, *17*, 2-7

58. Ghamari, P.; Niazi, M. R.; Perepichka, D. F. Controlling Structural and Energetic Disorder in High-Mobility Polymer Semiconductors via Doping with Nitroaromatics. *Chem. Mater.* **2021**, *33*, 2937−2947.
59. Lamport, Z. A.; Barth, K. J.; Lee, H.; Gann, E.; Engmann, S.; Chen, H.; Guthold, M.; McCulloch, I.; Anthony, J. E.; Richter, L. J.; DeLongchamp, D. M.; Jurchescu, O. D. A simple and robust approach to reducing contact resistance in organic transistors. *Nat Commun*. **2018**, *9*, 1-8.
60. Waragai, K.; Akimichi, H.; Hotta, S.; Kano, H.; Sakaki, H. Charge transport in thin films of semiconducting oligothiophenes. *Physical Review B*. **1995**, *52*, 1786-1792.
61. Meng, H. F. *Polymer Electronics (Overview of Semiconducting Conjugated Polymers)*, Singapore: Pan Standford Publishing, **2013**.
62. Stallinga, P. Electronic Transport in Organic Materials: Comparison of Band Theory with Percolation/(Variable Range) Hopping Theory. *Adv. Mater.* **2011**, *23*, 3356- 3362.
63. Desai, M.S., Kandpal, K. and Goswami, R. A Multiple-trapping-and-release transport-based threshold voltage model for oxide thin film transistors. *J. Electron. Mater* **2021**, *50*, 4050-4057.
64. Tessler, N.; Preezant, Y.; Rappaport, N.; Roichman, Y. Charge Transport in Disordered Organic Materials and Its Relevance to Thin-Film Devices: A Tutorial Review. *Adv. Mate.* **2009**, *21*, 2741-2761.
65. Teyssedre, G.; Laurent, C. Charge Transport Modeling in Insulating Polymers: from Molecular to Macroscopic Scale. IEEE Trans. *Dielectr. Electr. Insul*. **2005**, *12*, 857−875.
66. Salleo A. Electronic Traps in Organic Semiconductors. *Organic Electronics*: WILEY-VCH Verlag GmbH & Co. **2013**, 341-380.
67. Haneef, H. F.; Zeidell, A. M.; Jurchescu, O. D. Charge carrier traps in organic semiconductors: a review on the underlying physics and impact on electronic devices. *J. Mater. Chem. C*. **2020**, *8*, 759− 787.
68. Kumar, B.; Kaushik, B. K.; Negi, Y. S. Organic Thin Film Transistors: Structures, Models, Materials, Fabrication, and Applications: A Review. *Polym. Rev.* **2014**, *54*, 33–11.
69. Torsi, L.; Magliulo, M.; Manoli, K.; Palazzo, G. Organic field-effect transistor sensors: a tutorial review. *Chem. Soc. Rev*. **2013**, *42*, 8612–8628.

70. Dimitrakopoulos, C. D.; Malenfant, P. R. L., Organic thin film transistors for large area electronics. *Adv. Mater.* **2002**, *14*, 99-117.
71. Zaumseil, J.; Sirringhaus, H. Electron and Ambipolar Transport in Organic FieldEffect Transistors. *Chem. Rev.* **2007**, *107*, 1296–1323.
72. Liu, C.; Xu, Y.; Noh, Y. Y. Contact engineering in organic field-effect transistors. *Mater. Today*, **2015**, *18*, 79–96.
73. Wang, Z. B.; Helander, M. G.; Greiner, M. T.; Qiu, J.; Lu, Z. H. Energy-level alignment, and charge injection at metal/C60/organic interfaces. *Appl. Phys. Lett.* **2009**, *95*, 43302.
74. Natali, D.; Caironi, M. Charge Injection in Solution-Processed Organic Field-Effect Transistors: Physics, Models and Characterization Methods. *Adv. Mater.* **2012**, *24*, 1357–1387.
75. Heimel, G.; Romaner, L.; Zojer, E.; Bredas, J. L. The Interface Energetics of Self-Assembled Monolayers on Metals. *Acc. Chem. Res.* **2008**, *41*, 721–729.
76. Chen, H.; Zhang, W.; Li, M.; He, G.; Guo, X. Interface Engineering in Organic Field-Effect Transistors: Principles, Applications, and Perspectives. *Chem. Rev.* **2020**, *120*, 2879−2949.
77. Richards, T. J. & Sirringhaus, H. Analysis of the contact resistance in staggered, top-gate organic field-effect transistors. *J. Appl. Phys.* **2007**, *102*, 94510.
78. Sirringhaus, H. 25th Anniversary Article: Organic Field-Effect Transistors: The Path Beyond Amorphous Silicon. *Advanced Materials*. **2014**, *26*,1319-1335.
79. Lu, X.; Minari, T.; Kumatani, A.; Liu, C.; Tsukagoshi, K. Effect of air exposure on metal/organic interface in organic field-effect transistors, *Appl. Phys. Lett.* **2011**, 98, 243301.
80. Nikolka, M., A perspective on overcoming water-related stability challenges in molecular and hybrid semiconductors, *MRS Communications*, **2020**, *10*, 98–111.
81. Nikolka, M.; Hurhangee, M.; Sadhanala, A.; Chen, H.; McCulloch, I.; Sirringhaus, H. Correlation of Disorder and Charge Transport in a Range of Indacenodithiophene-Based Semiconducting Polymers. *Adv. Electron. Mater.* **2018**, *4*, 1700410.
82. Un, H.; Zheng, Y. Q.; Shi, K.; Wang, J. Y.; Pei, J. Air- and Active Hydrogen-Induced Electron Trapping and Operational Instability in n-Type Polymer Field-Effect Transistors, *Adv. Funct. Mater.* **2017**, *27*, 1605058.
83. Lee, E. K.; Lee, M. Y.; Park, C. H.; Lee, H. R.; Oh, J. H. Toward Environmentally Robust Organic Electronics: Approaches and Applications. *Adv. Mater.* **2017**, *29*, 1703638.

84. Boukhili, W.; Mahdouani, M.; Erouel, M.; Puigdollers, J.; Bourguiga, R. Reversibility of humidity effects in pentacene based organic thin-film transistor: Experimental data and electrical modeling, *Synth. Met.* **2015** ,*199*, 303–309.
85. Quinn, J. T. E.; Zhu, J.; Li, X.; Wang, J.; Li, Y. Recent progress in the development of n-type organic semiconductors for organic field effect transistors. *J. Mater. Chem. C,* **2017**, *5*, 8654−8681.
86. Lu, G.; Blakesley, J.; Himmelberger, S.; Pingel, P.; Frisch, J.; Lieberwirth, I.; Salzmann, I.; Oehzelt, M.; Di Pietro, R.; Salleo, A.; et al. Moderate Doping Leads to High Performance of Semiconductor/Insulator Polymer Blend Transistors. *Nat. Commun.* **2013**, *4*, 1-8.
87. Abdou, M. S. A.; Orfino, F. P.; Son, Y.; Holdcroft, S. Interaction of Oxygen with Conjugated Polymers: Charge Transfer Complex Formation with Poly(3-alkylthiophenes). *J. Am. Chem. Soc.* **1997**, *119*, 4518−4524.
88. Barf, M.-M.; Benneckendorf, F. S.; Reiser, P.; Bäuerle, R.; Köntges, W.; Müller, L.; Pfannmöller, M.; Beck, S.; Mankel, E.; Freudenberg, J.; et al. Compensation of Oxygen Doping in P-Type Organic Field-Effect Transistors Utilizing Immobilized n-Dopants. *Adv. Mater. Technol.* **2020**, 2000556.
89. Zuo, G.; Linares, M.; Upreti, T.; Kemerink, M. General rule for the energy of water-induced traps in organic semiconductors. *Nat. Mater.* **2019**, *18*, 588−593.
90. Nikolka, M.; Nasrallah, I.; Rose, B.; Ravva, M. K.; Broch, K.; Sadhanala, A.; Harkin, D.; Charmet, J.; Hurhangee, M.; Brown, A.; Illig, S.; Too, P.; Jongman, J.; McCulloch, I.; Bredas, J. L.; Sirringhaus, H. High operational and environmental stability of high-mobility conjugated polymer field-effect transistors through the use of molecular additives. *Nat. Mater.* **2017**, *16*, 356–362.
91. Phan, H.; Wang, M.; Bazan, G. C.; Nguyen, T.-Q. Electrical Instability Induced By Electron Trapping in Low-Bandgap Donor-Acceptor Polymer Field-Effect Transistors. *Adv. Mater.* **2015**, *27*, 7004−7009.
92. Phan, H.; Ford, M. J.; Lill, A. T.; Wang, M.; Bazan, G. C.; Nguyen, T.-Q. Improving Electrical Stability, and Ideality in Organic Field-Effect Transistors by the Addition of Fullerenes: Understanding the Working Mechanism. *Adv. Funct. Mater.* **2017**, 27, 1701358.
93. Bobbert, P. A.; Sharma, A.; Mathijssen, S. G. J.; Kemerink, M.; De Leeuw, D. M. Operational Stability of Organic Field-Effect Transistors. *Adv. Mater.* **2012**, *24*, 1146−1158.

94. Park, S.; Kim, S. H.; Choi, H. H.; Kang, B.; Cho, K. Recent Advances in the Bias Stress Stability of Organic Transistors. *Adv. Funct. Mater.* **2019**, *30*, 1904590.
95. Tseng, H. R.; Phan, H.; Luo, C.; Wang, M.; Perez, L. A.; Patel, S. N.; Ying, L.; Kramer, E. J.; Nguyen, T. Q.; Bazan, G. C.; Heeger, A. J. High-mobility field-effect transistors fabricated with macroscopic aligned semiconducting polymers. *Adv. Mater.* **2014**, *26*, 2993−2998.
96. Luo, C.; Kyaw, A. K.; Perez, L. A.; Patel, S.; Wang, M.; Grimm, B.; Bazan, G. C.; Kramer, E. J.; Heeger, A. J. General strategy for self-assembly of highly oriented nanocrystalline semiconducting polymers with high mobility. *Nano Lett.* **2014**, *14*, 2764−2771.
97. Chen, M. S.; Lee, O. P.; Niskala, J. R.; Yiu, A. T.; Tassone, C. J.; Schmidt, K.; Beaujuge, P. M.; Onishi, S. S.; Toney, M. F.; Zettl, A.; Frechet, J. M. Enhanced solid-state order and field-effect hole mobility through control of nanoscale polymer aggregation. *J. Am. Chem. Soc.* **2013**, *135*, 19229−19236.
98. Paterson, A. F.; Treat, N. D.; Zhang, W.; Fei, Z.; Wyatt-Moon, G.; Faber, H.; Vourlias, G.; Patsalas, P. A.; Solomeshch, O.; Tessler, N.; Heeney, M.; Anthopoulos, T. D. Small Molecule/Polymer Blend Organic Transistors with Hole Mobility Exceeding 13 $cm^2V^{-1}s^{-1}$. *Adv. Mater*. **2016**, *28*, 7791−7798.
99. Colleaux, F.; Ball, J. M.; Wo´bkenberg, P. H.; Hotchkiss, P. J.; Marder, S. R.; Anthopoulos, T. D. Bias-Stress Effects in Organic Field Effect Transistors Based on Self-Assembled Monolayer Nanodielectrics. *Phys. Chem*. **2011**, *13*, 14387−14393.
100. Lee, W. H.; Park, Y. D. Organic Semiconductor/Insulator Polymer Blends for High-Performance Organic Transistors. *Polymers* **2014**, 6, 1057−1073.
101. Riera-Galindo, S.; Leonardi, F.; Pfattner, R.; Mas-Torrent, M. Organic Semiconductor/Polymer Blend Films for Organic Field Effect Transistors. *Adv. Mater. Technol.* **2019**, *4*, 1900104.
102. Campos, A.; Riera-Galindo, S.; Puigdollers, J.; Mas-Torrent, M. Reduction of Charge Traps and Stability Enhancement in Solution Processed Organic Field-effect Transistors Based on a Blended N type Semiconductor. *ACS Appl. Mater. Interfaces.* **2018**, *10*, 15952–15961.
103. Iqbal, H. F.; Waldrip, M.; Chen, H.; McCulloch, I. and Jurchescu, O.D., Elucidating the Role of Water-Related Traps in the Operation of Polymer Field-Effect Transistors. *Adv. Electron. Mater.* **2021**, *7*, 2100393.

104. Xu, Y.; Sun, H.; Liu, A.; Zhu, H. H.; Li, W.; Lin, Y. F.; Noh, Y. Y. Doping: A Key Enabler for Organic Transistors. *Adv. Mater*. **2018**, *30*, 1801830.

105. Scaccabarozzi, A. D.; Basu, A.; Anies, F.; Liu, J.; Zapata-Arteaga, O.; Warren, R.; Firdaus, Y.; Nugraha, M. I.; Lin, Y.; Campoy-Quiles, M.; Koch, N.; Muller, C.; Tsetseris, L.; Heeney, M.; Anthopoulos, T. D. Doping Approaches for Organic Semiconductors. *Chem. Rev*. **2022**, *122*, 4420−4492.

106. Rossbauer, S.; Muller, C.; Anthopoulos, TD. Comparative Study of the N-Type Doping Efficiency in Solution-processed Fullerenes and Fullerene Derivatives. *Adv. Funct. Mater*. **2014**, *24*, 7116-7124.

107. Hein, M. P.; Zakhidov, A. A.; Luessem, B.; Jankowski, J.; Tietze, M. L.; Riede, M. K.; Leo, K. Molecular Doping for Control of Gate Bias Stress in Organic Thin Film Transistors. *Appl. Phys. Lett.* **2014**, *104*, 013507.

108. Nikolka, M.; Schweicher, G.; Armitage, J.; Nasrallah, I.; Jellett, C.; Guo, Z.; Hurhangee, M.; Sadhanala, A.; McCulloch, I.; Nielsen, C. B.; et al. Performance Improvements in Conjugated Polymer Devices by Removal of Water-Induced Traps. *Adv. Mater*. **2018**, *30*, 1801874.

109. Lüssem, B.; Keum, C. M.; Kasemann, D.; Naab, B.; Bao, Z.; Leo, K. Doped Organic Transistors. *Chem. Rev*. **2016**, *116*, 13714− 13751.

110. Mendez, H.; Heimel, G.; Opitz, A.; Sauer, K.; Barkowski, P.; Oehzelt, M.; et al. Doping of Organic Semiconductors: Impact of Dopant Strength and Electronic Coupling. *Angew. Chem., Int. Ed. Engl.* **2013**, *52*, 7751-7755.

111. Rienstra-Kiracofe, J. C.; Tschumper, G. S.; Schaefer, H. F.; Nandi, S.; Ellison, G. B. Atomic and Molecular Electron Affinities: Photoelectron Experiments and Theoretical Computations. *Chem. Rev*. **2002**, *102*, 231−282.

112. Chiang, C. K.; Fincher, C., Jr; Park, Y. W.; Heeger, A. J.; Shirakawa, H.; Louis, E. J.; Gau, S. C.; MacDiarmid, A. G. Electrical Conductivity in Doped Polyacetylene. *Phys. Rev. Lett.* **1977**, *39*, 1098− 1101.

113. Meyer, J.; Hamwi, S.; Kröger, M.; Kowalsky, W.; Riedl, T.; Kahn, A. Transition Metal Oxides for Organic Electronics: Energetics, Device Physics and Applications. *Adv. Mater.* **2012**, *24*, 5408−5427.

114. Meyer, J.; Hamwi, S.; Schmale, S.; Winkler, T.; Johannes, H.-H.; Riedl, T.; Kowalsky, W. A Strategy towards P-Type Doping of Organic Materials with HOMO Levels beyond 6 EV Using Tungsten Oxide. *J. Mater. Chem*. **2009**, *19*, 702−705.

115. Jacobs, I. E.; Moule, A. J. Controlling Molecular Doping in Organic Semiconductors. Adv. Mater. 2017, *29*, 1703063.

116. El-Khatib, N.; Boudjema, B.; Guillaud, G.; Maitrot, M.; Chermette, H. Theoretical and Experimental Doping of Molecular Materials: P and N Doping of Zinc Phthalocyanine. *J. Less-Common Met.* **1988**, *143*, 101−112.

117. Lim, E.; Peterson, K. A.; Su, G. M.; Chabinyc, M. L. Thermoelectric Properties of Poly(3-Hexylthiophene) (P3HT) Doped with 2,3,5,6-Tetrafluoro-7,7,8,8-Tetracyanoquinodimethane (F4TCNQ) by Vapor-Phase Infiltration. *Chem. Mater*. **2018**, *30*, 998−1010.

118. Kang, K.; Schott, S.; Venkateshvaran, D.; Broch, K.; Schweicher, G.; Harkin, D.; Jellett, C.; Nielsen, C. B.; McCulloch, I.; Sirringhaus, H. Investigation of the Thermoelectric Response in Conducting Polymers Doped by Solid-State Diffusion. *Mater. Today Phys.* **2019**, *8*, 112−122.

119. Karpov, Y.; Kiriy, N.; Formanek, P.; Hoffmann, C.; Beryozkina, T.; Hambsch, M.; Al-Hussein, M.; Mannsfeld, S. C. B.; Büchner, B.; Debnath, B.; et al. Sequentially Processed P3HT/CN6-CP •- NBu 4+ Films: Interfacial or Bulk Doping? *Adv. Electron. Mater*. **2020**, *6*, 1901346.

120. Saska, J.; Gonel, G.; Bedolla-Valdez, Z. I.; Aronow, S. D.; Shevchenko, N. E.; Dudnik, A. S.; Moulé, A. J.; Mascal, M. A Freely Soluble, High Electron Affinity Molecular Dopant for Solution Processing of Organic Semiconductors. *Chem. Mater*. **2019**, *31*, 1500−1506.

121. Liu, Y.; Nell, B.; Ortstein, K.; Wu, Z.; Karpov, Y.; Beryozkina, T.; Lenk, S.; Kiriy, A.; Leo, K.; Reineke, S. High Electron Affinity Molecular Dopant CN6-CP for Efficient Organic Light-Emitting Diodes. *ACS Appl. Mater. Interfaces* **2019**, *11*, 11660−11666.

122. Meerheim, R.; Olthof, S.; Hermenau, M.; Scholz, S.; Petrich, A.; Tessler, N.; Solomeshch, O.; Lüssem, B.; Riede, M.; Leo, K. Investigation of C60F36 as Low-Volatility p-Dopant in Organic Optoelectronic Devices. *J. Appl. Phys.* **2011**, *109*, 103102.

123. Nell, B.; Ortstein, K.; Boltalina, O. V.; Vandewal, K. Influence of Dopant-Host Energy Level Offset on Thermoelectric Properties of Doped Organic Semiconductors. *J. Phys. Chem. C* **2018**, *122*, 11730− 11735.

124. Babuji, A.; Temiño, I.; Pérez-Rodríguez, A.; Solomeshch, O.; Tessler, N.; Vila, M.; Li, J.; Mas-Torrent, M.; Ocal, C.; Barrena, E. Double Beneficial Role of Fluorinated Fullerene Dopants on Organic Thin-Film Transistors: Structural Stability and Improved Performance. *ACS Appl. Mater. Interfaces* **2020**, *12*, 28416−28425.

125. Dai, A.; Zhou, Y.; Shu, A. L.; Mohapatra, S. K.; Wang, H.; Fuentes-Hernandez, C.; Zhang, Y.; Barlow, S.; Loo, Y. L.; Marder, S. R.; et al. Enhanced Charge-Carrier Injection and Collection via Lamination of Doped Polymer Layers p-Doped with a Solution-Processible Molybdenum Complex. *Adv. Funct. Mater*. **2014**, *24*, 2197−2204.

126. Paniagua, S. A.; Baltazar, J.; Sojoudi, H.; Mohapatra, S. K.; Zhang, S.; Henderson, C. L.; Graham, S.; Barlow, S.; Marder, S. R. Production of Heavily N- and p-Doped CVD Graphene with SolutionProcessed Redox-Active Metal-Organic Species. *Mater. Horiz.* **2014**, *1*, 111−115.

127. Harada, K.; Werner, A. G.; Pfeiffer, M.; Bloom, C. J.; Elliott, C. M.; Leo, K. Organic Homojunction Diodes with a High Built-in Potential: Interpretation of the Current-Voltage Characteristics by a Generalized Einstein Relation. *Phys. Rev. Lett*. **2005**, *94*, 036601.

128. Ćirić-Marjanović, G. Recent Advances in Polyaniline Research: Polymerization Mechanisms, Structural Aspects. *Synth. Met.* **2013**, *177*, 1−47.

129. Ausserlechner, S. J.; Gruber, M.; Hetzel, R.; Flesch, H.-G.; Ladinig, L.; Hauser, L.; Haase, A.; Buchner, M.; Resel, R.; Schü rrer, F.; Stadlober, B.; Trimmel, G.; Zojer, K.; Zojer, E. Mechanism of Surface Proton Transfer Doping in Pentacene Based Organic Thin-Film Transistors. *Phys. Status Solidi A.* **2012**, *209*, 181−192.

130. Kao, C. Y.; Lee, B.; Wielunski, L. S.; Heeney, M.; McCulloch, I.; Garfunkel, E.; Feldman, L. C.; Podzorov, V. Doping of Conjugated Polythiophenes with Alkyl Silanes. *Adv. Funct. Mater.* **2009**, *19*, 1906− 1911.

131. Duclaux, L. Review of the Doping of Carbon Nanotubes (Multiwalled and Single-walled). *Carbon* **2002**, *40*, 1751−1764.

132. Cappel, U. B.; Daeneke, T.; Bach, U. Oxygen-induced Doping of Spiro-MeOTAD in Solid-state Dye-Sensitized Solar Cells and its Impact on Device Performance. *Nano Lett*. **2012**, *12*, 4925−4931.

133. Han, Y.; Barnes, G.; Lin, Y.-H.; Martin, J.; Al-Hashimi, M.; AlQaradawi, S. Y.; Anthopoulos, T. D.; Heeney, M. Doping of Large Ionization Potential Indenopyrazine Polymers via Lewis Acid Complexation with Tris(Pentafluorophenyl)Borane: A Simple Method for Improving the Performance of Organic Thin-Film Transistors. *Chem. Mater*. **2016**, *28*, 8016−8024.

134. Poverenov, E.; Zamoshchik, N.; Patra, A.; Ridelman, Y.; Bendikov, M. Unusual Doping of Donor-Acceptor-Type Conjugated Polymers Using Lewis Acids. *J. Am. Chem. Soc*. **2014**, *136*, 5138−5149.

135. Fediai, A.; Symalla, F.; Friederich, P.; Wenzel, W. Disorder Compensation Controls Doping Efficiency in Organic Semiconductors. *Nat. Commun*. **2019**, *10*, 2−8.

136. Brown, A. R.; de Leeuw, D. M.; Havinga, E. E.; Pomp, A. A Universal Relation between Conductivity and Field-Effect Mobility in Doped Amorphous Organic Semiconductors. *Synth. Met.* **1994**, *68*, 65−70.

137. Meijer, E. J.; Detcheverry, C.; Baesjou, P. J.; Van Veenendaal, E.; De Leeuw, D. M.; Klapwijk, T. M. Dopant Density Determination in Disordered Organic Field-Effect Transistors. *J. Appl. Phys*. **2003**, *93*, 4831−4835.

138. Kristiansen, M.; Smith, P.; Chanzy, H.; Baerlocher, C.; Gramlich, V.; McCusker, L.; Weber, T.; Pattison, P.; Blomenhofer, M.; Schmidt, H.-W. Structural Aspects of 1,3,5-Benzenetrisamides-A New Family of Nucleating Agents. *Cryst. Growth Des*. **2009**, *9*, 2556−2558.

139. Yee, P. Y.; Scholes, D. T.; Schwartz, B. J.; Tolbert, S. H. DopantInduced Ordering of Amorphous Regions in Regiorandom P3HT. *J. Phys. Chem. Lett*. **2019**, *10*, 4929−4934.

140. Ma, L.; Lee, W. H.; Park, Y. D.; Kim, J. S.; Lee, H. S.; Cho, K. High Performance Polythiophene Thin-Film Transistors Doped with Very Small Amounts of an Electron Acceptor. *Appl. Phys. Lett.* **2008**, *92*, 063310.

141. Jarrett, C. P.; Friend, R. H.; Brown, A. R.; de Leeuw, D. M. Field Effect Measurements in Doped Conjugated Polymer Films: Assessment of Charge Carrier Mobilities. *J. Appl. Phys*. **1995**, *77*, 6289−6294.

142. Tada, K.; Harada, H.; Yoshino, K. Field-Effect Mobility of Molecularly Doped Poly(3-Hexylthiophene). *Jpn. J. Appl. Phys*. **1997**, *36*, L718−L720.
143. Zhang, F.; Mohammadi, E.; Qu, G.; Dai, X.; Diao, Y. Orientation-Dependent Host-Dopant Interactions for Manipulating Charge Transport in Conjugated Polymers. *Adv. Mater*. **2020**, *32*, 2002823.
144. Zessin, J.; Xu, Z.; Shin, N.; Hambsch, M.; Mannsfeld, S. C. B. Threshold Voltage Control in Organic Field-Effect Transistors by Surface Doping with a Fluorinated Alkylsilane. *ACS Appl. Mater. Interfaces* **2019**, *11*, 2177−2188.
145. Huseynova, G.; Xu, Y.; Nketia Yawson, B.; Shin, E.-Y.; Lee, M. J.; Noh, Y.-Y. P-Type Doped Ambipolar Polymer Transistors by Direct Charge Transfer from a Cationic Organic Dye Pyronin B Ferric Chloride. *Org. Electron*. **2016**, *39*, 229−235.
146. Barf, M.-M.; Benneckendorf, F. S.; Reiser, P.; Bäuerle, R.; Köntges, W.; Müller, L.; Pfannmöller, M.; Beck, S.; Mankel, E.; Freudenberg, J.; et al. Compensation of Oxygen Doping in P-Type Organic Field-Effect Transistors Utilizing Immobilized n-Dopants. *Adv. Mater. Technol*. **2020**, 2000556.
147. Panidi, J.; Paterson, A. F.; Khim, D.; Fei, Z.; Han, Y.; Tsetseris, L.; Vourlias, G.; Patsalas, P. A.; Heeney, M.; Anthopoulos, T. D. Remarkable Enhancement of the Hole Mobility in Several Organic Small-Molecules, Polymers, and Small-Molecule: Polymer Blend Transistors by Simple Admixing of the Lewis Acid p-Dopant B(C6F5)3. *Adv. Sci*. **2018**, *5*, 1700290.
148. Choi, H. H.; Paterson, A. F.; Fusella, M. A.; Panidi, J.; Solomeshch, O.; Tessler, N.; Heeney, M.; Cho, K.; Anthopoulos, T. D.; Rand, B. P.; et al. Hall Effect in Polycrystalline Organic Semiconductors: The Effect of Grain Boundaries. *Adv. Funct. Mater*. **2020**, *30*, 1903617.
149. Mun, J.; Kang, J.; Zheng, Y.; Luo, S.; Wu, Y.; Gong, H.; Lai, J. C.; Wu, H. C.; Xue, G.; Tok, J. B. H.; Bao, Z. F4-TCNQ as an Additive to Impart Stretchable Semiconductors with High Mobility and Stability. *Adv. Electron. Mater*. **2020**, *6*, 2000251.
150. Huseynova, G.; Xu, Y.; Nketia Yawson, B.; Shin, E.-Y.; Lee, M. J.; Noh, Y.-Y. P-type doped ambipolar polymer transistors by direct charge transfer from a cationic organic dye Pyronin B ferric chloride. *Org. Electron*. **2016**, *39*, 229−235.

151. Zhou, Y.; Fuentes-Hernandez, C.; Shim, J.; Meyer, J.; Giordano, A. J.; Li, H.; Winget, P.; Papadopoulos, T.; Cheun, H.; Kim, J.; et al. A Universal Method to Produce Low-Work Function Electrodes for Organic Electronics. *Science* **2012**, *336*, 327−332.
152. Hou, J. L.; Kasemann, D.; Widmer, J.; Günther, A. A.; Lüssem, B.; Leo, K. Reduced Contact Resistance in Top-Contact Organic FieldEffect Transistors by Interface Contact Doping. *Appl. Phys. Lett*. **2016**, *108*, 103303.
153. Minari, T.; Miyadera, T.; Tsukagoshi, K.; Aoyagi, Y.; Ito, H. Charge Injection Process in Organic Field-Effect Transistors. *Appl. Phys. Lett*. **2007**, *91*, 053508.
154. Oh, J. H.; Wei, P.; Bao, Z. Molecular N-Type Doping for AirStable Electron Transport in Vacuum-Processed n-Channel Organic Transistors. *Appl. Phys. Lett*. **2010**, *97*, 243305.
155. Melville, O. A.; Grant, T. M.; Lochhead, K.; King, B.; Ambrose, R.; Rice, N. A.; Boileau, N. T.; Peltekoff, A. J.; Tousignant, M.; Hill, I. G.; et al. Contact Engineering Using Manganese, Chromium, and Bathocuproine in Group 14 Phthalocyanine Organic Thin-Film Transistors. *ACS Appl. Electron. Mater*. **2020**, *2*, 1313−1322.
156. Zhang, J.; Geng, B.; Duan, S.; Huang, C.; Xi, Y.; Mu, Q.; Chen, H.; Ren, X.; Hu, W. High-Resolution Organic Field-Effect Transistors Manufactured by Electrohydrodynamic Inkjet Printing of Doped Electrodes. *J. Mater. Chem*. C **2020**, *8*, 15219−15223.
157. Kim, Y.; Broch, K.; Lee, W.; Ahn, H.; Lee, J.; Yoo, D.; Kim, J.; Chung, S.; Sirringhaus, H.; Kang, K.; et al. Highly Stable Contact Doping in Organic Field Effect Transistors by Dopant-Blockade Method. *Adv. Funct. Mater*. **2020**, *30*, 2000058.

Chapter 3: Photoelectrochemical CO_2 Reduction into Syngas with the Metal/Oxide Interface

Photoelectrochemical CO_2 reduction is a promising route for producing value-added chemical feedstocks and fuels, as well as to cut CO_2 emissions. Syngas is a mixture of CO and H_2 that is used in industry to make methanol and other commercial hydrocarbons. However, due to the problems associated with the chemical inertness of CO_2 and the complex reaction network of CO_2 conversion, achieving effective and stable PEC CO_2 reduction into syngas with controllable composition is challenging. In this study, we report a benchmarking solar-to-syngas efficiency of 0.87 percent, a high turnover number of 24800, and a desirable high stability of 10 hours using a metal/oxide interface that spontaneously activates CO_2 molecules and stabilizes the main chemical intermediates in this study. Furthermore, with a total unity Faradaic efficiency, the CO/H_2 ratios in the composition can be modified in a wide range between 4:1 and 1:6. According to the experimental observations and theoretical calculations we reveal that the metal/oxide interface affords multifunctional catalytic sites with complementary chemical properties for CO_2 activation and conversion, leading to a novel pathway that is inaccessible with the individual components, Our proposed strategy opens up new possibilities for developing high-performance PEC systems for controllable CO_2 reduction into valuable carbon-based products and fuels. This chapter is based on the published journal: Photo electrochemical CO_2 Reduction into Syngas with the Metal/Oxide Interface, Chu, S.* Ou, P.* Ghamari, P.* Vanka, S. Zhou, B. Shih, I. Song, J, Mi, Z, *J. Am. Chem. Soc*. 2018. [* Authors contributed equally to this work].

3.1 Introduction

The development of solar-powered CO_2 reduction with H_2O holds the promise to mitigate greenhouse gas (CO_2) emission into the atmosphere, while simultaneously convert renewable solar energy into storable value-added chemicals and fuels.[1-5] The photoelectrochemical (PEC) route, which combines light harvesting photovoltaic and electrochemical components into a monolithically integrated device, has received considerable attention for application in CO_2 reduction recently.[6-9] Among the wide variety of CO_2 reduction products, CO is a gaseous product that requires only two proton-electron transfers, and thus a kinetically feasible choice compared to CH_3OH and CH_4, which require six and eight proton-electron transfers to form one molecule,

respectively.[10-11] Moreover, CO is an important bulk chemical to form methanol and other commodity hydrocarbons via syngas intermediate, a mixture of CO and H_2, by using well-established standard industrial processes such as Fischer-Tropsch technology.[12-15] These attributes, together with the almost inevitable H_2 evolution in aqueous PEC cell can be valorized to produce syngas mixtures, render the proposed syngas production from CO_2 and H_2O conversion a technologically and economically viable pathway to leverage established commercial processes for liquid fuels synthesis. Providing different CO/H_2 ratio in syngas mixtures can also be used for different downstream products (e.g. 1:3, 1:2 and 1:1 for methane, methanol and oxo-alcohols, respectively).[16-18] Therefore, the syngas route would allow a flexible platform for integration with a wide window of catalytic systems in a broad CO_2-recycling scheme without the strict requirement of suppression of H_2 evolution reaction.[19-31]

To date, various semiconductor photocathodes, including p-Si,[32-34] ZnTe,[35-36] CdTe,[37] p-InP,[37] Cu_2O[38-39] and p-NiO[40-41], have been investigated for PEC CO_2 reduction into CO, usually in conjunction with a molecular metal-complex or metal co-catalyst (e.g. Au, Ag and derivatives) to realize selective CO production. However, it remains challenging to develop efficient and stable PEC catalytic system that can activate inert CO_2 molecule at low overpotential or even spontaneously, and selectively produce syngas with controlled composition in a wide range to meet different downstream products. It has been reported that pure metal catalyst with a simple monofunctional site usually has a weak interaction with CO_2 molecule and cannot provide multiple sites for stabilizing the key reaction intermediates with optimal binding strength, which leads to impractically high overpotential and low catalytic efficiency/stabilty.[42-43] Here we show that efficient and stable syngas production with tunable composition from PEC CO_2 reduction can be achieved with the introduction of a completely different type of sites: metal/oxide interface. On the basis of experiments and first-principles theoretical calculations, it is found that the metal/oxide interface can spontaneously activate CO_2 and stabilize the key reaction intermediates for facilitating CO production. The intimate metal/oxide interface provides the multifunctional combination of metal and oxide catalytic sites with complementary chemical properties, which opens new reaction channels that are not possible with the individual components. The versatility of using metal/oxide interface is demonstrated by the combination of different metals (Pt and Pd) and oxides (TiO_2 and ZnO). Remarkably, although pristine metal catalytically favors the proton reduction to evolve H_2, the coverage of metal with oxide to form metal/oxide interface shows

preferential activity for CO_2 reduction over H_2 evolution. As an example, by rationally integrating the Pt/TiO_2 co-catalyst with the strong light harvesting of p-n Si junction and efficient electron extraction effect of GaN nanowire arrays (Pt-TiO_2/GaN/n^+-p Si), a record half-cell solar-to-syngas (STS) efficiency of 0.87% and a benchmark turnover number (TON) of 24800 have been achieved in an aqueous PEC system. The durability of the PEC system for highly stable syngas production of 10 h has been demonstrated as well.

3.2 Results and Discussion

3.2.1 Design and Synthesis of Pt-TiO_2/GaN/n^+-p Si

We choose Pt-TiO_2 as an example to demonstrate the validity of metal/oxide interface for PEC CO_2 reduction. GaN nanowire on p-n Si junction was selected as the platform to load the Pt-TiO_2 system. The schematic design of Pt-TiO_2/GaN/n^+-p Si is illustrated in Figure 3.1 a. The sample was prepared in two major steps. First, GaN nanowire arrays were grown on p-n Si wafer by plasma-assisted molecular beam epitaxy, as described in experimental methods in appendix A. Such a structure takes advantage of the strong light absorption capability of Si (bandgap of 1.1 eV) and efficient electron extraction effect as well as large surface area provided by GaN nanowires. [31,44] Moreover, the light absorption and catalytic reaction sites are decoupled spatially in the structure, providing an ideal platform to investigate the effect of co-catalysts on the catalytic performance without affecting the optical properties. Second, Pt nanoparticles and TiO_2 ultrathin layer were deposited on GaN nanowires surface in sequential order using photodeposition and atomic-layer deposition (ALD) process, respectively (see the experimental methods). The intimate Pt/TiO_2 interface provides multiple sites and unique channels that facilitate the CO_2 activation and reaction pathways for syngas production.

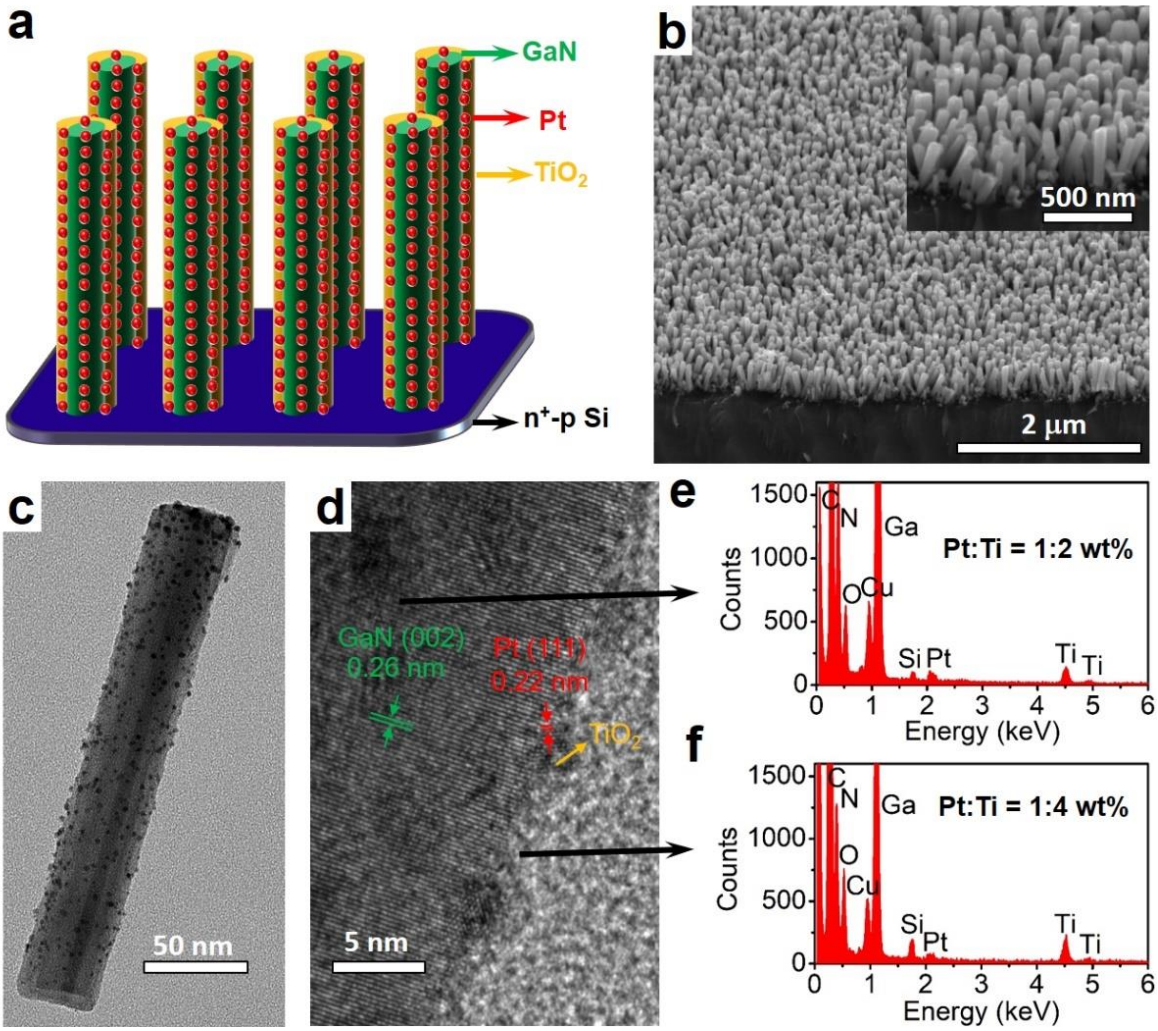

Figure 3.1: Characterization of Pt-TiO_2/GaN/n^+-p Si sample. (a) Schematic illustration of the structure, (b) 45°-tilted SEM image shows GaN nanowire growth vertically on the Si substrate, (c) TEM image illustrates Pt nanoparticles distributed uniformly on the GaN nanowire surface, (d) HRTEM image, and EDX analysis of the center (e) and edge region (f) indicates the coating of GaN nanowire and Pt nanoparticles with ultrathin TiO_2 layer. The Cu peaks in EDX arise from the TEM sample grid.

3.3 Characterization of structure

The morphology and chemical component of the Pt-TiO_2/GaN/n^+-p Si heterostructures were studied using scanning electron microscopy (SEM), transmission electron microscopy (TEM), energy-dispersive X-ray spectroscopy (EDX) and inductively coupled plasma–atomic emission spectroscopy (ICP-AES) analysis. The cross-sectional SEM image (Figure 3.1 b) shows that the GaN nanowires are aligned vertically to the Si substrate with an average diameter of ~50 nm (±15

nm) and height of 250 nm (±50 nm). TEM image in Figure 3.1c reveals that Pt nanoparticles of 2-3 nm size are uniformly deposited on the GaN nanowires surface. High-resolution TEM (HRTEM) image (Figure 3.1 d), along with EDX analysis in the centre and edge regions of nanowire (Figures 3.1e and f, respectively), indicates the coating of GaN nanowire with ultrathin TiO_2 layer. The TiO_2 layer is amorphous and has a thickness of ~1 nm, which corresponds to 18 ALD cycles of TiO_2 deposition. The lattice spacings of 0.22 nm and 0.26 nm corresponds to the (111) facet of Pt and (002) lattice plane of GaN, indicating the preferred nanowire growth along 〈0001〉 direction (c-axis). The loading amounts of Pt and Ti in Pt-TiO_2/GaN/n^+-p Si were determined to be 4.9 and 48.3 nmol/cm^2, respectively, by using ICP-AES analysis.

3.3.1 Photoelectrochemical properties

PEC performance of the sample was investigated in CO_2-saturated 0.5 M $KHCO_3$ solution (pH 7.5) under 300 W xenon lamp irradiation (800 mW/cm^{-2}) in a conventional three-electrode cell. To reveal the interaction of photocathode with CO_2, the current-potential (*J-V*) curves of Pt-TiO_2/GaN/n^+-p Si in a CO_2 or Ar-saturated electrolyte was compared as shown in Figure 3.2 a. There is a considerable enhancement in the photocurrent generation under CO_2 atmosphere

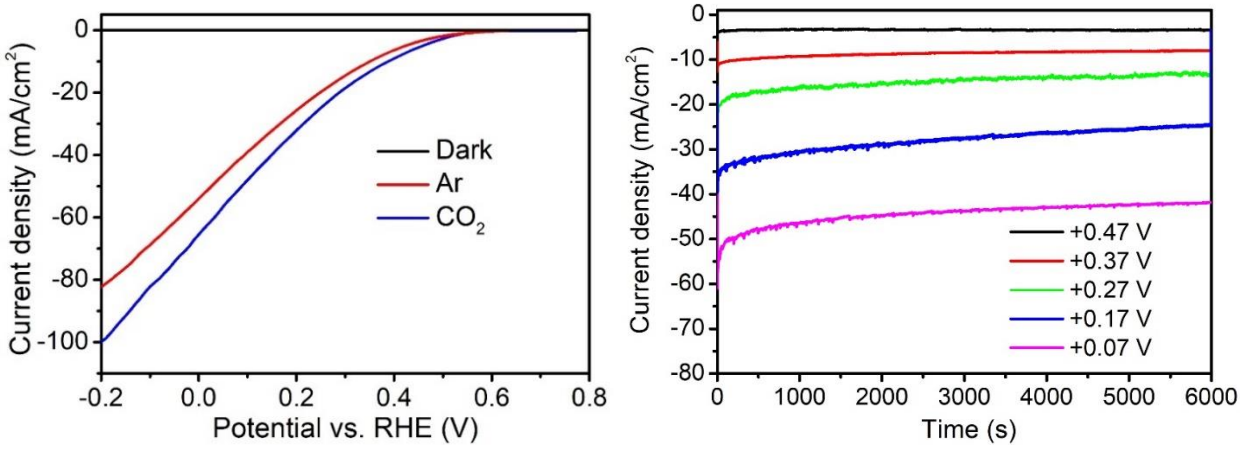

Figure 3.2: a) J-V curves of Pt-TiO_2/GaN/n^+-p Si in Ar and CO_2-saturated 0.5 M $KHCO_3$ solution. The pH values of Ar and CO_2-saturated 0.5 M $KHCO_3$ solution are 8 and 7.5, respectively. b) Chronoamperometry data of Pt-TiO_2/GaN/n^+-p Si at different applied potentials in CO_2-saturated 0.5 M $KHCO_3$ (pH 7.5).

compared to that of Ar atmosphere, indicating an interaction between the electrode surface and CO_2 molecule for CO_2 reduction. The corresponding chronoamperometry data at different applied potentials are shown in Figure 3.2 b.

Figure 3.3 shows the Faradaic efficiencies (FEs) for CO and H_2 on Pt-TiO_2/GaN/n^+-p Si at applied potential between +0.47 V and +0.07 V vs. reversible hydrogen electrode (RHE) in CO_2-saturated electrolyte (hereafter, all the potentials are referenced to the RHE unless otherwise specified). At an applied potential of +0.47 V, the photocathode exhibited a high CO FE of 78%, indicating the major extracted photogenerated electrons were used for selectively CO_2-to-CO conversion at the catalyst surface. By tuning the potential from +0.47 V to +0.07 V, the CO/H_2 ratio can be tuned in a large range between 4:1 and 1:6. At +0.27 V, a CO/H_2 ratio of 1:2 is obtained, which is a desirable composition of syngas mixtures for methanol synthesis and Fischer-Tropsch hydrocarbon formation.[45] The decreased CO FE at a more negative potential than +0.37 V is mainly due to the limited CO_2 mass transport in the electrolyte at high CO generation rate.[46-47]

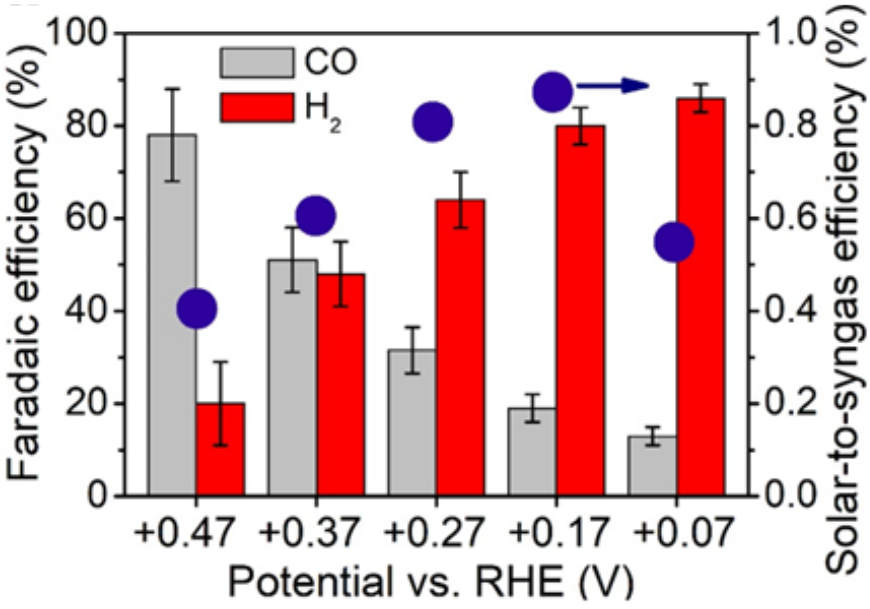

Figure 3.3: Faradaic efficiencies for CO (grey bars) and H_2 (red bars), and solar-to-syngas efficiency of Pt-TiO_2/GaN/n^+-p Si photocathode as a function of potential in CO_2-saturated 0.5 M $KHCO_3$ solution (pH 7.5).

The kinetic limitation was evidenced by the saturated current density for CO generation in the high applied bias region as depicted in Figure 3.4 a. In addition, different Tafel slopes for the CO_2 reduction and H_2 evolution reactions could lead to the above-mentioned bias-dependent reaction

selectivity. To evaluate their contribution, the Tafel plots for CO and H_2 evolution were drawn by using the corresponding partial current density, as shown in Figure 3.4 b. The Tafel slopes were calculated by using data points more positive than +0.37 V vs. RHE, as the slope increases dramatically at more negative potentials due to the mass-transport limitations.[48-49] It was found that the Tafel slopes for CO and H_2 evolution were 386 and 119 mV dec^{-1}, respectively. The different Tafel slopes result in the bias-dependent reaction selectivity largely in the low bias region.

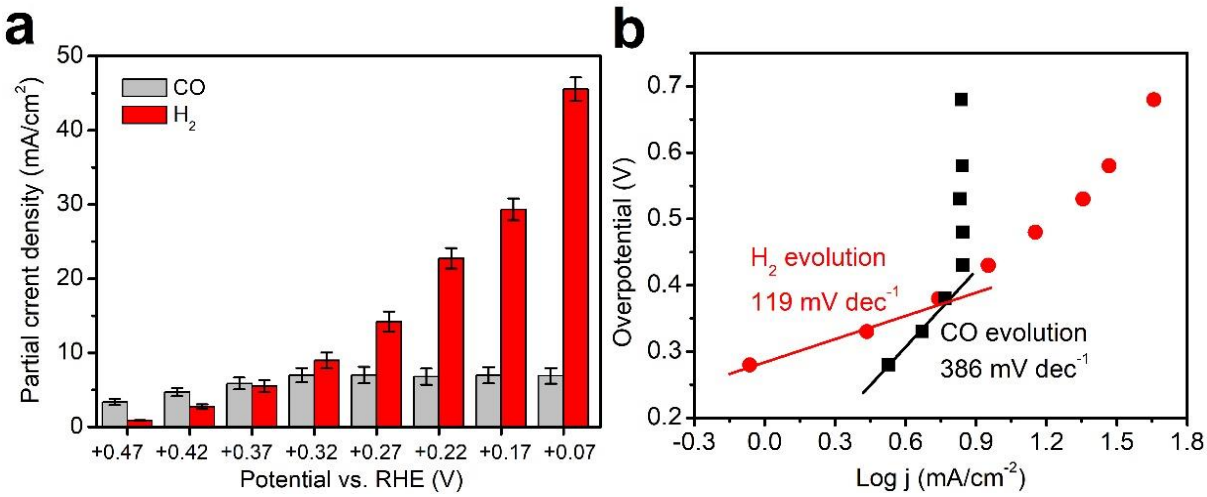

Figure 3.4: a) Partial current density for CO (grey bars) and H_2 (red bars) of Pt-TiO_2/GaN/n^+-p Si photocathode as a function of applied potential. b) Tafel plots for CO and H_2 evolution. The overpotential was calculated as: 0.75 V minus the applied potential. The value of 0.75 V is the open circuit potential of n^+-p Si solar cell as reported in our previous work.[2]

At all the applied potentials, a total FE of 97±8% was obtained for the co-generation of CO and H_2, with no appreciable amount of other gas products detected by gas chromatograph (GC) and liquid products (e.g. HCOOH and CH_3OH) analyzed by nuclear magnetic resonance (NMR) spectroscopy. To demonstrate that the generated CO from CO_2 reduction, isotopic experiment using $^{13}CO_2$ was conducted. The signal at m/z = 29 assigned to ^{13}CO appeared in the gas chromatography-mass spectrometry analysis (shown in Figure 3.5), indicating the CO product is formed from the reduction of CO_2.

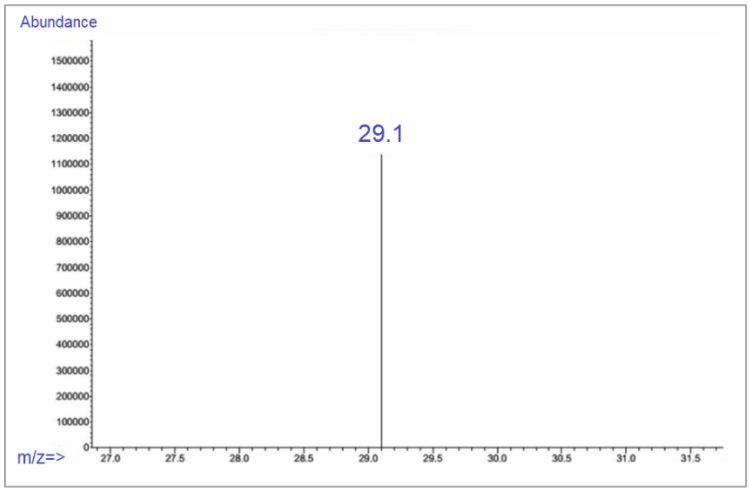

Figure 3.5: Mass spectrometry chromatogram of the gas phase analysis after 13C-labeled isotope experiment.

A highlight of our system is the highly positive onset potential of +0.47 V (underpotential of 580 mV to the CO_2/CO equilibrium potential at −0.11 V) for producing high CO FE of 78% in an aqueous PEC cell. The reported onset potentials, FEs and solar energy conversion efficiency of different photocathodes for CO production in an aqueous PEC cell are compared in Table 3.1. Among various reported photocathodes, our system features the lowest onset potential, which is 170 mV positive shifted compared with the best value reported in the literature.[36] The extremely low onset potential of our photocathode is attributed to coupling effects including strong light harvesting of p-n Si junction, efficient electron extraction of GaN nanowire arrays, and extremely fast syngas production kinetics on Pt-TiO_2 dual co-catalysts. The STS efficiencies of our system at different applied potentials are calculated according to the measured photocurrent density and FEs for CO and H_2 (see Appendix A.5). As shown in Figure 3.3, at +0.17 V, the STS efficiency reached 0.87%, which greatly outperforms other reported photocathodes and sets a new benchmark reported to date (Table 3.1).

The durability of Pt-TiO_2/GaN/n^+-p Si photocathode was investigated at a constant potential of +0.27 V by five consecutive runs with each run of 2 h (Figure 3.6). After each cycle, the products of CO and H_2 were analyzed by GC, the electrode was thoroughly cleaned by deionized water and the PEC cell was purged by CO_2 for 20 min. During the five runs of 10 h operation, the electrode

showed similar behavior in terms of photocurrent density and product selectivity, indicating the high stability of the sample during the syngas production process.

Table 3.1: Performance comparison of photocathodes for PEC CO_2 reduction into CO at underpotential (more positive than the equilibrium potential $E^o(CO_2/CO)$ = -0.11 V vs. RHE).

Photocathode	Onset potential (V vs. RHE) [a]	Underpotential (V) [b]	FE_{CO} (%) [c]	Solar-to-syngas efficiency (%) [d]	Ref
Au/p-Si	-0.09	+0.02	62	~0.02	32
Au/p-ZnTe	-0.10	+0.01	26[e]	0.005	35
Au/ZnO@ZnTe@CdTe	+0.30	+0.41	66.7	0.18[f]	36
$Au_3Cu/TiO_2/n^+$-p Si	-0.09	+0.02	44.9[g]	0.07	33
Au/n^+-p Si	+0.22	+0.33	16[h]	0.12	34
Cu-ZnO/GaN/n^+-p Si	+0.07	+0.18	70	~0.01	31
Pt-TiO_2/GaN/n^+-p Si	+0.47	+0.58	78	0.87	This work

[a] Defined as the reported most positive potentials for CO evolution. The potentials were converted to RHE values by the following equation: $V_{RHE} = V + (0.059 * pH) + V_{Ref}$, Where V_{Ref} = 0.244 and 0.197 for SCE and Ag/AgCl respectively.

[b] This is referred to the equilibrium potential of CO_2/CO at -0.11 V vs. RHE.

[c] FE for CO reported at the onset potential.

[d] Estimated using Equation 1 in Appendix A.5.

[e] The highest FE for CO reported in the system was 63% at -0.5 V vs. RHE.

[f] Solar-to-syngas efficiency of 0.43% was reported when connected the photocathode with a perovskite solar cell in tandem.

[g] The highest FE for CO reported in the system was 80% at -0.2 V vs. RHE.

[h] The highest FE for CO reported in the system was 91% at -0.2 V vs. RHE.

The initial decrease of high photocurrent density in each run is likely due to the limited mass transfer of reactants or products at high reaction rates, which can be recovered in the next run after

the cleaning of photoelectrode surface. The CO/H_2 ratio in the products was kept nearly 1:2 during the five cycles of operation, which is a desirable syngas composition for synthetizing downstream products including methanol and liquid hydrocarbons.[45]

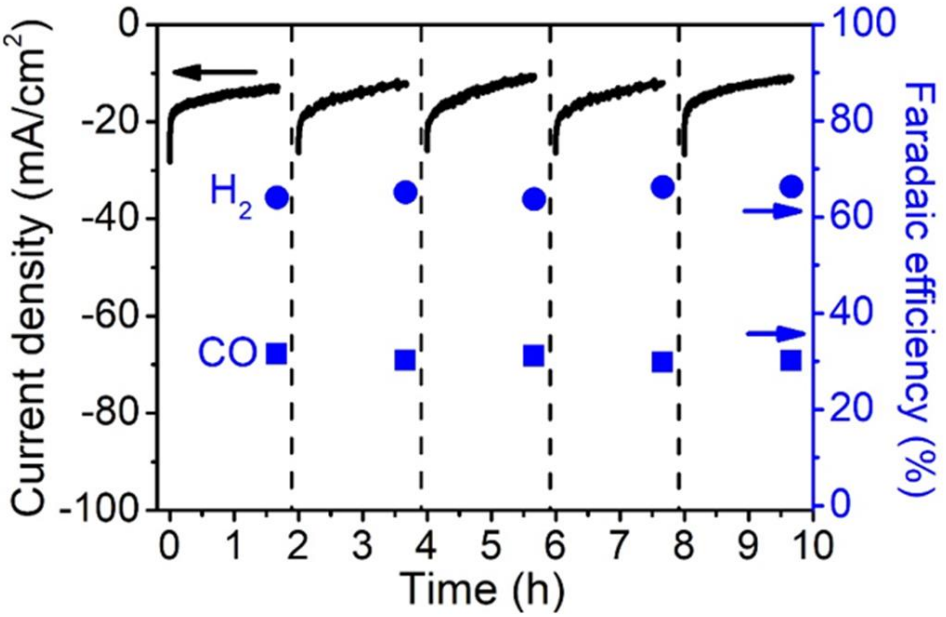

Figure 3.6: (a) Faradaic efficiencies for CO (grey bars) and H_2 (red bars), and solar-to-syngas efficiency of Pt-TiO_2/GaN/n^+-p Si photocathode as a function of potential in CO_2-saturated 0.5 M $KHCO_3$ solution (pH 7.5). (b) Chronoamperometry data and FEs for CO and H_2 of Pt-TiO_2/GaN/n^+-p Si photocathode at +0.27 V vs. RHE. The dashed lines denote cleaning of photoelectrode and purging of the PEC cell with CO_2.

The SEM, TEM, and XPS analysis of Pt-TiO_2/GaN/n^+-p Si photocathode after the PEC reaction were performed, as shown in Figure 3.7. No appreciable change of GaN nanowires and Pt-TiO_2 catalysts were found. The total turnover number (TON), defined as the ratio of the total amount of syngas evolved (264 μmol) to the amount of Pt-TiO_2 catalyst (10.64 nmol, calculated from the loadings and electrode sample area of 0.2 cm^2), reached 24800, which is at least 1 or 2 orders of magnitude higher than previously reported values for syngas or CO formation from PEC or photochemical CO_2 reduction.[31, 50-53]

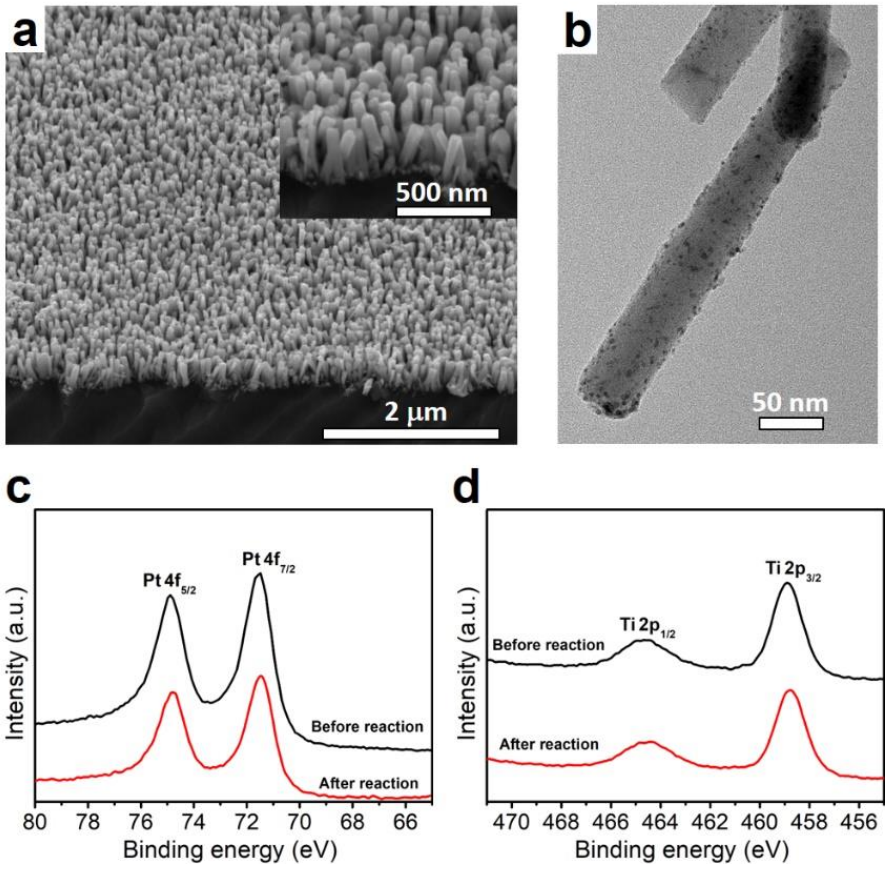

Figure 3.7: (a) SEM and (b) TEM images of Pt-TiO_2/GaN/n^+-p Si photocathode after PEC stability test. XPS of (c) Pt 4f and (d) Ti 2p of Pt-TiO_2/GaN/n^+-p Si photocathode before and after PEC stability test.

3.3.2 Investigation of the catalytic mechanisms

To understand the underlying catalytic mechanism and the role of basic components for the PEC performance of the Pt-TiO_2/GaN/n^+-p Si photocathode, we conducted a series of control experiments. Figures 3.8 a shows the comparison of LSV curves for bare GaN/n^+-p Si, GaN/n^+-p Si with individual Pt or TiO_2 co-catalyst, and Pt-TiO_2/GaN/n^+-p Si. The bare GaN/n^+-p Si displays a poor PEC performance with a negligible photocurrent density and highly negative onset potential. The loading of Pt co-catalyst can greatly improve the PEC performance with an onset potential of about +0.47 V and photocurrent density of ~50 mA cm^{-2} at −0.33 V, while TiO_2 alone shows a small photocurrent density of 5 mA cm^{-2} at −0.33 V. Compared to bare Pt, significantly higher photocurrent density of ~120 mA cm^{-2} at −0.33 V is attained when Pt and TiO_2 are loaded simultaneously.

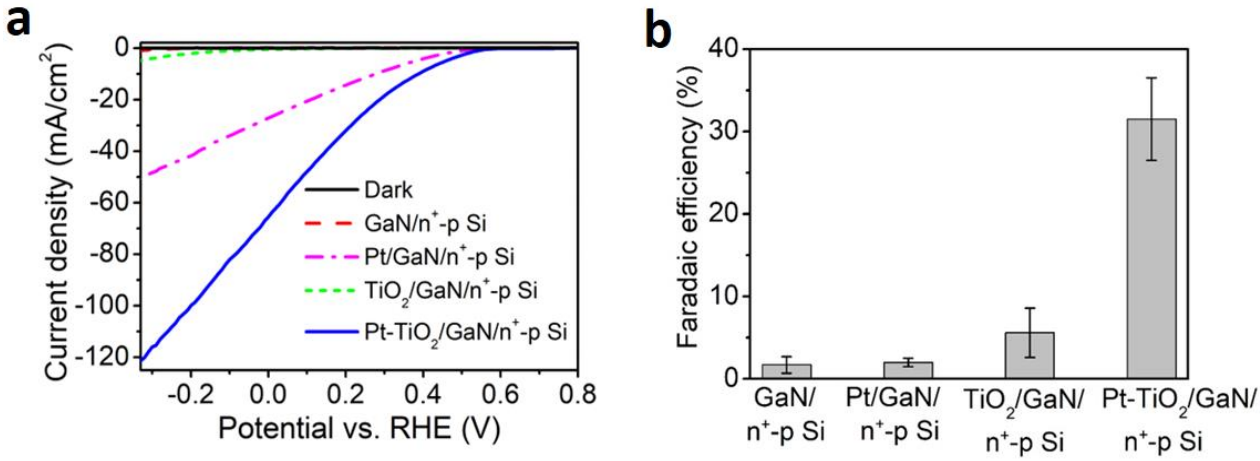

Figure 3.8: (c) *J-V* curves of bare GaN/n^+-p Si, GaN/n^+-p Si with individual Pt or TiO_2 co-catalyst, and Pt-TiO_2/GaN/n^+-p Si. (d) Faradaic efficiencies for CO at +0.27 V vs. RHE. The FEs for CO of GaN/n^+-p Si and TiO_2/GaN/n^+-p Si photocathodes were measured at -0.33 V vs. RHE due to the negligible photocurrent at an applied positive potential.

It is proposed that the formation of intimate Pt/TiO_2 interface stabilizes the reaction intermediates and reduces the activation barrier for syngas production, which are validated by theoretical calculations discussed below. In addition, the ultrathin TiO_2 overlayer may passivate the nanowire surface states and reduce the probability of electron-hole recombination at the surface.[54-55] It is also supposed that Pt/TiO_2 interface is more resistant to CO poisoning than Pt alone as shown in thermochemical catalysis,[56-58] which could also contribute to the enhanced syngas production on metal/oxide interface. Figure 3.8 b shows the comparison of FEs of CO for the four samples. Besides CO product, the remaining balance of photocurrent drives H_2 evolution from proton reduction. It is shown that CO FEs are very low on bare GaN/n^+-p Si, and with individual Pt or TiO_2 co-catalyst (1.7%, 2% and 5.6%, respectively). In contrast, the CO formation selectivity increases greatly to 32% by loading Pt-TiO_2 dual co-catalyst, indicating a synergetic effect between Pt and TiO_2. We attribute the synergy to the strong interaction at the intimate metal/oxide interface, which provides the multifunctional adsorption/reaction sites for CO_2 activation and conversion. It is worth mentioning that there is an optimized thickness of ~1 nm TiO_2 for maximum catalytic activity and CO selectivity as shown in Figure 3.9. Very thin TiO_2 deposition yields less interfacial reactive sites, while increasing the TiO_2 thickness over 1 nm resulted in limited mass transport of reactants to the interfacial sites and large tunneling resistance to charge carrier transport associated with thick TiO_2 layer.[59-60]

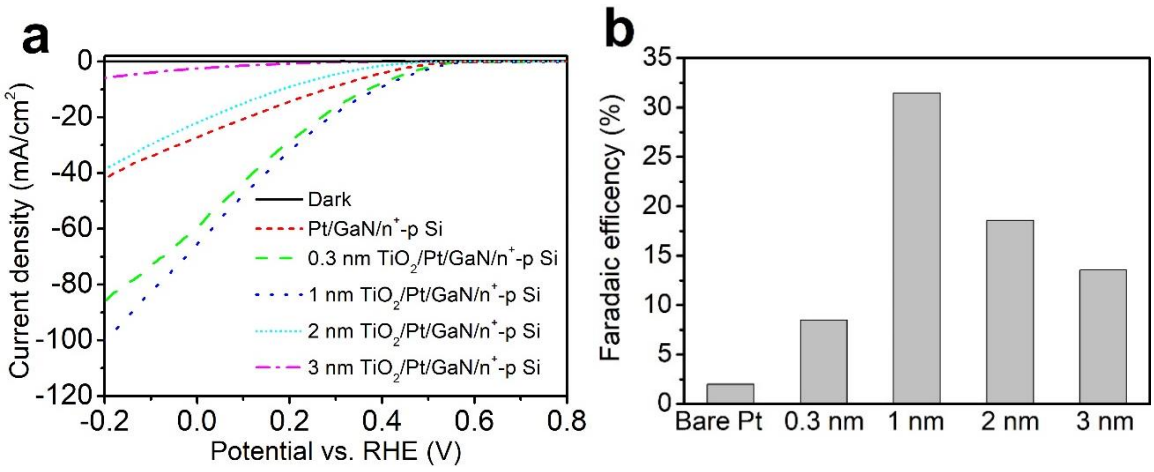

Figure 3.9: (a) J-V curves and (b) FEs for CO at +0.27 V vs. RHE of Pt-TiO_2/GaN/n^+-p Si with different TiO_2 thicknesses in CO2-saturated 0.5 M $KHCO_3$ solution (pH 7.5).

3.3.3 Strong Metal/Oxide Interaction

In addition to the important role of the metal/oxide interface in activating CO_2 and stabilizing the key reaction intermediates, the electronic modification of the Pt catalyst owing to the strong interaction between metal and oxide may also contribute to the selective CO_2 reduction into CO on Pt-TiO_2/GaN/n^+-p Si photocathode. The electronic properties of Pt were evaluated using the peak energy of Pt 4f by X-ray photoelectron spectroscopy (XPS) analysis (Figure 3.10a). Compared to Pt/GaN/n^+-p Si, a notable shift of ca. 0.5 eV to higher binding energy position was observed for Pt 4f in Pt-TiO_2/GaN/n^+-p Si. This shift is less pronounced than the binding energy difference between Pt^0 and Pt^{2+} in PtO (ca. 1.5 eV),[61] indicating the presence of electron deficient Pt species (Pt^{n+}) in Pt-TiO_2/GaN/n^+-p Si. A significant electronic modification by strong metal/oxide interaction is likely responsible for this change of Pt oxidation state.[62-65] To confirm the strong interaction between the metal and oxide, we computed the electron localized function (ELF) for $Ti_3O_6H_6$/Pt (111) system, as shown in Figure 3.10b. Topology analysis of ELF can effectively characterize the nature of different chemical bonding schemes,[66] and has been used to estimate the degree of metal-support interactions.[67] The ELF map of $Ti_3O_6H_6$/Pt (111) shows that there is a significant electron redistribution in the regions between Pt and $Ti_3O_6H_6$, indicating strong interactions between them. The strong interactions can modify the electronic property of Pt and hence enhance CO_2 reduction.

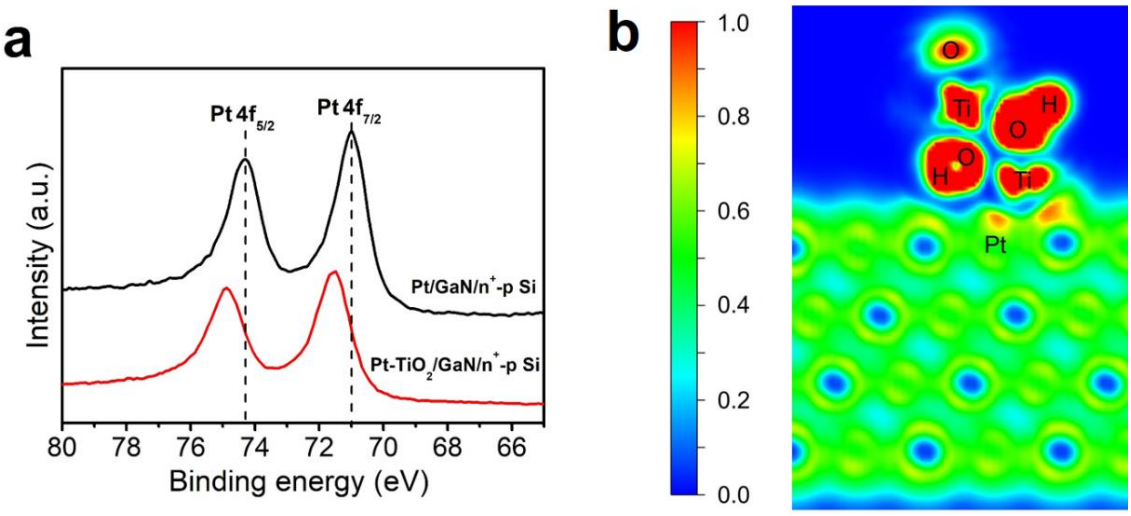

Figure 3.10: (a) XPS of Pt 4f of Pt/GaN/n^+-p Si and Pt-TiO_2/GaN/n^+-p Si. (b) Electron localized function (ELF) of $Ti_3O_6H_6$/Pt (111). The probability of finding electron pairs varies from 0 (blue color) to 1 (red color).

3.3.4 Generalization to other metal/oxide systems

By understanding the CO_2 activation and conversion at the Pt/TiO_2 interface on an atomic level, we propose that the findings can be extended to other metal/oxide systems. To show the generality, Pd-TiO_2/GaN/n^+-p Si and Pt-ZnO/GaN/n^+-p Si were synthesized by varying either metal or oxide components. The chemical components and structures were confirmed by TEM and EDX analysis as shown in Figure 3.11. By using ICP-AES analysis, the loading amounts of Pd and Ti in Pd-TiO_2/GaN/n^+-p Si, Pt and Zn in Pt-ZnO/GaN/n^+-p Si were determined to be 5.4 and 46.1, 4.7 and 39.1 nmol/cm^2, respectively.

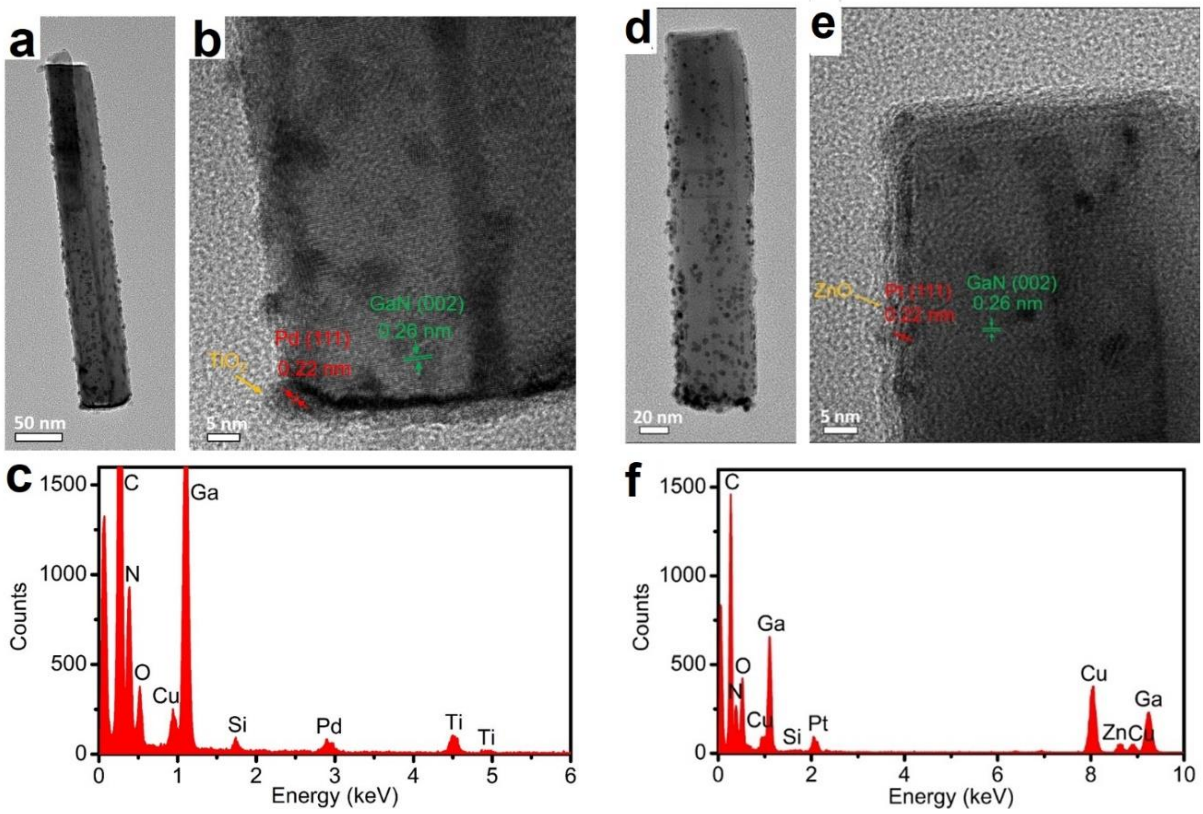

Figure 3.11: (a) TEM image, (b) HRTEM image, and (c) EDX analysis of Pd-TiO_2/GaN/n^+-p Si sample. The Cu peaks in EDX arise from the TEM sample grid. (d) TEM image, (e) HRTEM image, and (f) EDX analysis of Pt-ZnO/GaN/n^+-p Si sample. The Cu peaks in EDX arise from the TEM sample grid.

The FEs of CO for Pd-TiO_2/GaN/n^+-p Si and Pt-ZnO/GaN/n^+-p Si were measured and compared with Pd/GaN/n^+-p Si and Pt/GaN/n^+-p Si, respectively (Figure 3.12). The CO FEs of Pd-TiO_2/GaN/n^+-p Si and Pt-ZnO/GaN/n^+-p Si are four and eleven times higher than that with individual metal co-catalysts, similar to the trend observed in Pt-TiO_2/GaN/n^+-p Si system. Although quantitative differences exist between different systems, similar qualitative trend indicates the critical role of metal/oxide interfaces in activating CO_2, and stabilizing the key reaction intermediates for facilitating CO production. The present study could therefore provide a promising set of principles to enhance the CO_2 reduction performance by tuning the compositions and structures of metal/oxide interface.

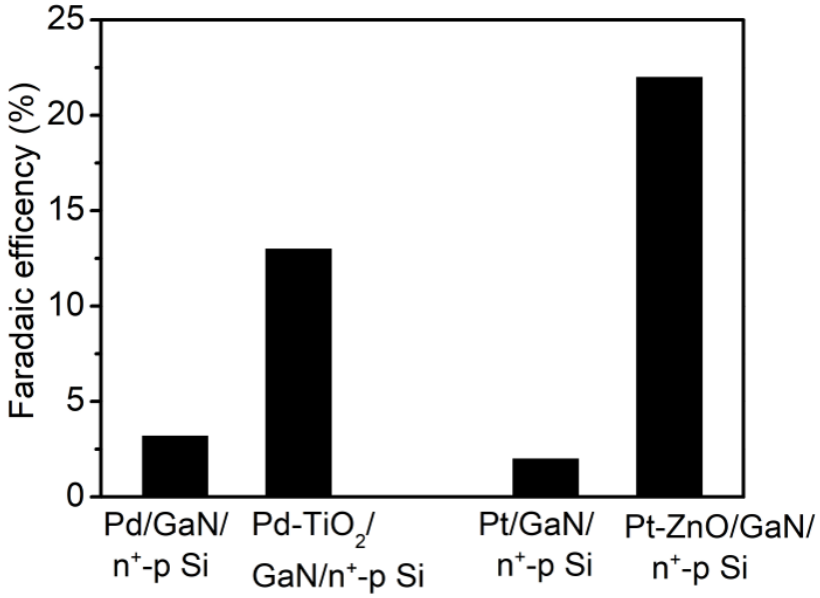

Figure 3.12: (a) Faradaic efficiencies for CO of Pd/GaN/n^+-p Si, Pd-TiO_2/GaN/n^+-p Si, Pt/GaN/ n^+-p Si and Pt-ZnO/GaN/n^+-p Si. The measurements were performed at +0.3 V vs. RHE for 100 min.

3.4 Conclusions

In summary, we have demonstrated an efficient and stable PEC CO_2 reduction system for syngas production with controlled composition, by employing a metal/oxide interface to activate inert CO_2 molecule and stabilize the key reaction intermediates. Using Pt/TiO_2 as an example, a benchmarking solar-to-syngas efficiency of 0.87% and a high turnover number of 24800 were achieved. Moreover, the PEC system exhibited highly stable syngas production in the 10 h duration test. On the basis of experimental measurements and theoretical calculations, it was found that the synergistic interactions at the metal/oxide interface provide unique reaction channels that structurally and electronically facilitate CO_2 conversion into CO. This work may open new opportunities for the design and development of high-performance photoelectrochemical systems for selective CO_2 reduction.

3.5 References

1. Kumar, B.; Llorente, M.; Froehlich, J.; Dang, T.; Sathrum, A.; Kubiak, C. P. Photochemical and Photoelectrochemical Reduction of CO2. *Annu. Rev. Phys. Chem*. **2012**, *63*, 541-569.

2. White, J. L.; Baruch, M. F.; Pander Iii, J. E.; Hu, Y.; Fortmeyer, I. C.; Park, J. E.; Zhang, T.; Liao, K.; Gu, J.; Yan, Y.; Shaw, T. W.; Abelev, E.; Bocarsly, A. B. Light-Driven Heterogeneous Reduction of Carbon Dioxide: Photocatalysts and Photoelectrodes. *Chem. Rev.* **2015,** *115*, 12888-12935.

3. Habisreutinger, S. N.; Schmidt-Mende, L.; Stolarczyk, J. K. Photocatalytic Reduction of CO_2 on TiO_2 and Other Semiconductors, *Angew. Chem. Int. Ed*. **2013**, 52, 7372-7408.

4. Tu, W. G.; Zhou, Y.; Zou, Z. G. Photocatalytic conversion of CO_2 into value-added and renewable fuels. *Adv. Mater*. **2014**, *26*, 4607-4626.

5. Xie, S. J.; Zhang, Q. H.; Liu, G. D.; Wang, Y. Photocatalytic and photoelectrocatalytic reduction of CO_2 using heterogeneous catalysts with controlled nanostructures, *Chem. Commun*. **2016**, *52*, 35-59.

6. Wang, P.; Wang, S.; Wang, H.; Wu, Z.; Wang, L. Recent Progress on Photo-Electrocatalytic Reduction of Carbon Dioxide. *Part. Part. Syst. Char*. **2018**, *35*, 1700371.

7. Pang, H.; Masuda, T.; Ye, J. H., Semiconductor-Based Photoelectrochemical Conversion of Carbon Dioxide: Stepping Towards Artificial Photosynthesis. *Chem. Asian J*. **2018**, 13, 127.

8. Zhang, N.; Long, R.; Gao, C.; Xiong, Y. Recent progress on advanced design for photoelectrochemical reduction of $CO_2$to fuels. *Sci. China Mater*. **2018**, *61*, 771-805.

9. Kalamaras, E.; Maroto-Valer, M.; Shao, M.; Xuan, J.; Wang, H. Catal. Today **2018**.

10. Vesborg, P. C. K.; Seger, B. Performance limits of photoelectrochemical CO_2 reduction based on known electrocatalysts and the case for two-electron reduction products, *Chem. Mater*. **2016**, *28*, 8844-8850.

11. Karatairi, E.; Miller, J. E. Splitting CO_2 to produce syngas and hydrocarbon fuels: PEC and STC. *MRS Bull*. **2017**, *42*, 878-879.

12. Bell, A. T. Catalytic Synthesis of Hydrocarbons over Group VIII Metals. A Discussion of the Reaction Mechanism. *Catal. Rev*. **1981**, *23*, 203-232.

13. Waugh, K. C. Methanol Synthesis. *Catal. Today* **1992**, *15*, 51-75.

14. Dry, M. E. The Fischer–Tropsch process: 1950–2000. *Catal. Today* **2002**, *71*, 227-241.

15. Khodakov, A. Y.; Chu, W.; Fongarland, P. Advances in the Development of Novel Cobalt Fischer−Tropsch Catalysts for Synthesis of Long-Chain Hydrocarbons and Clean Fuels. *Chem. Rev*. **2007**, *107*, 1692-1744.

16. Wenzel, M.; Rihko-Struckmann, L.; Sundmacher, K. Thermodynamic analysis and optimization of RWGS processes for solar syngas production from CO_2. *AIChE J*. **2017**, *63*, 15-22.

17. Foit, S. R.; Vinke, I. C.; de Haart, L. G. J.; Eichel, R. A. Power-to-Syngas: An Enabling Technology for the Transition of the Energy System? *Angew. Chem. Int. Ed*. **2017**, *56*, 5402.

18. Hernandez, S.; Farkhondehfal, M. A.; Sastre, F.; Makkee, M.; Saracco, G.; Russo, N. Syngas production from electrochemical reduction of CO_2: current status and prospective implementation. *Green Chem.* **2017**, *19*, 2326−2346.

19. Ross, M. B.; Dinh, C. T.; Li, Y.; Kim, D.; De Luna, P.; Sargent, E. H.; Yang, P. D. J. Tunable Cu Enrichment Enables Designer Syngas Electrosynthesis from CO_2. *Am. Chem. Soc.* **2017**, *139*, 9359-9363.

20. Sheng, W. C.; Kattel, S.; Yao, S. Y.; Yan, B. H.; Liang, Z. X.; Hawxhurst, C. J.; Wu, Q. Y.; Chen, J. G. G. Electrochemical reduction of CO_2 to synthesis gas with controlled CO/H_2 ratios. *Energy Environ. Sci.* **2017**, *10*, 1180-1185.

21. Xu, J. Q.; Li, X. D.; Liu, W.; Sun, Y. F.; Ju, Z. Y.; Yao, T.; Wang, C. M.; Ju, H. X.; Zhu, J. F.; Wei, S. Q.; Xie, Y. Carbon Dioxide Electroreduction into Syngas Boosted by a Partially Delocalized Charge in Molybdenum Sulfide Selenide Alloy Monolayers. *Angew. Chem. Int. Ed*. **2017**, *56*, 9121-9125.

22. Guo, S. J.; Zhao, S. Q.; Wu, X. Q.; Li, H.; Zhou, Y. J.; Zhu, C.; Yang, N. J.; Jiang, X.; Gao, J.; Bai, L.; Liu, Y.; Lifshitz, Y.; Lee, S. T.; Kang, Z. H. A Co_3O_4-CDots-C_3N_4 three component electrocatalyst design concept for efficient and tunable CO_2 reduction to syngas. *Nat. Commun*. **2017**, *8*, 1828.

23. He, R.; Zhang, A.; Ding, Y. L.; Kong, T. Y.; Xiao, Q.; Li, H. L.; Liu, Y.; Zeng, J. Achieving the Widest Range of Syngas Proportions at High Current Density over Cadmium Sulfoselenide Nanorods in CO_2 Electroreduction. *Adv. Mater*. **2018**, *30*, 1705872.

24. Furler, P.; Scheffe, J. R.; Steinfeld, A. Syngas production by simultaneous splitting of H_2O and CO2via ceria redox reactions in a high-temperature solar reactor. *Energy Environ. Sci*. **2012**, *5*, 6098-6103.

25. Kumar, B.; Smieja, J. M.; Sasayama, A. F.; Kubiak, C. P. Tunable, light-assisted co-generation of CO and H_2 from CO_2 and H_2O by Re(bipy-tbu)$(CO)_3$Cl and p-Si in non-aqueous medium. *Chem. Commun.* **2012**, *48*, 272-274.

26. Kang, P.; Chen, Z. F.; Nayak, A.; Zhang, S.; Meyer, T. J. Single catalyst electrocatalytic reduction of CO_2 in water to H_2+CO syngas mixtures with water oxidation to O_2. *Energy Environ. Sci*. **2014**, *7*, 4007-4012.

27. Lee, J. S.; Won, D. I.; Jung, W. J.; Son, H. J.; Pac, C.; Kang, S. O. Controllable Syngas Production by a Dye-Sensitized TiO_2 Hybrid System with ReI and CoIII Catalysts under Visible-Light Irradiation. *Angew. Chem. Int. Ed*. **2017**, *56*, 976-980.

28. Li, F. F.; Lau, J.; Licht, S. Sungas Instead of Syngas: Efficient Coproduction of CO and H_2 with a Single Beam of Sunlight. *Adv. Sci*. **2015**, *2*, 1500260.

29. Li, D. W.; Ouyang, S. X.; Xu, H.; Lu, D.; Zhao, M.; Zhang, X. L.; Ye, J. H. Synergistic effect of Au and Rh on SrTiO3 in significantly promoting visible-light-driven syngas production from CO_2 and H_2O. *Chem. Commun*. **2016**, *52*, 5989-5992.

30. Urbain, F.; Tang, P. Y.; Carretero, N. M.; Andreu, T.; Gerling, L. G.; Voz, C.; Arbiol, J.; Morante, J. R. A prototype reactor for highly selective solar-driven CO_2 reduction to synthesis gas using nanosized earth-abundant catalysts and silicon photovoltaics. *Energy Environ. Sci*. **2017**, *10*, 2256-2266.

31. Chu, S.; Fan, S. Z.; Wang, Y. J.; Rossouw, D.; Wang, Y. C.; Botton, G. A.; Mi, Z. Tunable Syngas Production from CO_2 and H_2O in an Aqueous Photoelectrochemical Cell. *Angew. Chem. Int. Ed.* **2016**, *55*, 1426-14266.

32. Hinogami, R.; Nakamura, Y.; Yae, S.; Nakato, Y. J. An Approach to Ideal Semiconductor Electrodes for Efficient Photoelectrochemical Reduction of Carbon Dioxide by Modification with Small Metal Particles. *Phys. Chem. B* **1998**, *102*, 974-980.

33. Kong, Q.; Kim, D.; Liu, C.; Yu, Y.; Su, Y.; Li, Y.; Yang, P. D. Directed Assembly of Nanoparticle Catalysts on Nanowire Photoelectrodes for Photoelectrochemical CO_2 Reduction. *Nano lett.* **2016**, *16*, 5675-5680.

34. Song, J. T.; Ryoo, H.; Cho, M.; Kim, J.; Kim, J. G.; Chung, S. Y.; Oh, J. Nanoporous Au Thin Films on Si Photoelectrodes for Selective and Efficient Photoelectrochemical CO_2 Reduction. *Adv. Energy Mater.* **2017**, *7*, 1601103.

35. Jang, Y. J.; Jang, J. W.; Lee, J.; Kim, J. H.; Kumagai, H.; Lee, J.; Minegishi, T.; Kubota, J.; Domen, K.; Lee, J. S. Selective CO production by Au coupled ZnTe/ZnO in the photoelectrochemical CO_2 reduction system. *Energy Environ. Sci.* **2015**, *8*, 3597-3604.

36. Jang, Y. J.; Jeong, I.; Lee, J.; Lee, J.; Ko, M. J.; Lee, J. S. Unbiased Sunlight-Driven Artificial Photosynthesis of Carbon Monoxide from CO_2 Using a ZnTe-Based Photocathode and a Perovskite Solar Cell in Tandem. *ACS Nano* **2016**, *10*, 6980−6987.

37. Yoneyama, H.; Sugimura, K.; Kuwabata, S. J. Effects of electrolytes on the photoelectrochemical reduction of carbon dioxide at illuminated p-type cadmium telluride and p-type indium phosphide electrodes in aqueous solutions. *Electroanal. Chem.* **1988**, *249*, 143.

38. Torralba-Penalver, E.; Luo, Y.; Compain, J. D.; Chardon-Noblat, S.; Fabre, B. Selective Catalytic Electroreduction of CO_2 at Silicon Nanowires (SiNWs) Photocathodes Using Non-Noble Metal-Based Manganese Carbonyl Bipyridyl Molecular Catalysts in Solution and Grafted onto SiNWs. *ACS Catal.* **2015**, *5*, 6138-6147.

158. Schreier, M.; Luo, J. S.; Gao, P.; Moehl, T.; Mayer, M. T.; Gratzel, M. J. Covalent Immobilization of a Molecular Catalyst on Cu_2O Photocathodes for CO_2 Reduction. *Am. Chem. Soc.* **2016**, *138*, 1938-1946.

39. Sahara, G.; Abe, R.; Higashi, M.; Morikawa, T.; Maeda, K.; Ueda, Y.; Ishitani, O. Photoelectrochemical CO_2 reduction using a Ru(ii)–Re(i) multinuclear metal complex on a p-type semiconducting NiO electrode. *Chem. Commun.* **2015**, *51*, 10722-10725.

40. Sahara, G.; Kumagai, H.; Maeda, K.; Kaeffer, N.; Artero, V.; Higashi, M.; Abe, R.; Ishitani, O. J. Photoelectrochemical Reduction of CO_2 Coupled to Water Oxidation Using a Photocathode with a Ru(II)–Re(I) Complex Photocatalyst and a CoOx/TaON Photoanode. *Am. Chem. Soc.* **2016**, *138*, 14152-14158.

41. Hansen, H. A.; Varley, J. B.; Peterson, A. A.; Norskov, J. K. Understanding Trends in the Electrocatalytic Activity of Metals and Enzymes for CO_2 Reduction to CO. *J. Phys. Chem. Lett*. **2013**, *4*, 388-392.

42. Hansen, H. A.; Shi, C.; Lausche, A. C.; Peterson, A. A.; Norskov, J. K. Bifunctional alloys for the electroreduction of CO_2 and CO. *Phys. Chem. Chem. Phys*. **2016**, *18*, 9194-9201.

43. Fan, S. Z.; AlOtaibi, B.; Woo, S. Y.; Wang, Y. J.; Botton, G. A.; Mi, Z. High Efficiency Solar-to-Hydrogen Conversion on a Monolithically Integrated InGaN/GaN/Si Adaptive Tunnel Junction Photocathode. *Nano lett*. **2015**, *15*, 2721-2726.

44. Rostrup-Nielsen, J. R. New aspects of syngas production and use. *Catal. Today* **2000**, 63, 159.

45. Kuhl, K. P.; Hatsukade, T.; Cave, E. R.; Abram, D. N.; Kibsgaard, J.; Jaramillo, T. F. Electrocatalytic Conversion of Carbon Dioxide to Methane and Methanol on Transition Metal Surfaces. *J. Am. Chem. Soc*. **2014**, *136*, 14107-14113.

46. Singh, M. R.; Clark, E. L.; Bell, A. T. Effects of electrolyte, catalyst, and membrane composition and operating conditions on the performance of solar-driven electrochemical reduction of carbon dioxide. *Phys. Chem. Chem. Phys*. **2015**, *17*, 18924-18936.

47. Rosen, J.; Hutchings, G. S.; Lu, Q.; Rivera, S.; Zhou, Y.; Vlachos, D. G.; Jiao, F. Mechanistic Insights into the Electrochemical Reduction of CO_2 to CO on Nanostructured Ag Surfaces. *ACS Catal.* **2015**, *5*, 4293-4299.

48. Kim, S. K.; Zhang, Y.-J.; Bergstrom, H.; Michalsky, R.; Peterson, A. Understanding the Low-Overpotential Production of CH4 from CO_2 on Mo_2C Catalysts. *ACS Catal*. **2016**, *6*, 2003.

49. Takeda, H.; Ohashi, K.; Sekine, A.; Ishitani, O. Photocatalytic CO_2 Reduction Using Cu(I) Photosensitizers with a Fe(II) Catalyst. J. *Am. Chem. Soc*. **2016**, *138*, 4354-4357.

50. Hong, D. C.; Tsukakoshi, Y.; Kotani, H.; Ishizuka, T.; Kojima, T. Visible-Light-Driven Photocatalytic CO_2Reduction by a Ni(II) Complex Bearing a Bioinspired Tetradentate Ligand for Selective CO Production. *J. Am. Chem. Soc*. **2017**, *139*, 6538-6541.

51. Rao, H.; Bonin, J.; Robert, M. Visible-light Homogeneous Photocatalytic Conversion of CO_2 into CO in Aqueous Solutions with an Iron Catalyst. *ChemSusChem* **2017**, *10*, 4447-4450.

52. Lian, S. C.; Kodaimati, M. S.; Weiss, E. A. Photocatalytically Active Superstructures of Quantum Dots and Iron Porphyrins for Reduction of CO_2 to CO in Water. *ACS Nano* **2018**, *12*, 568-575.

53. Lin, Y. J.; Kapadia, R.; Yang, J. H.; Zheng, M.; Chen, K.; Hettick, M.; Yin, X. T.; Battaglia, C.; Sharp, I. D.; Ager, J. W.; Javey, A. J. Role of TiO_2 Surface Passivation on Improving the Performance of p-InP Photocathodes. *Phys. Chem. C* **2015**, *119*, 2308-2313.

54. Qiu, J.; Zeng, G. T.; Ha, M. A.; Ge, M. Y.; Lin, Y. J.; Hettick, M.; Hou, B. Y.; Alexandrova, A. N.; Javey, A.; Cronin, S. B. Artificial Photosynthesis on TiO2-Passivated InP Nanopillars. *Nano lett.* **2015**, *15*, 6177-6181.

55. Hepel, M.; Kumarihamy, I.; Zhong, C. Nanoporous TiO_2-supported bimetallic catalysts for methanol oxidation in acidic media. *J. Electrochem. Commun*. **2006**, *8*, 1439-1444.

56. Guo, X.; Guo, D.; Qiu, X.; Chen, L.; Zhu, W. Excellent dispersion and electrocatalytic properties of Pt nanoparticles supported on novel porous anatase TiO_2 nanorods. *J. Power Sources* **2009**, *194*, 281-285.

57. Shi, F.; Baker, L. R.; Hervier, A.; Somorjai, G. A.; Komvopoulos, K. Tuning the Electronic Structure of Titanium Oxide Support to Enhance the Electrochemical Activity of Platinum Nanoparticles. *Nano Lett*. **2013**, *13*, 4469-4474.

58. Chen, Y. W.; Prange, J. D.; Duhnen, S.; Park, Y.; Gunji, M.; Chidsey, C. E. D.; McIntyre, P. C. Atomic layer-deposited tunnel oxide stabilizes silicon photoanodes for water oxidation. *Nat. Mater*. **2011**, 10, 539-544.

59. Kim, H. J.; Kearney, K. L.; Le, L. H.; Haber, Z. J.; Rockett, A. A.; Rose, M. J. Charge-Transfer through Ultrathin Film TiO_2 on n-Si (111) Photoelectrodes: Experimental and Theoretical Investigation of Electric Field-Enhanced Transport with a Nonaqueous Redox Couple. *J. Phys. Chem. C* **2016**, *120*, 25697.

60. Li, Y. H.; Xing, J.; Chen, Z. J.; Li, Z.; Tian, F.; Zheng, L. R.; Wang, H. F.; Hu, P.; Zhao, H. J.; Yang, H. G. Unidirectional suppression of hydrogen oxidation on oxidized platinum clusters. *Nat. Commun*. **2013**, *4*, 2500.

61. Tauster, S. J.; Fung, S. C.; Garten, R. L. Strong metal-support interactions. Group 8 noble metals supported on titanium dioxide. *J. Am. Chem. Soc*. **1978**, *100*, 170-175.

62. Li, Q. Y.; Wang, K.; Zhang, S. L.; Zhang, M.; Yang, H. J.; Jin, Z. S. Effect of photocatalytic activity of CO oxidation on Pt/TiO_2 by strong interaction between Pt and TiO_2 under oxidizing atmosphere. *J. Mol. Catal. A* ***2006****, 258,* 83-88.

63. Park, J. Y.; Baker, L. R.; Somorjai, G. A. Role of Hot Electrons and Metal–Oxide Interfaces in Surface Chemistry and Catalytic Reactions. *Chem. Rev*. **2015**, *115*, 2781-2817.

64. Chen, P. R.; Khetan, A.; Yang, F. K.; Migunov, V.; Weide, P.; Sturmer, S. P.; Guo, P. H.; Kahler, K.; Xia, W.; Mayer, J.; Pitsch, H.; Simon, U.; Muhler, M. Experimental and Theoretical Understanding of Nitrogen-Doping-Induced Strong Metal–Support Interactions in Pd/TiO_2 Catalysts for Nitrobenzene Hydrogenation. *ACS Catal.* **2017**, *7*, 1197-1206.

65. Silvi, B.; Savin, A. Classification of chemical bonds based on topological analysis of electron localization functions. *Nature* **1994**, *371*, 683-686.

66. Vidal, A. B.; Feria, L.; Evans, J.; Takahashi, Y.; Liu, P.; Nakamura, K.; Illas, F.; Rodriguez, J. A. CO_2 Activation and Methanol Synthesis on Novel Au/TiC and Cu/TiC Catalysts. *J. Phys. Chem. Lett*. **2012**, *3*, 2275-2280.

Chapter 4 : Controllable Syngas Generation from Photoelectrochemical CO_2 Reduction with Dual Cocatalysts

The photoelectrochemical conversion of CO_2 into syngas offers a potential way to reduce greenhouse gas emissions while storing solar energy as a sustainable fuel source. In previous chapter we demonstrated an efficient PEC system for CO_2 reduction based on GaN NWs and a metal-oxide cocatalyst. Herein, we show a decoupling strategy using dual cocatalysts to improve the selectivity for CO_2 reduction toward CO generation and increase the solar to syngas conversion efficiency. We demonstrated that syngas generation can be optimized by coupling an Au CO-generating catalyst and a Pt H_2-generating catalyst with GaN nanowires on Si photoelectrode. As a result, a record high half-cell solar-to-syngas efficiency of 1.88 % under one-sun illumination is obtained. Furthermore, the CO/H_2 ratio in the syngas mixture could be controllably regulated in a broad range between 1:99 and 10:1 with a total unity Faradaic efficiency by varying the ratio of dual cocatalysts.

This chapter is based on the published journal: Decoupling Strategy for Enhanced Syngas Generation from Photoelectrochemical CO_2 Reduction, S. Chu* P. Ou*, R Rashid*, P. Ghamari*, R. Wang, N. Tran, S. Zhao, H. Zhang, J. Song, Z. Mi, *iScience*, 2020. [* These authors contributed equally to this work].

4.1 Introduction

As stated in the last chapter, the PEC approach which imitates natural photosynthesis by combining light-harvesting platforms with appropriate electrocatalysis, represents a potential path for reduction of CO_2 emission and efficiently converting it into storable fuels such as syngas.[1] Syngas is a critical feedstock to produce a variety of synfuels and high-value chemicals such as methanol.[2-7] Production of distinct downstream needs varying CO/H_2 ratios.[8-14] For example, the CO/H_2 ratio necessary for hydroformylation, methanol synthesis, and methanation reactions, is 1:1, 1:2, and 1:3, respectively.[15-20] However, in aqueous solutions, the CO_2 reduction reaction (CO_2RR) is challenging to compete with the kinetically more viable hydrogen evolution reaction (HER), hindering efficient syngas production with a widely tunable CO/H_2 ratio. Various photocatalysts, including p-Si, ZnO, ZnTe, CdTe, Cu_2O and perovskite which are commonly coupled with a CO_2RR active cocatalyst (e.g., Au, Pd, Ag, and Cu), have been developed for PEC CO_2 to CO

reduction and syngas production.[21-29] However, establishing a balanced and optimized CO_2RR and HER activity with a single monofunctional catalyst is still challenging.[30-32] To overcome this problem, we suggest a spatially separated dual cocatalyst decoupling approach. By assembling a CO-generating Au site at the tip and an H_2-generating Pt site on the side of GaN nanowires. Integrating the suggested dual catalyst system with an efficient light harvesting p-n Si and GaN electron extraction platform resulted in a record high solar-to-syngas (STS) efficiency of 1.88% and a benchmark turnover number (TON) of ~60000. Furthermore, by simply changing the composition of the dual cocatalysts, the CO/H_2 ratio in the syngas product could be controlled in a wide range between 1:99 and 10:1.

4.2 Results and discussion

4.2.1 Design and Characterization of Photoelectrocatalyst with Dual Cocatalysts

We integrated dual cocatalysts of an Au CO-generating site and a Pt H_2-generating site separately with GaN nanowire arrays on an n^+-p Si platform, to develop the $AuPt_x/GaN/n^+$-p Si structure, where x represents the Pt/Au molar ratio. Figure 4.1a, b illustrates the schematic design and energy band diagram of $AuPt_x/GaN/n^+$-p Si.

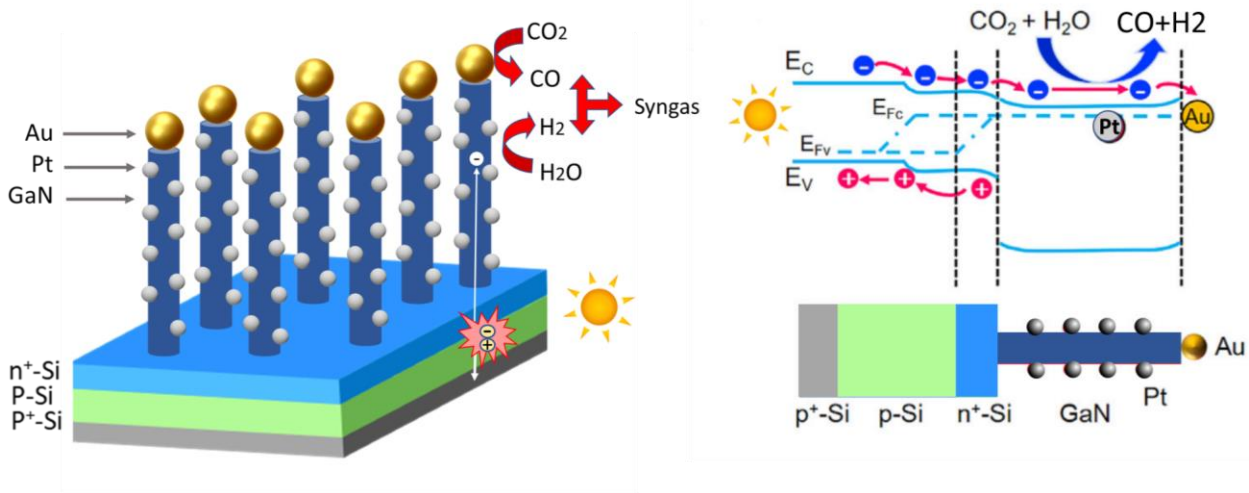

Figure 4.1: (a) Schematic and (b) energy band diagram of $AuPt_x/GaN/n^+$-p Si photocathode.

The samples were made in two steps. First, GaN nanowires were grown using molecular beam epitaxy on an n^+-p Si wafer. Following that, Au nanoparticles were deposited on the tip of GaN nanowires using e-beam evaporation followed by thermal annealing, and Pt nanoparticles were

decorated on the side of GaN nanowires via photo deposition using H_2PtCl_6 as Pt precursor (see Appendix A for experimental details).

The GaN/n^+-p Si platform benefits from strong light harvesting of Si (bandgap of 1.1 eV), and effective electron extraction/transportation effect, and vast surface area afforded by GaN nanowires.[33-34] The nanowires enable high electrocatalyst mass loadings and increase light absorption while decreasing light reflection.[35] Significantly, the optical absorption and electrochemical reaction are spatially and functionally segregated in the multidimensional structure, providing a unique platform for controllable product distribution by altering the cocatalyst composition. The narrow bandgap of n^+-p Si junction facilitates photo exciton and the formation of electron-hole pairs under light illumination, whereas the light absorption of GaN nanowires is negligible due to their high bandgap of 3.4 eV. Because of the alienated conduction band and highly n-type doping of GaN and Si, photogenerated electrons transfer readily from Si to GaN. The separation of Au cocatalysts on the polar surface (top surface) and Pt on the nonpolar surface (side surface) of GaN nanowires could enable variable syngas composition by tuning the CO and H_2 evolution rates.

The morphology and chemical component of $AuPt_{0.2}$/GaN/n^+-p Si sample were explored by SEM, TEM, XRD, EDX mapping, XPS, and inductively coupled plasma-atomic emission spectroscopy (ICP-AES) analysis as shown in Figure 4.2. The SEM and TEM images shown in Figure 4.2 b reveal GaN nanowires with an average length of 350 nm and a diameter of 40 nm, Au nanoparticles sizing from 20 to 40 nm on GaN NWs tips, Pt nanoparticles (and 1–2 nm) on the GaN side surface. Figures 4.2 c and d show high-resolution TEM images of (111) Au and Pt facets and (002) GaN lattice planes, indicating nanowire growth along the c-axis direction. The elemental mapping of a single nanowire using scanning transmission electron microscopy EDX (STEM-EDX) shown in Figure 4.2e revealed the Au-tipped structure and Pt nanoparticles distributed uniformly on the lateral surface of the nanowire.

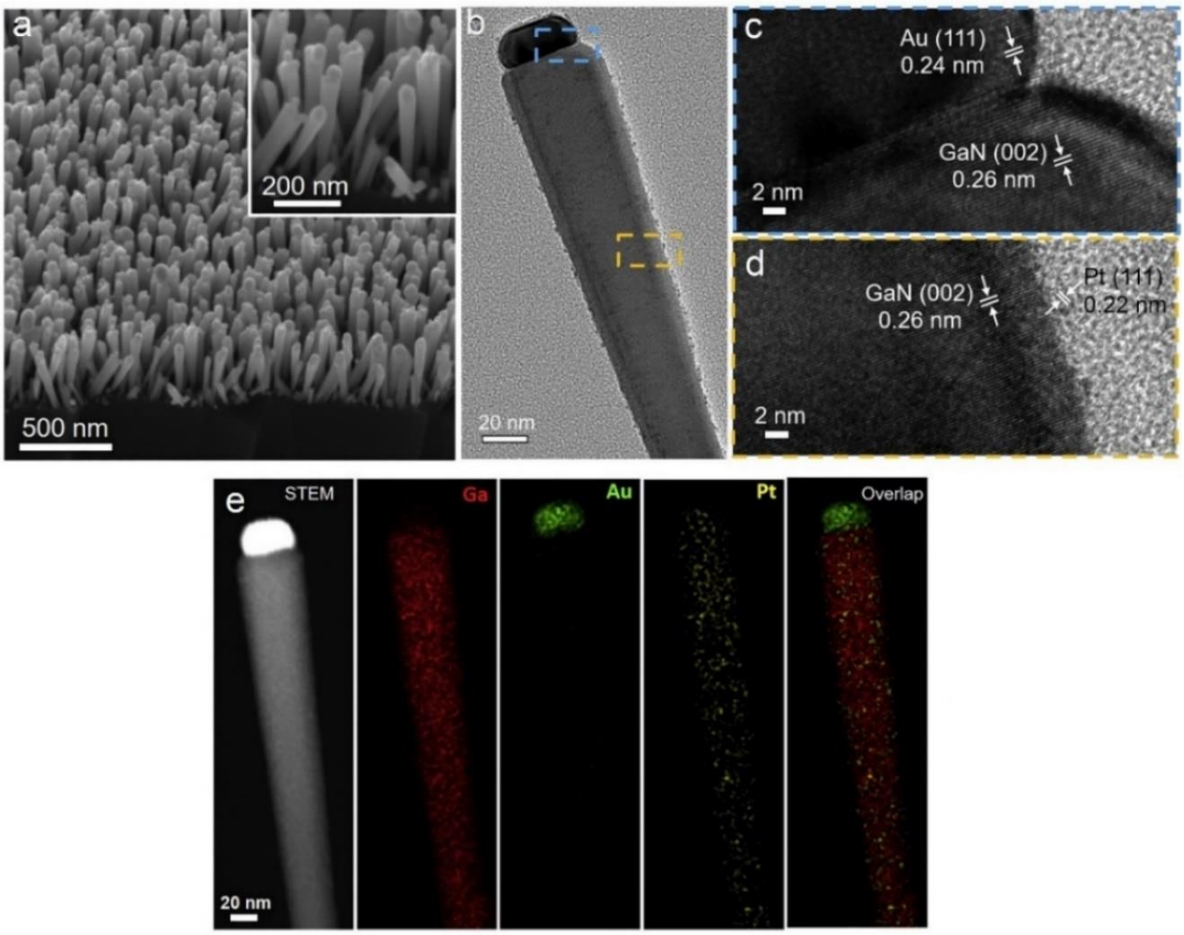

Figure 4.2: Characterization of $AuPt_{0.2}/GaN/n^{+}$-p Si sample. (a) 45°-tilted SEM, (b) TEM, (c) and (d) HRTEM images. The HRTEM images of (c) and (d) are obtained from the blue and yellow boxed areas in (b), respectively. (e) STEM-EDX elemental mapping images.

XRD analysis represented in Figure 4.3a shows the (111) plain of Au and (002) plane of GaN. The lack of XRD peaks for Pt nanoparticles is most likely due to the low loading amount and small crystalline size of 1–2 nm. XPS analysis of the samples show Au (Au^0) and Pt (Pt^0) as shown Figures 4.3 b,c. The loading amounts of Au and Pt in $AuPt_{0.2}/GaN/n^{+}$-p Si were determined to be 8.5 and 1.7 nmol cm^2 with Au/Pt molar ratio of 5 using ICP-AES analysis.

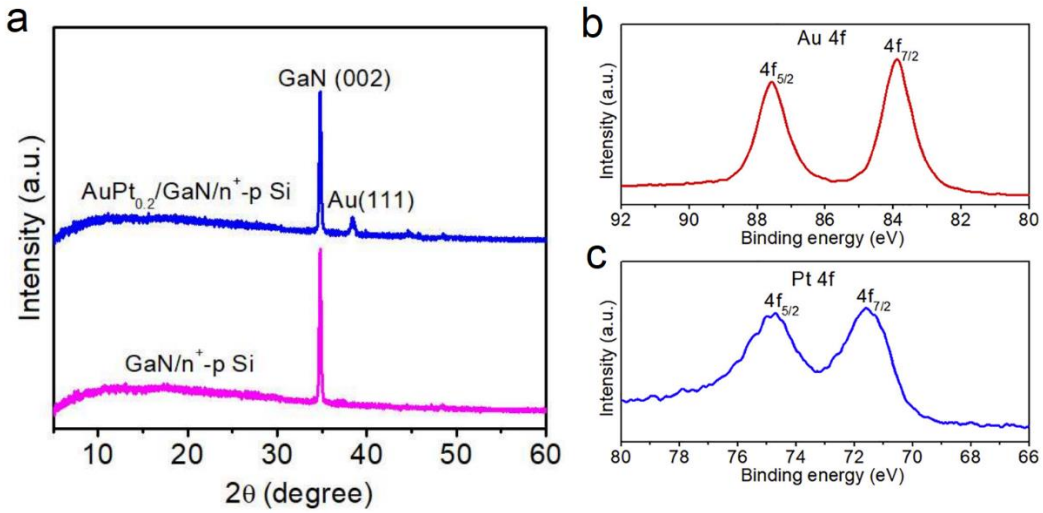

Figure 4.3: (a) XRD patterns of GaN/n^+-p Si and $AuPt_{0.2}$/GaN/n^+-p Si. XPS of (b) Au 4f and (c) Pt 4f.

4.2.2 Realization of Efficient and Tunable PEC Syngas generation

By varying the introduced amount of Pt precursor, $AuPt_x$/GaN/n^+-p Si samples with different cocatalyst ratios ($AuPt_{0.1}$, $AuPt_{0.2}$, $AuPt_{0.4}$) were prepared. The TEM images of $AuPt_x$/GaN/n^+-p Si with different cocatalyst compositions (Figure 4.4a-e) show that Au located at the tip and the well dispersion of Pt nanoparticles across the nanowire.

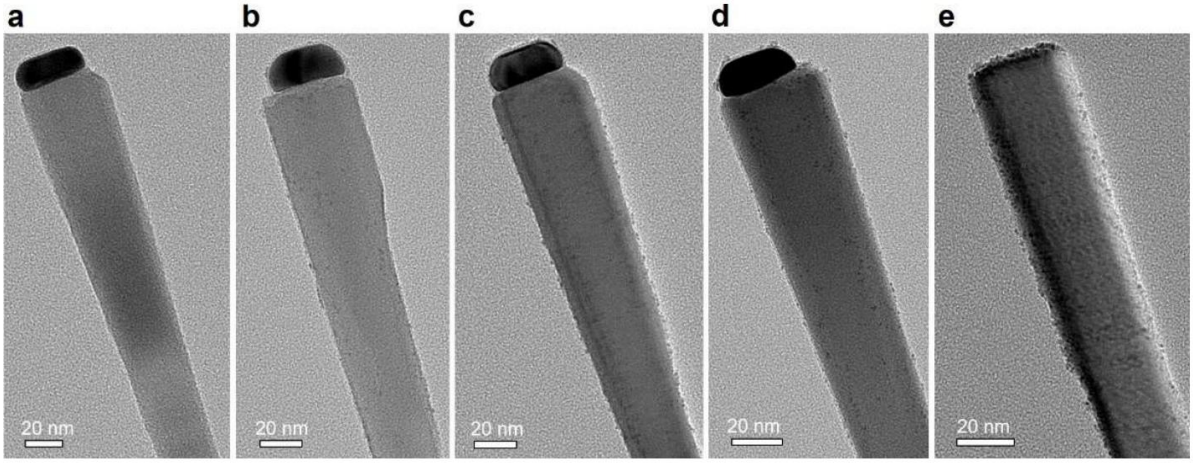

Figure 4.4: TEM images of (a) Au/GaN/n^+-p Si, (b) AuPt0.1/GaN/n+ -p Si, (c) $AuPt_{0.2}$/GaN/n^+-p Si, (d) $AuPt_{0.4}$/GaN/n^+-p Si and (e) Pt/GaN/n^+-p Si. (Related to Figure 4.5).

$AuPt_x/GaN/n^+$-p Si photocathodes with different cocatalyst compositions were examined in CO_2-saturated 0.5M $KHCO_3$ solution (pH 7.5) using a three-electrode PEC configuration, with standard one-sun illumination (100 mW cm^{-2}), AM 1.5G. Faradaic efficiencies (FEs) for CO and H_2 at applied potential of +0.17 V vs RHE are shown in Figure 4.5 b, which were calculated from the chronoamperometry data displayed in Figure 4.5 a. $Au/GaN/n^+$-p Si and $Pt/GaN/n^+$-p Si, respectively, showed dominant CO and H_2 evolution.

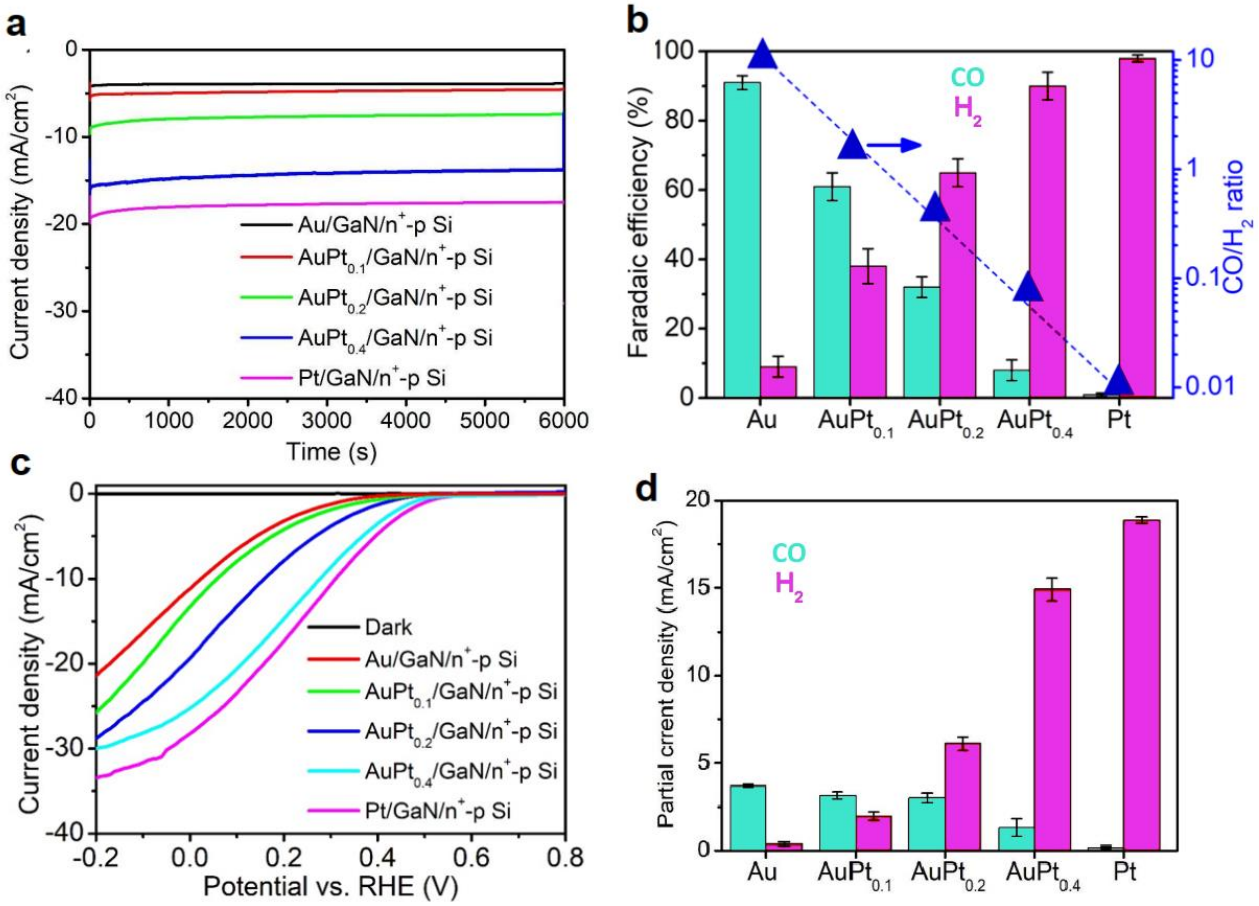

Figure 4.5: (a) Chronoamperometry data of $AuPt_x/GaN/n^+$-p Si photocathodes at +0.17 V vs RHE in CO_2-saturated 0.5 M $KHCO_3$ (pH 7.5) under AM 1.5G one-sun illumination (100 mW cm^{-2}). (b) FEs for CO (gray bars) and H_2 (red bars), and CO/H_2 ratio of $AuPt_x/GaN/n^+$-p Si photocathodes at +0.17 V vs RHE. (c) J-V curves. (d) Partial current density for CO (purple bars) and H_2 (red bars) of $AuPt_x/GaN/n^+$-p Si photocathodes at +0.17 V vs RHE.

The FE for H_2 evolution increased linearly with the rise of x from 0.1 to 0.4 in $AuPt_x/GaN/n^+$-p Si, while the FE for CO evolution dropped. The CO/H_2 ratio could be customized in a wide range from 1:99 to 10:1 by adjusting the cocatalyst composition. $AuPt_{0.2}/GaN/n^+$-p Si, in instance,

produced syngas with a CO/H_2 ratio of 1:2, which is a favorable composition for the synthesis of methanol and hydrocarbon fuels.

The cogeneration of CO and H_2 yielded a unity FE in all samples, with no additional products observed. The photocurrent density-potential (J-V) curves of different photocathodes are compared in Figure 4.5 (c). Au/GaN/n^+-p Si exhibits a photocurrent density of 21 mA cm^{-2} at -0.2 V with an onset potential of ~0.4 V, whereas this value is negligible for bare GaN/n^+-p Si. Incorporation of Pt shifts the onset potential gradually to ~0.5 V and increases photocurrent up to 30 mA cm^{-2} due to high activity of Pt for HER. As demonstrated in Figure 4.5 e, the partial current density for H_2 at +0.17 V increases as the Pt concentration increases. Importantly, partial current density for CO remained almost unchanged with the increase of Pt/Au ratio up to 0.2, revealing the balanced and high CO_2RR and HER activity in $AuPt_{0.2}$/GaN/n^+-p Si sample.

The FEs for CO and H_2 of $AuPt_{0.2}$/GaN/n^+-p Si at +0.37 V to +0.07 V reveal that the CO/H_2 ratio is nearly constant at 1:2, as illustrated in Figure 4.6. (a). STS rate was obtained using the measured photocurrent density and FEs for CO and H_2 at various applied potentials, with the maximum of 1.88 % at +0.17 V as shown in Figure 4.6 a. The achieved STS is more than two times that of state-of-the-art photocathodes according to Figure 4.6b and Table 4.1.

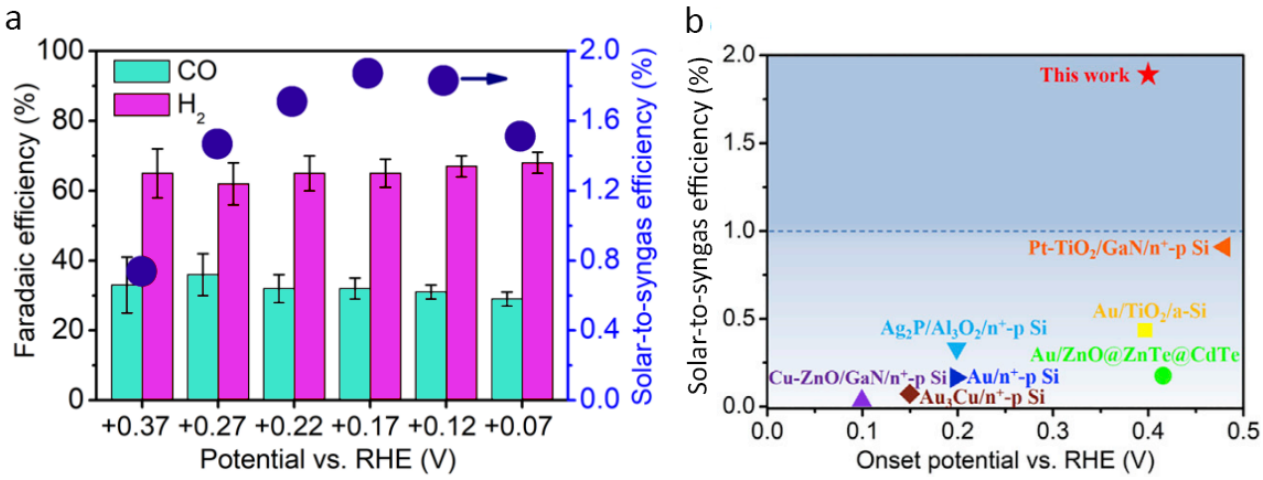

Figure 4.6: (a) FEs for CO (gray bars) and H_2 (red bars), and solar-to-syngas efficiency of $AuPt_{0.2}$/GaN/n^+-p Si as a function of applied potential. (b) Performance comparison of $AuPt_{0.2}$/GaN/n^+-p Si with state-of-the-art photocathodes for PEC CO_2 reduction into CO/ syngas.

Table 4.1: Performance comparison of photocathodes for PEC CO_2 reduction into CO/syngas at underpotential (more positive than the equilibrium potential Eo (CO_2/CO) = −0.11 V vs RHE). Related to Figure 4.6b.

Photocathode	Light intensity (mW cm^{-2})	Onset potential (V vs RHE) [a]	FE_{CO} (%)[b]	STS (%)[c]	Refs
Cu-ZnO/GaN/n^+-p Si	800	0.1	70	~0.01	Chu et al., 2016
Au_3Cu/n^+-p Si	20	0.15	80	0.07	Kong et al., 2016
Au/n^+-p Si	100	0.2	91	0.12	Song et al., 2017
Au/ZnO@ZnTe@CdTe	100	0.45	67	0.18	Jang et al., 2016
Ag_2P/Al_2O_3/n^+-p Si	100	0.3	67	0.3	Li et al., 2019
Au/TiO_2/a-Si	100	0.4	50	0.42	Li et al., 2019
Pt-TiO_2/GaN/n^+-p Si	800	0.5	78	0.87	Chu et al., 2018
$Cu_3(BTC)_2$/Cu_2O	100	−1.77 V vs Fc/Fc^+	95	0.83	Deng et al., 2019
Pt Au /GaN/n^+-p Si	100	0.45	91	1.88	This Work

[a] The potential reported at photocurrent density of 0.5 mA cm^{-2}

[b] The highest FE reported in the system.

[c] Calculated using equation 1 in Appendix A.

The stability of $AuPt_{0.2}$/GaN/n^+-p Si photocathode was recorded as demonstrated in Figure 4.7. Both the photocurrent density and product selectivity remain constant for a period of 10h. Furthermore, following the PEC stability test, SEM, TEM, and XPS investigation of $AuPt_{0.2}$/GaN/n^+-p Si sample reveal no change in GaN nanowires or Au-Pt cocatalysts (Figure 4.8).

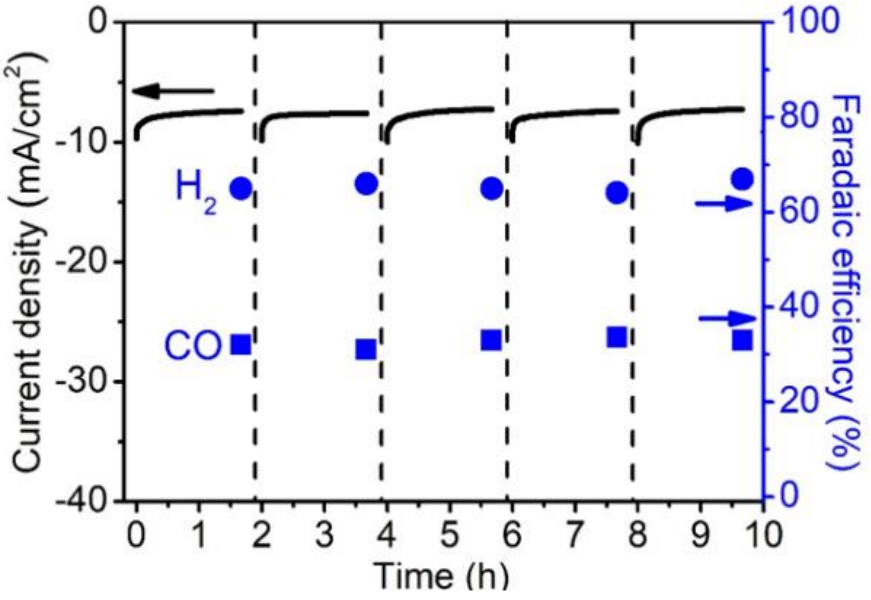

Figure 4.7: Chronoamperometry data and FEs for CO and H_2 of $AuPt_{0.2}/GaN/n^+$-p Si photocathode at +0.17 V vs RHE. The dashed lines indicate cleaning of photoelectrode with DI water and purging of the PEC chamber with CO_2.

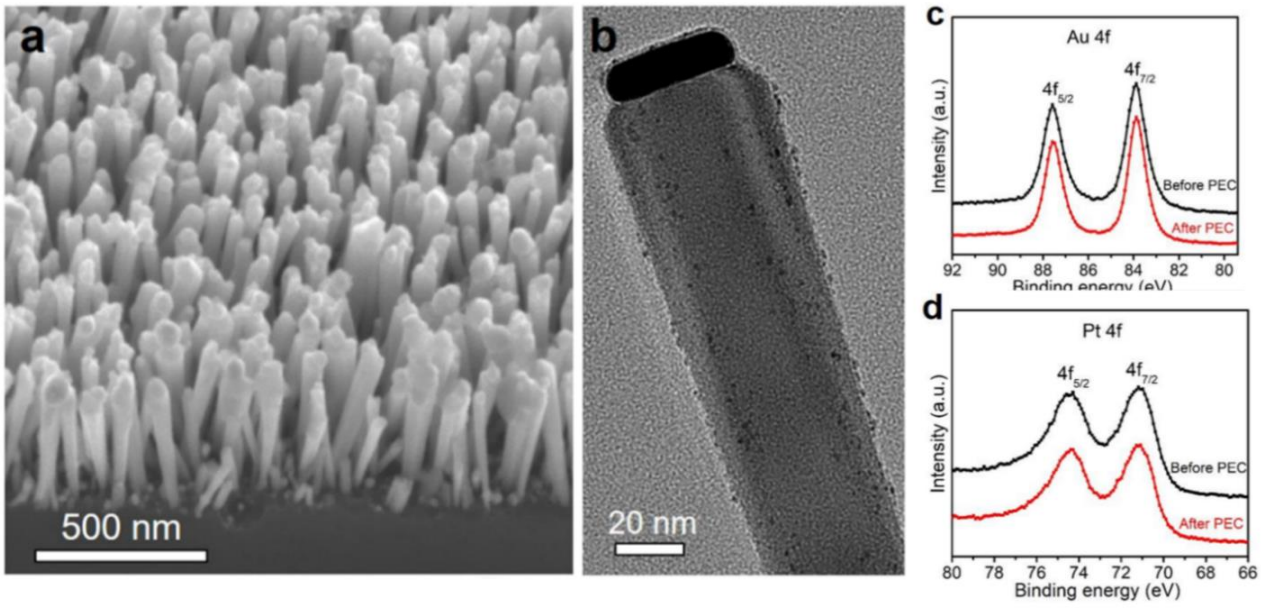

Figure 4.8: (a) SEM and (b) TEM images of $AuPt_{0.2}/GaN/n^+$-p Si photocathode after PEC stability test. XPS analysis of (c) Au 4f and (d) Pt 4f of $AuPt_{0.2}/GaN/n^+$-p Si photocathode before and after PEC stability test.

4.2.3 Photocatalytic mechanism

We hypothesized that controlling syngas composition with a wide CO/H_2 ratio is enabled by topological separation of CO and H_2 evolution sites. To explore this hypothesis, the Pt nanoparticles were synthesized on the polar surface of GaN nanowires in close to Au tips using $Pt(NH_3)_4Cl_2$ as a Pt precursor (Figure 4.9 a). To do this control experiment, a 3 cm^2 wafer sample was immersed in 50 mL of H_2PtCl_6 or $Pt(NH_3)_4Cl_2$ aqueous solution (0.01 mmol/L) overnight. The Pt content in the solution was determined using ICP-AES, and the amount of adsorbed Pt was estimated. The results show that PtCl6 2- anions have stronger adsorption on GaN surface than $Pt(NH_3)_4^{2+}$ cations, resulting in different photo deposition behavior. Pt nanoparticles were preferentially synthesized on the sidewall of GaN nanowires using H_2PtCl_6 precursor, due to a sorption-determined deposition mechanism. On the other hand, using Pt $(NH_3)_4Cl_2$ as Pt precursor results in photodeposition of Pt nanoparticles on nanowire tips close to Au (where electrons reside) due to negligible adsorption of $Pt(NH_3)_4^{2+}$ cations on nanowire.

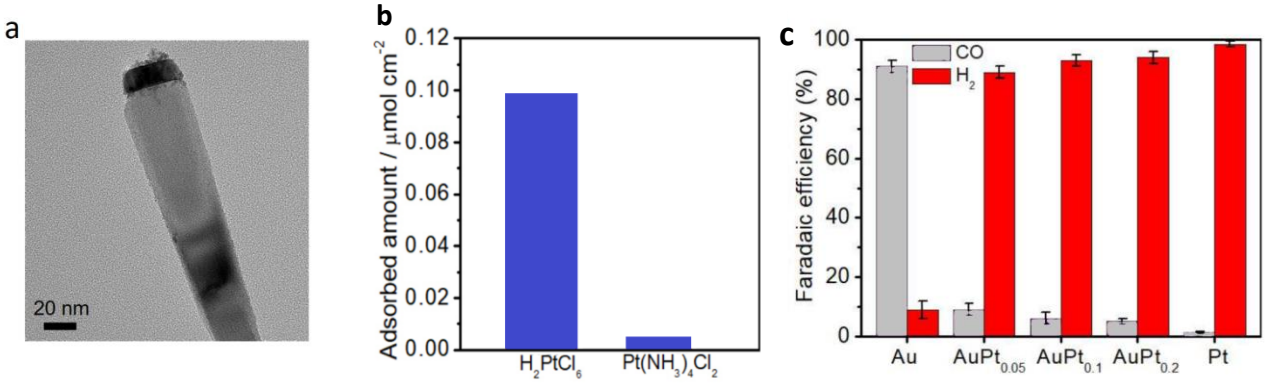

Figure 4.9: TEM image of $AuPt_{0.1}/GaN/n^+$-p Si using Pt $(NH_3)_4Cl_2$ as Pt precursor. (b) FEs for CO (purple bars) and H_2 (red bars) of $AuPt_x/GaN/n^+$-p Si with different cocatalyst compositions at +0.17 V vs RHE using Pt $(NH_3)_4Cl_2$ as Pt precursor. Error bars represent one standard deviation of multiple independent measurements.

In contrast to the spatially separated dual cocatalysts, the cocatalyst mixture results in a dominant H_2 evolution with FEs above 90% and a low controllability of syngas composition as a function of cocatalyst composition (Figure 4.9 c). It is a highly competitive process for electron transfer between neighboring Pt and Au, which favors the HER on Pt over CO_2RR, due to its kinetic feasibility.

To further understand the role of GaN nanowires, control studies were carried out with an $AuPt_{0.2}/n^+$-p Si planar sample in the absence of GaN nanowires. The $AuPt_{0.2}/n^+$-p Si planar sample's J-V curve shows a low photocurrent density (0.5 mA cm^2 at +0.17 V) and a low onset potential of 0.25 V. The FE for CO of $AuPt_{0.2}/n^+$-p Si is 9% at +0.17 V, which is significantly lower than the FE for $AuPt_{0.2}/GaN/n^+$-p Si, which is 32% as shown in Figure 4.10. These findings highlight the important role of GaN nanowires as a superior structural framework for improving PEC performance. The large surface-to-volume ratio of GaN nanowire allows high-density catalytic sites with a significantly reduced loading amount compared to the planar structure.

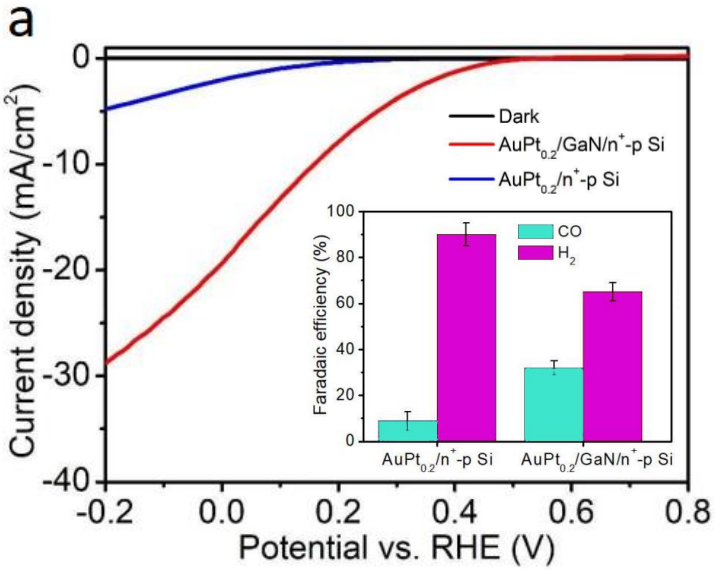

Figure 4.10: J-V curves of $AuPt_{0.2}/n^+$-p Si and $AuPt_{0.2}/GaN/n^+$-p Si. Inset: FEs for CO (green bars) and H_2 (purple bars) of $AuPt_{0.2}/n^+$-p Si and $AuPt_{0.2}/GaN/n^+$-p Si at +0.17 V vs RHE. The low FE for CO on $AuPt_{0.2}/n^+$-p Si might be ascribed to the close proximity of Au and Pt cocatalysts when they deposited on planar Si substrate.

An isotopic experiment with $^{13}CO_2$ was carried out to confirm that the CO created via CO_2 reduction. In the gas chromatography-mass spectrometry study, the signal at m/z = 29 ascribed to ^{13}CO was identified, but no signal of ^{12}CO was detected (Figure 4.11). Furthermore, a blank test in Ar-purged Na_2SO_4 aqueous solution revealed no CO production, confirming that the CO product originated from CO_2 reduction.

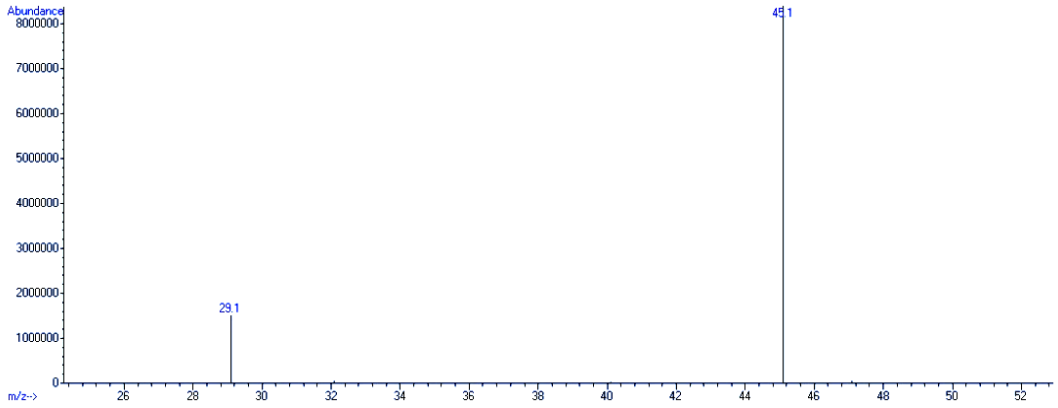

Figure 4.11: Mass spectrometry chromatogram of the gas phase analysis after 13C-labeled isotope experiment.

4.3 Conclusion

In conclusion, we demonstrated CO_2RR and HER decoupling employing dual cocatalysts to overcome the efficiency bottleneck and composition uncontrollability of PEC syngas generation from aqueous CO_2. On a planar Si photocathode, a record STS of 1.88 % was achieved by spatially coupling an Au CO-generating cocatalyst and a Pt H_2-generating cocatalyst on the polar and nonpolar surfaces of GaN nanowires, respectively. In addition, the CO/H_2 ratio in the syngas mixture was controllably tuned in a wide range between 1:99 and 10:1 with a total unity Faradaic efficiency, by simply varying the composition of dual cocatalysts. This work provides a promising route for the rational design of high-performance PEC syngas generation with controllable composition from aqueous CO_2 reduction.

4.4 References

1. Foit, S. R.; Vinke, I. C.; de Haart, L. G. J.; Eichel, R. A., Power-to-syngas: An enabling technology for the transition of the energy system? *Angew. Chem. Int. Ed*. **2017**, *56*, 5402-5411.

2. Urbain, F.; Tang, P. Y.; Carretero, N. M.; Andreu, T.; Gerling, L. G.; Voz, C.; Arbiol, J.; Morante, J. R., A prototype reactor for highly selective solar-driven CO_2 reduction to synthesis gas using nanosized earth-abundant catalysts and silicon photovoltaics. *Energy Environ. Sci*. **2017**, *10*, 2256-2266.

3. Furler, P.; Scheffe, J. R.; Steinfeld, A., Syngas production by simultaneous splitting of H_2O and CO_2 via ceria redox reactions in a high-temperature solar reactor. *Energy Environ. Sci*. **2012**, *5*, 6098-6103.

4. Li, F. F.; Lau, J.; Licht, S., Sungas instead of syngas: Efficient coproduction of CO and H_2 with a single beam of sunlight. *Adv. Sci.* **2015**, *2*, 1500260.

5. Li, D. W.; Ouyang, S. X.; Xu, H.; Lu, D.; Zhao, M.; Zhang, X. L.; Ye, J. H., Synergistic effect of Au and Rh on $SrTiO_3$ in significantly promoting visible-light-driven syngas production from CO_2 and H_2O. *Chem. Commun*. **2016**, *52*, 5989-5992.

6. Zhang, H. W.; Ming, J. T.; Zhao, J. W.; Gu, Q.; Xu, C.; Ding, Z. X.; Yuan, R. S.; Zhang, Z. Z.; Lin, H. X.; Wang, X. X.; Long, J. L., High-rate, tunable syngas production with artificial photosynthetic cells. *Angew. Chem. Int. Ed*. **2019**, *58*, 7800-7804.

7. Li, A.; Wang, T.; Chang, X.; Zhao, Z. J.; Li, C.; Huang, Z.; Yang, P.; Zhou, G.; Gong, J., Tunable syngas production from photocatalytic CO_2 reduction with mitigated charge recombination driven by spatially separated cocatalysts. *Chem. Sci.* **2018**, *9*, 5334-5340.

8. Ross, M. B.; Dinh, C. T.; Li, Y.; Kim, D.; De Luna, P.; Sargent, E. H.; Yang, P. D., Tunable Cu enrichment enables designer syngas electrosynthesis from CO_2. *J. Am. Chem. Soc*. **2017**, *139*, 9359-9363.

9. Hernandez, S.; Farkhondehfal, M. A.; Sastre, F.; Makkee, M.; Saracco, G.; Russo, N., Syngas production from electrochemical reduction of CO_2: Current status and prospective implementation. *Green Chem*. **2017**, *19*, 2326−2346.

10. Kang, P.; Chen, Z.; Nayak, A.; Zhang, S.; Meyer, T. J., Single catalyst electrocatalytic reduction of CO_2 in water to H_2+CO syngas mixtures with water oxidation to O_2. *Energy Environ. Sci.* **2014**, *7*, 4007-4012.

11. Mistry, H.; Reske, R.; Zeng, Z.; Zhao, Z. J.; Greeley, J.; Strasser, P.; Cuenya, B. R., Exceptional size-dependent activity enhancement in the electroreduction of CO_2 over Au nanoparticles. J. *Am. Chem. Soc.* **2014**, *136*, 16473.

12. Lee, J. H.; Kattel, S.; Jiang, Z.; Xie, Z.; Yao, S.; Tackett, B. M.; Xu, W.; Marinkovic, N. S.; Chen, J. G., Tuning the activity and selectivity of electroreduction of CO_2 to synthesis gas using bimetallic catalysts. *Nat. Commun.* **2019**, *10*, 3724.

13. He, R.; Zhang, A.; Ding, Y.; Kong, T.; Xiao, Q.; Li, H.; Liu, Y.; Zeng, J., Achieving the widest range of syngas proportions at high current density over cadmium sulfoselenide nanorods in CO_2 electroreduction. *Adv. Mater*. **2018**, *30*, 1705872.

14. Kumar, B.; Brian, J. P.; Atla, V.; Kumari, S.; Bertram, K. A.; White, R. T.; Spurgeon, J. M., Controlling the product syngas H_2:CO ratio through pulsed-bias electrochemical reduction of CO_2 on copper. *ACS Catal.* **2016**, *6*, 4739-4745.

15. Karatairi, E.; Miller, J. E., Splitting CO_2 to produce syngas and hydrocarbon fuels: PEC and STC. *MRS Bull*. **2017**, *42*, 878-879.

16. Chu, S.; Fan, S. Z.; Wang, Y. J.; Rossouw, D.; Wang, Y. C.; Botton, G. A.; Mi, Z., Tunable syngas production from CO_2 and H_2O in an aqueous photoelectrochemical cell. *Angew. Chem. Int. Ed*. **2016**, *55*, 14260-14266.

17. Chu, S.; Ou, P.; Ghamari, P.; Vanka, S.; Zhou, B.; Shih, I.; Song, J.; Mi, Z., Photoelectrochemical CO_2 reduction into syngas with the metal/oxide interface. *J. Am. Chem. Soc.* **2018**, *140*, 7869−7877.

18. Li, C. C.; Wang, T.; Liu, B.; Chen, M. X.; Li, A.; Zhang, G.; Du, M. Y.; Wang, H.; Liu, S. F.; Gong, J. L., Photoelectrochemical CO_2 reduction to adjustable syngas on grain-boundary-mediated a-Si/TiO2/Au photocathodes with low onset potentials. *Energy Environ. Sci*. **2019**, *12*, 923–928.

19. Pang, H.; Yang, G.; Li, P.; Huang, H.; Ichihara, F.; Takei, T.; Ye, J., Wafer-scale Si nanoconed arrays induced syngas in the photoelectrochemical CO_2 reduction. *Catal. Today* **2019**, *339*, 321− 327.

20. Wei, L.; Lin, J.; Xie, S.; Ma, W.; Zhang, Q.; Shen, Z.; Wang, Y., Photoelectrocatalytic reduction of CO_2 to syngas over ag nanoparticle modified p-si nanowire arrays. *Nanoscale* **2019**, *11*, 12530-12536.

21. Kong, Q.; Kim, D.; Liu, C.; Yu, Y.; Su, Y.; Li, Y.; Yang, P.D. Directed assembly of nanoparticle catalysts on nanowire photoelectrodes for photoelectrochemical CO_2 reduction. *Nano Lett.* **2016**, *16*, 5675–5680.

22. Song, J.T.; Ryoo, H.; Cho, M.; Kim, J.; Kim, J.G.; Chung, S.Y.; Oh, J. Nanoporous Au thin films on Si photoelectrodes for selective and efficient photoelectrochemical CO_2 reduction. *Adv. Energy Mater.* **2017,** *7*, 1601103.

23. Chu, S.; Fan, S.Z.; Wang, Y.J.; Rossouw, D.; Wang, Y.C.; Botton, G.A.; Mi, Z. Tunable syngas production from CO_2 and H_2O in an aqueous photoelectrochemical cell. *Angew. Chem. Int. Ed.* **2016**, *55*, 14260–14264.

24. Li, C.C.; Wang, T.; Liu, B.; Chen, M.X.; Li, A.; Zhang, G.; Du, M.Y.; Wang, H.; Liu, S.F.; Gong, J.L. Photoelectrochemical CO_2 reduction to adjustable syngas on grain boundary-mediated a-Si/TiO2/Au photocathodes with low onset potentials. *Energy Environ. Sci*. **2019,** *12*, 923–928.

25. Jang, J.-W., Cho, S.; Magesh, G.; Jang, Y.J.; Kim, J.Y.; Kim, W.Y.; Seo, J.K.; Kim, S.; Lee, K.-H.; and Lee, J.S. Aqueous-solution route to zinc telluride films for application to CO_2 reduction. *Angew. Chem. Int. Ed.* **2014,** *53*, 5852–5857.

26. Jang, Y.J.; Jang, J.W.; Lee, J.; Kim, J.H.; Kumagai, H.; Lee, J.; Minegishi, T.; Kubota, J.; Domen, K.; and Lee, J.S. Selective CO production by Au coupled ZnTe/ZnO in the photoelectrochemical CO_2 reduction system. *Energy Environ. Sci.* **2015,** *8*, 3597–3604.

27. Schreier, M.; Gao, P.; Mayer, M.T.; Luo, J.S.; Moehl, T.; Nazeeruddin, M.R.; Tilley, S.D.; Gratzel, M. Efficient and selective carbon dioxide reduction on low cost protected Cu2O photocathodes using a molecular catalyst. *Energy Environ. Sci*. **2015,** *8*, 855–861.

28. Feng, J.Y.; Huang, H.T.; Yan, S.C.; Luo, W.J.; Yu, T.; Li, Z.S.; and Zou, Z.G. Non-oxide semiconductors for artificial photosynthesis: progress on photoelectrochemical water splitting and carbon dioxide reduction. **2020**, *Nano Today 30*, 100830.

29. Andrei, V.; Reuillard, B.; and Reisner, E. Bias-free solar syngas production by integrating a molecular cobalt catalyst with perovskite-BiVO4 tandems. **2020,** *Nat. Mater*. *19*, 189–194.

30. Zhang, Y.-J.; Sethuraman, V.; Michalsky, R.; Peterson, A. A., Competition between CO_2 reduction and H_2 evolution on transition-metal electrocatalysts. *ACS Catal.* **2014**, *4*, 3742-3748.

31. Landers, A. T.; Fields, M.; Torelli, D. A.; Xiao, J.; Hellstern, T. R.; Francis, S. A.; Tsai, C.; Kibsgaard, J.; Lewis, N. S.; Chan, K.; Hahn, C.; Jaramillo, T. F.; The predominance of

hydrogen evolution on transition metal sulfides and phosphides under CO_2 reduction conditions: An experimental and theoretical study. *ACS Energy Lett.* **2018**, *3*, 1450-1457.

32. Ross, M. B.; Li, Y.; De Luna, P.; Kim, D.; Sargent, E. H.; Yang, P.; Electrocatalytic rate alignment enhances syngas generation. *Joule* **2019**, *3*, 257-264.

33. Vanka, S.; Arca, E.; Cheng, S.; Sun, K.; Botton, G. A.; Teeter, G.; Mi, Z., High efficiency Si photocathode protected by multifunctional GaN nanostructures. *Nano Lett.* **2018**, *18*, 6530.

34. Zhou, B.; Kong, X.; Vanka, S.; Chu, S.; Ghamari, P.; Wang, Y.; Pant, N.; Shih, I.; Guo, H.; Mi, Z., Gallium nitride nanowire as a linker of molybdenum sulfides and silicon for photoelectrocatalytic water splitting. *Nat. Commun*. **2018**, *9*, 3856.

35. Deng, J.; Su, Y.; Liu, D.; Yang, P.; Liu, B.; Liu, C., Nanowire photoelectrochemistry. *Chem. Rev*. **2019**, *119*, 9221−9259.

36. Rosser, T. E.; Windle, C. D.; Reisner, E., Electrocatalytic and solar-driven CO_2 reduction to CO with a molecular manganese catalyst immobilized on mesoporous TiO_2. *Angew. Chem. Int.* Ed. **2016**, *55*, 7514-7518

37. Kumagai, H.; Sahara, G.; Maeda, K.; Higashi, M.; Abe, R.; Ishitani, O., Hybrid photocathode consisting of a CuGaO2 p-type semiconductor and a Ru(II)-Re(I) supramolecular photocatalyst: Non-biased visible-light-driven CO_2 reduction with water oxidation. *Chem. Sci*. **2017**, *8*, 4242-4249.

38. Feng, X.; Jiang, K.; Fan, S.; Kanan, M. W. Grain-boundary-dependent CO_2 electroreduction activity. *J. Am. Chem. Soc.* **2015**, *137*, 4606-4609.

39. Sun, K.; Cheng, T.; Wu, L.; Hu, Y.; Zhou, J.; Maclennan, A.; Jiang, Z.; Gao, Y.; Goddard, W. A., 3rd; Wang, Z., Ultrahigh mass activity for carbon dioxide reduction enabled by gold-iron coreshell nanoparticles. *J. Am. Chem. Soc*. **2017**, *139*, 15608-15611.

Chapter 5 : High-Performance Solution-Processed Organic Field-Effect Transistors via Doping with Nitroaromatics

In the previous two chapters we focused on the development of efficient and stable PEC systems based on III-nitrides nanostructure for reduction of CO_2 to syngas fuel. In this chapter we investigated the impact of doping strategy on the performance of polymer OFETs. OFETs are emerging as promising building blocks for large-area printable and flexible electronics. Despite major advances in material and device architecture designing to improve charge transport properties, OFETs have yet to be implemented in practical applications. The bottlenecks are operational challenges such as low carrier mobility and device instability, both of which are inextricably linked to charge carrier trapping phenomena in organic semiconductors (OSCs). Intentional molecular doping has been found to be a low-cost and effective approach for mitigating trap states and tuning the charge transport properties in OSCs. However, the limited toolbox of molecular dopants and unresolved challenges of stability, uniform doping, and matching the energy levels, constrain the achieved OFET device performance and thwart the practical applications. Here, nitrofluorene acceptors (NFs) are introduced as effective p-dopants in polymer OFETs, resulting in outstanding device performance of a standard commercial diketopyrrolopyrrole-thienothiophene (DPP-DTT) polymer. An ~5-fold enhancement in saturation field-effect mobility (up to ~8 $cm^2V^{-1}s^{-1}$) is realized in ambient air operation, after doping with 2,4,5,7-tetranitrofluorenenone. Importantly, the achieved effective mobility (which accounts for device non-ideality) exceeds 6 $cm^2V^{-1}s^{-1}$ which is among the highest μ_{eff} values reported for polymer OFETs. The spectroscopic, microscopic, X-ray diffraction and electrical investigations elucidate the role of NF dopants in mitigating charge-carrier traps, lowering the contact resistance, and maximizing the structural order of the polymer films. Energetic disorder reduces significantly upon doping as revealed via variable temperature mobility measurements. This chapter is based on the published journal: Controlling Structural and Energetic Disorder in High-Mobility Polymer Semiconductors via Doping with Nitroaromatics, P. Ghamari, M. R. Niazi and D. F. Perepichka, *Chem. Mater*. 2021, 33, 2937-2947.

5.1 Introduction

Printable, flexible, wearable, and disposable OFETs based on π-conjugated polymers are emerging as promising building blocks for large-area displays, (bio)chemical sensing, neuromorphic devices, security, and healthcare monitoring devices.[1, 2] While the charge carrier mobility (μ) of semiconducting polymers lags behind that of many inorganic crystalline semiconductors, it has already surpassed the amorphous silicon benchmark (1 $cm^2V^{-1}s^{-1}$).[1]

Continuous improvement of the charge carrier mobility has been one of the key objectives in the field of organic electronics [3], and several polymer semiconductors with μ >10 $cm^2V^{-1}s^{-1}$ have been reported.[4, 5] At the same time, overestimations (sometimes by more than an order of magnitude) of the μ values extracted via the electrical characterization of non-ideal devices have also been pointed out.[6, 7] To this end, it was recently proposed that effective mobility (μ_{eff}) based on electrically equivalent ideal transistor is used to avoid overestimations of the saturation mobility (μ_{sat}). Apparently, of all state-of-art polymer OFETs reported in the last decade, there are less than a handful number of examples of μ_{eff} >4 $cm^2V^{-1}s^{-1}$ (see Figure 2.8 and Table 2.2).[8, 9] The key challenge in realizing high-mobility OFETs is that the charge transport in polymers is inherently limited by the charge carrier trapping due to: (1) dynamic disorder induced by thermal motions of molecules,[10] (2) chemical impurities, (3) structural disorder,[11, 12] (4) interfacial trap states at a semiconductor/dielectric interface [13, 14] and (5) environmental traps (mainly due to atmospheric water and oxygen).[15]

To overcome OFET operational challenges, significant efforts have been made to design new polymers (with varied substituents and heteroatoms, donor-acceptor copolymers, improved backbone planarity, etc.)[16-18], to better understand the device physics, and to engineer new device architectures and interfaces.[19-21] Aligning the polymer backbone chains in the OFET channel direction (nano-grooving, blade coating, etc.),[22, 23] post-processing strategies (thermal and solvent vapor annealing), additives (solvents or ionic additives),[15, 24] blending approaches (with insulating or semiconducting materials,[25] to name but a few, have also lead to enhanced charge transport properties of polymer OFETs. On the other hand, for over a half-century doping has been used to induce electrical conductivity in organic materials.[26, 27] Doping has also been employed to modulate the electrical characteristics of thermoelectrics[28] and photovoltaics (OPVs).[29] In the context of OFETs, this old strategy of doping has only recently emerged as a viable approach to

mitigation of the trap states.[30, 31] The contact doping (carried out via vacuum deposition) using metal oxides (MoO_3, WO_3, V_2O_5) and π-electron acceptors (such as TCNQ derivatives), aimed at decreasing the contact resistance has been shown to improve the OFET charge mobility and lower the threshold voltage. However, the diffusion of dopants into bulk often leads to unstable device operation and accelerated degradation of performance (low current ON/OFF ratio).[32-35] Various types of solution processable p-dopants (Figure 5.1) such as Lewis acids ($B(C_6F_5)_3$, $Zn(C_6F_5)_2$),[36-38] π-electron acceptor (fullerene derivatives PCBM and $C_{60}F_{48}$, TCNQ; F4-TCNQ),[39, 40] metal oxides, halides (Mn_3O_4, $FeCl_3$),[41] and ionic additives (NMe_4I)[42] have been explored in bulk doping of OFETs (usually carried out via solution processing). The noticeable improvements in OFET charge mobility, lowered threshold voltage, reduced bias stress, and enhanced environmental stability have been primarily associated with lowered contact resistance and density of trap states.[36, 39, 40, 43] However, the unexpected role of molecular dopants acting as 'seeds' in polymer crystallization, enhancing the nano/micro-structural order of semiconducting films have also been reported.[44,45] Nevertheless, technological challenges with the existing molecular dopants such as poor solubility and phase separation, poor chemical stability, and limited range of electron affinities limit the wide implementation of the doping in OFETs.[30, 31, 46]

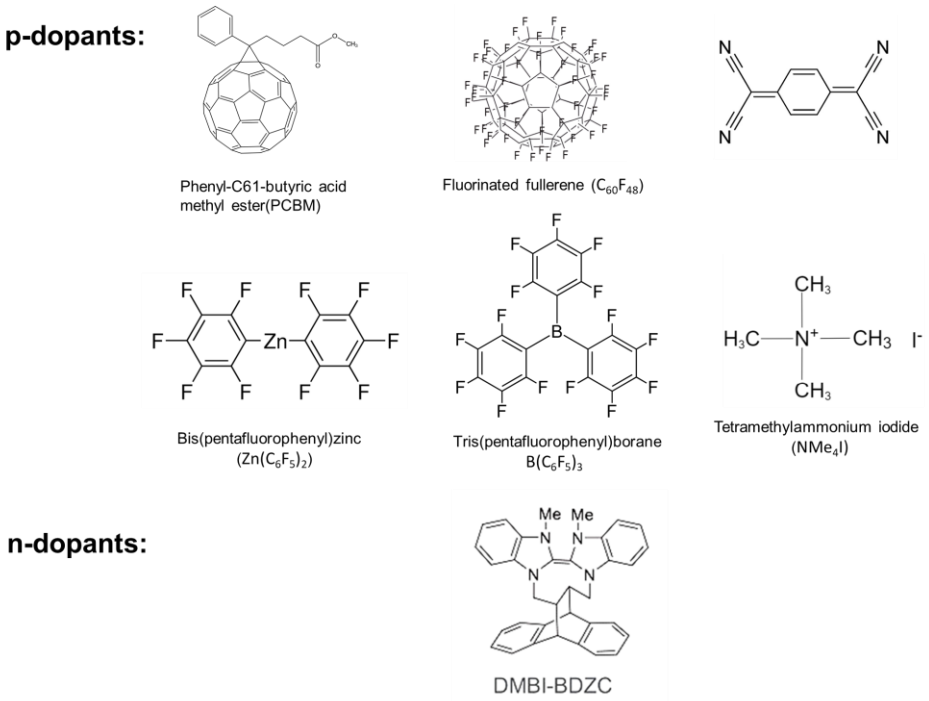

Figure 5.1: Molecular structures of dopants mentioned in this study.

It is also noteworthy that all major successes in doping strategy to enhance μ of OFET have been reported polycrystalline small molecule semiconductors. For instance, doping of molecular semiconducting films (C8-BTBT, in blends with C_{16}IDT-B) with $Zn(C_6F_5)_2$ Lewis acid or $C_{60}F_{48}$ electron acceptor has resulted in remarkable μ enhancement from ~2 to ~20 $cm^2V^{-1}s^{-1}$.[25, 38] On the other hand, polymer semiconductors are considered a better choice for many future applications such as flexible and wearable electronics owing to their superior film-forming and mechanical properties. Only a few papers report significant enhancement of charge mobility in polymer-based OFET. For example, TCNQ derivatives, the most common molecular p-dopants, has been explored and shown to enhance the hole mobility (*e.g.* from 1.03 to 1.2 $cm^2V^{-1}s^{-1}$ DPP-DTT doped with F4-TCNQ.[15, 47] Doping of the indenopyrazine-thiophene polymer with $B(C_6F_5)_3$ Lewis acid showed an increase of hole mobility from 0.08 to 0.6 $cm^2V^{-1}s^{-1}$.[37] An even more pronounced mobility enhancement in hole mobility in DPP-DTT OFETs, from 0.6 to 3.5 $cm^2V^{-1}s^{-1}$, was reported using Pyronin B dye (3,6-bis(diethylamino)xanthylium tetrachlroferrate).[48] However, the complexity of the processes (mixture of 6 solvents), intrinsic chemical instability and low purity (40%) of this $FeCl_3$-containing dye, as well as limited understanding of mechanism of doping do not lend the process to wide practical implementation. Here, we report nitrofluorenone (NFs) derivatives (Figure 5.2a) as new p-dopants for polymer OFETs and carry out detailed mechanistic studies of the doping via spectroscopic, electrical, and microstructural characterization. The ease of synthesis of NFs with various functional groups allows for facile tuning of their EA (between 3 to 4.8 eV) and solubility.[49] In the past, charge transfer complexes of NFs have been used as sensitizers of photoconductive polymers [50,51] and we have also recently demonstrated n-type OFETs based on NF semiconductors.[52] Now, we show the addition of NFs in the DPP-DTT polymer OFET significantly improves the charge mobility and suppresses the parasitic effects (contact resistance, charge carrier trapping, the gate-source voltage dependence of the mobility), while operating in ambient air. Atomic force microscopy (AFM) revealed larger polymer fibers in doped DPP-DTT films, and an improved lamellar order was confirmed by 2-D grazing-incidence wide-angle X-ray scattering (GIWAXS). UV-vis-NIR absorption spectra showed the enhanced absorption in doped films in line with the increased order. Variable temperature mobility measurements also reveal a significant reduction (from ~58 to ~36 meV) of the charge-transport activation energies suggesting reduced energetic disorder in TeNF doped film.

5.2 Results and discussion

5.2.1 Establishing NFs as p-dopants for DPP-DTT based OFETs.

DPP-DTT was chosen as a model semiconducting polymer owing to its wide commercial availability and good charge carrier mobility of >1 $cm^2V^{-1}s^{-1}$ (Figure 5.2b).[4, 42] We selected 2,7-dinitrofluorenone (DNF), 2,4,5,7-tetranitrofluorenone (TeNF), and 9-(dicyanomethylidene)-2,4,5,7-tetranitrofluorene (DCN-TeNF) from a large library of the known NF derivatives,[49, 52] to cover a range of electron affinities from 3.9 to 4.8 eV (Figure 5.2c). Note that although polynitroaromatics are known as highly energetic compounds and used as explosives, the DPP-DTT/TeNF retain very high thermal stability (T_{dec} > 350 ºC, Figure 5.3).

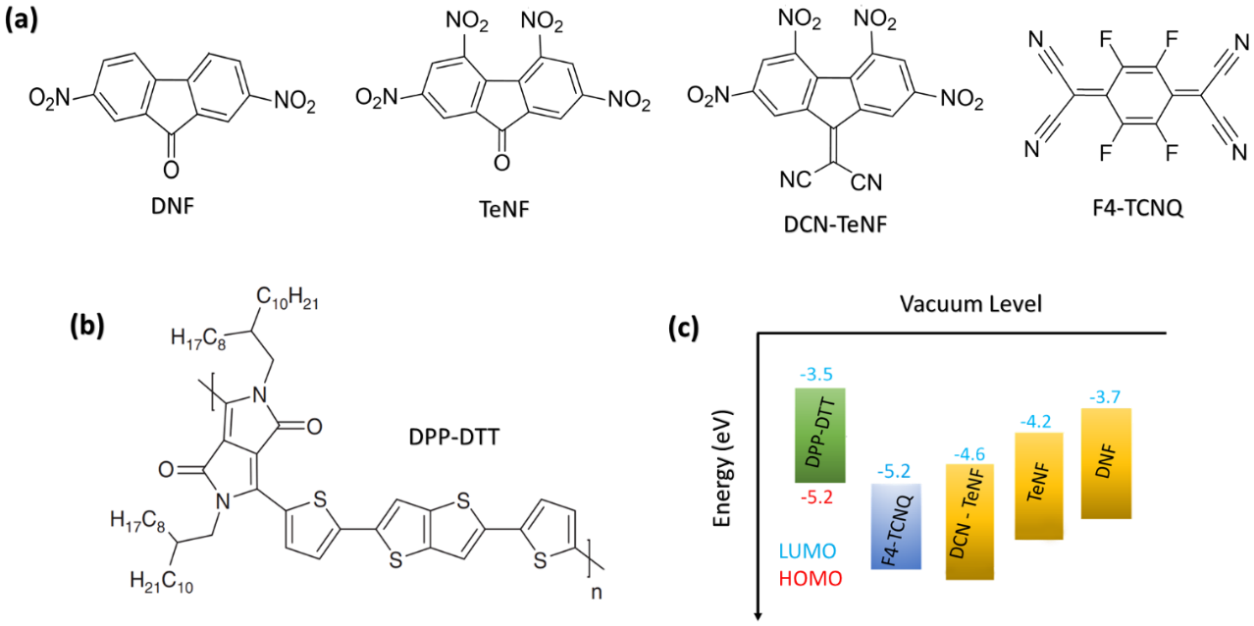

Figure 5.2: Molecular structures of (a) dopants and (b) semiconducting polymer used in this work, and (c) their respective HOMO [4,53] and LUMO [49,54] energies, as determined by cyclic voltammetry (vs ferrocene oxidation, assumed at –4.8 eV vs vacuum).

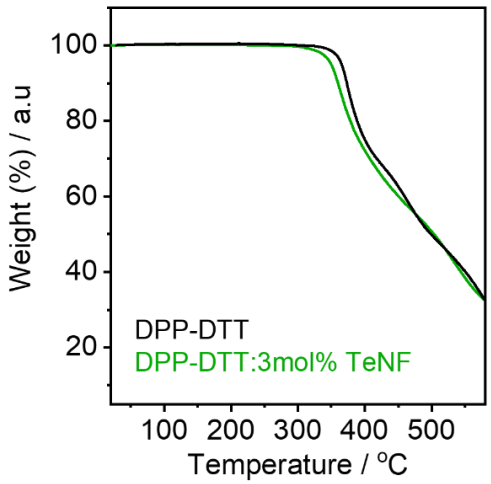

Figure 5.3: Thermal stability of TeNF doped DPP-DTT OFETs.

We also used F4-TCNQ, a high electron affinity acceptor, as a reference dopant which has been explored previously.[15, 47] The electrochemically measured HOMO of DPP-DTT (–5.2 eV)[4, 53] is close to LUMO of F4-TCNQ (–5.2 eV)[47, 54] suggesting very strong donor-acceptor interaction and, likely, full electron transfer. Formation of moderately strong charge transfer complexes (CTC) is predicted for TeNF and DCN-TeNF and has been previously reported for MEH-PPV polymer (HOMO = −5.0 eV).[49] However, no significant charge transfer can be expected between DPP-DTT donor and DNF acceptor due to the large energy barrier (1.5 eV) between them.

As the charge carriers in *p*-type semiconducting polymers are commonly presented by polarons (radical-cations),[55] we used electron paramagnetic resonance (EPR) spectroscopy to measure the concentration of unpaired electrons in the pristine and doped films (Figure 5.4a). EPR spectroscopy of the pristine DPP-DTT shows a weak symmetric signal at *g*-value ≈ 2.0069 (ΔHpp = 0.15 mT), which can be attributed to the presence of intrinsic impurities and defects in the polymer, either created during synthesis or formed upon storage in the presence of oxygen[36, 56]. Quantitative EPR measurements show a spin concentration of $\sim 10^{16}$ spins cm^{-3} (10^{-5} spins per DPP-DTT repeat unit), which may correspond to a background hole density of undoped DPP-DTT films. Doping with strong acceptor F4-TCNQ (10 mol%) results in some broadening (ΔHpp = 0.25 mT) and a marked enhancement of the EPR signal which shifts to *g*-value ≈ 2.0049) and the total spin density increases to 5×10^{17} spins cm^{-3} (~0.005 spins/dopant molecule). While two EPR signals (due to radical-anion of F4-TCNQ, at *g*-value ~2.004 and radical-cation of DPP-DTT, at *g*-value ~2.007) are expected upon doping, these could not be resolved in the X-band EPR

spectra.[56, 57] Weak dopant DNF showed no notable EPR signal amplification. Doping with TeNF and DCN-TeNF yields a higher spin concentration of 8×10^{17} spins cm^{-3} and 9×10^{17} spins cm^{-3} (~0.01 spins/dopant molecule) and a significant EPR signal broadening (ΔHpp = 0.67 mT), while the *g*-value of shifts back close to that of the pristine polymer (2.0060). The generation of unpaired electrons in the doped films suggests an electron transfer from DPP-DTT host (or impurities) to the dopant despite a substantial energetic barrier between the HOMO of DPP-DTT and the LUMO of all dopant molecules (except for F4-TCNQ, Figure 5.2c).

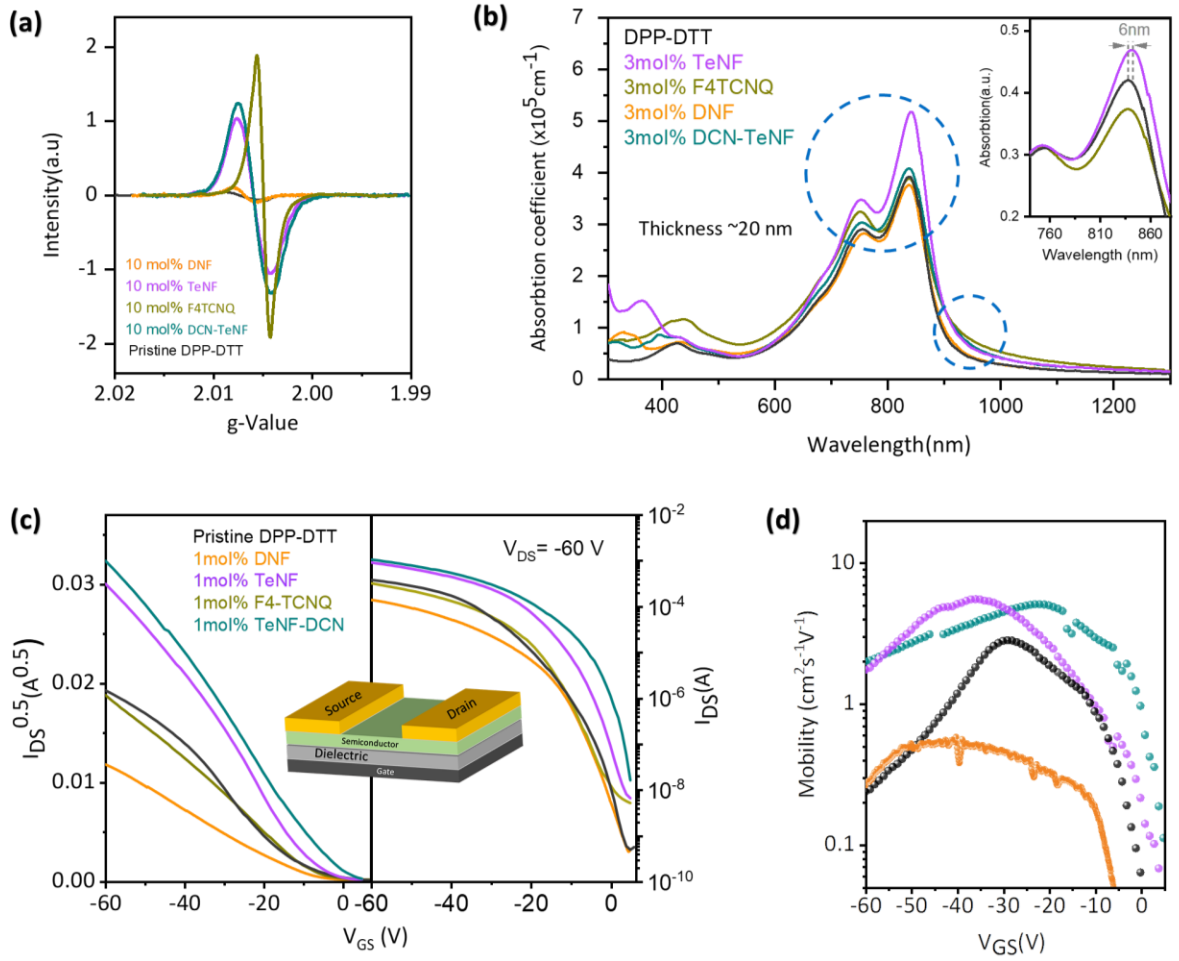

Figure 5.4: (a) EPR spectra of pristine and doped DPP-DTT polymer (b) UV-Vis-NIR absorption spectra of pristine and doped DPP-DTT. (c) Transfer curves of pristine and doped devices measured at V_{DS} = -60 V. (d) Saturated hole mobility (μ_{sat}) versus applied gate-source bias (V_{GS}) for the pristine and doped devices.

The Vis-NIR absorption spectrum of DPP-DTT film shows a strong near-IR absorption band with clear vibronic peaks at λ_{max} = 750 nm (0–1) and 835 nm (0–0) (Figure 5.4b). The absorption shoulder above 900 nm in the doped films can be attributed to charge transfer absorption.[47] This shoulder is the strongest for F4-TCNQ and non-existence for DNF, as could be expected from the LUMO energies of the used dopants (Figure 5.2). The most significant change of DPP-DTT absorption was observed upon doping with TeNF which results in ~30% increase of absorption coefficient (α), ~6 nm redshift, and increase of the relative intensity of the 0–0 vibronic peak comparing to the 0–1 peak (see Figure 5.4b and Table 5.1). These changes can be ascribed to the higher order of the doped polymer films.[58-60] On the other hand, doping with F4-TCNQ does not increase the absorptivity and reduces the relative intensity of the 0–0 peak indicating an increased disorder, as previously observed by Bao et al.[47]

Table 5.1: Vibronic peaks maxima and their relative intensity in the NIR absorption spectra of pristine and doped (3 mol%) DPP-DTT films.

	λ_{max}^{0-1} (nm)	λ_{max}^{0-0} (nm)	A^{0-0}/A^{0-1}
Pristine DPP-DTT	753	837	1.35
TeNF	753	842	1.52
DCN-TeNF	753	838	1.34
F4TCNQ	752	837	1.20
DNF	754	837	1.33

To assess the effect of NFs dopants on OFET performance of DPP-DTT, we first optimized the thin film coating conditions (solvent, annealing temperature, and dielectric surface treatment, Figure 5.5 to 5.7, and Tables 5.2 and 5.3) and fabricated bottom gate top contact (BGTC) OFETs with pristine polymer, using Si/SiO_2 (300 nm) substrates modified with octadecyltrichlorosilane (ODTS) monolayer (The details of ink preparation and OFET fabrication are in Appendix B.1).

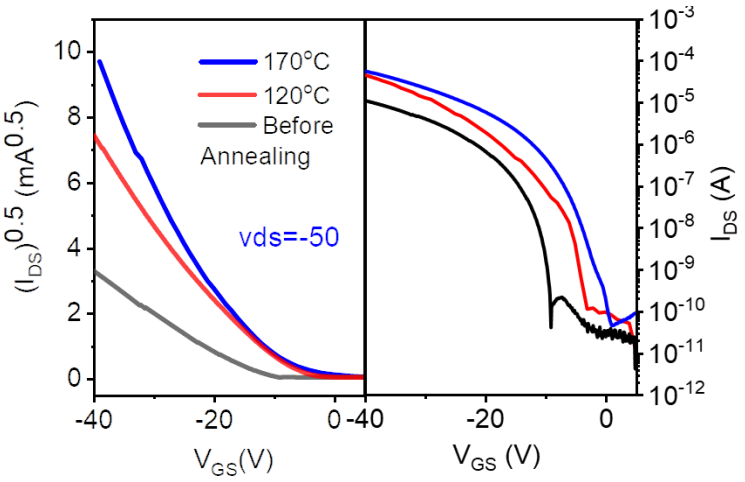

Figure 5.5: Effect of the film annealing on pristine DPP-DTT OFET transfer curves.

Table 5.2: The OFET parameters of DPP-DTT transistors for different annealing temperatures.

Condition	μ_{sat} ($cm^2V^{-1}s^{-1}$)	V_{TH} (V)	I_{ON}/I_{OFF}
As prepared	0.2±0.05	-16±2	10^6
120°C	0.6±0.1	-10 ±2	10^6
170°C	1.0±0.2	-8±2	10^5

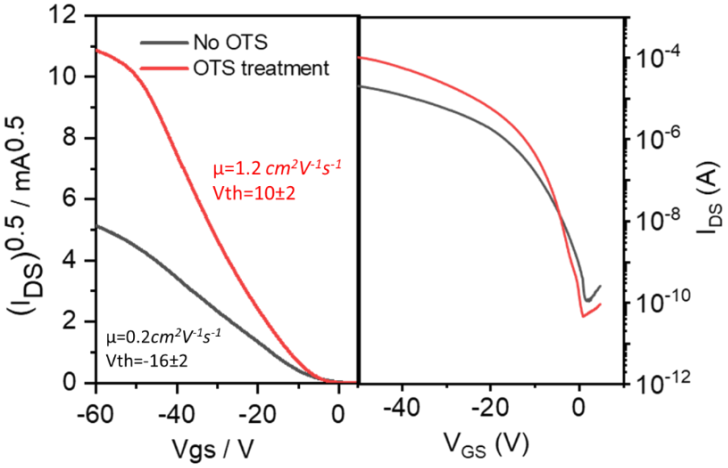

Figure 5.6: Effect of ODTS functionalization of the dielectric surface on pristine OFET transfer curves.

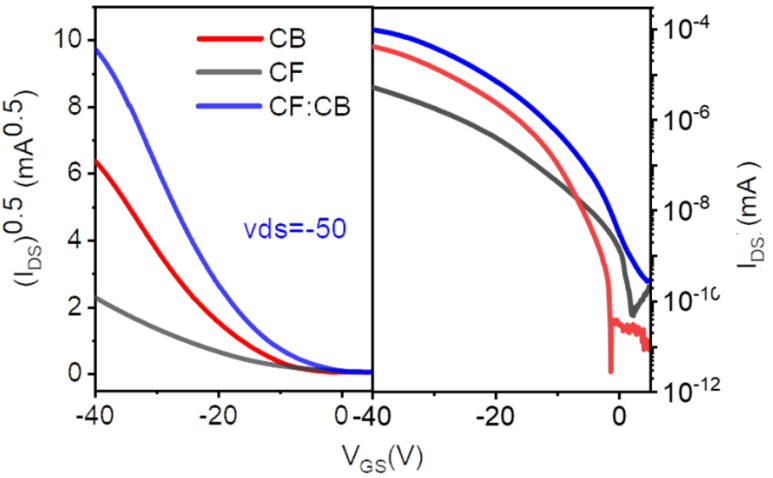

Figure 5.7: Effect of the processing solvent (chlorobenzene, CB; chloroform, CF and their 1:1 mixture) on pristine DPP-DTT OFET transfer curves.

Table 5.3: The OFET parameters of DPP-DTT transistors for different solvents system, spin-coated from 5 g L^{-1} solution.

Solvent	μ_{sat} ($cm^2V^{-1}s^{-1}$)	V_{TH} (V)	$I_{ON/IOFF}$
$CHCl_3$	0.1±0.02	-15±3	10^6
PhCl	1.3±0.2	-10±2	10^7
$CHCl_3$: PhCl (1:1 v/v)	1.8±0.3	-8 ±2	10^5

The polymer films and top Au contacts were deposited by spin coating and thermal evaporation, respectively. The transfer characteristics show non-linear $\sqrt{I_{SD}}$ vs V_{GS} behavior revealing a gate dependent carrier mobility (Figure 5.4c, d). This phenomenon is common in polymer OFETs and often resulted in massive over-estimation in reported mobility values.[6, 42] Therefore, along with the achieved saturated charge carrier mobility (μ_{sat}), we also report the reliability factor (r_{sat}) and effective mobility (μ_{eff}), using Equations 2.6 and 2.7, as proposed in ref 61.

Table 5.4: NF-doped DPP-DTT transistors Figure of merits

Dopant (1mol%)	E_{LUMO} /eV	μ_{sat} [a] /$cm^2V^{-1}s^{-1}$	r_{sat} [b] /%	μ_{eff} [c] /$cm^2V^{-1}s^{-1}$	Δh^+ [d] (10^{11}) /cm^{-2}	V_{TH} [e] /V	on/off [f] /10^5	I_{OFF} [g] /nA
Pristine	-3.5	1.5±0.7	57	1.05±0.2	0	-8.3±1	1.5	3.3
DNF	-3.7	0.4±0.3	70	0.4±0.1	1.10	-11±2	5	2.8
TeNF	-4.2	4.2±0.5	68	2.9±0.3	2.86	-5.5±1.2	1	23
DCN-TeNF	-4.6	4.1±0.4	75	3.1±0.3	5.53	-4±0.6	0.7	51
F4-TCNQ	-5.2	1.4±0.4	70	1.1±0.2	4.49	-6±0.8	0.2	20

[a] hole mobility in saturation regime; [b] reliability factor; [c] hole effective mobility in saturation regime; [d] induced excess holes; [e] threshold voltage; [f] ratio of ON current to OFF current; [g] off current.

Doping of DPP-DTT with the strongest acceptor F4-TCNQ (1 mol%) does not significantly change the μ_{eff} (μ_{sat} slightly decreases from 2.2 to 1.8 $cm^2V^{-1}s^{-1}$), while the weakest acceptor DNF causes a significant decrease of μ_{eff} to 0.5 $cm^2V^{-1}s^{-1}$ (Table 5.4). On the other hand, doping with TeNF and DCN-TeNF lead to more than a two-fold enhancement of μ_{eff} (and μ_{sat} up to ~4.5 $cm^2V^{-1}s^{-1}$, at 1 mol%). All doped devices showed a weaker mobility dependence on the gate-source voltage comparing to pristine DPP-DTT (Figure 5.4d). This also results in a higher reliability factor of the doped transistors.

5.2.2 Effect of TeNF doping on field-effect mobility and charge carrier injection

Considering the excellent performance of TeNF-doped devices and high chemical stability and ease of synthesis of this acceptor, we carried out in-depth investigation of its effect on electrical characteristics of DPP-DTT OFETs at different concentrations (Figure 5.8, Table 5.5). Both the μ_{lin} and μ_{sat} showed a gradual enhancement with increasing concentration of TeNF, reaching 3.5 and 7.9 $cm^2\ V^{-1}\ s^{-1}$ at 3 mol%, respectively. Further increase of the TeNF, however, leads to decrease of device performance, plausibly due to perturbed microstructure. Higher μ_{sat} were realized for the doped comparing to pristine DPP-DTT films at any given $V_{GS}/V_{DS,}$ and the statistics (Figure 5.8d) based on 200 OFETs also show an improved reproducibility in doped devices.

The gate-dependent mobility plot (Figure 5.8b) reveals a dramatic ~10 times drop in μ_{sat} of pristine DPP-DTT devices with increasing gate-source bias, as previously reported for the same polymer OFETs.[4,42]This behavior is progressively suppressed with increasing dopant concentrations, and in the case of 3 mol% TeNF doping the μ_{sat} only drops from 7.9 to 4.3 $cm^2V^{-1}s^{-1}$. Gate-dependent mobility in donor-acceptor polymers has previously been associated with the electron trapping at dielectric-semiconductor interface as well as the field dependent contact resistance effects.[6,62-65]

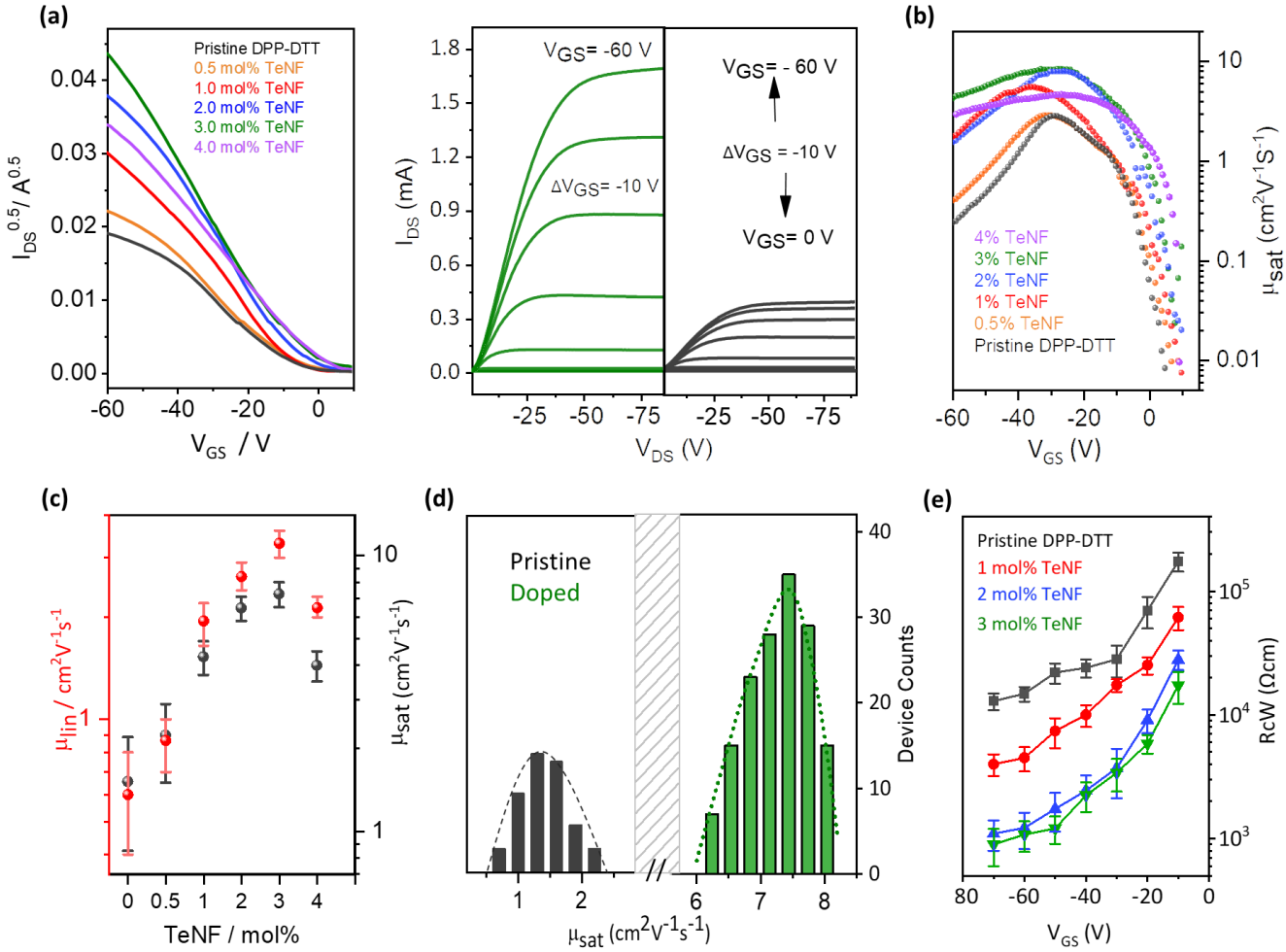

Figure 5.8: Representative transfer (left, V_{DS} = -60 V) and output (right) characteristics for OFETs with dopant concentration varying from 0 to 4 mol%. (b) Gate-source bias (V_{GS}) dependence of μ_{sat} of OFETs with 0 and 3 mol% of TeNF dopant; (c) linear and saturation mobility as a function of TeNF concentration; (d) The maximum hole mobility distribution measured for 50 pristine and 150 doped OFETs. (e) Channel-width normalized contact resistance (RCW) vs VGS plots of OFETs with various dopant concentrations.

Table 5.5: Effect of TeNF concentration of OFET figures of merit of DPP-DTT polymer.

Dopant (mol%)	μ_{sat}/ $cm^2V^{-1}s^{-1}$	r_{sat} /%	μ_{eff}/ $cm^2V^{-1}s^{-1}$	μ_{lin}^{*}/ $cm^2V^{-1}s^{-1}$	$\Delta h^+(10^{11})$ /cm^{-2}	V_{TH} /V	SS†/ $Vdec^{-1}$	$N_{it}(10^{12})^{‡}$ /$eV^{-1}cm^{-2}$	on/off /10^5	I_{OFF} /nA	RcW§ /KΩ.cm
0.0%	1.5±0.7	57	1.05±0.2	0.6±0.2	0	-8.3±1	6.1	11.1	~1.5	3.3	14.8
0.5 %	2.3±0.6	61	1.4±0.3	0.9±0.1	0.85	-7.5±1.3	6	10.8	~1.1	4.8	12.9
1 %	4.2±0.5	68	2.9±0.3	2.0±0.2	2.86	-5.5±1.2	5.3	9.6	~1	23	4.5
2 %	6.5±0.6	76	5.1±0.3	2.6±0.2	4.46	-4.1±1	4.1	7.4	~0.7	18	1.3
3 %	7.3±0.6	81	6.2±0.2	3.4±0.2	7.11	-1.6±0.5	3.9	6.8	~0.2	61	1.1
4%	4.0±0.5	88	3.6±0.3	2.2±0.1	7.65	-1±0.4	5.1	9.2	~0.12	80	1.1

* hole mobility in linear regime; † subthreshold swing; ‡ interfacial trap density; § contact resistance.

To understand the impact of TeNF doping on charge injection and device operation, the contact resistance (R_C) values were estimated from OFET output characteristics measured for different channel lengths, using the transmission line method (Figure 5.9).[20, 33] The channel width normalized contact resistance (R_CW) values were calculated as a function of V_{GS} for different doping concentrations (Figure 5.8e). The contact resistance decreases with increasing TeNF concentrations in DPP-DTT film, falling to 1.1 kΩ·cm. This is one of the lowest R_CW values reported for DPP-DTT based OFETs (Figure 5.10) and it indicates the improved charge injection in doped DPP-DTT devices, as typically observed upon doping..[41, 48, 66] The contact resistance in BGTC devices includes both the interfacial and the bulk components. The latter reflects the transport of the charges between the top electrode through the film to the interface with the bottom gate dielectric. The decrease of this out-of-plane resistance of the film upon doping can explain the lowered contact resistance. [30, 33, 66] We also note that the lower contact resistance of doped films can partially explain the reduced gate-dependence of the mobility (Figure 5.8b).[6, 64, 65]

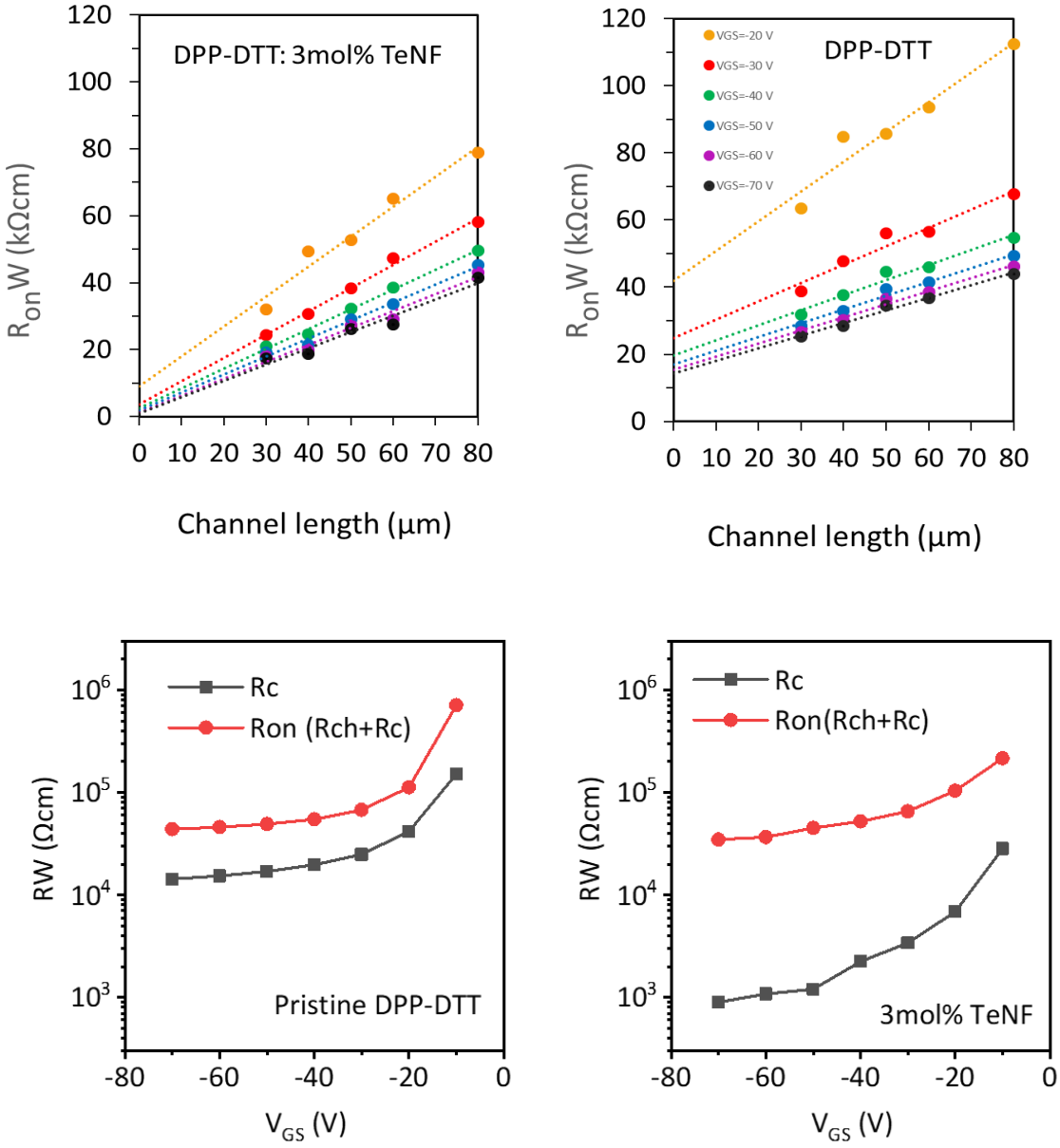

Figure 5.9: Total device resistance versus channel length (top); contact resistance and total resistance versus gate-source voltage (bottom) in pristine (left) and doped (right) DPP-DTT devices.

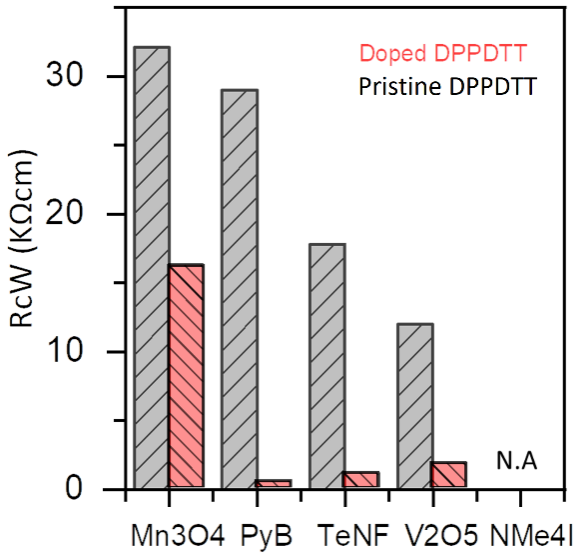

Figure 5.10: Comparison of the effect of different dopants on the contact resistance of DPP-DTT based OFETs. TeNF (this work), Mn3O4 (contact doping)8, FeCl3-Pyronin (PyB, bulk doping), V2O5 (contact doping).

5.2.3 Effect of doping on DPP-DTT film microstructure

We used AFM (tapping mode), X-ray diffraction (XRD), and GIWAXS to characterize the effect of doping on the film morphology and microstructure (Figure 5.11a). Pristine DPP-DTT film exhibits a fibrillar morphology with root mean square surface roughness (RMS) of 3.4 nm. TeNF doped films reveal a progressive decrease in RMS down to 1.3 nm and an increase in crystalline domain sizes with increasing TeNF content.

The average grain lengths are calculated by Gwyddion software using two methods. The first method specifies a threshold height value to define grain masks (Figure 5.12). A statistical analysis is then applied on marked grains to calculate the average fiber lengths. The second method is manual grain scaling and calculating the average length over 100 grains in each film. The obtained size from both methods is comparable and shows an increase from ~140 nm in pristine film to ~480 nm in 3 mol% doped film. The average length of grains in F4-TCNQ doped film is very close to pristine film (~150 nm). The average fiber length increases from ~140 nm for the pristine film to ~480 nm in TeNF-doped film. A similar increase in the size of the fibers was also observed for DCN-TeNF but not for DNF and F4-TCNQ doped films, both of which showed similar surface

morphology to pristine DPP-DTT (Figure 5.13). These observations are consistent with the improved charge mobility in TeNF and DCN-TeNF doped devices.

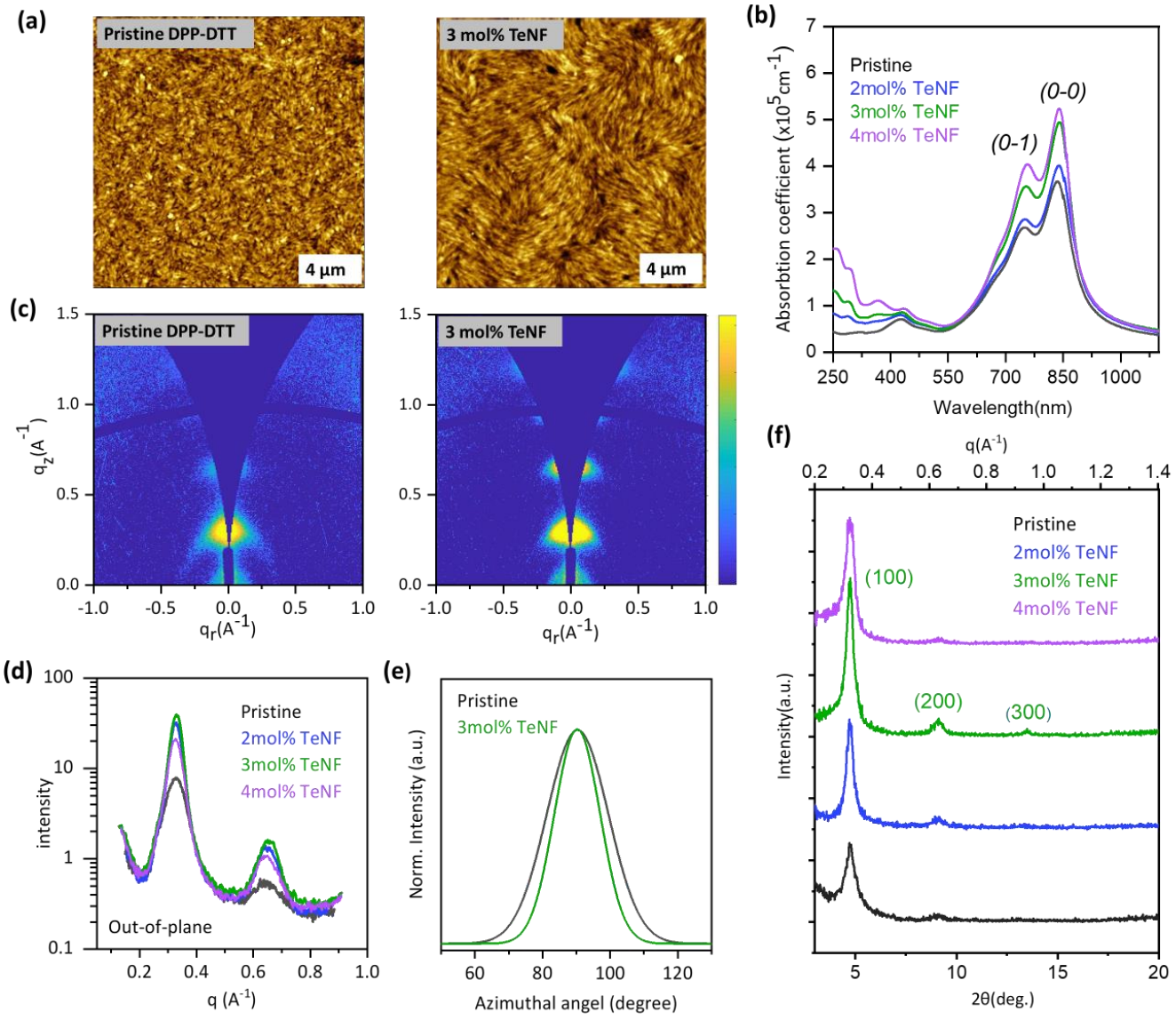

Figure 5.11: (a) AFM images of pristine and doped DPP-DTT films. (b) Absorption spectra of TeNF-doped DPP-DTT (20 nm films) (c) 2D-GIWAXS images of pristine and TeNF doped DPP-DTT films. (d) Out-of-plane GIWAXS diffraction profiles extracted along q_z direction. (e) Normalized Azimuthal angel profile of pristine and doped polymer extracted from GIWAXS. (f) Out-of-plane X-ray diffraction profiles of doped film different concentration.

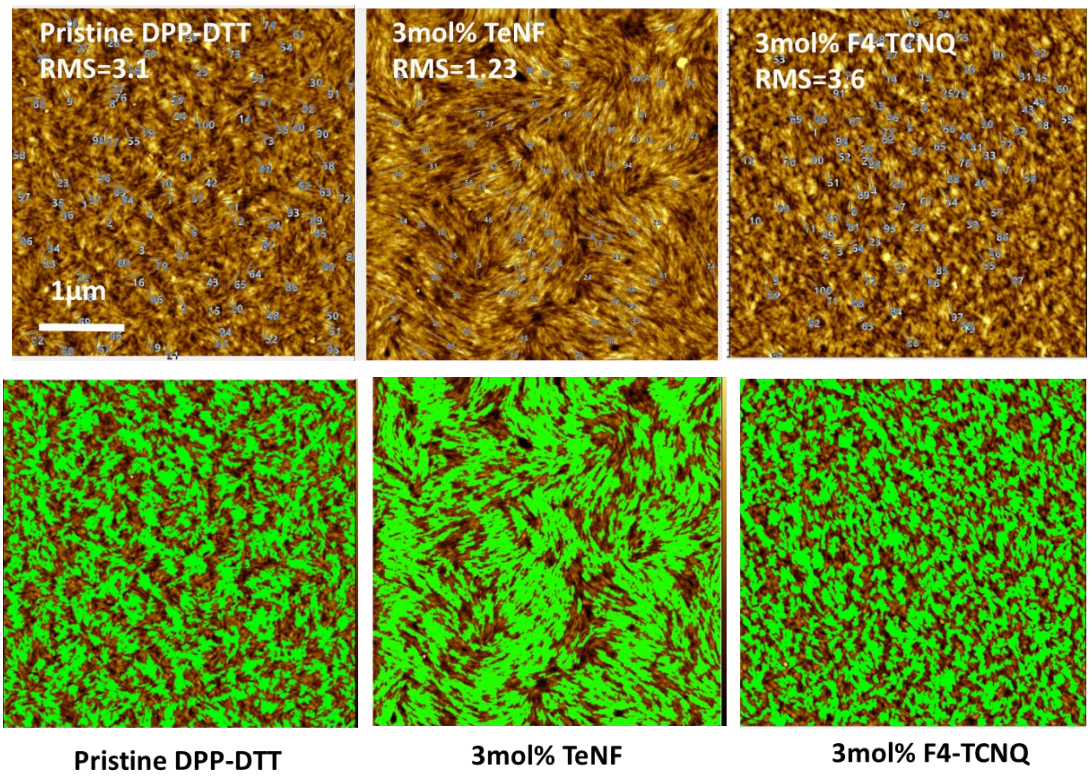

Figure 5.12: Statistical analysis of pristine and doped DPP-DTT films fiber length. Manual grain scaling (top) and defined mask (bottom).

As discussed earlier, TeNF doping enhances the NIR absorption of DPP-DTT. The absorption coefficient (α) of the longest-wavelength (π–π^*) transition raises progressively with increasing TeNF concentration (Figure 5.11b). A higher absorption coefficient is ascribed to the improved order in conjugated polymers.[58, 59] The ratio of the 0–0/0–1 vibronic peaks intensity, another measure of order,[47, 60] also increases from 1.35 to 1.52 at 3 mol% TeNF, which coincides with the best device performance (Table 4.6). XRD measurements for pristine (annealed) DPP-DTT film showed a first order lamellar stacking peak (100) at $2\theta = 4.65°$ ($d_{100} = 1.93$ nm), along with a very weak (200) peak at $2\theta = 9.2°$ (Figure 5.11f). Upon TeNF doping, the intensity of out-of-plane diffraction peaks progressively increases up to 3 mol% but then decreases at higher (4 mol%) doping. At 3 mol% (which gives the best device performance), the (100) peak intensity is ~3.5 times higher than that in the pristine film with identical thickness and experimental parameters. Also, (300) diffraction peak at $2\theta = 13.5°$ became discernable.

Figure 5.13: AFM images of pristine and doped DPP-DTT films with TeNF dopant (concentration of 1 to 4 mol%), and with F4TCNQ, DNF, and DCN-TeNF dopants with concentration of 1 to 3 mol%, and corresponding RMS values.

The out-of-plane lamellar coherence length, calculated for (100) using Debye-Scherrer equation, significantly increases from 6.5 nm for pristine DPP-DTT to 12.1 nm for 3 mol% TeNF-doped film. The increased lamellar diffraction intensity and coherence length suggest increased crystallinity and/or better out-of-plane order of DPP-DTT lamellae in the doped films. The ordering effect is maximized at 3 mol% of TeNF, and it start decreasing at higher doping lead, in agreement with the observed drop of charge mobility (Figure 5.8).

The microstructure of films was further investigated using 2-D grazing incidence wide-angle X-ray scattering (2D-GIWAXS) (Figure 5.12c, d). The pristine film shows (100) peak at q_z = 0.327 A^{-1} (d_{100} = 1.92 nm) and a weak second order (200) peak at q_z = 0.645 A^{-1} corresponding to the lamellar packing of the alkylated polymer chains. Upon doping with TeNF, both peaks progressively increase in intensity and a third-order peak (q_z = 0.982 A^{-1}) emerges. The azimuthal full width half maximum (FWHM) of the (100) Bragg sheet decreases from 21.5^o to 15.9^o upon TeNF doping, indicating a somewhat increased in-plane orientation of the polymer lamellae. The highest intensity of the scattering peaks and the lowest FWHM is observed at 3mol% doping level, in agreement with the XRD data discussed above. The average grain lengths are calculated by Gwyddion software using two methods. The first method specifies a threshold height value to define grain masks. A statistical analysis is then applied on marked grains to calculate the average fiber lengths. The second method is manual grain scaling and calculating the average length over 100 grains in each film. The obtained size from both methods is comparable and shows an increase from ~140 nm in pristine film to ~480 nm in 3 mol% doped film. The average length of grains in F4-TCNQ doped film is very close to pristine film (~150 nm).

5.2.4 Effect of TeNF doping on charge carrier traps

The negative V_{TH} values in *p*-type OFETs are typically associated with in-gap deep trap states present in organic semiconductors, that become filled (with holes) at $V_{GS} = V_{TH}$.[39] With increasing TeNF concentration, the threshold voltage shifts in the positive direction, approaching 0 V at high TeNF concentration (Table 5.5). This decrease of V_{TH} upon doping can be attributed to the passivation of the deep trap states (strong electron donors) by interaction with TeNF acceptor. The increasing dopant concentration is also accompanied by an almost linear increase of the EPR signal (Figure 5.14a), attributed to electron transfer from the trap states to TeNF. However, as noted before, the resulting spin density in the film is only ~1% of the dopant concentration, which is not

surprising considering that the polymer HOMO is ~1 eV below the LUMO of TeNF (Figure 5.2c). The spin density increases almost linearly with the concentration of TeNF but remains low (~2.4´10^{17} cm^{-3} at 3mol% doping, Figure 5.14b).

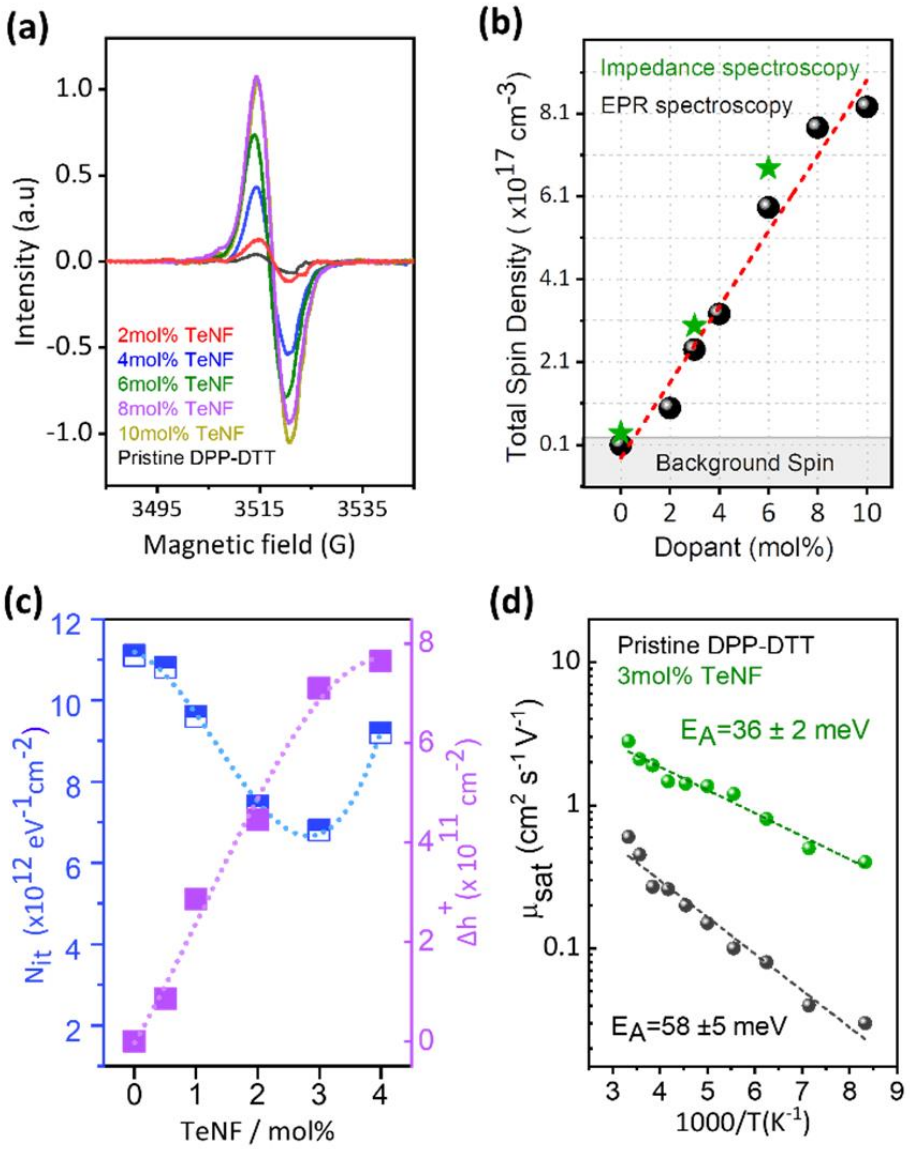

Figure 5.14: (a) EPR signal of TeNF doped DPP-DTT films and (b) induced spin densities (black circles) measured by EPR and hole carrier density (green stars) measured by impendence spectroscopy. (c) Excess of induced holes and interfacial trap density at varied dopant concentrations. (d) Temperature dependence of μsat and calculated activation energies.

The interfacial trap density (N_{it}) estimated from the subthreshold swing decreases with an increasing TeNF concentration (Equation 5.1), reaching the minimum at 3 mol% and starts raising again at higher doping (Figure 4.15c).[37]

$$N_{it} = \frac{C_i}{q}\left(\frac{qSS}{k_B T ln(10)} - 1\right) \quad 5.1$$

This trend coincides with the evolution of hole mobility (Table 5.5) and can be attributed to improved crystallinity/microstructural order upon TeNF doping up to 3 mol% (Figure 5.11). However, a higher concentration of the dopant leads to disorder and N_{it} rises again. We used the V_{TH} shift to estimate the *areal* density of the excess of holes (Δh+) induced in the doped OFET channel calculated from the shift in threshold voltage according to the equation 5.2: [78,79]

$$\Delta h^+ = C_i e^{-1}\left|Vth_{(doped)} - Vth_{(pristine)}\right| \quad 5.2$$

The Δh+ indicates the extra accumulated holes at the semiconductor-dielectric interface upon doping.[37, 68] The Δh+ progressively increases with dopant loading reaching ~7.2×10^{11} cm^{-2} at 3 mol% of TeNF. Interestingly, if one takes the AFM-measured 20 nm film thickness as a channel depth, the resulting areal spin density (~4.8×10^{11} cm^{-2}) measured by EPR and areal hole density (~6.1×10^{11} cm^{-2}) measured by the impedance spectroscopy are similar to the mentioned above Δh+ value. These doping-induced excess holes also explain the observed moderate (up to an order of magnitude) increase of the OFET off-current (I_{OFF}, Table 5.5).

We have also applied impedance spectroscopy on metal–insulator–semiconductor (MIS) devices (Figure 5.15) to measure corresponding holes density in the pristine and doped polymer films[36, 67]

Capacitance of MIS devices were calculated according to the equation 5.3 and from the real and imaginary parts of measured impedance at different DC bias. The total capacitance is corrected by the effect of the series resistance Rs and parasitic inductance of electrical cables Li and known as corrected capacitance (Ccor) and is shown in Figure 4.16. [80]

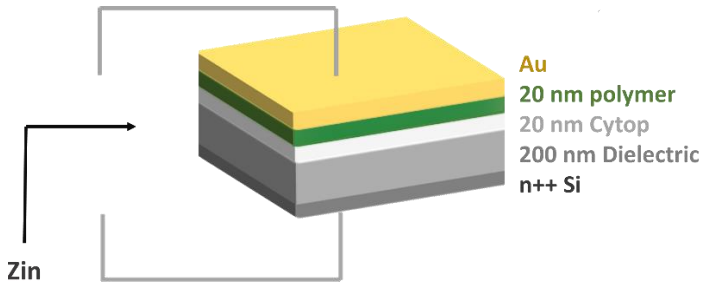

Figure 5.15: The scheme of MIS structure used in impedance spectroscopy measurements.

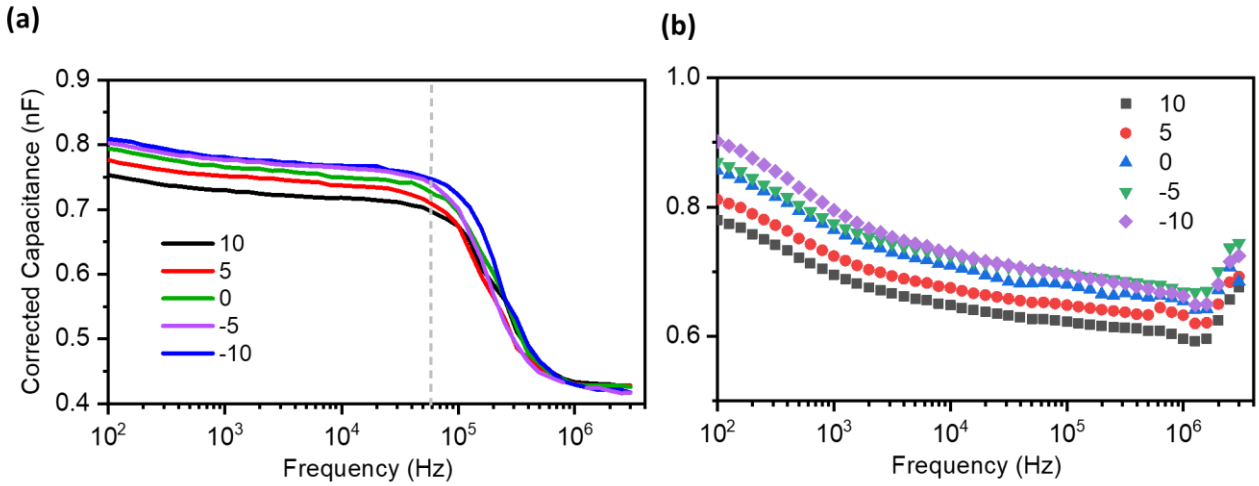

Figure 5.16: Impedance spectroscopy of pristine and doped DPP-DTT polymer in a metal-insulator-semiconductor (MIS) device architecture. Corrected capacitance of **(a)** 6mol% TeNF-doped and **(b)** pristine DPP-DTT measured as a function of AC frequency with various DC biases.

$$C_{cor} = -\frac{1}{\omega}\left[\frac{Z'' - \omega L_i}{(Z' - R_s)^2 + (Z'' - \omega L_i)^2}\right] \qquad 5.3$$

The capacitance-voltage (C-V) characteristic, determined at the medium frequency of 50 kHz (Figure 5.17, left) and the concentration of free hole carriers is calculated from the slope of the Mott-Schottky plot (Figure 5.17, right) according to following equation: [80]

$$\rho = \frac{2}{q\varepsilon\varepsilon_0 \frac{d(A/C)^2}{dV}} \quad 5.4$$

where ρ is the density of free carrier, A = 0.06 cm^2 is the area of the MIS structure, ε_0 is the dielectric permittivity of vacuum and ε is the effective dielectric constant of total capacitor determined from the geometric capacitance C_g at saturated high frequency (3 MHz). The total capacitance C_{cor} at high frequency is equal to the geometric capacitance of the stack of the insulator and polymer layer:

$$C_{cor} \text{ (3 MHz)} = C_g = C_p' C_i / (C_p + C_i). \quad 5.5$$

where the C_i is insulator's capacitance and C_p is the polymer's capacitance. The holes densities calculated from Mott-Shockley plots are in good agreement with the spin density measured by EPR (Figure 5.14b).

Variable temperature OFET measurements in 120-300 K range reveals a thermally activated charge transport behavior for both the pristine and doped devices (Figure 5.14d) as most commonly observed for polymer semiconductors.[33, 69] However, the activation energy E_A, estimated from Arrhenius equation: $\ln(\mu) = -E_A/k_BT$, is almost twice lower for TeNF-doped ($E_A = 36 \pm 2$ meV) as compared to pristine ($E_A = 58 \pm 5$ meV) DPP-DTT devices. The lower E_A values once again suggest reduced shallow traps/energetic disorder which is responsible for improved charge mobility in doped DPP-DTT devices.[70]

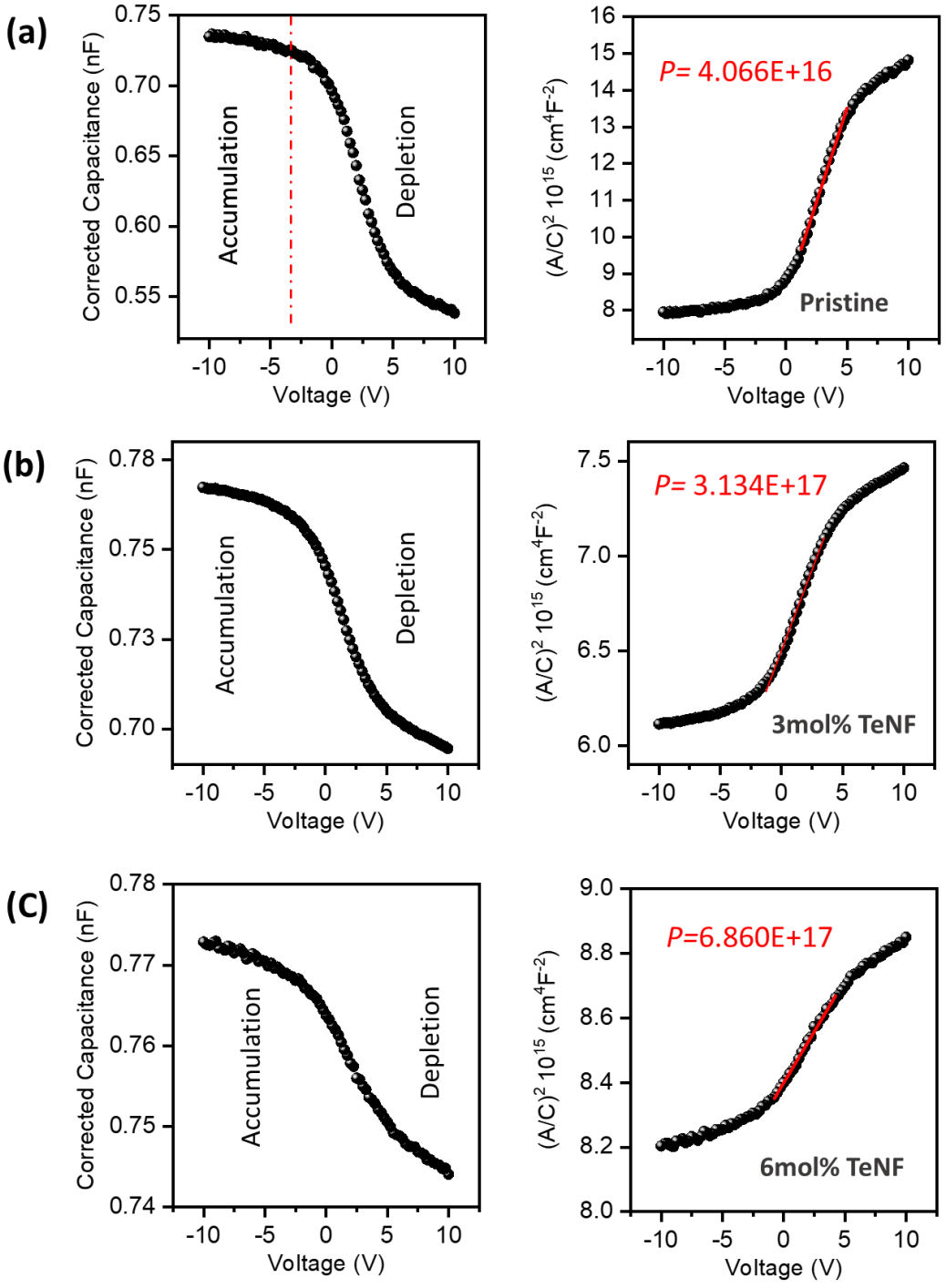

Figure 5.17: Corrected capacitance (left) and Mott-Schottky plots (right) versus DC bias measured at frequency of 50 kHz for (a) pristine, (b) 3 mol% and (c) 6 mol% TeNF doped DPP-DTT, used to determine the concentration of free charge carriers, *p*.

Figure 5.18 gives a schematic picture of the possible mechanism of action of TeNF doping in improving the charge transport properties of DPP-DTT OFETs. The pristine DPP-DTT film is a disordered semicrystalline material that contains both chemical (*eg*, ADDA mislink in the chain)[71] and structural (*eg*, amorphous regions, twisted chains) defects, which can act as deep and shallow traps of the charge carriers.

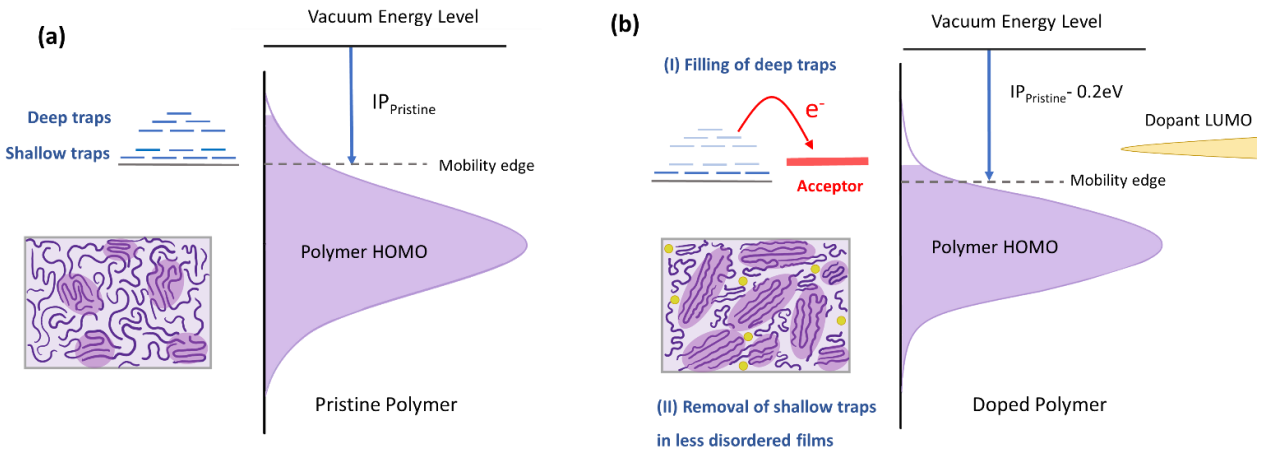

Figure 5.18: Proposed mechanism of TeNF-induced improvement of mobility in DPP-DTT OFETs. The schematic depicts density of states, shallow and deep trap states, and microstructure of pristine (a) and doped (b) DPP-DTT films. The LUMO of TeNF lies above the HOMO of DPP-DTT (mobility edge) but below deep-trap states. Doping deactivates (by electron transfer to TeNF) and reduces the polymer ionization potential (IP) by 0.2 eV (I). Also, the improved structural order/crystallinity mitigates the shallow traps close to the mobility edge (II).

The LUMO of TeNF dopant is above the valence band of the polymer, therefore doping does not lead to a significant amount of free charge carriers, as concluded from the moderate increase of the off current and low spin concentration (~0.01 per TeNF molecule). However, the TeNF LUMO appears to lie below and interact with some of the in-gap (deep trap) states of DPP-DTT. This interaction is confirmed by photoelectron yield spectroscopy in air (PESA) which reveals a 0.2 eV deeper IP value in TeNF doped DPP-DTT from $IP_{pristine}$=5.1 eV to IP_{doped} = 5.3 eV (Figure 5.19).[72] It is also manifested in the increased excess hole density $\Delta h+$ measured from the shift of the V_{TH} (Table 5.5).

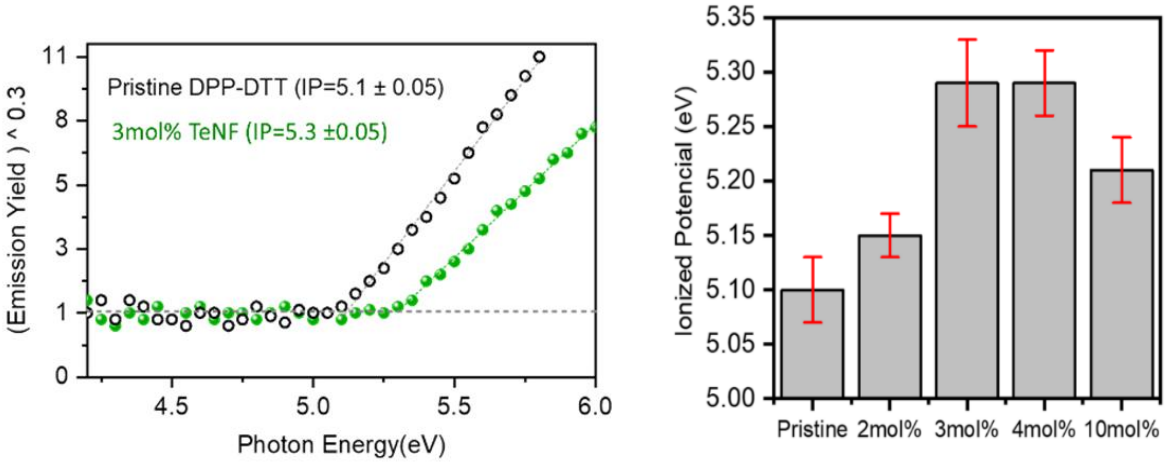

Figure 5.19: (a) Photoelectron yield spectroscopy in air (PESA) of doped and pristine films. (b) Photoelectron yield spectroscopy in air (PESA). All measurements carried out on 2´2 cm^2 thin films of doped (3 mol%) and pristine polymer (left) prepared from 5 g L^{-1} solution on glass slides. The PESA derived ionization potential of doped polymer with different TeNF concentration (right). Each IP value was obtained as an average of 5 different measurements.

Furthermore, the improved crystallinity (established by microstructural and spectroscopic analysis) and the associated reduction of energetic disorder (evident from the lower activation energy of transport and lower interfacial trap density measured from subthreshold swing) lead to suppression of shallow traps (narrower density of states dispersion) in TeNF doped film.[73] Accordingly, the improved charge transport observed in TeNF doped DPP-DTT OFETs is a synergistic effect of deep traps filling (dopant-host interaction) and shallow trap removal (modified microstructure).

5.3 Conclusion

In summary, we introduce nitrofluorenes (NFs) as a new family of tunable *p*-dopants for high-performance of air-stable polymer OFETs. For strong electron acceptors (LUMO ≤ –4.4 eV), doping of DPP-DTT is manifested in increased EPR signal and low-intensity absorption shoulder >900 nm. The 3 mol% doped TeNF films yielded maximum mobility of ~8 $cm^2V^{-1}s^{-1}$ and 6-fold enhancement in effective mobility up to 6.4 cm^2 V^{-1} S^{-1}) in comparison to pristine DPP-DTT OFETs. The detailed analysis of OFET electrical characteristics revealed significant improvements in all device figures of merit: threshold voltage, contact resistance, and interfacial trap state density. The expected increase of the OFF current in the doped device is relatively small (from ~3 to ~60 nA, at 3 mol% TeNF) which may be due to significant (~1 eV) barrier between the polymer

HOMO and dopant LUMO. It is also partially compensated by larger ON current, so the on-off ratio remains relatively high (>2×10^{-4}). Variable temperature mobility measurements revealed lower activation energies in doped films, suggesting reduced energetic disorder. AFM and 2D-GIWAXS measurements showed improved fibrillar interconnections, increased polymer fiber size as well as enhanced coherence lengths, thus corroborating the device results. UV-Vis-NIR spectroscopy revealed an up to 30% increase in the absorption coefficient of TeNF doped polymer films, especially for the 0-0 vibronic transition, in line with the enhanced order. We conclude that significantly improved device performance of doped DPP-DTT films is a joint effect of filling the deep traps and improved film morphology. This work highlights the potential for nitroaromatic acceptors as effective and chemically stable *p*-dopants in soft electronics.

5.4 References

1. Sirringhaus, H. 25th anniversary article: organic field-effect transistors: the path beyond amorphous silicon. *Adv. Mater.* **2014**, *26*, 1319-1335.

2. Kumar, B.; Kaushik, B. K.; Negi, Y. S. Organic Thin Film Transistors: Structures, Models, Materials, Fabrication, and Applications: A Review. *Polym. Rev.* **2014**, *54*, 33-111.

3. Klauk, H. Organic thin-film transistors. *Chem. Soc. Rev.* **2010**, 39, 2643-2666.

4. Li, J.; Zhao, Y.; Tan, H. S.; Guo, Y.; Di, C. A.; Yu, G.; Liu, Y.; Lin, M.; Lim, S. H.; Zhou, Y.; Su, H.; Ong, B. S. A stable solution-processed polymer semiconductor with record high-mobility for printed transistors. *Sci. Rep.* **2012**, *2*, 754.

5. Kang, I.; Yun, H. J.; Chung, D. S.; Kwon, S. K.; Kim, Y. H. Record high hole mobility in polymer semiconductors via side-chain engineering. *J. Am. Chem. Soc.* **2013**, *135*, 14896-14899.

6. Phan, H.; Ford, M. J.; Lill, A. T.; Wang, M.; Bazan, G. C.; Nguyen, T.-Q. Electrical Double-Slope Nonideality in Organic Field-Effect Transistors. *Adv. Funct. Mater*. **2018,** *28*, 1707221.

7. Uemura, T.; Rolin, C.; Ke, T. H.; Fesenko, P.; Genoe, J.; Heremans, P.; Takeya, J. On the Extraction of Charge Carrier Mobility in High-Mobility Organic Transistors. *Adv. Mater*. **2016**, *28*, 151-155.

8. Lamport, Z. A.; Barth, K. J.; Lee, H.; Gann, E.; Engmann, S.; Chen, H.; Guthold, M.; McCulloch, I.; Anthony, J. E.; Richter, L. J.; DeLongchamp, D. M.; Jurchescu, O. D. A simple and robust approach to reducing contact resistance in organic transistors. *Nat Commun*. **2018,** *9*, 5130.

9. Kim, M.; Ryu, S. U.; Park, S. A.; Choi, K.; Kim, T.; Chung, D.; Park. T. Donor−Acceptor-Conjugated Polymer for High-Performance Organic Field-Effect Transistors: A Progress Report. *Adv. Funct. Mater*. **2019**, *30*, 1904545.

10. Rivnay, J.; Noriega, R.; Northrup, J. E.; Kline, R. J.; Toney, M. F.; Salleo, A. Structural origin of gap states in semicrystalline polymers and the implications for charge transport. *Phys. Rev. B*. **2011**, *83*, 121306.

11. Haneef, H. F.; Zeidell, A. M.; Jurchescu, O. D. Charge carrier traps in organic semiconductors: a review on the underlying physics and impact on electronic devices. *J. Mater. Chem. C*. **2020**, *8*, 759-787.

12. Coropceanu, V.; Cornil, J.; Filho, D. A.; Olivier, Y.; Silbey, R.; Cornil, J.-L. Charge Transport in Organic Semiconductors. *Chem. Rev.* **2007**, *107*, 926−952.

13. Pei, M.; Guo, J.; Zhang, B.; Jiang, S.; Hao, Z.; Xu, X.; Li, Y. Semiconductor/dielectric interface in organic field-effect transistors: charge transport, interfacial effects, and perspectives with 2D molecular crystals. *Adv. Phys. X*. **2020**, 5, 1747945.

14. Park, Y. D.; Lim, J. A.; Lee, H. S.; Cho, K. Interface engineering in organic transistors. *Mater. Today.* **2007**, *10*, 46-54.

15. Nikolka, M.; Nasrallah, I.; Rose, B.; Ravva, M. K.; Broch, K.; Sadhana, A.; Harkin, D.; Charmet, J.; Hurhangee, M.; Brown, A.; Illig, S.; Too, P.; Jongman, J.; McCulloch, I.; Bredas, J. L.; Sirringhaus, H. High operational and environmental stability of high-mobility conjugated polymer field-effect transistors through the use of molecular additives. *Nat. Mater.* **2017**, *16*, 356-362.

16. Zhang, X.; Bronstein, H.; Kronemeijer, A. J.; Smith, J.; Kim, Y.; Kline, R. J.; Richter, L. J.; Anthopoulos, T. D.; Sirringhaus, H.; Song, K.; Heeney, M.; Zhang, W.; McCulloch, I.; DeLongchamp, D. M. Molecular origin of high field-effect mobility in an indacenodithiophene-benzothiadiazole copolymer. *Nat. Commun.* **2013**, *4*, 2238.

17. Zhao, Z.; Yin, Z.; Chen, H.; Zheng, L.; Zhu, C.; Zhang, L.; Tan, S.; Wang, H.; Guo, Y.; Tang, Q.; Liu, Y. High-Performance, Air-Stable Field-Effect Transistors Based on Heteroatom-Substituted Naphthalenediimide-Benzothiadiazole Copolymers Exhibiting Ultrahigh Electron Mobility up to 8.5 cm V (-1) s (-1). *Adv. Mater.* **2017**, *29*, 1602410.

18. Li, Y.; Sonar, P.; Murphya, L.; Honga, W. High mobility diketopyrrolopyrrole (DPP)-based organic semiconductor materials for organic thin film transistors and photovoltaics. *Energy Environ. Sci.* **2013**, *6*, 1684-1710.

19. Zaumseil, J.; Sirringhaus, H. Electron and Ambipolar Transport in Organic Field-Effect Transistors. *Chem. Rev.* **2007**, *107*, 1296−1323.

20. Paterson, A. F.; Mottram, A. D.; Faber, H.; Niazi, M. R.; Fei, Z.; Heeney, M.; Anthopoulos, T. D. Impact of the Gate Dielectric on Contact Resistance in High-Mobility Organic Transistors. *Adv. Electron. Mater.* **2019**, *5*, 1800723.

21. Shi, Y.; Zheng, Y.; Wang, J.; Zhao, R.; Wang, T.; Zhao, C.; Chang, K. C.; Meng, H.; Wang, X. Hysteresis-Free, High-Performance Polymer-Dielectric Organic Field-Effect. Transistors Enabled by Supercritical Fluid. *Research.* **2020**, 6587102.

22. Tseng, H. R.; Phan, H.; Luo, C.; Wang, M.; Perez, L. A.; Patel, S. N.; Ying, L.; Kramer, E. J.; Nguyen, T. Q.; Bazan, G. C.; Heeger, A. J. High-mobility field-effect transistors fabricated with macroscopic aligned semiconducting polymers. *Adv. Mater.* **2014**, *26*, 2993-2998.

23. Luo, C.; Kyaw, A. K.; Perez, L. A.; Patel, S.; Wang, M.; Grimm, B.; Bazan, G. C.; Kramer, E. J.; Heeger, A. J. General strategy for self-assembly of highly oriented nanocrystalline semiconducting polymers with high mobility. *Nano Lett.* **2014**, *14*, 2764-2771.

24. Chen, M. S.; Lee, O. P.; Niskala, J. R.; Yiu, A. T.; Tassone, C. J.; Schmidt, K.; Beaujuge, P. M.; Onishi, S. S.; Toney, M. F.; Zettl, A.; Frechet, J. M. Enhanced solid-state order and field-effect hole mobility through control of nanoscale polymer aggregation. *J. Am. Chem. Soc.* **2013**, *135*, 19229-19236.

25. Paterson, A. F.; Treat, N. D.; Zhang, W.; Fei, Z.; Wyatt-Moon, G.; Faber, H.; Vourlias, G.; Patsalas, P. A.; Solomeshch, O.; Tessler, N.; Heeney, M.; Anthopoulos, T. D. Small Molecule/Polymer Blend Organic Transistors with Hole Mobility Exceeding 13 cm (2) V (-1) s (-1). *Adv. Mater.* **2016**, *28*, 7791-7798.

26. Akamuta, H.; Inokuchi, H.; Matsunaga, Y. Electrical Conductivity of the Perylene–Bromine Complex. *Nature*. **1954**, *173*, 168-169.

27. Chiang, C. K.; Fincher, C. R.; Park, Y. W.; Heeger, A. J.; Shirakawa, H.; Louis, E. J.; Gau, S. C.; MacDiarmid, A. G. Electrical Conductivity in Doped Polyacetylene. *Phys. Rev. Lett.* **1977**, *39*, 1098-1101.

28. Yoon, S. E.; Kang, Y.; Noh, S. Y.; Park, J.; Lee, S. Y.; Park, J.; Lee, D. W.; Whang, D. R.; Kim, T.; Kim, G. H.; Seo, H.; Kim, B. G.; Kim, J. H. High Efficiency Doping of Conjugated Polymer for Investigation of Intercorrelation of Thermoelectric Effects with Electrical and Morphological Properties. *ACS Appl. Mater. Interfaces*, **2020**, *12*, 1151-1158.

29. Steim, R.; Kogler, F. R.; Brabec, C. J. Interface materials for organic solar cells. J. Mater. Chem. C. 2010, 20, 2499–2512.

30. Xu, Y.; Sun, H.; Liu, A.; Zhu, H. H.; Li, W.; Lin, Y. F.; Noh, Y. Y. Doping: A Key Enabler for Organic Transistors. *Adv. Mater.* **2018**, *30*, 1801830.

31. Jacobs, I. E.; Moule, A. J. Controlling Molecular Doping in Organic Semiconductors. *Adv. Mater.* **2017**, *29*, 1703063.

32. Xu, Y.; Sun, H.; Shin, E. Y.; Lin, Y. F.; Li, W.; Noh, Y. Y. Planar-Processed Polymer Transistors. *Adv. Mater.* **2016**, *28*, 8531-8537.

33. Lussem, B.; Keum, C. M.; Kasemann, D.; Naab, B.; Bao, Z.; Leo, K. Doped Organic Transistors. *Chem. Rev.* **2016**, *116*, 13714-13751.

34. Kim, Y.; Chung, S.; Cho, K.; Harkin, D.; Hwang, W. T.; Yoo, D.; Kim, J. K.; Lee, W.; Song, Y.; Ahn, H.; Hong, Y.; Sirringhaus, H.; Kang, K.; Lee, T. Enhanced Charge Injection Properties of Organic Field-Effect Transistor by Molecular Implantation Doping. *Adv. Mater.* **2019**, *31*, 1806697.

35. Baeg, K. J.; Bae, G. T.; Noh, Y. Y. Efficient charge injection in p-type polymer field-effect transistors with low-cost molybdenum electrodes through V_2O_5 interlayer. *ACS Appl. Mater. Interfaces*. **2013**, *5*, 5804-5810.

36. Pingel, P.; Arvind, M.; Kölln, L.; Steyrleuthner, R.; Kraffert, F.; Behrends, J.; Janietz, S.; Neher, D. p-Type Doping of Poly(3-hexylthiophene) with the Strong Lewis Acid Tris (pentafluorophenyl)borane. *Adv. Electron. Mater.* **2016**, *2*, 1600204.

37. Han, Y.; Barnes, G.; Lin, Y.-H.; Martin, J.; Al Qaradawi, S. Y.; Anthopoulos, T. D.; Heeney, M. Doping of Large Ionization Potential Indenopyrazine Polymers via Lewis Acid Complexation with Tris(pentafluorophenyl)borane: A Simple Method for Improving the Performance of Organic Thin-Film Transistors. *Chem. Mater.* **2016**, *28*, 8016-8024.

38. Paterson, A. F.; Tsetseris, L.; Li, R.; Basu, A.; Faber, H.; Emwas, A. H.; Panidi, J.; Fei, Z.; Niazi, M. R.; Anjum, D. H.; Heeney, M.; Anthopoulos, T. D. Addition of the Lewis Acid Zn(C6 F5)2 Enables Organic Transistors with a Maximum Hole Mobility in Excess of 20 cm(2) V(-1) s(-1). *Adv Mater.* **2019**, *31*, 1900871.

39. Paterson, A. F.; Lin, Y.-H.; Mottram, A. D.; Fei, Z.; Niazi, M. R.; Kirmani, A. R.; Amassian, A.; Solomeshch, O.; Tessler, N.; Heeney, M.; Anthopoulos, T. D. The Impact of Molecular p-Doping on Charge Transport in High-Mobility Small-Molecule/Polymer Blend Organic Transistors. *Adv. Electron. Mater.* **2018**, *4*, 1700464.

40. Ma, L.; Lee, W. H.; Park, Y. D.; Kim, J. S.; Lee, H. S.; Cho, K. High performance polythiophene thin-film transistors doped with very small amounts of an electron acceptor. *Appl. Phys. Lett.* **2008**, *92*, 063310.

41. Long, D. X.; Choi, E. Y.; Noh, Y. Y. Manganese Oxide Nanoparticle as a New p-Type Dopant for High-Performance Polymer Field-Effect Transistors. *ACS Appl. Mater. Interfaces***. 2017**, *9*, 24763-24770.

42. Luo, H.; Yu, C.; Liu, Z.; Zhang, G.; Geng, H.; Yi, Y.; Broch, K.; Hu, Y.; Sadhanala, A.; Jiang, L.; Qi, P.; Cai, Z.; Sirringhaus, H.; Zhang, D. Remarkable enhancement of charge carrier mobility of conjugated polymer field-effect transistors upon incorporating an ionic additive. *Sci. Adv.* **2016**, *2*, 1600076.

43. Nikolka, M.; Schweicher, G.; Armitage, J.; Nasrallah, I.; Jellett, C.; Guo, Z.; Hurhangee, M.; Sadhanala, A.; McCulloch, I.; Nielsen, C. B.; Sirringhaus, H. Performance Improvements in Conjugated Polymer Devices by Removal of Water-Induced Traps. *Adv. Mater.* **2018**, *30*, 1801874.

44. Treat, N. D.; Nekuda Malik, J. A.; Reid, O.; Yu, L.; Shuttle, C. G.; Rumbles, G.; Hawker, C. J.; Chabinyc, M. L.; Smith, P.; Stingelin, N. Microstructure formation in molecular and polymer semiconductors assisted by nucleation agents. *Nat. Mater.* **2013**, *12*, 628-633.

45. Liu, C.; Jang, J.; Xu, Y.; Kim, H.-J.; Khim, D.; Park, W.-T.; Noh, Y.-Y.; Kim, J.-J. Effect of Doping Concentration on Microstructure of Conjugated Polymers and Characteristics in N-Type Polymer Field-Effect Transistors. *Adv. Funct. Mater*. **2015**, *25*, 758-767.

46. Tietze, M. L.; Pahner, P.; Schmidt, K.; Leo, K.; Lüssem, B. Doped Organic Semiconductors: Trap-Filling, Impurity Saturation, and Reserve Regimes. *Adv. Funct. Mater*. **2015**, *25*, 2701-2707.

47. Mun, J.; Kang, J.; Zheng, Y.; Luo, S.; Wu, Y.; Gong, H.; Lai, J. C.; Wu, H. C.; Xue, G.; Tok, J. B. H.; Bao, Z. F4-TCNQ as an Additive to Impart Stretchable Semiconductors with High Mobility and Stability. *Adv. Electron. Mater***. 2020**, *6*, 2000251.

48. Huseynova, G.; Xu, Y.; Nketia Yawson, B.; Shin, E.-Y.; Lee, M. J.; Noh, Y.-Y. P-type doped ambipolar polymer transistors by direct charge transfer from a cationic organic dye Pyronin B ferric chloride. *Org. Electron*. **2016**, *39*, 229-235.

49. Pavelyev, V. G.; Parashchuk, O. D.; Krompiec, M.; Orekhova, T. V.; Perepichka, I. F.; van Loosdrecht, P. H. M.; Paraschuk, D. Y.; Pshenichnikov, M. S. Charge Transfer Dynamics in Donor–Acceptor Complexes between a Conjugated Polymer and Fluorene Acceptors. *J. Phys. Chem. C*. **2014**, *118*, 30291-30301.

50. Bruni, P.; Cardillo, B.; Giorgini, E.; TosI, G.; Bocelli, G.; Cantoni, A. Molecular complexes of hydrazones-VIII. Nitrofluorenes and arylhydrazones. *Spectrochimica Acta*. **1990**, *46*, 389-396.

51. Booth, G., Nitro Compounds, Aromatic. In Ullmann's Encyclopedia of Industrial Chemistry, **2000**, *24*, 301-347.

52. Niazi, M. R.; Hamzehpoor, E.; Ghamari, P.; Perepichka, I. F.; Perepichka, D. F. Nitroaromatics as n-type organic semiconductors for field effect transistors. *Chem. Commun*. **2020**, *56*, 6432-6435.

53. Mun, J.; Kang, J.; Zheng, Y.; Luo, S.; Wu, H. C.; Matsuhisa, N.; Xu, J.; Wang, G. N.; Yun, Y.; Xue, G.; Tok, J. B.; Bao, Z. Conjugated Carbon Cyclic Nanorings as Additives for Intrinsically Stretchable Semiconducting Polymers. Adv Mater. **2019**, *31*, 1903912.

54. Li, J.; Zhang, G.; Holm, D. M.; Jacobs, I. E.; Yin, B.; Stroeve, P.; Mascal, M.; Moulé, A. J. Introducing Solubility Control for Improved Organic P-Type Dopants. Chemistry of Materials. **2015**, *27*, 5765-5774.

55. Bredas, J. L.; Street, G. B. Polarons, Bipolarons, and Solitons in Conducting Polymers. *Acc. Chem. Res*. **1985**, *18*, 309-315.

56. Sperlich, A.; Kraus, H.; Deibel, C.; Blok, H.; Schmidt, J.; Dyakonov, V. Reversible and irreversible interactions of poly(3-hexylthiophene) with oxygen studied by spin-sensitive methods. J. Phys. Chem. B. **2011**, *115*, 13513-13518.

57. Kim, J.; Kang, M.; Cho, J.; Yu, S. H.; Chung, D. S. Doping-Dedoping Interplay to Realize Patterned/Stacked All-Polymer Optoelectronic Devices. *ACS Appl. Mater. Interfaces*. **2019**, *11*, 18580-18589.

58. Vezie, M. S.; Few, S.; Meager, I.; Pieridou, G.; Dorling, B.; Ashraf, R. S.; Goni, A. R.; Bronstein, H.; McCulloch, I.; Hayes, S. C.; Campoy-Quiles, M.; Nelson, J. Exploring the origin of high optical absorption in conjugated polymers. *Nat. Mater*. **2016**, *15*, 746-753.

59. Zhokhavets, U.; Erb, T.; Gobsch, G.; Al-Ibrahim, M.; Ambacher, O. Relation between absorption and crystallinity of poly(3-hexylthiophene)/fullerene films for plastic solar cells. *Chem. Phys. Lett.* **2006**, *418*, 347-350.

60. Lei, Y.; Deng, P.; Li, J.; Lin, M.; Zhu, F.; Ng, T. W.; Lee, C. S.; Ong, B. S. Solution-Processed Donor-Acceptor Polymer Nanowire Network Semiconductors for High-Performance Field-Effect Transistors. *Sci. Rep*. **2016**, *6*, 24476.

61. Choi, H. H.; Cho, K.; Frisbie, C. D.; Sirringhaus, H.; Podzorov, V. Critical assessment of charge mobility extraction in FETs. *Nat. Mater*. **2017**, *17*, 2-7.

62. Ford, M. J.; Wang, M.; Phan, H.; Nguyen, T.-Q.; Bazan, G. C. Fullerene Additives Convert Ambipolar Transport to p-Type Transport while Improving the Operational Stability of Organic Thin Film Transistors. *Adv. Funct. Mater*. **2016**, *26*, 4472-4480.

63. Phan, H.; Wang, M.; Bazan, G. C.; Nguyen, T. Q. Electrical Instability Induced by Electron Trapping in Low-Bandgap Donor-Acceptor Polymer Field-Effect Transistors. *Adv. Mater*. **2015**, *27*, 7004-7009.

64. Liu, C.; Li, G.; Di Pietro, R.; Huang, J.; Noh, Y.-Y.; Liu, X.; Minari, T. Device Physics of Contact Issues for the Overestimation and Underestimation of Carrier Mobility in Field-Effect Transistors. *Phys. Rev. Appl*. **2017**, *8*, 034020

65. Bittle, E. G.; Basham, J. I.; Jackson, T. N.; Jurchescu, O. D.; Gundlach, D. J. Mobility overestimation due to gated contacts in organic field-effect transistors. *Nat. Commun.* **2016**, *7*, 10908.

66. Waldrip, M.; Jurchescu, O. D.; Gundlach, D. J.; Bittle, E. G. Contact Resistance in Organic Field-Effect Transistors: Conquering the Barrier. *Adv. Funct. Mater*. **2019,** *30*, 1904576.

67. Yurash, B.; Cao, D. X.; Brus, V. V.; Leifert, D.; Wang, M.; Dixon, A.; Seifrid, M.; Mansour, A. E.; Lungwitz, D.; Liu, T.; Santiago, P. J.; Graham, K. R.; Koch, N.; Bazan, G. C.; Nguyen, T. Q. Towards understanding the doping mechanism of organic semiconductors by Lewis acids. *Nat. Mater*. **2019**, *18*, 1327-1334.

68. Horowitz, G.; Delannoy, P. An analytical model for organic-based thin-film transistors. *J. Appl. Phys*. **1991,** *70*, 469-475.

69. Hunter, S.; Mottram, A. D.; Anthopoulos, T. D. Temperature and composition-dependent density of states in organic small-molecule/polymer blend transistors. *J. Appl. Phys.* **2016**, *120*, 025502.

70. Hu, Y.; Rengert, Z. D.; McDowell, C.; Ford, M. J.; Wang, M.; Karki, A.; Lill, A. T.; Bazan, G. C.; Nguyen, T. Q. Doping Polymer Semiconductors by Organic Salts: Toward High-Performance Solution-Processed Organic Field-Effect Transistors. *ACS. Nano*. **2018**, *12*, 3938-3946.

71. Chen, H.; Wadsworth, A.; Ma, C.; Nanni, A.; Zhang, W.; Nikolka, M.; Luci, A. M. T.; Perdigao, L. M. A.; Thorley, K. J.; Cendra, C.; Larson, B.; Rumbles, G.; Anthopoulos, T. D.; Salleo, A.; Costantini, G.; Sirringhaus, H.; McCulloch, I. The Effect of Ring Expansion in Thienobenzo[b]indacenodithiophene Polymers for Organic Field-Effect Transistors. *J. Am. Chem. Soc.* **2019**, *141*, 18806-18813.

72. Olthof, S.; Mehraeen, S.; Mohapatra, S. K.; Barlow, S.; Coropceanu, V.; Bredas, J. L.; Marder, S. R.; Kahn, A. Ultralow doping in organic semiconductors: evidence of trap filling. *Phys. Rev. Lett.* **2012**, *109*, 176601.

73. Zuo, G.; Li, Z.; Andersson, O.; Abdalla, H.; Wang, E.; Kemerink, M. Molecular Doping and Trap Filling in Organic Semiconductor Host–Guest Systems. *J. Phys. Chem. C*. **2017**, *121*, 7767-7775.

74. Kim, M.; Ryu, S. U.; Park, S. A.; Choi, K.; Kim, T.; Chung, D.; Park. T. Donor−Acceptor-Conjugated Polymer for High-Performance Organic Field-Effect Transistors: A Progress Report. *Adv. Funct. Mater*. **2019**, *30*, 1904545.

75. Luo, H.; Yu, C.; Liu, Z.; Zhang, G.; Geng, H.; Yi, Y.; Broch, K.; Hu, Y.; Sadhanala, A.; Jiang, L.; Qi, P.; Cai, Z.; Sirringhaus, H.; Zhang, D. Remarkable enhancement of charge carrier mobility of conjugated polymer field-effect transistors upon incorporating an ionic additive. *Sci. Adv.* **2016**, *2*, 1600076.

76. Huseynova, G.; Xu, Y.; Nketia Yawson, B.; Shin, E.-Y.; Lee, M. J.; Noh, Y.-Y. P-type doped ambipolar polymer transistors by direct charge transfer from a cationic organic dye Pyronin B ferric chloride. *Org. Electron*. **2016**, *39*, 229-235.

77. Lamport, Z. A.; Barth, K. J.; Lee, H.; Gann, E.; Engmann, S.; Chen, H.; Guthold, M.; McCulloch, I.; Anthony, J. E.; Richter, L. J.; DeLongchamp, D. M.; Jurchescu, O. D. A simple and robust approach to reducing contact resistance in organic transistors. *Nat Commun*. **2018,** *9*, 5130.

78. Choi, H. H.; Cho, K.; Frisbie, C. D.; Sirringhaus, H.; Podzorov, V. Critical assessment of charge mobility extraction in FETs. *Nat. Mater*. **2017**, *17*, 2-7.

79. Han, Y.; Barnes, G.; Lin, Y.-H.; Martin, J.; Al-Hashimi, M.; AlQaradawi, S. Y.; Anthopoulos, T. D.; Heeney, M. Doping of Large Ionization Potential Indenopyrazine Polymers via Lewis Acid Complexation with Tris(pentafluorophenyl)borane: A Simple Method for Improving the Performance of Organic Thin-Film Transistors. *Chem. Mater.* **2016**, *28*, 8016-8024

80. Brus, V. V.; Proctor, C. M.; Ran, N. A.; Nguyen, T.-Q. Capacitance Spectroscopy for Quantifying Recombination Losses in Nonfullerene Small-Molecule Bulk Heterojunction Solar Cells. *Adv. Energy. Mater.* **2016,** 6, 1502250.

Chapter 6: Improved Environmental and Operational Stability of Polymer Field-effect transistors via Doping with Tetranitrofluorenone

OFETs are fundamental components of flexible microelectronics. Despite significant advances in OFET performance in recent years, they have yet been implemented in real-world applications. The bottleneck of OFET commercialization is low carrier mobility, operational and environmental instability, all of which are linked to the charge carrier trapping. In previous chapter, we investigated intentional molecular doping as a potential technique for mitigating trap states and improving OFETs performance. We introduced NF acceptors as a novel family of molecular p-dopants and demonstrated their effectiveness in improving polymer OFET figure of merits. In this chapter we have explored the impact of NF doping on OFET environmental and operational stability challenges. This chapter is based on a manuscript under preparation: Improved environmental and operational stability of polymer field-effect transistors via doping with tetranitrofluorenone. Ghamari, P.; Niazi, M. N.; Perepichka, D. F. *to be submitted*.

6.1 Introduction

Since the early work of 1980s organic field effect transistors (OFET) have sparked a lot of research interest due to their flexibility, biocompatibility and the possibility for low-cost fabrication (e.g., printing).[1,2] Over the years, many advancements in material design, processing methods, and device interface engineering have led to impressive improvements in OFETs figures-of-merit.[3-5] The charge carrier mobilities (μ) in polymer semiconductors can now *reliably* reach ~5–10 cm^2/Vs which is sufficiently high for a number of applications.[6-8] Nonetheless, OFETs have not yet found widespread commercialization, owing in large part to environmental and operational stability challenges.[9-11] Such instabilities manifest in threshold voltage (V_{th}) shift, decrease of μ and on/off current ratio, hysteresis of current-voltage characteristics, and lead to shortening of operational lifetime.[12-15] This behavior is generally associated with interactions of the charge-carriers with either intrinsic trap states (e.g., conformational defects in the polymer) or extrinsic traps such as environmental species (e.g., water and oxygen).[16-19]

The detrimental effect of ambient air on n-type OFET is well-established and is associated with electron trapping by O_2 and H_2O, which is thermodynamically favorable for semiconductors with LUMO >–4 eV.[20,21] However, the impact of air exposure on p-type OFET performance is more

ambiguous. In principle, oxygen can act as a p-dopant (electron acceptor) increasing the charge-carrier density in the p-type semiconductors. However, oxygen doping would only be significant for highly electron-rich conjugated polymers with HOMO level >–5 eV (*e.g.*, P3HT, PEDOT).[22-26] The formation of polymer-oxygen charge transfer complex[27,28] could cause an unwanted rise in the zero-gate current in OFETs but, by itself, should not increase the intrinsic carrier mobility. Nevertheless, several studies have indeed shown mobility improvement of polymer OFET upon exposure to air.[26,28,29] On the other hand, many studies have pinned the degradation of OFETs performance (i.e. decreased mobility, increased off-current, hysteresis, etc.) to water-induced traps created upon exposure to ambient air (during or after the fabrication).[18,30,31] Due to its strong dipole moment, water molecules can interact ('solvate') with the charge carriers (polarons) in the semiconductor, creating energy-stabilized "trap" states.[18,30] Water is omnipresent in ambient environment; it can be strongly physisorbed on many surfaces especially on the commonly used SiO_2 dielectric (where it can also be chemisorbed as silanol species) leading to significant charge trapping, directly in the conducting channel.[32-34] It was also noted that trace amounts of water can be present in nanocavities in polymer films, and even fabrication of OFETs inside the glove-box or exposure to high vacuum does not fully mitigate the effect of water.[31,33,35]

Various strategies have been explored to improve OFETs environmental and operational stability. Although passivation of dielectric surface using hydrophobic self-assembled monolayers (SAMs) was shown to improve OFETs characteristics and ambient stability, they do not eliminate all surface traps. Also, SAMs may suffer from their own chemical and physical instability, creating new surface trap states.[21,33,36] Various polymer dielectrics (either as an ad-layer on SiO_2 or the sole dielectric layer) can significantly improve the OFET stability, reducing trap density at the interface.[37-41] Flame annealing the SiO_2 surface prior to the semiconductor film coating has been recently shown as another effective method in reducing the water-induced traps at the OSC/dielectric interface.[35] It was also reported that some high-boiling solvents and molecular additives can reduce water-induced traps in polymer OFETs by filling the nanocavities in the polymer film, although long-term stability of such devices may be limited by slow release (evaporation) of such additives.[30,31]

Recently, doping of polymer OFETs with electron-acceptor molecules has emerged as an effective approach to mitigating the charge trapping and enhancing the device stability.[34, 42-44] In addition to replacing the water from nanocavity voids in the polymer, the electron-accepting molecules can

passivate the water-induced (and other) traps in p-type semiconductors through charge-transfer interactions. However, widespread application of this strategy is thwarted by several technological challenges such as limited solubility (and phase separation with the polymer semiconductor) and poor chemical stability of the known molecular dopants.[45,46] Recently, we reported the nitrofluorenes as new energy-tunable (by substituents) p-dopants for polymer FETs and shown a significant improvement of the effective charge mobility in polymer OFETs upon doping.[8] In this work, we report that doping of the donor-acceptor polymer semiconductor DPP-DTT with 2,4,5,7-tetranitrofluorenone (TeNF) markedly improves the environmental and operational stability of OFET devices. We explore the mechanism of environmental instability of pristine DPP-DTT OFETs by individually addressing the effects of O_2 and H_2O. We show that short-term air exposure improves the hole mobility by passivating the hole traps, while longer exposure leads to water-induced traps and device degradation. Notably, both effects are suppressed in TeNF-doped OFETs, resulting in reliable, environmentally independent performance and excellent long-term stability of unencapsulated devices in ambient air (<10% degradation after 4 months storage). The doped OFETs also show a greatly diminished hysteresis and reduced (reversible) current drop under bias stress. Our data suggests that the improved performance of doped OFET is due to suppression of the injected minority carrier (electron).

6.2 Results

6.2.1 Environmental stability of pristine DPP-DTT OFET

Top contact bottom gate OFETs were fabricated by spin-coating ~20 nm DPP-DTT films on octadecyltrichlorosilane (ODTS) modified Si/SiO_2 substrates, followed by annealing at 170° C in air for 30 minutes and vacuum deposition of the Au source and drain electrodes (Figure 6.1). The transfer curve (drain-source current (I_{DS}) vs gate voltage (V_{GS})) of the as-prepared DPP-DTT OFETs measured in vacuum (10^{-5} mbar) exhibits a clear ambipolar behavior with hole as a major carrier (hole mobility, μ_h = 0.6 $cm^2V^{-1}s^{-1}$; electron mobility, μ_e = 0.008 $cm^2V^{-1}s^{-1}$). Upon exposure of the OFETs to ambient air (relative humidity, RH ~ 40%) the electron current (measured at positive V_{GS}) is completely suppressed, the threshold voltage (V_{th}) shifts from –10 to –6V and the μ_h increases to 1.2 $cm^2V^{-1}s^{-1}$(Figure 6.1c).

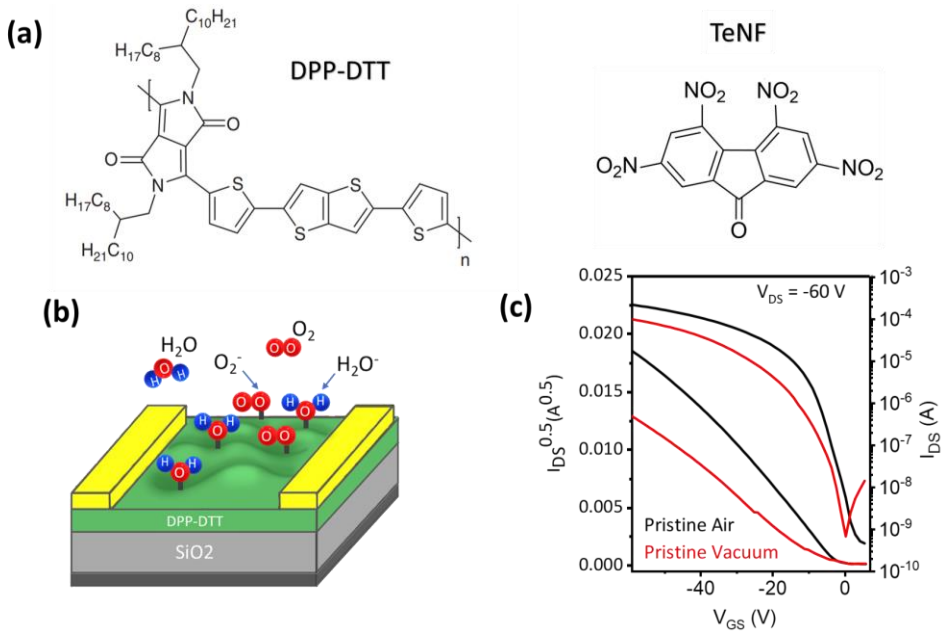

Figure 6.1: Molecular structures of semiconducting polymers (DPP-DTT) and dopant (TeNF) used in this work. (b) Device structure of bottom gate top contact OFET showing interactions with air. (c) Transfer curves of pristine (non-doped) OFETs measured in vacuum and air.

These changes are fully reversible and the initial OFET performance is gradually restored after evacuation. Figure 6.2 shows the gradual changes of OFET I-V curve over 12 hours of air exposure and evacuation respectively.

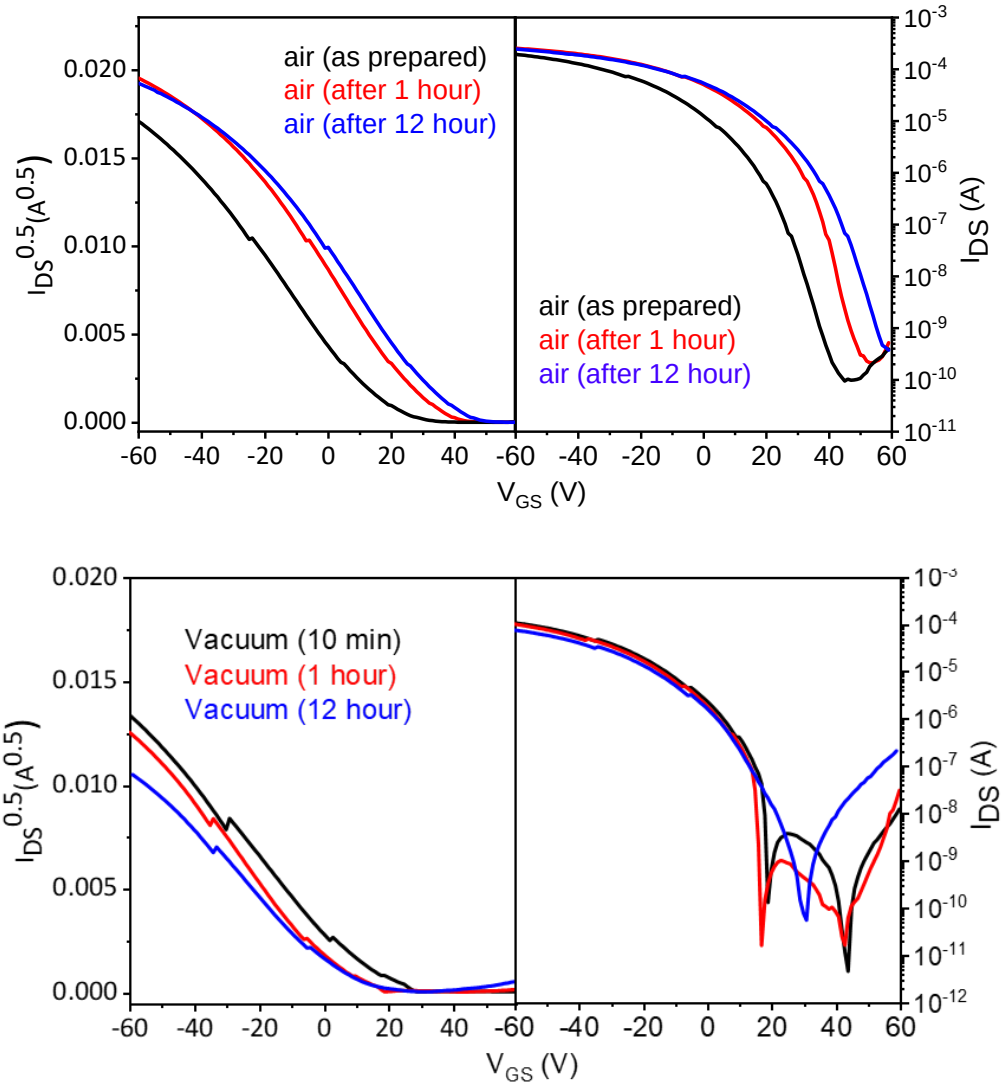

Figure 6.2: The evolution of the DPP-DTT OFET transfer curves in ambient air and under vacuum over time.

The suppression of electron current in n-type OFETs in air is well-established and associated with trapping of negative charge carriers by oxidation with O_2/H_2O redox pair (for OSC with LUMO > –4 eV).[21] However, the origin of the increased hole current is less obvious. In order to understand the origin of the air exposure impact on OFET performance, the role of each environmental species (O_2, H_2O, and H_2O/O_2 mixture) has been investigated by sequentially introducing dry air, pure oxygen, humid nitrogen, and humid air into the vacuum chamber of the probe station (evacuated $\leq 10^{-5}$ mbar before these exposures).

The resulting OFET characteristics are shown in Figure 6.3a. Introducing dry air (O_2: 21% and H_2O: <5 ppm) to the evacuated chamber increased the hole current by ~40% while decreasing the electron current, similar to the effect of the ambient air exposure (relative humidity (RH) = 45%, ~10,000 ppm H_2O). The saturated μ_h is enhanced from 0.6 $cm^2\ V^{-1}\ s^{-1}$ (in vacuum) to 1.3 and 1.7 $cm^2\ V^{-1}\ s^{-1}$ in dry air and pure oxygen, respectively. On the other hand, pure oxygen and dry air have only a minor impact on V_{th} shift (~1 V) while the ambient air (RH = 45%) causes a more significant (~5 V) positive shift of V_{th} (Figure 6.3c).

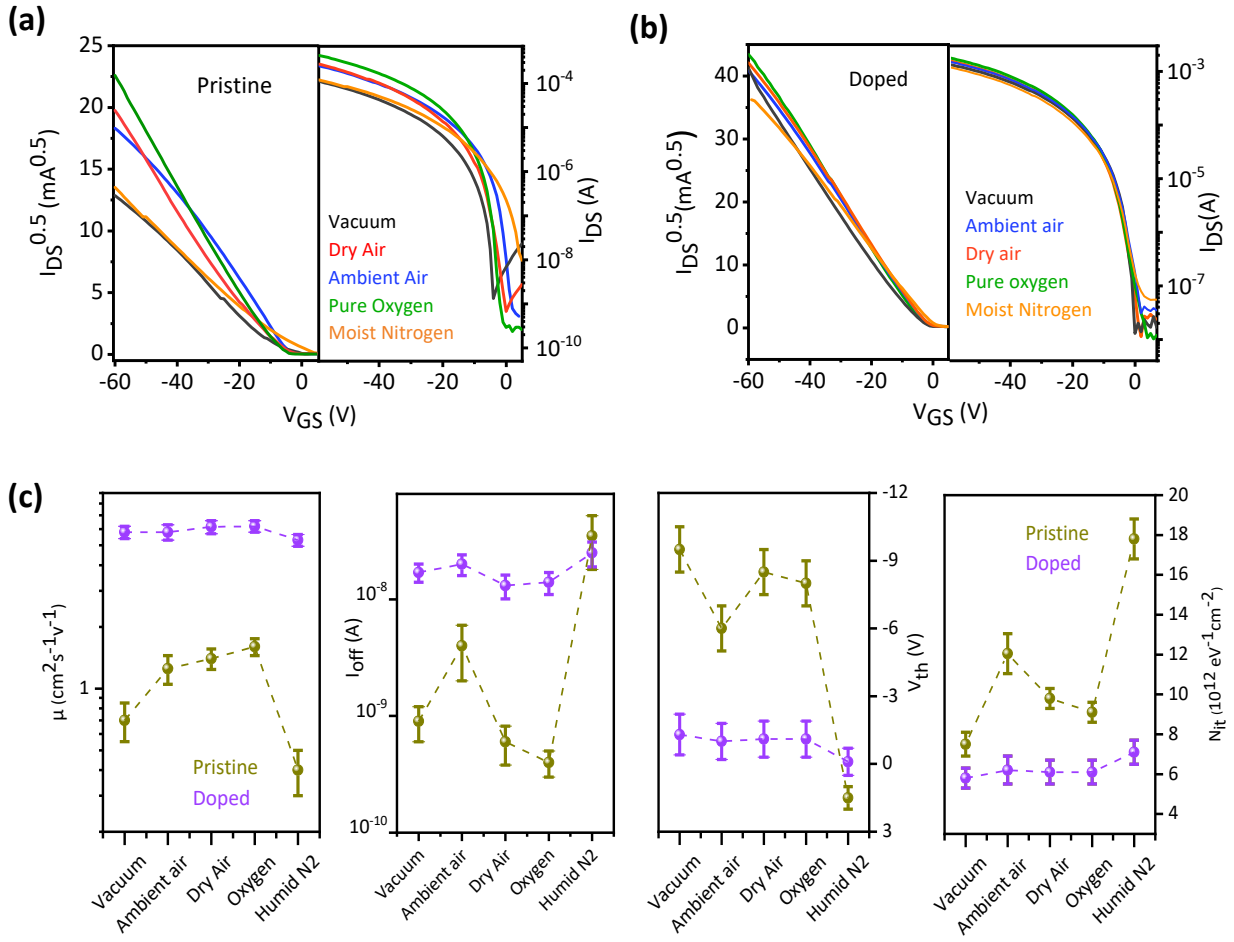

Figure 6.3: (a) and (b) Transfer curves of pristine and doped (3% TeNF) DPP-DTT OFETs (at VDS = -60 V) measured at different environmental conditions (vacuum, ambient air, dry air, pure oxygen, humid nitrogen (RH = 75%). (c) Representative OFETs figures of merits (μ, I_{off}, V_{th}) and interfacial trap density at different environments.

The impact of pure oxygen (O_2: 99% and H_2O: <1 ppm) on the hole current is even more significant. The hole current is increased by 70% and the electron current is completely suppressed within 30 minutes (Figure 6.3a and Figure 6.4).

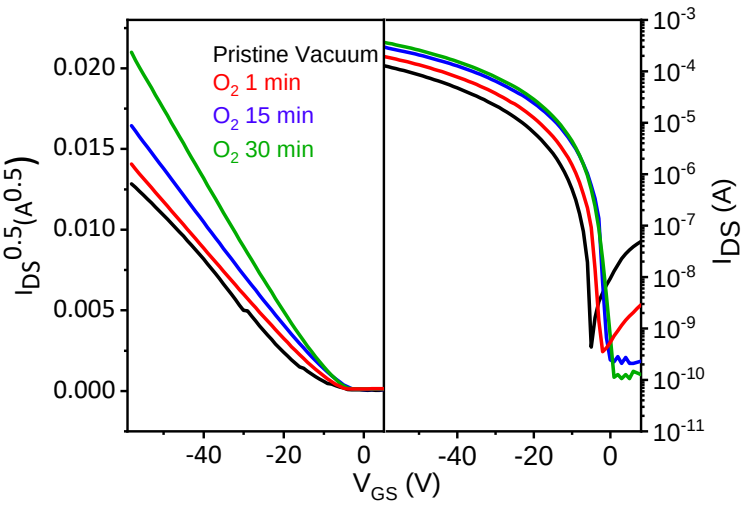

Figure 6.4: The evolution of the DPP-DTT OFET transfer curves over time (operating in oxygen).

To investigate the effect of water, OFETs have been measured in humid N_2 (RH = 75%) revealing a decreased electron current but no effect on the saturated hole current. As shown in Figure 6.3c, the V_{th} undergoes the largest positive shift (ΔV_{th} =12 V vs vacuum) and the off-current increases to 5×10^{-8} A. Even larger V_{th} shift has been observed in water-saturated air with RH = 95% (Figure 6.5), and continuous exposure of OFET to such atmosphere leads to irreversible device damage (drop of the saturated hole current).

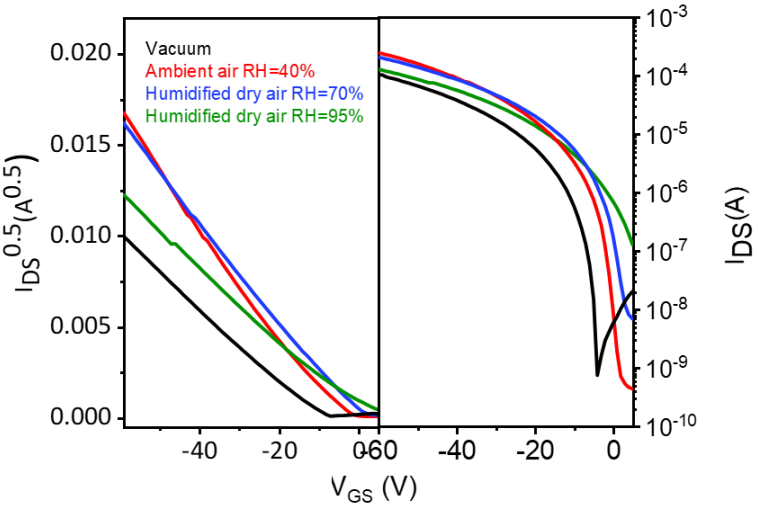

Figure 6.5: DPP-DTT OFET transfer curves operating in humified dry air and nitrogen.

The density of trap states at the polymer-dielectric interface (N_{it}), estimated from the shift of subthreshold swing (SS) according to the equation 5.1,[47] is significantly higher at humid N_2 than in ambient air, implying the role of water molecules in inducing interfacial trap states (Figure 6.3c). The above experiments reveal that the observed increases in the hole transport upon environmental exposure is due to interaction with O_2; either H_2O or O_2 can suppress the electron current, while the shift of Vth is primarily caused by interaction with H_2O molecules. Figure 6.6 shows the impact of different environment on OFETs transfer curves under full range bias (V_{GS} from 40 to -40 V).

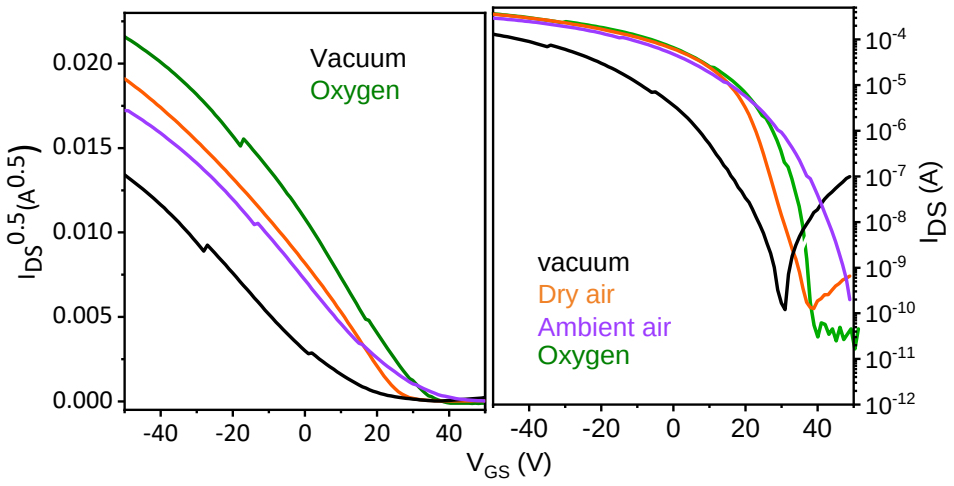

Figure 6.6: DPP-DTT OFET transfer curves (full range bias) operating in different environments.

6.2.2 Environmental stability of doped DPP-DTT OFET

Although air exposure evidently improves the hole mobility of DPP-DTT, it also leads to environmental dependency of OFET current making the device output unreliable. We have recently demonstrated that doping of DPP-DTT OFET with of nitrofluorenone acceptors significantly improves the hole mobility (from 1.25 to 6.4 $cm^2V^{-1}s^{-1}$) and suppresses gate voltage dependence of the mobility.[8] Now we explore the impact of TeNF doping (3 mol%) on the environmental stability of polymer OFET. Figure 6.3b depicts doped OFET characteristics measured under various environmental conditions. In contrast to pristine devices (Figure 6.3a), all electrical characteristic show only a minor variation with irrespective of environment: saturated mobility and maximum on-current variations are <10%, the V_{th} shift is <1V, and the off-current remains within the range of 15 to 30 nA. The largest variations have been observed in high

humidity atmosphere (RH = 75% in N_2) while ambient air or oxygen has no statistically significant effect on doped device performance.

6.2.3 Operational stability

One of the primary hindrances to developing stable p-type OFETs is operational instability which manifests as hysteresis or V_{th} shift during cyclic V_{GS} sweeping. Operational instability generally caused by ionic displacement in the gate dielectric, photoexcitation, or charge trapping at defect states in organic semiconductors or at the semiconductor/dielectric interface.[48,49] The cyclic V_{GS} sweeping of the pristine DPP-DTT OFETs (Figure 6.7a) reveals a significant hysteresis (lower back sweep current). Such behavior is generally associated with the minority and/or majority charge carrier trapping where the rate of trapping exceeds the rate of de-trapping.[9,49,50]

The impact of minority carrier (electron) trapping on OFET hysteresis was evaluated by starting the bias sweep at different V_{GS} (Figure 6.8a). When the device bias starts at positive gate voltages, electrons are injected in the channel and can be trapped at dielectric-semiconductor interface, attracting more holes and resulting in a larger current at a given V_{GS} in the forward sweep. The trapped electron population decays during forward sweep by annihilation with the injected holes, causing lower I_{DS} in the back sweep.[9,33,34,51] The more positive starting gate voltage (V_{GS}= 5, 20 and 60 V) results in more accumulated electrons and larger hysteresis (ΔVth = –5, –8 and –21 V, respectively). The hysteresis is reduced (ΔV_{th} = –2V) but not eliminated when the measurement starts at negative gate voltages (V_{GS}= –1V, Figure 6.8a). No electron accumulation is expected in this regime and the remaining hysteresis implies trapping of holes. Increasing the sweep rate results in a greater hysteresis (Figure 6.8b), which is consistent with trapping of majority carriers where the rate of release is slower than the sweeping rate.[9,50]

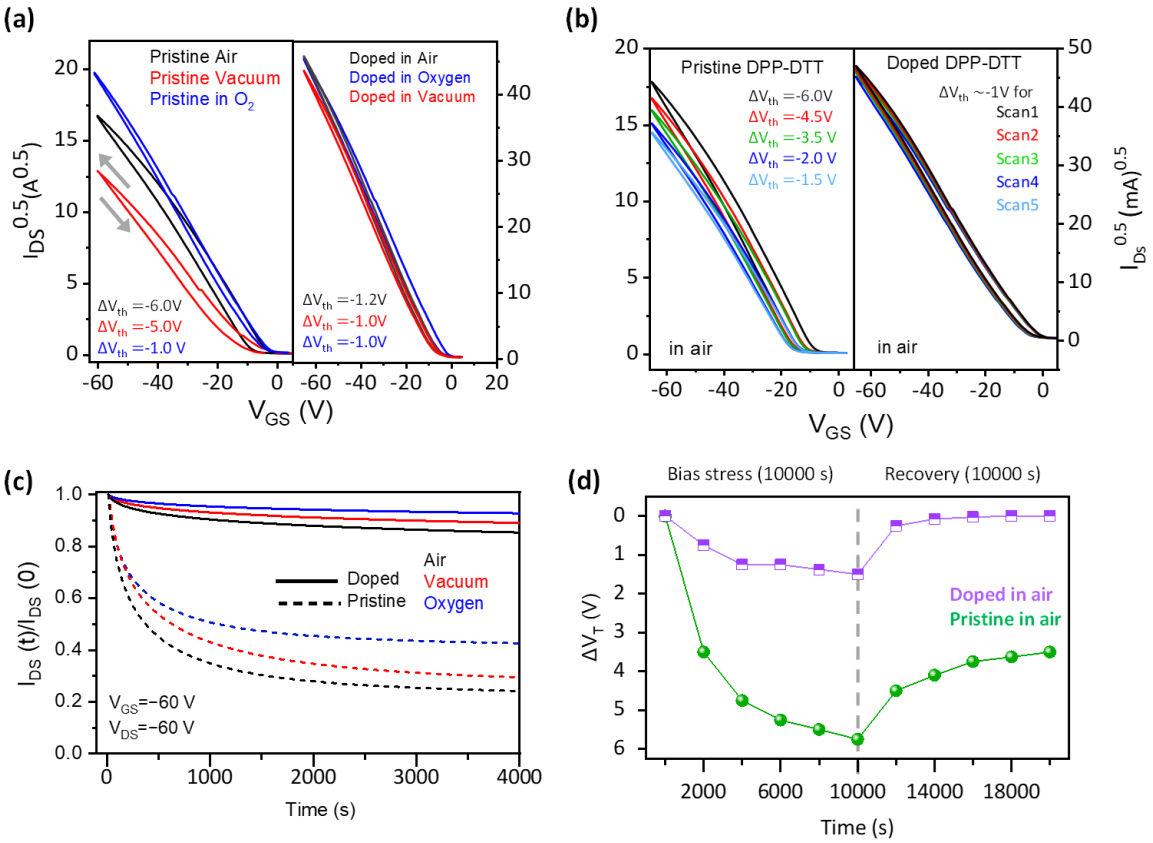

Figure 6.7: (a) cyclic transfer characteristics of pristine and doped DPP-DTT OFET in different environments (the arrows indicate the V_{GS} sweep direction); (b) multiple sweeps stability measured in ambient air; (c) hole current degradation and (d) Threshold voltage shift under continuous gate bias stress.

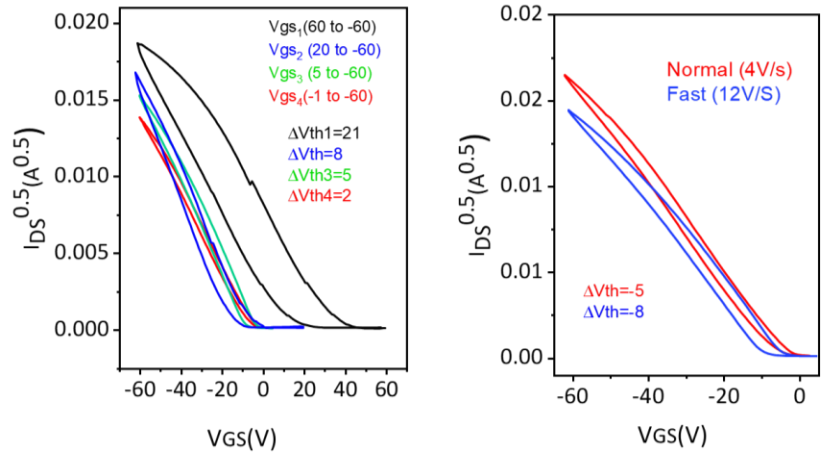

Figure 6.8: (a) Effect of positive gate bias (electron accumulation) and negative gate bias (hole accumulation) on pristine OFET hysteresis. (b) Effect scan rate on pristine OFET hysteresis.

The hysteresis is reduced by exposing the OFETs to air and oxygen indicating the suppression of donor-like traps by interaction with O_2, as already implied by increased hole mobility (Figure 6.7a). The same suppression of hysteresis is achieved after doping the polymer with TeNF acceptor, and same low-hysteresis response (ΔVth = –1) was observed in doped OFETs in all environments (Figure 6.7a). Furthermore, multiple gate sweeps of pristine OFETs lead to a progressive negative shift of threshold voltage and current drop, suggesting an accumulation of trapped majority carriers (Figure 6.7b). On the other hand, the doped OFETs show a much more stable operation upon multiple cycling.

Figure 6.7c shows the retention of hole current in pristine and doped OFETs under the constant gate bias stress in different environments. The I_{DS} of pristine OFETs decay significantly (by ~70%) after biasing for 4000 s in vacuum. This bias-stress instability is less pronounced in oxygen (55%), which is consistent with a smaller hysteresis window, which we previously linked to the suppression of charge trapping in oxygen atmosphere. An even more remarkable improvement of bias-stress stability is observed in TeNF-doped devices. The current drop does not exceed 10% and the Vth shift is only 2V after 3 hours of high bias stress in doped devices (vs 12 V in pristine devices, Figure 6.7d). Importantly, the effect of bias stress in doped OFETs is highly reversible; after 1 h of recovery (no bias) period, the initial device characteristics are fully restored. In contrast, even after 3 hours the current recovery in pristine OFETs was less than 50% (Figure 6.7d).

6.2.4 Long-term stability

In addition to operational lifetime, the long-term storage stability is another crucial aspect of the practical applications of OFETs, but the lack of standard testing protocols makes it difficult to compare the reported storage stability data.[52] Using different storage conditions, the stability of OFETs has been reported to range from days to months.[26,31,35,53-62] Various strategies for improving the OFET long-term stability have been explore, including molecular design of more stable semiconductors (e.g., higher ionization energy for p-type semiconductors), encapsulation, device and interface engineering, and alloying polymers with insulators.[53-62]

To assess the impact of TeNF doping on long-term stability, the performance changes of pristine and doped encapsulated transistors stored in ambient air was periodically monitored for four months (Figure 6.9). As discussed before, the hole mobility of freshly-fabricated non-doped OFET increases upon air exposure (from 0.4±0.25 to 1.4±0.3 $cm^2V^{-1}s^{-1}$) but after 24 hours it starts to

decrease. After four months storage in ambient air, the hole mobility drops back to 0.5±0.1 $cm^2V^{-1}s^{-1}$, the off current increases by two orders of magnitude and Vth shifts by +15 V. In contrast, the TeNF doped OFETs maintained their charge transport characteristics: the hole mobility value remained stable over a month (6.2 ± 0.3 $cm^2V^{-1}s^{-1}$) and only minor drop (7%) is seen after four months. The off-current of doped OFETs also remained near constant (~3 × 10^{-8} A) and the Vth change was < 2 V.

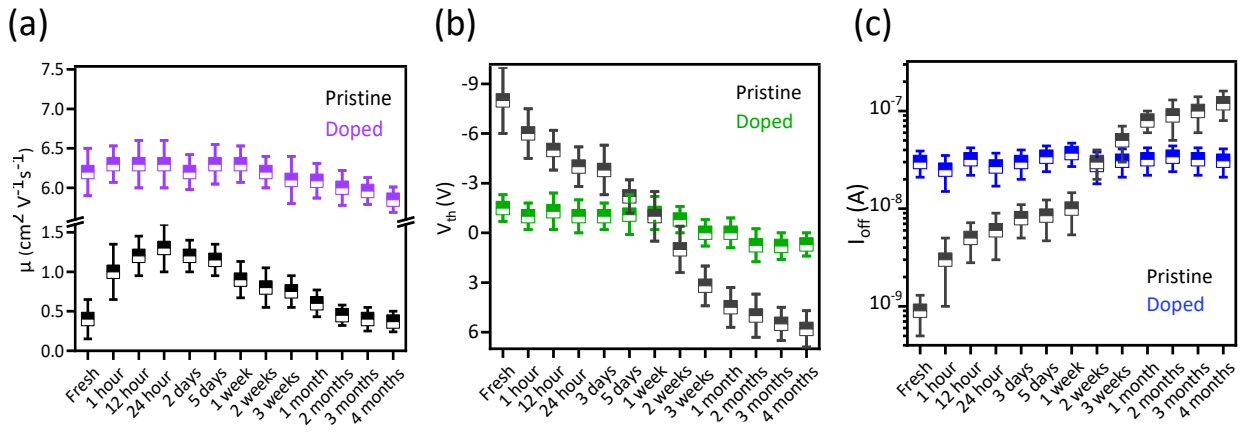

Figure 6.9: The change of hole mobility (a), threshold voltage (b) and off-current (c) of pristine and TeNF doped DPP-DTT OFETs upon storage in ambient air in dark condition.

6.2.5 Temperature-dependent study

To gain insights in charge transport and trapping in DPP-DTT, a temperature-dependent OFET measurements and EPR spectroscopy were carried out on pristine and TeNF-doped polymer films (Figure 6.10). Upon cooling, the hole current decreases in both pristine and doped OFET as expected for hopping transport mechanism (Figure 6.10a, b). The electron current of pristine and doped OFETs, on the other hand, increases as the temperature decreases, until it exhibits a balanced ambipolar characteristic at 200 K. Since the band transport mechanism is not expected for disordered polymer film, the increasing electron currents suggest that electron traps are being deactivated by lowering the temperature. The electrical neutrality points of pristine OFET (a gate voltage corresponding to the lowest current on the transfer curves) moves from 27V at room temperature to 3V at 120K, so as the device reaches a fully balanced ambipolarity at low temperature (Figure 6.10c). The effect is somewhat less pronounced in the doped films in which holes remain the majority carrier even at the low temperature.

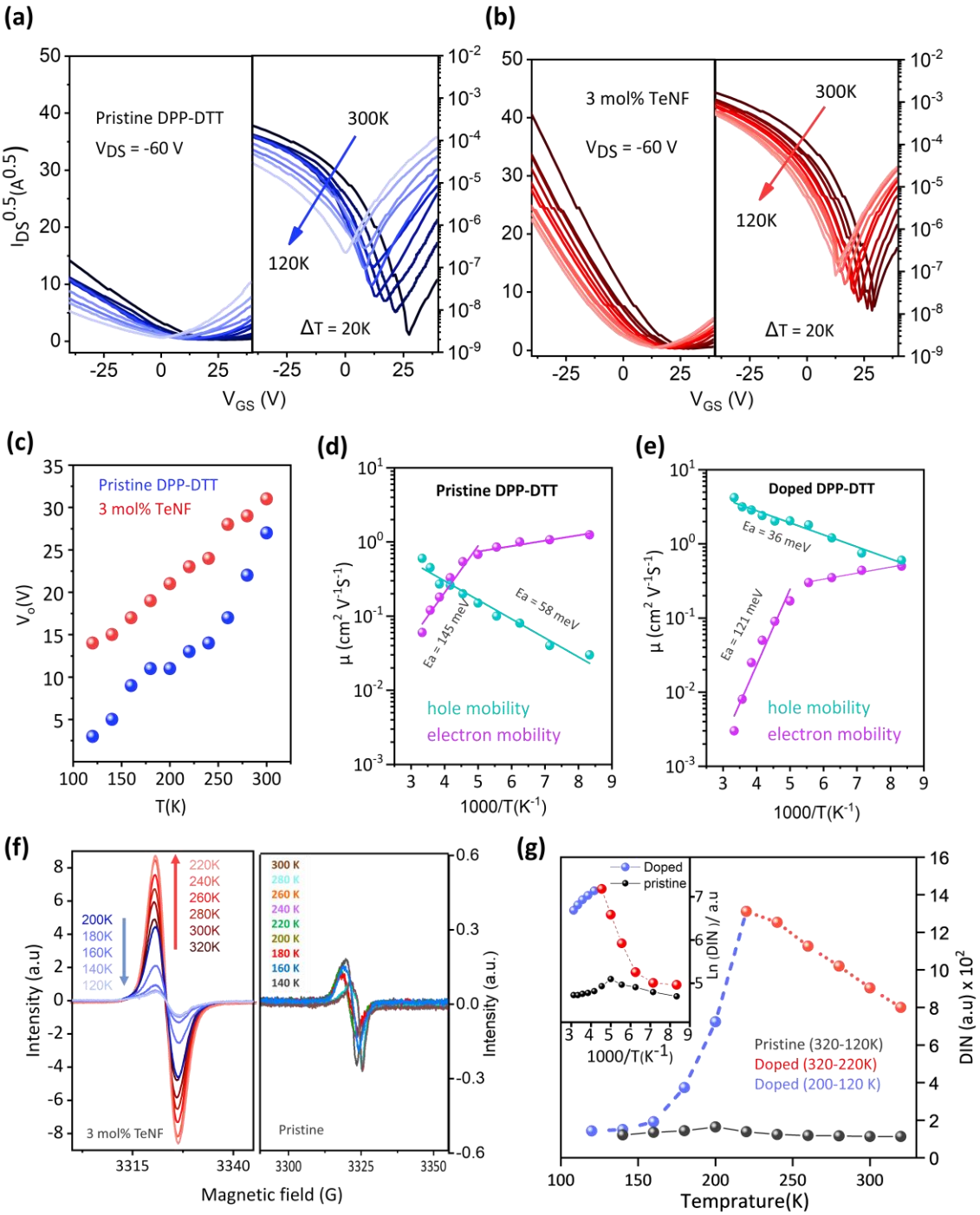

Figure 6.10: Transfer curves of (a) pristine and (b) doped DPP-DTT OFETs in vacuum at various temperatures. (c) Temperature dependence of the threshold voltage. Temperature dependence of μ with calculated transport activation energies for (d) pristine and (e) doped OFETs. (f) Temperature dependent EPR spectra of doped and pristine DPP-DTT films and (g) corresponding change of the double integrated EPR signal (DIN).

At all temperatures, the electron current is lower in the doped OFETs. This is expected because with LUMO of -4.2 eV, TeNF should act as a deep trap for electron carriers in DPP-DTT (LUMO = -3.5 eV). The activation energies E_A for hole transport in both pristine and doped films were estimated using the Arrhenius equation $\ln(\mu) = -E_A/k_BT$, as shown in Figure 6.10d, e. As previously discussed, the lower activation energy for hole transport in doped films (36 meV) compared to pristine films (58 meV) is a result of lower energetic disorder of doped films.[8] On the other hand, the electron mobility in both doped and pristine films increases rapidly with lowering the temperature. The slop of this change is noticeably and abruptly educed below ~220 K. This behavior has been observed before in other donor-acceptor polymers and was explained by nanodroplets of water acting electron carrier traps. Indeed, this temperature is very close to freezing point of supercooled water (homogeneous crystal nucleation temperature 224 K). Despite the high vacuum in the measurement chamber, the nanodroplets of water may not be fully eliminated from the polymer network and can interact with electron carriers. Their interactions with charge carrier are impeded by lowering the temperature and are almost fully arrested below 200 K due to freezing.[33,52,66]

Figure 6.10f shows the temperature dependent EPR spectra of the doped and pristine DPP-DTT. As expected, the EPR signal is significantly stronger in the doped films. In both cases, the magnetic susceptibility of the materials (measured as a double integrated intensity of the EPR signal) increases upon cooling down to ~220 K, as expected for paramagnetic radical-ion species (Figure 6.10g). However, further cooling below 200 K leads to marked decrease of DIN; such behavior indicates either strong antiferromagnetic coupling or temperature-activated electron transfer. It is notable that the breakpoint in the temperature dependence of the EPR occurs at the same temperature as the sharp change in the Arrhenius plot of electron mobility (Figure 6.10d, e).

6.3 Discussion

The proposed energy diagrams and schematics of charge transport and trapping mechanism in pristine and doped DPP-DTT OFETs in the presence of environmental species are shown in Figure 6.11. Minority carriers can be injected into (low-lying) LUMO of D–A polymers OFETs resulting in electron current and ambipolar characteristics, as seen in DPP-DTT OFET characteristics in vacuum (Figure 6.3a and 6.6). These mobile electrons can be partially trapped at in-gap states and consequently act as donor-like traps for holes (Figure 6.11a).[63,65]

When OFET is exposed to O_2-rich environment, the electron current is suppressed while the hole current is increased (Figures 6.3a, 6.6), suggesting that oxygen traps electron carriers and also suppresses the (donor-like) traps of hole carriers. [18,30] This increases the effective gate voltage for hole accumulation, resulting in positive V_{th} shifts and higher hole current at a given voltage. Also, the negatively charged interface induces additional mobile holes to the channel and increases the hole mobility (Figure 6.11b).[33,34] Furthermore, the interaction of physically absorbed water molecules with the polymer chain may result in the formation of acceptor-like shallow traps.[18,31,63] This would explain a significant positive shift in threshold voltage and a drop in hole current observed in high-humidity environment or after long exposure to ambient air (Figures 6.3a, 6.5). It's worth mentioning that traces of water may not be fully eliminated from the polymer films, even when the devices are operated in vacuum.

On the other hand, doped DPP-DTT OFETs show environmental independent performance, as well as superior lifetime stability. These improvements appear to be the results of passivation of minority carrier induced trap states by chemically stable electron acceptor.[41] The high electron affinity TeNF (LUMO = –4.2 eV) can intercept the injected electrons as evidenced by the unipolar characteristic in all environments (Figures 6.3b). The electrons are thus prevented from interacting with ambient species, forming traps and causing unintentional performance changes and device degradation (Figure 6.11c).

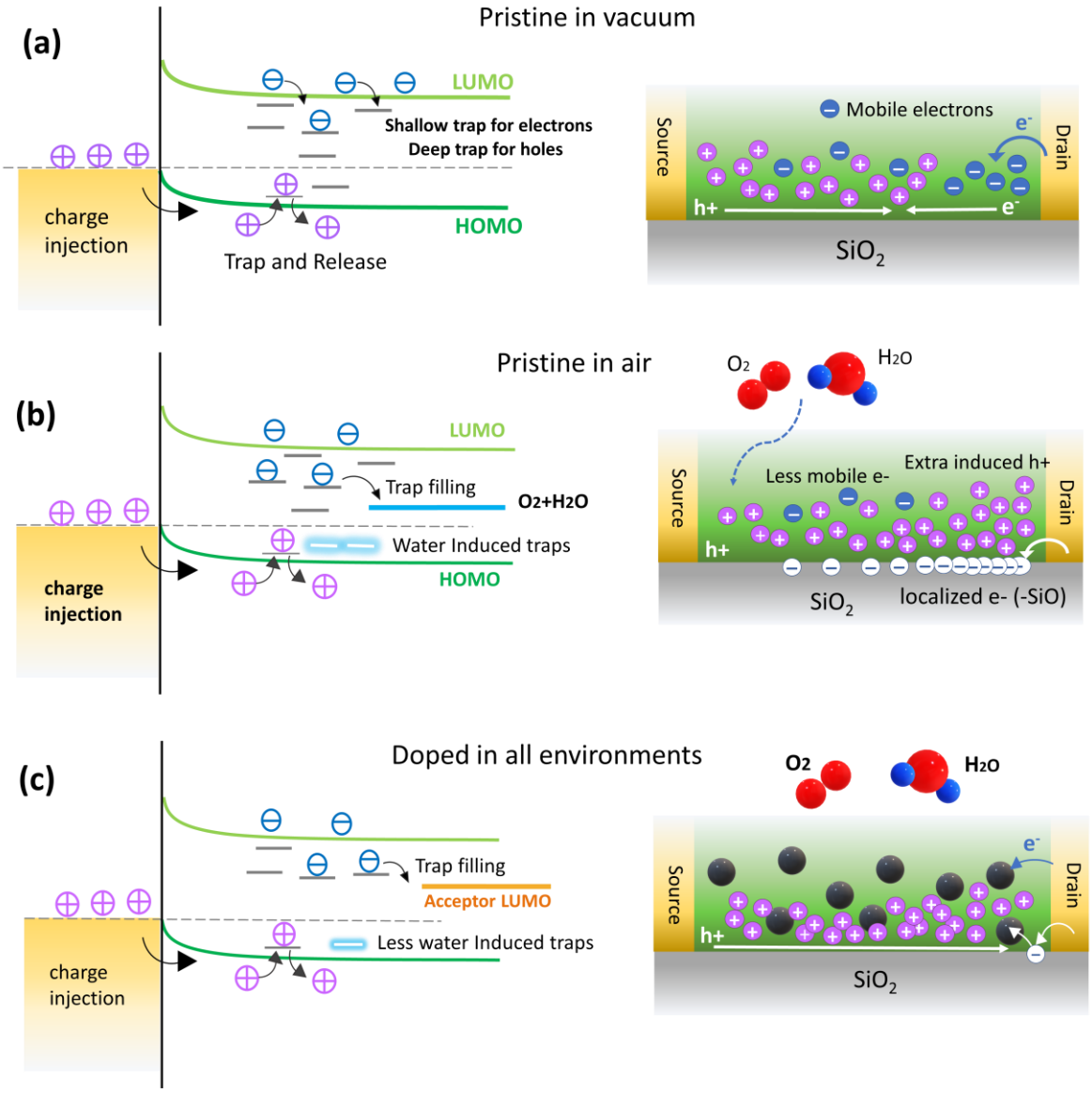

Figure 6.11: Schematic of carrier trapping mechanism at the dielectric interface and energy band diagram of pristine OFET in (a) vacuum; (b) ambient air. (c) Doped OFET in all environments.

We also note that the improved microstructural order in TeNF-doped DPP-DTT films[8] could minimize defect sites and the TeNF molecules could also fill the nanovoids in the polymer network minimizing the effects of water.[18,31] The role of improved microstructure in the environmental stability is evident from comparing the effect of TeNF dopant with that of its derivative DCN-TeNF with slightly higher electron affinity (LUMO = –4.6 eV). Although DCN-TeNF acceptor shows an improvement of the hole mobility in DPP-DTT OFETs that is even more pronounced

than that of TeNF, the AFM images show that DCN-TeNF doped films are rough and porous (Figure 6.12). As a result, these devices start to show degradation after 2 days in air, similar to the behavior observed in pristine DPP-DTT and different from TeNF-doped devices.

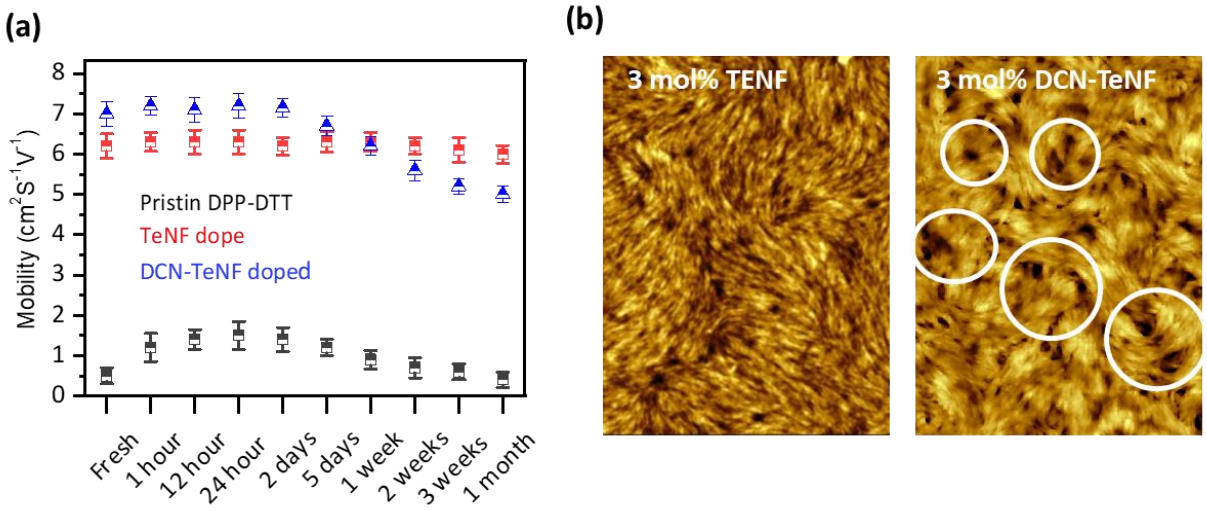

Figure 6.12: (a) The changes of mobility, pristine, TeNF doped and DCN-TeNF doped OFET over 2 months. (b) AFM images of TeNF and DCN-TeNF doped films.

In terms of operational stability, both minority carrier trapping (electrons localization at dielectric interface) and majority carrier trapping (high density of hole traps) in pristine polymer films led to significant hysteresis and bias stress instability. Therefore, the suppressed electron injection and lower trap states in less disordered doped films (larger polymer fibrillar and long-range molecular order) are the primary factors improving the operational stability of OFETs.[67]

6.4 Conclusion

In summary, we investigated the impact of air exposure on environmental and operational stability of OFETs based on pristine and doped donor-acceptor DPP-DTT polymer. The effects of the air species (O2, H_2O) are separately assessed by examining the changes in OFET performance when operating under various environmental conditions. Based on our observations, we hypothesize that air exposure has two competing effects on D-A polymer OFETs: first, passivation of electron-induced deep traps due to oxygen doping, second, inducing additional acceptor-like shallow traps in the OFET channel polymer caused by water molecules. This leads to enhanced OFET

performance in the short-term ambient air exposure (or O_2-rich environment) and degraded performance after long-term exposure to ambient air (or H_2O-rich environment), resulting in overall unreliable and unstable performance. We show that TeNF doping is an effective and simple strategy for suppressing both effects, resulting in reliable, environmentally independent performance and excellent long-term stability of unencapsulated devices in ambient air (<10% degradation after 4 months storage). The doped OFETs also show significantly reduced bias stress effect and hysteresis. Such improvement of the environmental and operational stabilities is achieved by suppressing the majority carrier trap (including electron-induced deep traps), better microstructural order /reduced nanovoids in TeNF doped polymer films.

6.5 References

1. Sirringhaus, H. 25th anniversary article: organic field-effect transistors: the path beyond amorphous silicon. *Adv. Mater*. **2014**, *26*, 1319−1335.
2. Peng, X. Z.; Horowitz, G.; Fichou, D.; Garnier, F. *Appl. Phys. Lett.* **1990**, *57*, 2013-2015
3. Zhang, X.; Bronstein, H.; Kronemeijer, A. J.; Smith, J.; Kim, Y.; Kline, R. J.; Richter, L. J.; Anthopoulos, T. D.; Sirringhaus, H.; Song, K.; Heeney, M.; Zhang, W.; McCulloch, I.; DeLongchamp, D. M. Molecular origin of high field-effect mobility in an indacenodithiophene-benzothiadiazole copolymer. *Nat. Commun.* **2013**, *4*,1-9.
4. Zhao, Z.; Yin, Z.; Chen, H.; Zheng, L.; Zhu, C.; Zhang, L.; Tan, S.; Wang, H.; Guo, Y.; Tang, Q.; Liu, Y. High-Performance, Air-Stable Field-Effect Transistors Based on Heteroatom-Substituted Naphthalenediimide-Benzothiadiazole Copolymers Exhibiting Ultrahigh Electron Mobility up to 8.5 cm V(-1) s(-1). *Adv. Mater.* **2017**, *29*, 1602410.
5. Li, Y.; Sonar, P.; Murphya, L.; Honga, W. High mobility diketopyrrolopyrrole (DPP)-based organic semiconductor materials for organic thin film transistors and photovoltaics. Energy Environ. Sci. **2013**, *6*, 1684−1710
6. Lamport, Z. A.; Barth, K. J.; Lee, H.; Gann, E.; Engmann, S.; Chen, H.; Guthold, M.; McCulloch, I.; Anthony, J. E.; Richter, L. J.; DeLongchamp, D. M.; Jurchescu, O. D. A simple and robust approach to reducing contact resistance in organic transistors. *Nat Commun*. **2018**, *9*, 1-8.

7. Kim, M.; Ryu, S. U.; Park, S. A.; Choi, K.; Kim, T.; Chung, D.; Park, T. Donor−Acceptor-Conjugated Polymer for High-Performance Organic Field-Effect Transistors: A Progress Report. *Adv. Funct. Mater*. **2019**, *30*, 1904545.
8. Ghamari, P.; Niazi, M. R.; Perepichka, D. F. Controlling Structural and Energetic Disorder in High-Mobility Polymer Semiconductors via Doping with Nitroaromatics, Chem. Mater. **2021**, *33*, 2937-2947.
9. Egginger, M.; Bauer, S.; Schwö diauer, R.; Neugebauer, H.; Sariciftci, N. S. Current versus gate voltage hysteresis in organic field effect transistors, Monatsh. Chem. **2009**, *140*, 735-750
10. Paterson, A. F.; Singh, S.; Fallon, K. J.; Hodsden, T.; Han, Y.; Schroeder, B. C.; Bronstein, H.; Heeney, M.; McCulloch, I.; Anthopoulos, T. D. Recent Progress in High-Mobility Organic Transistors: A Reality Check. *Adv. Mater*. **2018**, *30*, 1801079.
11. Sirringhaus, H.; Ando, M. Materials Challenges and Applications of Solution-Processed Organic Field-Effect Transistors. *MRS Bull.* **2008**, *33*, 676–682
12. Un H, Zheng Y-Q, Shi K, Wang J-Y and Pei J, Air- and Active Hydrogen-Induced Electron Trapping and Operational Instability in n-Type Polymer Field-Effect Transistors, *Adv. Funct. Mater*. **2017**, *27*, 1605058
13. Haneef, H. F.; Zeidell, A. M.; Jurchescu, O. D. Charge carrier traps in organic semiconductors: a review on the underlying physics and impact on electronic devices. *J. Mater. Chem. C*. **2020**, *8*, 759−787.
14. Boukhili W, Mahdouani M, Erouel M, Puigdollers J and Bourguiga R, Reversibility of humidity effects in pentacene based organic thin-film transistor: Experimental data and electrical modeling, *Synth. Met.* **2015** ,*199* 303–309,
15. Lu, X.; Minari, T.; Kumatani, A.; Liu, C.; Tsukagoshi, K. Effect of air exposure on metal/organic interface in organic field-effect transistors, *Appl. Phys. Lett.* **2011**, 98 243301.
16. Hu, Y.; Dong, G.; Hu, Y.; Wang, L.; Qiu, Y.; Oxygen effect on the electrical characteristics of pentacene transistors, *J. Phys. D: Appl. Phys*. **2006**, *39* 4553–4556.
17. Lee, E. K.; Lee, M. Y.; Park, C. H.; Lee, H. R.; Oh, J. H. Toward Environmentally Robust Organic Electronics: Approaches and Applications. *Adv. Mater.* **2017**, *29*, 1703638.
18. M. Nikolka, A perspective on overcoming water-related stability challenges in molecular and hybrid semiconductors, *MRS Communications*, **2020**, *10*, 98–111.

19. Nikolka, M.; Hurhangee, M.; Sadhanala, A.; Chen, H.; McCulloch, I.; Sirringhaus, H. Correlation of Disorder and Charge Transport in a Range of Indacenodithiophene-Based Semiconducting Polymers. *Adv. Electron. Mater*. **2018**, *4*, 1700410.
20. Quinn, J. T. E.; Zhu, J.; Li, X.; Wang, J.; Li, Y. Recent progress in the development of n-type organic semiconductors for organic field effect transistors. *J. Mater. Chem. C,* **2017**, *5*, 8654−8681
21. Chua, L. L.; Zaumseil, J.; Chang, J. F.; Ou, E. C. W.; Ho, P. K. H.; Sirringhaus, H.; Friend, R. H. General observation of n-type field-effect behaviour in organic semiconductors. *Nature* **2005**, *434*, 194-199.
22. Ding, Z.; Abbas, G.; Assender, H. E.; Morrison, J. J.; Yeates, S. G.; Patchett, E. R.; Taylor, D. M. Effect of Oxygen, Moisture and Illumination on the Stability and Reliability of DNTT OTFTs during Operation and Storage, *ACS Appl. Mater. Interfaces*, **2014**, 6, 15224–15231.
23. Qiu, Y.; Wei, P.; Wang, Z.; Lu, W.; Jiang, Y.; Zhang, C.; Qu, Y.; Lu, G. Manipulating Doping of Organic Semiconductors by Reactive Oxygen for Field-Effect Transistors. *Phys. Status Solidi RRL* **2018**, *12*, 1800297.
24. Nayak, P. K.; Rosenberg. R; Nehoshtan, L.; Cahen, D. O_2 and organic semiconductors: Electronic effects. *Org. Electron.* **2013**, *14*, 966–972.
25. Liao, H-H.; Yang, C-M; Liu, C-C; Horng, S-F.; Meng, H.; Shy, J-T. Dynamics and reversibility of oxygen doping and de-doping for conjugated polymer, *J. Appl. Phys.* **2008**, *103*, 104506.
26. Lu, G.; Blakesley, J.; Himmelberger, S.; Pingel, P.; Frisch, J.; Lieberwirth, I.; Salzmann, I.; Oehzelt, M.; Di Pietro, R.; Salleo, A.; et al. Moderate Doping Leads to High Performance of Semiconductor/Insulator Polymer Blend Transistors. *Nat. Commun.* **2013**, *4*, 1588.
27. Abdou, M. S. A.; Orfino, F. P.; Son, Y.; Holdcroft, S. Interaction of Oxygen with Conjugated Polymers: Charge Transfer Complex Formation with Poly(3-alkylthiophenes). J. Am. Chem. Soc. 1997, *119*, 4518−4524.
28. Barf, M.-M.; Benneckendorf, F. S.; Reiser, P.; Bäuerle, R.; Köntges, W.; Müller, L.; Pfannmöller, M.; Beck, S.; Mankel, E.; Freudenberg, J.; et al. Compensation of Oxygen Doping in P-Type Organic Field-Effect Transistors Utilizing Immobilized n-Dopants. *Adv. Mater. Technol.* ***2020***, 2000556.

29. Janasz, L.; Borkowski, M.; Blom, P. W.; Marszalek, T.; Pisula, W. Organic Semiconductor/Insulator Blends for Elastic Field-Effect Transistors and Sensors. *Adv. Funct. Mater*. **2021**, *32*, 2105456.
30. Zuo, G.; Linares, M.; Upreti, T.; Kemerink, M. General rule for the energy of water-induced traps in organic semiconductors. *Nat. Mater*. **2019**, *18*, 588−593.
31. Nikolka, M.; Nasrallah, I.; Rose, B.; Ravva, M. K.; Broch, K.; Sadhanala, A.; Harkin, D.; Charmet, J.; Hurhangee, M.; Brown, A.; Illig, S.; Too, P.; Jongman, J.; McCulloch, I.; Bredas, J. L.; Sirringhaus, H. High operational and environmental stability of high-mobility conjugated polymer field-effect transistors through the use of molecular additives. *Nat. Mater*. **2017**, *16*, 356-362.
32. Boufflet, P.; Han, Y.; Fei, Z. P.; Treat, N. D.; Li, R. P.; Smilgies, D.; Stingelin, N.; Anthopoulos, T. D.; Heeney, M. Using Molecular Design to Increase Hole Transport: Backbone Fluorination in the Benchmark Material Poly(2,5-bis(3-alkylthiophen-2-yl)thieno[3,2-b]-thiophene (pBTTT). *Adv. Funct. Mater.* **2015**, 25, 7038−7048.
33. Phan, H.; Wang, M.; Bazan, G. C.; Nguyen, T.-Q. Electrical Instability Induced By Electron Trapping in Low-Bandgap Donor-Acceptor Polymer Field-Effect Transistors. *Adv. Mater.* **2015**, *27*, 7004−7009.
34. Phan, H.; Ford, M. J.; Lill, A. T.; Wang, M.; Bazan, G. C.; Nguyen, T.-Q. Improving Electrical Stability, and Ideality in Organic Field-Effect Transistors by the Addition of Fullerenes: Understanding the Working Mechanism. *Adv. Funct. Mater*. **2017**, *27*, 1701358.
35. Iqbal, H. F.; Waldrip, M.; Chen, H.; McCulloch, I. and Jurchescu, O.D., Elucidating the Role of Water-Related Traps in the Operation of Polymer Field-Effect Transistors. *Adv. Electron. Mater.* **2021**, *7*, 2100393.
36. Colleaux, F.; Ball, J. M.; Wo ́bkenberg, P. H.; Hotchkiss, P. J.; Marder, S. R.; Anthopoulos, T. D. Bias-Stress Effects in Organic Field Effect Transistors Based on Self-Assembled Monolayer Nanodielectrics. *Phys. Chem*. **2011**, 13, 14387−14393
37. Lee, W. H.; Park, Y. D. Organic Semiconductor/Insulator Polymer Blends for High-Performance Organic Transistors. *Polymers* **2014**, *6*, 1057−1073
38. Riera-Galindo, S.; Leonardi, F.; Pfattner, R.; Mas-Torrent, M. Organic Semiconductor/Polymer Blend Films for Organic Field Effect Transistors. *Adv. Mater. Technol.* **2019**, 4, 1900104.

39. Campos, A.; Riera-Galindo, S.; Puigdollers, J.; Mas-Torrent, M. Reduction of Charge Traps and Stability Enhancement in Solution Processed Organic Field-effect Transistors Based on a Blended N type Semiconductor. *ACS Appl. Mater. Interfaces.* **2018**, *10*, 15952–15961.
40. Kang, M.; Hwang, H.; Park, W. T.; Khim, D.; Yeo, J. S.; Kim, Y.; Kim, Y. J.; Noh, Y. Y.; Kim, D. Y. Ambipolar Small-Molecule: polymer Blend Semiconductors for Solution-Processable Organic Field-Effect Transistors. *ACS Appl. Mater. Interfaces* **2017**, 9, 2686−2692
41. Sun, Y.; Lu, X.; Lin, S.; Kettle, J.; Yeates, S. G.; Song, A. Polythiophene-Based Field-Effect Transistors with Enhanced Air Stability. *Org. Electron*. **2010**, *11*, 351−355.
42. Nikolka, M.; Schweicher, G.; Armitage, J.; Nasrallah, I.; Jellett, C.; Guo, Z.; Hurhangee, M.; Sadhanala, A.; McCulloch, I.; Nielsen, C. B.; et al. Performance Improvements in Conjugated Polymer Devices by Removal of Water-Induced Traps. *Adv. Mater*. **2018**, *30*, 1801874.
43. Belasco, J.; Mohapatra, S. K.; Zhang, Y.; Barlow, S.; Marder, S. R.; Kahn, A. Molecular Doping and Tuning Threshold Voltage in 6, 13-bis (triisopropylsilylethynyl) Pentacene/Polymer Blend Transistors. *Appl. Phys. Lett*. **2014**, *105*, 063301.
44. Hein, M. P.; Zakhidov, A. A.; Luessem, B.; Jankowski, J.; Tietze, M. L.; Riede, M. K.; Leo, K. Molecular Doping for Control of Gate Bias Stress in Organic Thin Film Transistors. *Appl. Phys. Lett.* **2014**, *104*, 013507.
45. Xu, Y.; Sun, H.; Liu, A.; Zhu, H. H.; Li, W.; Lin, Y. F.; Noh, Y. Y. Doping: A Key Enabler for Organic Transistors. *Adv. Mater.* **2018**, *30*, 1801830.
46. Lüssem, B.; Keum, C. M.; Kasemann, D.; Naab, B.; Bao, Z.; Leo, K. Doped Organic Transistors. *Chem. Rev*. **2016**, *116*, 13714− 13751.
47. Han, Y.; Barnes, G.; Lin, Y.-H.; Martin, J.; Al-Hashimi, M.; AlQaradawi, S. Y.; Anthopoulos, T. D.; Heeney, M. Doping of Large Ionization Potential Indenopyrazine Polymers via Lewis Acid Complexation with Tris(Pentafluorophenyl)Borane: A Simple Method for Improving the Performance of Organic Thin-Film Transistors. *Chem. Mater*. **2016**, *28*, 8016−8024.
48. Bobbert, P. A.; Sharma, A.; Mathijssen, S. G. J.; Kemerink, M.; De Leeuw, D. M. Operational Stability of Organic Field-Effect Transistors. *Adv. Mater*. **2012**, 24, 1146−1158.
49. Park, S.; Kim, S. H.; Choi, H. H.; Kang, B.; Cho, K. Recent Advances in the Bias Stress Stability of Organic Transistors. Adv. Funct. Mater. **2019**, *30*, 1904590.
50. Yang, C. Guo, C. Shi, D.-K. Wang, T. Zhang, Q. Zhu, Z.-H. Lu, Improving Bias-Stress Stability of p-Type Organic Field-Effect Transistors by Constructing an Electron Injection

Barrier at the Drain Electrode/Semiconductor Interfaces, *ACS Appl. Mater. Interfaces*, **2020**,*12*, 41886

51. Gu, G.; Kane, M. G.; Doty, J. E.; Firester, A. H. Electron traps and hysteresis in pentacene-based organic thin-film transistors *Appl. Phys. Lett*. **2005**, *87*, 243512.
52. Kimpel, J.; Michinobu, T. Conjugated Polymers for Functional Applications: Lifetime and Performance of Polymeric Organic Semiconductors in Organic Field-Effect Transistors. *Polym Int.* **2021**, *70*, 367–373.
53. Mun, J.; Kang, J.; Zheng, Y.; Luo, S.; Wu, Y.; Gong, H.; Lai, J. C.; Wu, H. C.; Xue, G.; Tok, J. B. H.; Bao, Z. F4-TCNQ as an Additive to Impart Stretchable Semiconductors with High Mobility and Stability. *Adv. Electron. Mater*. **2020**, *6*, 2000251
54. Han, S.; Yu, X.; Shi, W.; Zhuang, X.; Yu, J. Solvent-Dependent Electrical Properties Improvement of Organic Field-Effect Transistor Based on Disordered Conjugated Polymer/Insulator Blends. *Org. Electron*. **2015**, *27*, 160−166.
55. Knopfmacher, O.; Hammock, M. L.; Appleton, A. L.; Schwartz, G.; Mei, J.; Lei, T.; Pei, J.; Bao, Z. Highly stable organic polymer fieldeffect transistor sensor for selective detection in the marine environment. *Nat. Commun*. **2014**, 5, 2954.
56. Kim, D. H.; Lee, B.; Moon, H.; Kang, H. M.; Jeong, E. J.; Park, J.; Han, K.; Lee, S.; Yoo, B. W.; Koo, B. W.; Kim, J. Y.; Lee, W. H.; Cho, K.; Becerril, H. A.; Bao, Z. Liquid-Crystalline Semiconducting Copolymers with Intramolecular Donor-Acceptor Building Blocks for High-Stability Polymer Transistors, *J. Am. Chem. Soc.* **2009,** *131*, 6124-6132.
57. Choi, S.; Jeong, J. W.; Jo, G.; Ma, B. C.; Chang, M. Conjugated polymer/paraffin blends for organic field-effect transistors with high environmental stability. *Nanoscale* **2019**, *11*, 10004−10016.
58. Kim, Y.; Broch, K.; Lee, W.; Ahn, H.; Lee, J.; Yoo, D.; Kim, J.; Chung, S.; Sirringhaus, H.; Kang, K.; et al. Highly Stable Contact Doping in Organic Field Effect Transistors by Dopant-Blockade Method. *Adv. Funct. Mater*. **2020**, *30*, 2000058.
59. Schmoltner, K.; Schlütter, F.; Kivala, M.; Baumgarten, M.; Winkler, S.; Trattnig, R.; Koch, N.; Klug, A.; List, E. J. W.; Müllen, K. A heterotriangulene polymer for air-stable organic field-effect transistors. *Polym. Chem*. **2013**, *4*, 5337−5344.
60. Park, J. H.; Jung, E. H.; Jung, J. W.; Jo, W. H. A Fluorinated Phenylene Unit as a Building Block for High-Performance n-Type Semiconducting Polymer, *Adv. Mater.* **2013,** *25*, 2583.

61. Lei, T.; Cao, Y.; Fan, Y.; Liu, C.-J.; Yuan, S.-C.; Pei, J. High-Performance Air-Stable Organic Field-Effect Transistors: Isoindigo-Based Conjugated Polymers, *J. Am. Chem. Soc.* **2011**, *133*, 6099−6101.

62. Osaka, I.; Takimiya, K.; McCullough, R. D. Benzobisthiazole-Based Semiconducting Copolymers Showing Excellent Environmental Stability in High-Humidity Air. *Adv. Mater.* **2010**, *22*, 4993−4997.

63. Chen, Y.; Deng, W.; Zhang, X.; Wang, M.; Jie, J. Ambient instability of organic field-effect transistors and its improvement strategies. *J. Appl. Phys*. **2022**, *55*, 053001.

64. Mei, Y.; Diemer, P. J.; Niazi, M. R.; Hallani, R. K.; Jarolimek, K.; Day, C. S.; Risko, C.; Anthony, J. E.; Amassian, A.; Jurchescu, O. D. Crossover from Band-like to Thermally Activated Charge Transport in Organic Transistors Due to Strain-Induced Traps. Proc. Natl. Acad. *Sci. U. S. A.* **2017**, 6739−6748.

65. Un, H. I.; Wang, J. Y.; Pei, J. Recent Efforts in Understanding and Improving the Nonideal Behaviors of Organic Field-Effect Transistors. *Adv. Sci.* **2019**, *6*, 1900375.

66. Barra, M.; Girolamo, F. D.; Chiarella, F.; Salluzzo, M.; Chen, Z.; Facchetti, A.; Anderson, L.; Cassinese, A. Transport Property and Charge Trap Comparison for N-Channel Perylene Diimide Transistors with Different Air-Stability. *J. Phys. Chem. C,* **2010**, *114*, 20387−20393.

67. Lee, H.; Moon, B.; Son, S. Y.; Park, T.; Kang, B.; Cho, K. Charge Trapping in a Low-Crystalline High-Mobility Conjugated Polymer and Its Effects on the Operational Stability of Organic Field-Effect Transistors. *ACS Appl. Mater. Interfaces* **2021**, *13*, 16722−16731.

68. Han, Y.; Barnes, G.; Lin, Y.-H.; Martin, J.; Al-Hashimi, M.; AlQaradawi, S. Y.; Anthopoulos, T. D.; Heeney, M. Doping of Large Ionization Potential Indenopyrazine Polymers via Lewis Acid Complexation with Tris(pentafluorophenyl)borane: A Simple Method for Improving the Performance of Organic ThinFilm Transistors. *Chem. Mater*. **2016**, *28*, 8016-8024.

Chapter 7 : Conclusions and Future Perspectives

7.1 Conclusions and discussion

In this thesis, we have established the role of process-structure-property-performance relationship in the development of next generation high performance-stable semiconductor technology with two key directions: (1) production of sustainable energy by implementation of novel III-nitrides based photocathode for PEC reduction of CO_2 into storable syngas fuels, (2) development of flexible microelectronics by addressing the operational challenges of polymer OFETs using doping approach.

PEC CO_2 reduction is an alternative approach for reducing CO_2 emission impacts and converting it into valuable chemicals and storable fuels**.** However, due to the problems with thermodynamic stability of CO_2 and the complex reaction network of CO_2 conversion, obtaining effective and stable PEC CO_2 reduction into syngas with controllable composition has remained challenging. In this thesis we established a highly efficient and stable PEC system for reduction of CO_2 into syngas base on III-nitride nanostructure photocatalysts. We designed and synthesized a novel photocathode by monolithically integration of GaN NWs and Si p-n junction, in which NWs are decorated with Pt nano particles and coated in a thin layer of TiO_2 to offer a metal-oxide interface as co-catalyst. Implemented Pt-TiO_2/GaN/n^+-p Si photocathode featured a highly positive onset potential of +0.47 V (underpotential of 580 mV to the CO_2/CO equilibrium potential at −0.11 V) for producing high CO FE of 78% in an aqueous PEC cell. The achieved onset potential was the lowest value (170 mV positive shifted) as compared to the best value reported in the literature. Moreover, the PEC CO_2 reduction reaction using Pt-TiO_2/GaN/n^+-p Si photocathode resulted in a benchmarking solar-to-syngas efficiency of 0.87%, a record turnover number of 24800, as well as highly stable syngas production in the 10 h duration test. We also demonstrated that, CO/H_2 ratios of produced syngas could be tuned in a wide range between 4:1 and 1:6 at various applied potentials.

Theoretical and experimental analyses of photocatalytic reaction mechanism revealed that CO_2 absorption and activation on the TiO_2-Pt interface is substantially higher than on metallic Pt cocatalysts leading to highly efficient CO_2 reduction to CO. We generalized our designed co-cocatalyst to other metal/oxide combinations such as Pd- TiO_2 and Pt-ZnO and observed similar

catalytic performance. We proposed that the synergistic interactions at the metal/oxide interface provides unique reaction channels that structurally and electronically facilitate CO_2 conversion into CO. In this research, we demonstrated that integrating the efficient electron extraction effect of GaN nanowires arrays, the strong light harvesting of p-n Si junction, and extremely fast syngas production kinetics on Pt-TiO_2 co-catalysts provides superior efficient and stable platform for PEC reduction of CO_2 into syngas fuels, which is not possible in the absence of any of the components (Figure 7.1).

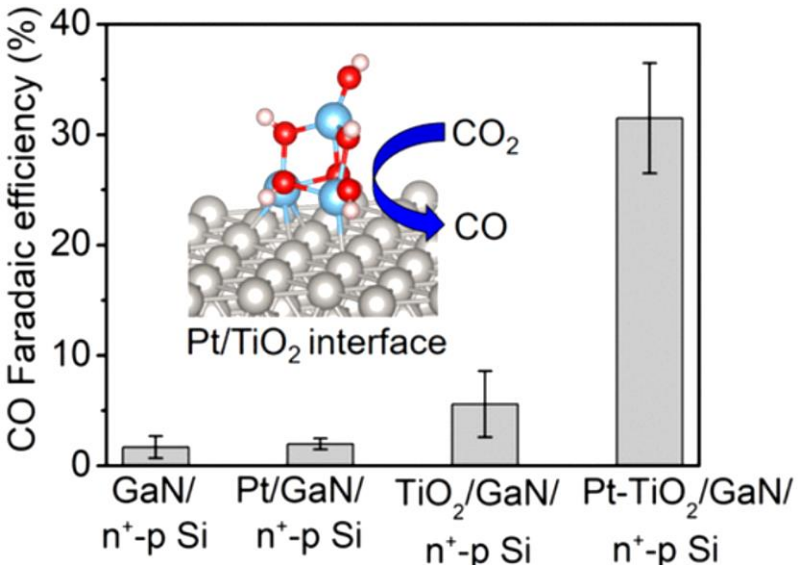

Figure 7.1: The impact of metal-oxide co-catalyst on improving CO2-to-CO selectivity (Reproduced with permission from ref 1).

In continue, to overcome the low efficiency challenges and increase controllability over PEC syngas composition in aqueous CO_2, we designed a new photocathode based on GaN/n-p Si by decoupling CO_2RR and HER catalytic sits using dual Pt-Au cocatalysts (Figure 7.2). PEC CO_2 reduction based on $AuPt_{0.2}$/GaN/n^+-p Si led to a record solar-to-syngas efficiency of 1.88 % and a benchmark turnover number of 58800 under standard one sun illumination. In addition, the CO/H_2 ratio in the syngas mixture could be controllably regulated in a broad range between 1:99 and 10:1 with a total unity Faradaic efficiency by varying the ratio of Au/Pt in dual cocatalysts. Such high efficiency and countability over syngas composition were achieved by spatially coupling off Au CO-generating cocatalyst and a Pt H_2-generating cocatalyst on the polar and nonpolar surfaces of GaN nanowires, respectively. This work provides a promising route for the rational design of high-performance PEC syngas generation with controllable composition from aqueous CO_2 reduction.

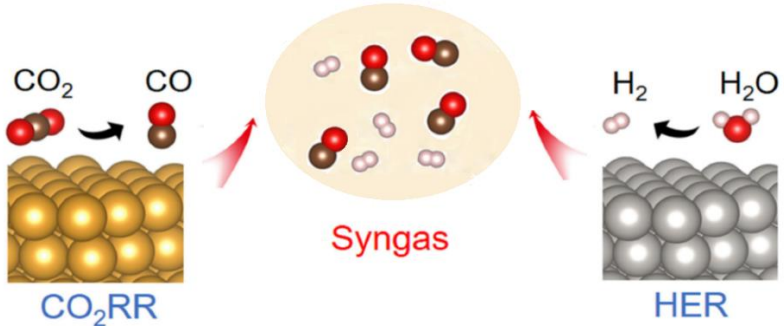

Figure 7.2: Decoupling CO_2RR and HER catalytic sits to increase CO_2 to syngas tunability using dual Pt-Au cocatalysts (Reproduced with permission from ref 2).

In the second study, we investigated the effect of molecular doping on the performance and stability of polymer OFETs, with the aim of addressing the operational challenges of OFETs. OFETs are fundamental building blocks for large-area printable and flexible electronics. Despite substantial advancements in OFET performance over the past decade, they have yet to be employed in practical applications. The bottleneck of OFET commercialization is limited carrier mobility, operational and environmental instability, all of which are induced by charge carrier trapping. Intentional molecular doping is potential technique for mitigating trap states and tuning the charge transport properties in OSCs. However, a limited toolbox of molecular dopants with appropriate energy levels and solubility, as well as serious concerns about unwanted increases in off current, prevent widespread use of the doping technique in OFET applications.

In this thesis, we introduced nitrofluorene derivatives (NFs) as a novel family of tunable *p*-dopants for polymer OFETs. We demonstrated the optimized 3 mol% TeNF doping of DPP-DTT OFETs resulted in 6-fold enhancement of saturation mobility, up ~8 $cm^2V^{-1}s^{-1}$. More importantly, the gate dependent mobility issue is significantly suppressed upon NF doping, resulting in reliable mobility of 6.4 $cm^2\ V^{-1}\ S^{-1}$ which is among the highest mobility reported for polymer OFETs (Figure 7.3). We demonstrated TeNF doping lead to improvement of all device figures of merit, such as lowering threshold voltage, contact resistance, and interfacial trap density. We highlighted that even at 3 mol% TeNF, doped devices showed relatively small OFF currents (from ~3 to ~60 nA) and on-off ratios in the acceptable range ($>2\times10^{-4}$). The controlled increase in off current is caused by a significant barrier (1 eV) between the polymer HOMO and dopant LUMO, resulting in interaction of dopant LUMO with in-gap deep traps rather than polymer HOMO.

Moreover, AFM and 2D-GIWAXS characterizations showed improved fibrillar interconnections, increased polymer fiber size as well as enhanced coherence lengths of doped films. Also, UV-Vis-NIR spectroscopy revealed an up to 30% increase in the absorption coefficient of TeNF doped polymer films, especially for the 0-0 vibronic transition, which is consistent with the enhanced ordering. The lower activation energies in doped films, suggesting reduced energetic disorder is confirmed by variable temperature mobility measurements. We proposed that significantly improved device performance in doped DPP-DTT OFETs is a synergetic effect of deep traps filling and improved film morphology. This work represents the potential for nitroaromatic acceptors as effective and chemically stable *p*-dopants in soft electronics.

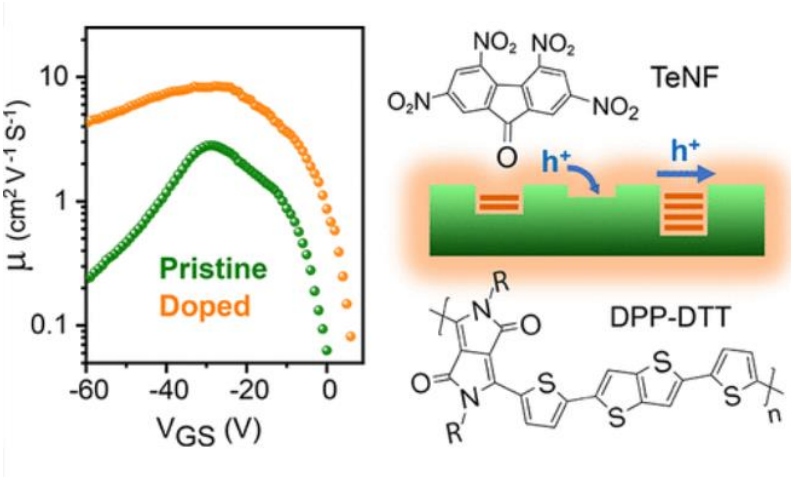

Figure 7.3: The impact of TeNF doping on DPPDTT OFET mobility and the schematic of trap filling mechanism (Reproduced with permission from ref 3).

In continue of addressing OFET operational challenges, we evaluated the impact of NF doping on environmental and operational stability of DPP-DTT polymer OFETs. By separately introducing the air species (O2, H_2O) to the operating OFETs and analysing the changes in transistor parameters, the effect of air exposure on device performance was evaluated. According to the experimental observations, we hypothesized that air exposure has two competing effects on DPP-DTT OFETs: first, passivation of electron-induced deep traps due to oxygen doping, second, inducing additional acceptor-like shallow traps in the OFET channel polymer caused by water molecules. This leads to improved OFET performance in the short-term air exposure (or O_2-rich environment) and degraded performance under prolonged air exposure (or H_2O-rich environment), leading to overall unstable performance of OFET in

ambient air. We demonstrated that TeNF doping is an effective approach for suppressing both effects, resulting in reliable and environmentally independent performance of OFETs, as well as excellent long-term stability of unencapsulated devices in ambient air (<10% degradation after 4 months storage). In addition, the bias stress effect and hysteresis are significantly reduced in the doped OFETs. We attributed the considerable improvement of environmental and operational stabilities to suppression of majority carrier trap (including electron-induced deep traps), as well as improved microstructural order and reduced nanovoids in TeNF doped polymer films. This work paves the path for the realization of high performance and stable OFETs in practical applications. We first investigate the impact of air exposure on pristine OFETs and revealed

7.2 Future Perspectives

7.2.1 Covalent organic frameworks photocatalysts for CO_2 reduction

In chapters 3 and 4, we demonstrated the potential of III-nitrides NWs as a high efficiency and stable photocatalyst for CO_2 conversion into chemicals. However, synthesising III-nitrides nanostructures and modifying their properties is a complex and costly procedure with limited tunability. Therefore, developing photocatalysts with the advantages of organic materials such as simple processing and ease of structural modification, while being highly efficient and stable has remained challenging.

Metal-organic frameworks (MOFs), launched in the 1990s,[4] and covalent organic frameworks (COFs), introduced in 2005, are two innovative classes of porous organic frameworks with substantial structural and functional adjustability.[5,6] The tunable porous structures of MOFs and COFs which provide plenitude of available active sites for catalytic reactions, and versatility with active metal loading, which facilitates efficient charge transfer, make them as promising compounds for electro/photo catalytic reactions, particularly for CO_2 reductions and water splitting.[7]

Despite their similarities, COFs are composed of light elements such as hydrogen and nitrogen rather than metal-based nodes in MOFs. Furthermore, COFs could form eighter 2D or 3D constructions, and unlike MOFs, are entirely made of covalent bonds. These differences make COFs a lighter compound than MOFs, and in some cases, with higher stability due to strong

covalent bonds.[7,8] However, owing to a significantly lower number of synthesised COFs compared to MOFs, COFs-based photocatalytic application is still in the early phases of research, leaving many undiscovered rooms in this field.

Perepichka group is one of the pioneers in development of novel COFs with rationally designed structure for various application. Access to such a diverse range of novel COFs as photocatalysts, combined with the expertise and knowledge obtained from this thesis study in designing and implementation of advanced CO_2 reduction applications, have provided significant potential for systematic investigation on development of high efficiency and stable organic catalysts for green sustainable energy (Figure 7.4).

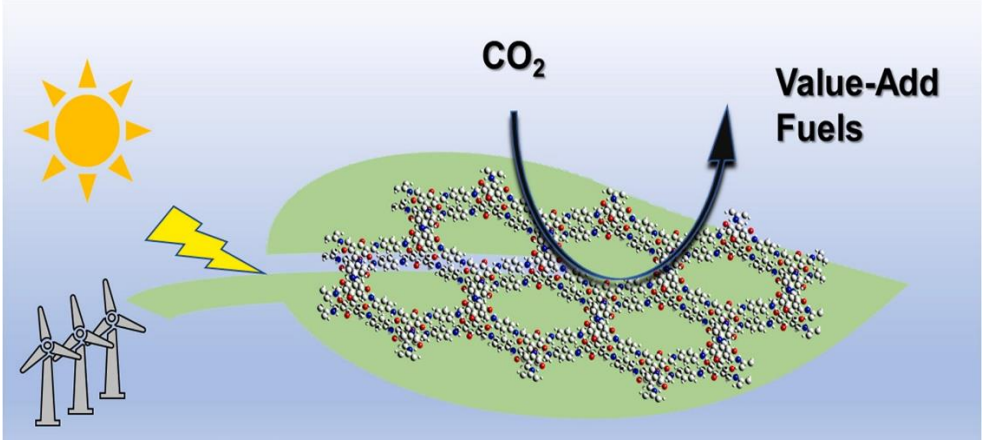

Figure 7.4 Electrochemical and photochemical CO_2 reduction based on COFs. (Reproduced with permission from ref 8)

7.2.2 Doping in organic photovoltaics

Organic photovoltaics (OPVs) have drawn a lot of interest as the next generation of solar energy harvesting platforms, due to their flexibility, low-cost manufacturing, and large-area roll-to-roll solution processability. Over the last decade, significant breakthroughs in device processing and photovoltaic material design have been made to improve the performance of OPVs, with power conversion efficiencies (PCE) exceeding ~20%.[10] However, the industrial development of OPVs is still hindered by moderate efficiency, poor reproducibility, and low stability concerns.

In a conventional bulk-heterojunction (BHJ) OPV with interpenetrating networks of donor polymer and acceptor molecules, the percolating charge transport pathway, and thus the OPV efficiency and stability, are highly sensitive to the interfacial and bulk morphological properties.[11]

Extensive efforts have been made to achieve an optimum morphology and manipulate phase separation for effective charge transport within OPVs such as: controlling surface energy and nucleation using additives, annealing, and SAM treatment, as well as tailoring chemical structure for desired phase separation, and inducing self-alignment, or solvent engineering to control miscibility.[11-13]

Despite the potential of doping technique for interfacial and bulk morphological modification, doping of OPV active layer is less investigated due to challenges such as dopants diffusion, uncontrollable induced disorder, and the limitations of adoptable dopants with donor-acceptor solvent system.[14] Recently, few studies have demonstrated that controlled BHJ doping could induce balanced carrier transport and improved charge extraction, as well as suppression of adverse processes such as space-charge effect and recombination losses, resulting in the enhanced J_{SC} and FF (Figure 7.5).[15]

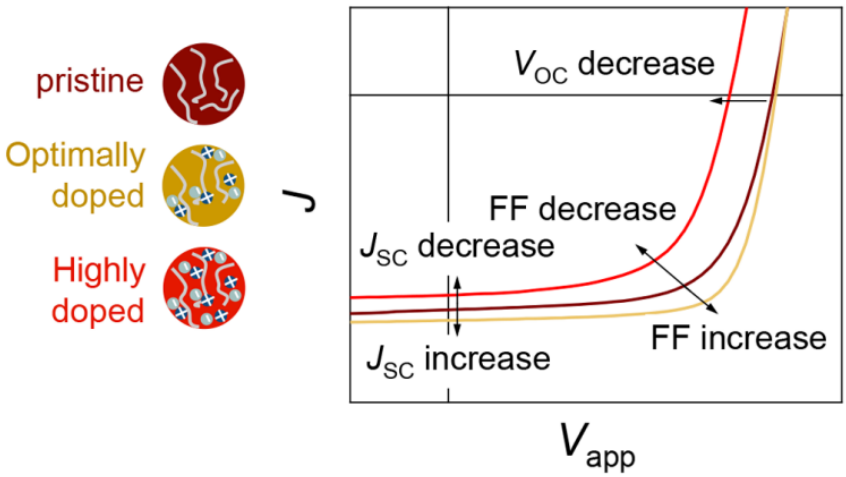

Figure 7.5: The schematic of anticipated impact of optimal doping on OPVs performance. (Reproduced with permission from ref 15)

In this thesis study (chapter 5,6) we have highlighted that NF doping in addition to the electrical doping which leading to generation of extra free carrier, enable the microstructural and morphological modification of polymer film. The dual functional effects of NF doping open up a wide range of opportunities for future investigations in other applications such as OPVs doping. The impact of NF doping on addressing OPV issues, could be evaluated with different strategies: 1) doping of hole transport layer, (2) microstructural modification of photoactive layer via bulk

doping (3) gradual doping of photoactive layer over limited depth with doped buffer layer (Figure 7.6)

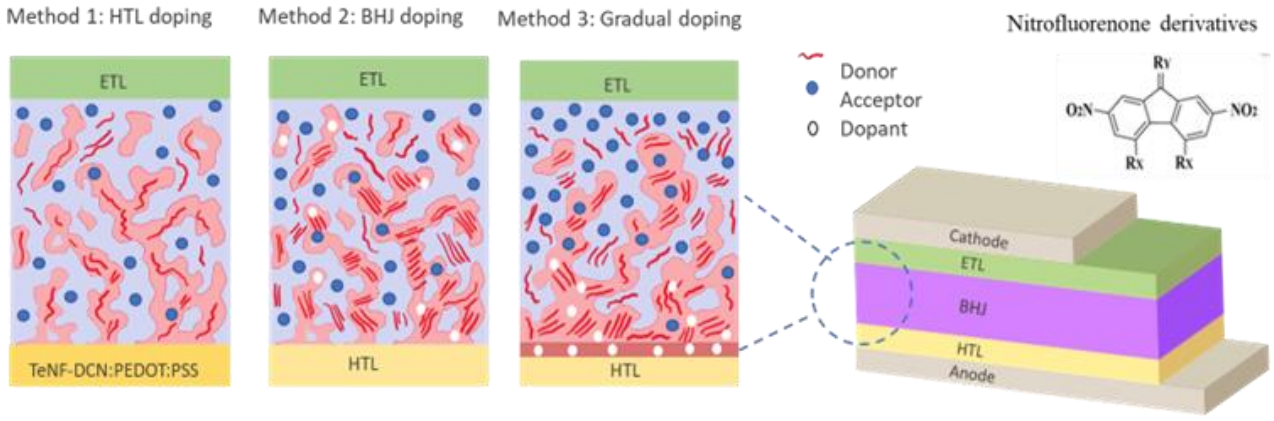

Figure 7.6: Proposed strategies for NF doping of OPVs.

I-Electrical doping of HTL:

Interfacial engineering aims to facilitate charge transport and collection, which is crucial to achieve high-efficiency OPV. Doping of HTL appears to be a potential method for improving ohmic contact and aligning the energy level with the electrode work function (WF), as well as modifying the interface morphology. Although NF dopants are not very strong dopant to increase the conductivity of HTL, they have shown to be beneficial for reducing the interfacial tarp density by modification of microstructure and subsequently improving the charge injection. The preliminary results of PEDEOT: PSS doping with TeNF-DCN showed a potential influence on interfacial morphology modification, prompting further investigation on this strategy.

II-Photoactive layer microstructural modification via Bulk heterojunction doping:

In chapter 5 we demonstrated that incorporating different NF derivatives (DCN-TeNF, TeNF, DNF, etc.) at varying concentrations into the polymer semiconductor can control the polymer domain size within the nm to μm range, as well as ordering and planarity of the polymer chain. The alignment of the polymer chains in a particular planar direction facilitates charge transfer in the active layer which is crucial for high efficiency.[13] Although additives tend to increase polymer film disorder, the versatility of nitroaromatics in polymer microstructural manipulation can provide substantial potential for bulk-heterojunction microstructural and morphological optimization by doping, which is less established in OPV studies.

III- Bulk-heterojunction gradual doping over limited depth via NF-doped buffer layer: In this method, morphological changes in the bulk heterojunction will be induced by inserting a buffer layer made of a doped-donor polymer between the HTL and bulk active layer. Because the microstructural properties of the underneath layer (buffer) play an important role in inducing specific microstructural features in the next layer (Bulk active layer), the doped donor polymer should be pre-optimized to achieve the desired domain size, optimum roughness, and desired planarity. Deposition of donor-acceptor mixed phase on top of the doped-donor buffer layer followed by the thermal annealing post-treatment, can induce vertical gradient phase separation in the active layer. In a previous study, we discovered that thermal annealing of a doped/non doped bilayer polymer causes NF dopant diffusion in a limited depth (10-20 nm) and the formation of a merged interface doped layer. As a result, this method could provide bulk gradual doping over limited depth with donor-enriched large domains at the anode while preserving the desired nm scale domains in the donor-acceptor interpenetrated region.

7.3 References

1. Chu, S.; Ou, P.; Ghamari, P.; Vanka, S.; Zhou, B.; Shih, I.; Song, J.; Mi, Z. Photoelectrochemical CO_2 reduction into syngas with the metal/oxide interface. *J. Am. Chem. Soc*. **2018**, *140*, 7869− 7877.
2. Chu, S.; Ou, P.; Rashid, R. T.; Ghamari, P.; Wang, R.; Tran, H. N.; Zhao, S.; Zhang, H.; Song, J.; Mi, Z. Decoupling Strategy for Enhanced Syngas Generation from Photoelectrochemical CO_2 Reduction. *iScience* **2020**, *23*, 101390.
3. Ghamari, P.; Niazi, M. R.; Perepichka, D. F. Controlling Structural and Energetic Disorder in High-Mobility Polymer Semiconductors via Doping with Nitroaromatics. *Chem. Mater.* **2021**, *33*, 2937−2947.
4. Singh, C.; Mukhopadhyay, S.; Hod, I. Metal−organic framework derived nanomaterials for electrocatalysis: Recent developments for CO_2 and N_2 reduction. *Nano Convergence* **2021**, *8*, 1-10.
5. Wang, H.; Wang, H.; Wang, Z.; Tang, L.; Zeng, G.; Xu, P.; Chen, M.; Xiong, T.; Zhou, C.; Li, X.; Covalent Organic Framework Photocatalysts: Structures and Applications. *Chem. Soc. Rev.* **2020**, *49*, 4135−4165.

6. Zhao, X.; Pachfule, P.; Thomas, A. Covalent Organic Frameworks (COFs) for Electrochemical Applications. *Chem. Soc. Rev.* **2021**, *50*, 6871−6913
7. Zhang, H.; Zhu, M.; Schmidt, O.G.; Chen, S.; Zhang, K. Covalent organic frameworks for efficient energy electrocatalysis: rational design and progress. *Adv. Energy Sustainability Res.* **2021**, *2*, 2000090.
8. He, Z.; Goulas, J.; Parker, E.; Sun, Y.; Zhou, X.D.; Fei, L. Review on covalent organic frameworks and derivatives for electrochemical and photocatalytic CO_2 reduction, *Catal. Today.* **2022**.
9. Hamzehpoor, E.; Jonderian, A.; McCalla, E., Perepichka, D.F. Synthesis of Boroxine and Dioxaborole Covalent Organic Frameworks via Transesterification and Metathesis of Pinacol Boronates. *J. Am. Chem. Soc.* **2021**, *143*, 13274-13280.
10. van der Staaij, F.M.; van Keulen, I.M.; von Hauff, E. Organic Photovoltaics: Where Are We Headed?, *Solar RRL*, **2021**, *5*, 2100167.
11. Hou, J.; Inganas, O.; Friend, R. H.; Gao, F. Organic Solar Cells¨Based on Non-Fullerene Acceptors. *Nat. Mater.* **2018**, 17, 119−128.
12. Zhang, H.; Li, Y.; Zhang, X.; Zhang, Y.; Zhou, H. Role of interface properties in organic solar cells: from substrate engineering to bulk-heterojunction interfacial morphology. *Mater. Chem. Front.* **2020**, *4*, 2863−2880.
13. Tumbleston, J. R.; Collins, B. A.; Yang, L.; Stuart, A. C.; Gann, E.; Ma, W.; You, W.; Ade, H. The Influence of Molecular Orientation on Organic Bulk Heterojunction Solar Cells. *Nat. Photonics* **2014**, *8*, 385−391.
14. Zhang, Y.; Zhou, H.; Seifter, J.; Ying, L.; Mikhailovsky, A.; Heeger, A. J.; Bazan, G. C.; Nguyen, T.-Q. Molecular doping enhances photoconductivity in polymer bulk heterojunction solar cells, *Adv. Mater.* **2013**, *25*, 7038−7044.
15. Scaccabarozzi, A. D.; Basu, A.; Anies, F.; Liu, J.; Zapata-Arteaga, O.; Warren, R.; Firdaus, Y.; Nugraha, M. I.; Lin, Y.; Campoy-Quiles, M.; Koch, N.; Muller, C.; Tsetseris, L.; Heeney, M.; Anthopoulos, T. D. Doping Approaches for Organic Semiconductors. *Chem. Rev.* **2022**, *122*, 4420−4492.

Appendix A

Experimental methods for PEC CO_2 reduction to syngas based on III-Nitride nanostructures

A.1 Molecular beam epitaxial (MBE) growth for III-Nitride nanostructures

Molecular-beam epitaxy (MBE) is a precise approach for the defect-free growth of various thin-film semiconductors. Molecular-beam epitaxy is performed in a high vacuum or ultra-high vacuum (UHV) growth chamber, which can reduce impurity inclusion in the epitaxial layers, resulting in high quality crystalline planar structures and nanowires. It is also well known as an efficient bottom-up strategy for growing III-nitride nanowires. The MBE systems are made up of three primary vacuum chambers: an intro chamber (or load lock chamber), a buffer chamber, and a growth chamber. Using a cryo pump and an ion pump, a 10^{-12} Torr base pressure is maintained in the growth chamber. MBE system consists of two or more Knudsen effusion cells (K-cells) in the bottom of a UHV chamber, aligned towards the middle of the chamber, where a sample holder with a substrate is located (Figure A.1).

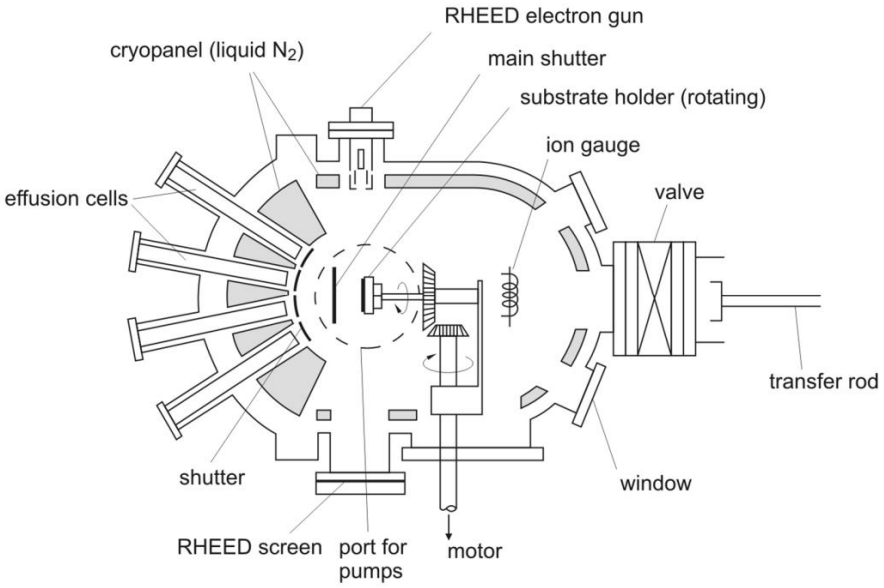

Figure A.1: Schematic of the MBE growth chamber.

Each K-cell contains a different element in ultra-pure solid form that will be employed in thin film synthesis. The MBE growth process begins with heating the K-cells to the required temperature until the elements in each cell reach a sublimation point. The shutters are then opened, allowing physical vapour from each K-cell to diffuse into the chamber until it reaches the substrate. The reflection high-energy electron diffraction (RHEED) unit is used to characterise the NWs in-situ during growth. Electrons generated by the RHEED gun and incident at a very low angle with respect to the sample surface are diffracted, and the resulting diffraction pattern is observed. The observed spotty patterns during the nanowire growing process would provide general information about the nanowires such as length, diameter, orientation, and density. The nanowires properties can be controlled by growth variables such as the III/V flux ratio, substrate temperature, and growth rate.

The GaN nanowires in this study were grown on a 2-inch p-n Si wafer at McGill University via the Veeco GENxplor MBE system under nitrogen-rich conditions. This system equipped with Ga, In, Al, Mg, and Si Knudsen effusion cells, as well as a substrate heater with continuous azimuthal rotation (CAR) to provide great uniformity for material deposition on the substrate. The GaN growth conditions are as follows: a growth temperature of 790 ^{o}C for 1.5 h, a Ga beam equivalent pressure of ~6×10^{-8} Torr, a nitrogen flow rate of 1 standard cubic centimeter per minute (sccm), and a plasma power of 350 W.

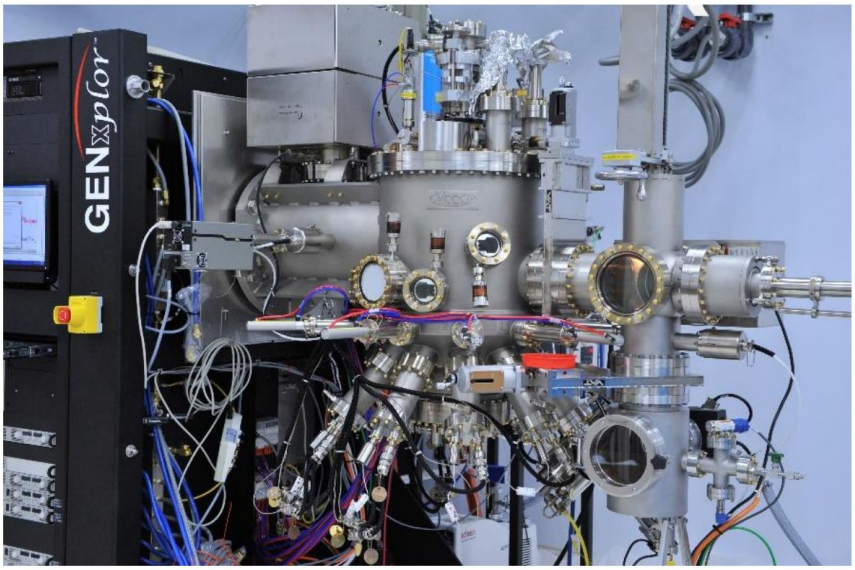

Figure A.2: The Vecco GENxplor Molecular Beam Epitaxy (MBE) system.

A.2 Fabrication of n^+-p Si substrates

To fabricate the n^+-p Si substrate, at first the double side polished p-type Si (100) wafer was spin-coated with liquid phosphorous dopant precursor on one side to form the n^+-Si layer, followed by liquid boron dopant precursor on the other side to form the p^+-Si back field layer. Next, the thermal diffusion process was performed about 950oC for 6 hr under argon gas flow in a horizontal furnace. Lastly, the residue of the precursor was carefully removed by buffered oxide (BHF) etch solution.

A.3 Co-catalyst deposition

To enhance the carrier extraction efficiency and reduce the overpotential required for CO_2 reduction co-catalysts are frequently required. In our study, several cocatalysts have been explored to improve the syngas performance such as Au/Pt, Au/TiO_2, Pt/ZnO and Pd-TiO_2. The deposition of such co-catalysts on the GaN nanowire surfaces can be done with various approaches, such photo deposition, electron beam, or atomic layer deposition.

A.2.1 Pt and TiO_2 deposition: Pt nanoparticles and TiO_2 ultrathin layer were deposited on GaN nanowires surface in sequential order using photodeposition and atomic-layer deposition (ALD), respectively. First, Pt nanoparticles were photodeposited on the GaN/n^+-p Si wafer sample in a sealed Pyrex chamber with a quartz lid. 60 mL deionized water (purged with Ar for 20 min prior to the usage), 15 mL methanol, and 20 μL of 0.2 M H_2PtCl_6 (99.9%, Sigma Aldrich) were added in the chamber. The chamber was then evacuated and irradiated for 30 min using 300 W Xe lamp (Excelitas Technologies) for the photodeposition of Pt nanoparticles. Then the Pt deposited sample was taken out and dried for TiO_2 deposition. TiO_2 ultrathin film was deposited with a Gemstar Arradiance 8 ALD tool using Tetrakis(dimethylamido)-titanium (TDMAT, Sigma-Aldrich) and deionized water as reactants at 225 °C. In an ALD cycle, TDMAT was pulsed into the chamber for 0.7 s with a N_2 purge time of 23 s, after which water was pulsed into the chamber for 0.022 s before another 23 s purge with N_2. The ALD cycling was repeated 18 times, which provided a TiO_2 film of 1 nm thickness. The TiO_2 coating thickness can be precisely tuned by varying the number of repeated ALD cycles. Finally, the as-prepared sample was annealed at 400 °C for 10 min in forming gas (5% H_2, balance N_2) at a flow rate of 200 sccm. For comparison, GaN/n^+-p Si with individual Pt or TiO_2 deposition were prepared in the same conditions.

A.2.2 Au nanoparticles: Au nanoparticles were deposited on GaN nanowires using an e-beam evaporator at a deposition rate of 0.1 Å/s for 500 s, followed with thermal annealing in Ar at 650

oC for 2 min. During the annealing process, small Au nanoparticles migrated and coalesced to form large Au nanoparticles on GaN nanowires for decreasing the surface energy. Au was favorable to grow on the c-plane of GaN nanowires as a tipped heterostructure. This can be explained by the smaller formation energy for Au on c-plane GaN, partly due to the smaller lattice mismatch between Au(111) and c-plane GaN compared to m-plane GaN (0.24, 0.26 and 0.28 nm, respectively). Prior to the Au e-beam deposition, the GaN nanowires on p-n Si substrate was pre-treated with concentrated HCl solution for 30 s to remove native oxide.

A.2.3 Other metal/oxide deposition: The synthesis procedure for Pd-TiO_2/GaN/n^+-p Si is similar to that of Pt-TiO_2/GaN/n^+-p Si described above, except for the use of Pd $(NO_3)_2$ (99%, Sigma Aldrich) instead of H_2PtCl_6 in the photodeposition process. Pt-ZnO/GaN/n^+-p Si was prepared by following the same protocol by depositing Pt nanoparticles and ZnO ultrathin layer on GaN nanowires surface in sequential order. Pt nanoparticles were photodeposited using the same conditions described above. ZnO ultrathin film was photodeposited by using 10 μL of 0.2 M $Zn(NO_3)_2$ (98%, Sigma Aldrich) as the precursor in 75 ml aqueous methanol (20 vol%) solution for 30 min under 300 W Xe lamp irradiation.[3]

A.4 Structural Characterization:

A.3.1 Scanning electron microscope (**SEM**): The morphology of nanowires (Length, diameter, and the areal density) was characterized by SEM. It is a type of electron microscope that produces images of a sample by scanning the surface with a focused beam of electrons. SEM images are obtained from an Inspect F-50 FE-SEM system at an accelerating voltage of 5-10 keV and emission current of 5-10 μA.

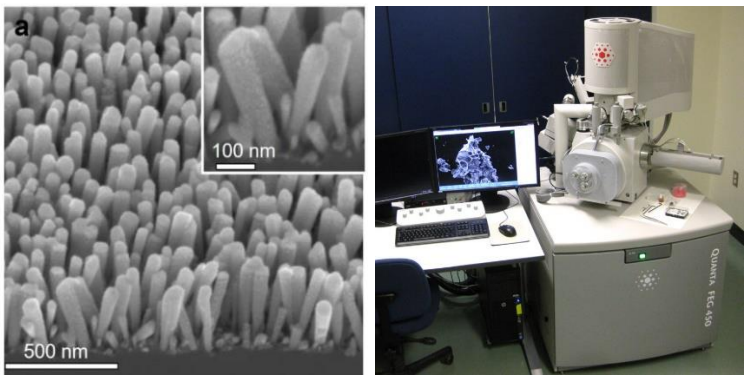

Figure A.3: SEM image of spontaneous grown nanowires where (Au deposited). (b) FEI Quanta 450 Environmental Scanning Electron Microscope (FE-ESEM)

A.3.2 Transmission Electron Microscopy (TEM) is a microscopy technique in which a beam of electrons is transmitted through a specimen to form an image with to atomic scale resolution. TEM images were obtained on FEI Tecnai G2 F20 microscope operated at 200 keV, with EDX. The nanowire samples were scratched off from the Si substrate onto a Cu grid prior to the TEM analysis.

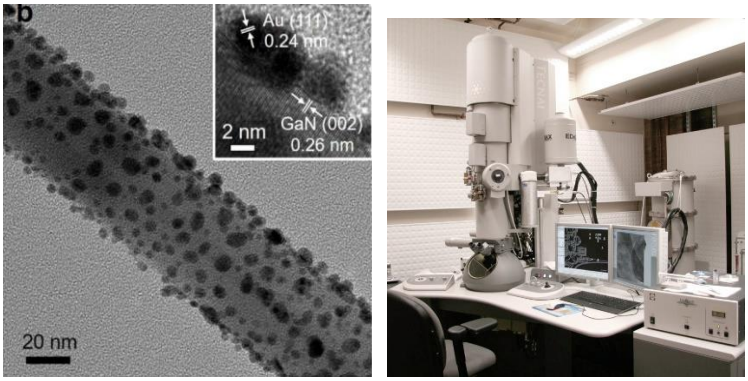

Figure A.4: (a) TEM image (and HRTEM image) of Au-deposited GaN NW(b) EI Tecnai G2 F20 200 kV Cryo-STEM.

A.3.3 X-ray Photoelectron Spectroscopy (XPS) is surface-sensitive technique for measuring chemical composition, chemical bonds, empirical formula and electronic states by analyzing the surface/near-surface region of a given material. Surface chemical compositions of MBE-grown nanostructures were analyzed by XPS in a Thermo Scientific K-Alpha XPS system with a monochromatic Al Kα source (hν = 1486.6 eV). The binding energies were calibrated using the C1s peak at 284.8 eV of surface adventitious carbon.

A.3.4 Inductively coupled plasma atomic emission spectroscopy (**ICP-AES**)

ICP-AES analyses were performed on a Thermo Scientific iCAP 6000 Series inductively coupled plasma–atomic emission spectroscopy instrument. The samples were digested in aqua regia (HNO_3:HCl=1:3) at 95 °C for 3 h prior to the analysis.

The CO_2 adsorption capability of the samples was evaluated according to previously described procedure.[1] A quarter of 2-inch sample was first degassed under vacuum at 300 ^oC for 1 h and then cooled to room temperature, followed by purging of high-purity CO_2 (Air Liquid, 99.995%) for 0.5 h to reach a saturation level. Then the system was flushed with Ar (Air Liquid, 99.999%) for 1 h to remove gas phase and weakly adsorbed CO_2. Then, the sample was heated at 400 ^oC. The desorbed CO_2 was quantitatively analyzed by gas chromatograph (GC, Shimadzu GC-2014).

A.5 PEC measurements

PEC CO_2 reduction was carried out in an air-tight, three-electrode cell using a Pt-TiO_2/GaN/n^+-p Si working electrode, a Pt wire counter electrode and a Ag/AgCl reference electrode. The working electrode (0.2-0.3 cm^2) was prepared as follows: a Ga-In eutectic (99.99%, Sigma-Aldrich) was applied on the backside of the Si substrate to form Ohmic contact, which was attached to a copper wire with silver paste (Ted Pella). After the drying of paste, the backside and edges of the Si wafer sample was then encapsulated with epoxy (PC-Clear) to prevent contacting with electrolyte. The electrolyte was CO_2-purged aqueous solution of 0.5 M $KHCO_3$ (Fisher Chemical).

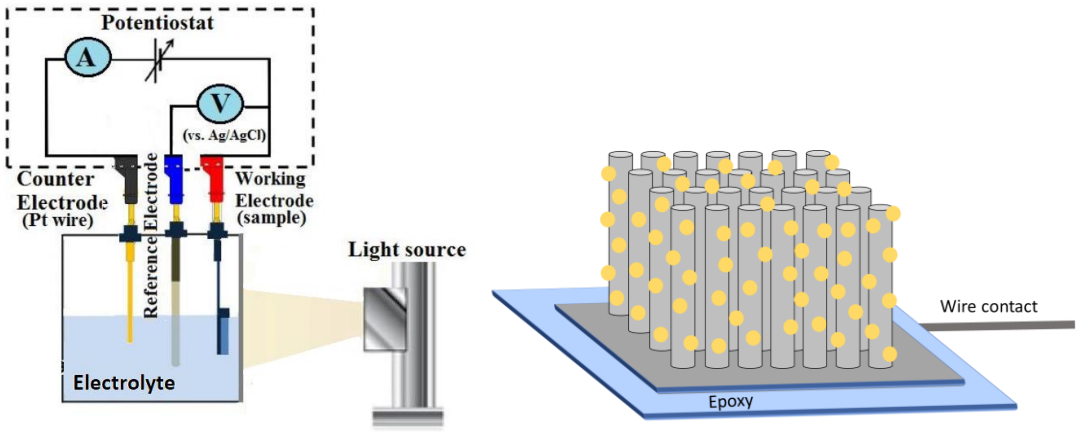

Figure A.5: (a) PEC experiment set up, (b) preparation of nanowire arrays as a photoelectrode.

Prior to the CO_2 reduction experiments, electrolyte (40 mL in the working compartment with gas headspace 40 mL) was added into the cell, which was saturated with CO_2 (Air Liquid, 99.995%) by sparging the solution for 20 min. The light source was a 300 W Xe lamp (Excelitas Technologies) with a calibrated light intensity of 800 mW cm^{-2} (~8 suns) on the sample surface. The current and potential data were collected by a potentiostat (Gamry Instruments, Interface 1000). The current-potential (J-V) curve was performed at a scan rate of 20 mV/s. The recorded potentials vs. Ag/AgCl were converted to vs. RHE by the following equation: E(vs. RHE) = E(vs. Ag/AgCl) + (0.0591 × pH) + 0.1976, where 0.1976 is a conversion factor from the Ag/AgCl electrode to RHE at 25 ^oC. After the photoelectrolysis, the gas products were analysed by a GC (Shimadzu GC-8A) with a thermal conductivity detector (for H_2) and a GC (Shimadzu GC-2014) with a flame ionization detector (for CO and hydrocarbons). Liquid products in electrolyte were analyzed afterwards by quantitative nuclear magnetic resonance (NMR, Bruker AV-500) using 4,4-dimethyl-4-silapentane-1-sulfonic acid (DSS, Sigma Aldrich) as an internal standard. Faradaic

efficiency (FE) was calculated by determining the amount of charge needed for each product and then dividing by the total charge passed during the test. To confirm the carbon source of the product, ^{13}C-labeled isotope experiment was conducted in $^{13}CO_2$ (99%, Sigma Aldrich)-saturated ^{13}C-bicarbonate solution ($NaH^{13}CO_3$, 98%, Sigma Aldrich) under otherwise identical conditions. The gas products were analyzed by gas chromatography mass spectrum (GC-MS, Agilent 5975).

The half-cell solar-to-syngas efficiency η_{STS} was calculated using the following equation:

$$\eta_{STS}(\%) = \left[\frac{J(\mathrm{mA \cdot cm^{-2}}) \times \mathrm{FE_{CO}}(\%) \times (1.34 - V_{\mathrm{bias}})(V) + J(\mathrm{mA \cdot cm^{-2}}) \times \mathrm{FE_{H_2}}(\%) \times (1.23 - V_{\mathrm{bias}})(V)}{P_{\mathrm{in}}(\mathrm{mW \cdot cm^{-2}})} \right]$$

where J is the photocurrent density, $\mathrm{FE_{CO}}$ and $\mathrm{FE_{H_2}}$ represent Faradaic efficiency towards CO and H_2 formation, V_{bias} is the applied bias, and P_{in} is the light power density (800 mW cm^{-2}).

Appendix B

Experimental methods for development of high performance and stable polymer OFETs using doping strategy

B.1 Thin film transistor fabrication

B.1.1 Material preparation: Poly[[2,3,5,6-tetrahydro-2,5-bis(2-octyldodecyl)-3,6-dioxopyrrolo[3,4-c]pyrrole-1,4-diyl]-2,5- thiophenediylthieno[3,2-b]thiophene-2,5-diyl-2,5-thiophenediyl] (DPP-DTT) was purchased from 1-Material (Mw = 50 kg mol^{-1}) and used as received. The DPP-DTT polymer solution with a concentration of 5 g L^{-1} in chlorobenzene−chloroform solvent mixture (1:1 volume ratio) was prepared by stirring overnight at 70 °C. NF acceptors were synthesized according to our previous reports (ref). The fresh dopant solution (5 g L^{-1}) in chlorobenzene was prepared separately by stirring at 50 °C. The NF solution was then added to the DPP-DTT solution in various ratios to achieve the desired dopant concentrations and stirred for an hour prior to spin coating.

B.1.2 Substrate preparation: Prior to deposition, the SiO_2 dielectric/ doped Si substrates were cleaned by immersing in piranha solution (2:1 mixture of conc. H_2SO_4 and 30% H_2O_2) for 15 min followed by sonication in acetone and isopropyl alcohol for 10 min in each solvent to remove any dust, physiosorbed impurities. The substrates were dried in a stream of nitrogen and treated by oxygen plasma cleaner (HARICK PDC-32G) for 5 to 10 min. The substrates then are functionalized with self-assembled monolayer (SAM) by immersing in octadecylsiloxane (ODTS) solution in toluene (1%) at 70 °C for 50 min, followed by rinsing with isopropyl alcohol and drying on a hot plate at 100 °C for 5 min.

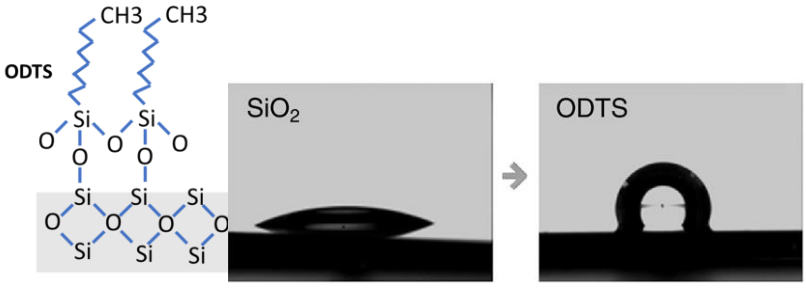

Figure B.1: ODTS SAM treatment of SiO_2.

B.1.3 Polymer film deposition: The polymer films in this study were deposited on the so-treated substrates using spin-coating. Spin coating is a solution deposition technique to produce a thin-film by using centrifugal force and requires a liquid–vapor interface. In a typical procedure, a liquid is placed at the center of a circular surface and is rapidly rotated to produce uniform films of 1–10 μm in thickness. The centripetal acceleration causes the liquid to spread across the substrate, dispersing any excess solution from the edges of the substrate. Final film thickness and other properties will depend on the nature of the coating (viscosity, drying rate, percent solids, surface tension, etc.) and the parameters chosen for the spin process such as the rotation speed and time. In this study, polymer films are spin-coated at 1500 rpm for 60 seconds on so-treated substrates in ambient air, resulting in a film thickness of 20-25 nm.

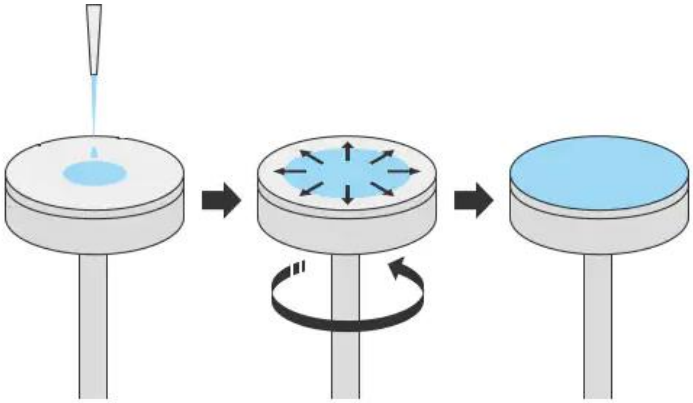

Figure B.2: Spin coating process.

B.1.4 Thermal annealing: As the solvent usually evaporates relatively quickly during spin coating, there often is not much time for any of the molecular ordering. Therefore, post-deposition treatments such as annealing are sometimes employed. We annealed pristine and doped DPP-DTT polymer films at 170°C for 30 min in air followed by slow cooling down. The annealing temperature is below decomposition temperature of NF dopants according to TGA measurements and above the melting temperature of polymer according to DSC analysis.

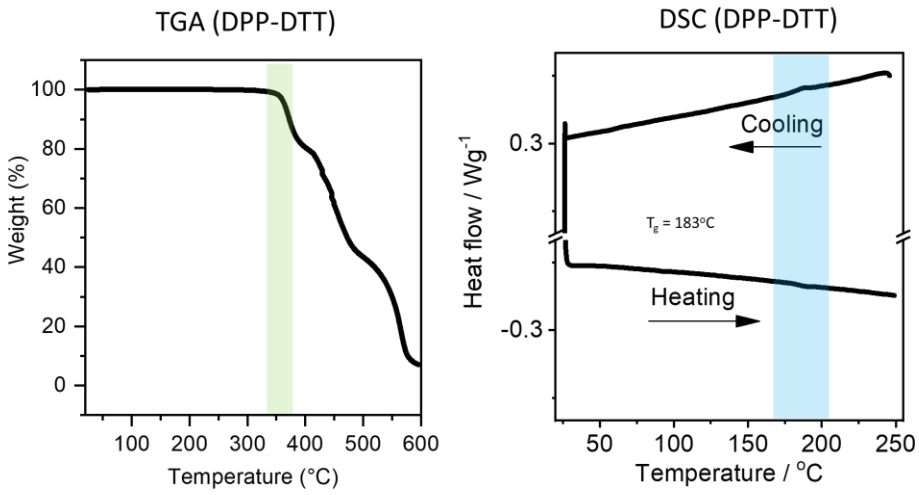

Figure B.3: TGA and DSC analysy of pristine DPP-DTT polymer.

B.1.5 Metal contacts

- Top-Contact configuration: The next step to fabricate Top-Contact bottom-gate (TC-BG) transistors is to deposit the source and drain electrodes onto the SC films. For p-type organic semiconductors, gold (Au) is a proper metal for the source/drain metal owing to its work function value of $\varphi m \approx -5.1$ eV, which compares well to the HOMO level of many p-type organic semiconductors. The source/drain Au electrodes for this thesis are deposited by thermal evaporator through shadow masks. The tungsten boat containing high purity gold is electrically heated while the substrates are positioned above it and the evaporation chamber is under vacuum (10^{-6} mbar). An oscillating quartz crystal monitors the rate of evaporation, and a feedback loop regulates the amount of electricity passing through the crucible. A shadow mask is placed on the surface of the substrate, enabling the evaporated metal to be deposited only in the exposed areas, resulting in 50 nm Au electrodes with varying channel dimensions. The 15 x 20 mm mask employed in this work allows for the patterning of 20 TFTs per substrate, with channel lengths ranging from 30 to 80 µm and a channel width of 1000 µm. The heavily doped Si on SiO_2/Si substrate is used as bottom gate contact.

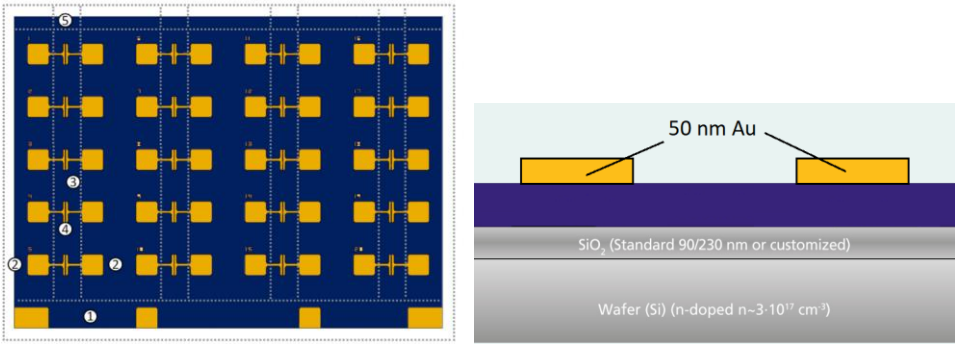

Figure B.4: Top-Contact configuration OFET.

- Bottom-Contact configuration: In this study we also used bottom contact bottom gate devices in which organic active films deposited on SiO_2 substrates with pre-patterned Au electrodes (The poor adhesion of Au on SiO_2 requires the use of a 10nm ITO film as an adhesion layer). This geometry is appropriate for fundamental studies because it ensures high injection efficiency and prevents reaction between the metal and the organic film. However, the growth of the organic film near the edges of the metal contacts frequently has a negative impact because the grain size is smaller at these critical locations, affecting device performance. This substrate offers OFETs with channel lengths ranging from 5 to 20 µm and channel widths of 10000 µm.

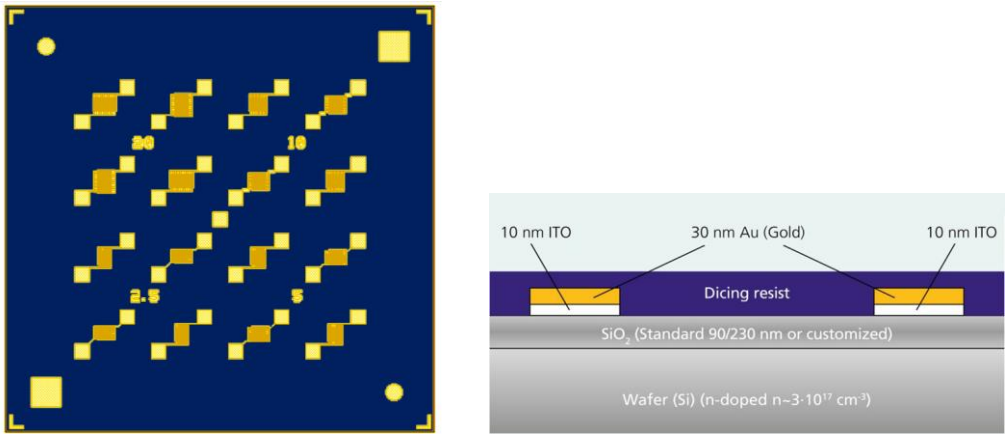

Figure B.5: Bottom-Contact configuration OFET.

B.2 Electrical characterization

Electrical characterization of OFET devices were carried out using a Keithley 4200 source measurement unit (SMU) as a semiconductor parameter analyzer. The measurements were taken with a probe station that was placed in a hermetically sealed chamber under various environmental

conditions such as vacuum, nitrogen, oxygen, or ambient atmosphere. These probes make contact with the source, drain, and gate electrodes using an optical microscope and video monitor, allowing voltages and currents to be applied and measured to characterize the transfer (I_{DS}-V_{GS}) and output characteristics (I_{DS}-V_{DS}). A continuous voltage is applied to the gate and/or drain in bias stress applications to study the device's transfer characteristic (I_{DS}-t). To study the activation energy the temperature-dependent measurement is performed on a thermal platform that contains both a resistive heating element and a cooling system in thermal contact with a semiconductor wafer and can reach temperatures ranging from 4.5 K to 475 K. To avoid parasitic current during device characterization, each OFET is isolated from the substrate and each other devices using a thin needle.

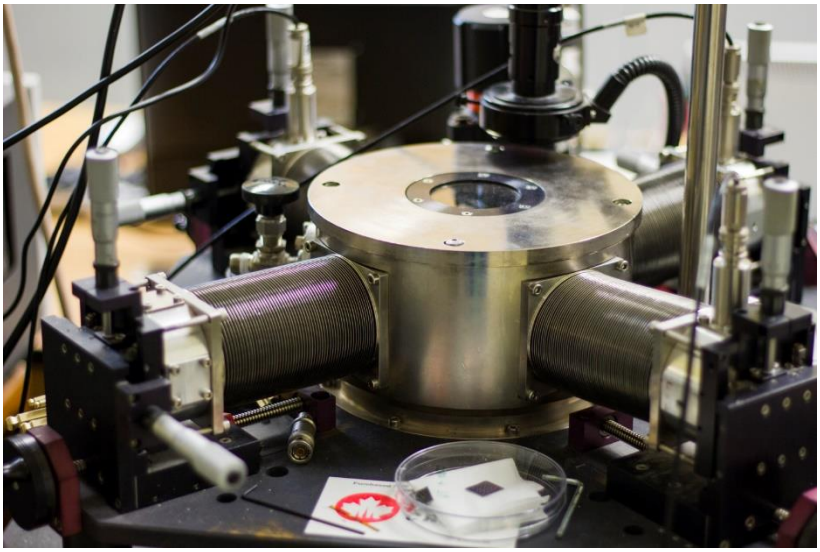

Figure B.6: Schematic of probe station equipment for measuring I-V characteristics of OFETs.

B.3 Atomic force microscopy

Atomic force microscopy (AFM) is a highly accurate imaging tool to to visualize the morphology of thin films. A Multimode 8-HR atomic force microscope (Bruker) operating in tapping mode was used to study the surface topography and phase of the polymer thin-films with nanoscale resolution. The AFM consists of a small cantilever which moves across the surface at a constant vibration frequency. Any interplay that the tip has with the surface will result in a change in the vibration frequency, which is detected by a change in a laser reflected from the cantilever; this change is measured by a photodiode and the output signal depicts an outline of the sample surface.

Once the imaging has taken place, Gwyddion 2.55 software is used for statistical and image analysis.

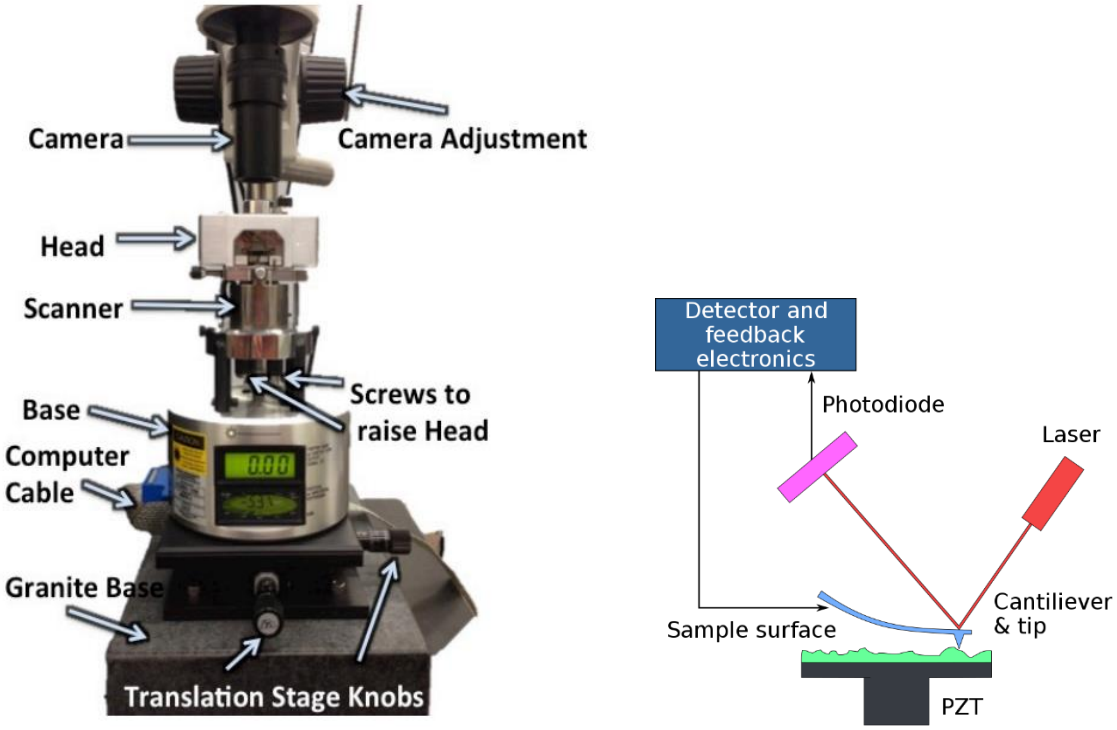

Figure B.7: Atomic force microscopy system.

B.4 Electron paramagnetic resonance measurement

Electron paramagnetic resonance (EPR) is a spectroscopic is a method for studying unpaired electrons in materials. We used EPR technic to explore the presence of unpaired electron in doped polymer and to measure the concentration of unpaired electrons in the pristine and doped polymer films. All EPR spectra were recorded at room temperature using a Bruker Elexsys E580 X-band continuous-wave spectrometer. The spectra were acquired at a microwave power of 63 μW and a 0.2 mT modulation amplitude. All samples are measured in solid form and prepared from the DPP-DTT polymer solution with a concentration of 5 g L^{-1} in chlorobenzene, doped with desired concentrations (0−10 mol %). EPR tubes were filled with 100 μL of each solution, and then the solvent was removed by freeze-drying. Spin-counting measurements are described in the SI, and the reported spin density is calculated assuming density of the films to be 1 g cm−3. 4.5. Atomic Force Microscopy. Topographical information was carried out using a Multimode 8 scanning

probe microscope (Bruker) operating in tapping mode. Subsequent data analysis was performed using Gwyddion 2.55 software.

B.5 Optical Spectroscopy

UV−vis−NIR spectroscopy is a powerful analytical technique to determine the optical properties (transmittance, reflectance, and absorbance) of materials. UV−vis−NIR spectroscopy was performed on thin films and solutions using a JASCO V-670 spectrophotometer. Solutions of NF-doped DPP-DTT were prepared in chlorobenzene, and the spectra were recorded in 10 mm path length quartz cuvettes. Solid-state absorption spectra were recorded for thin films spin-coated on quartz substrates at 1000 rpm from 5 g L^{-1} chlorobenzene DPP-DTT solutions doped with the desired concentration of NF.

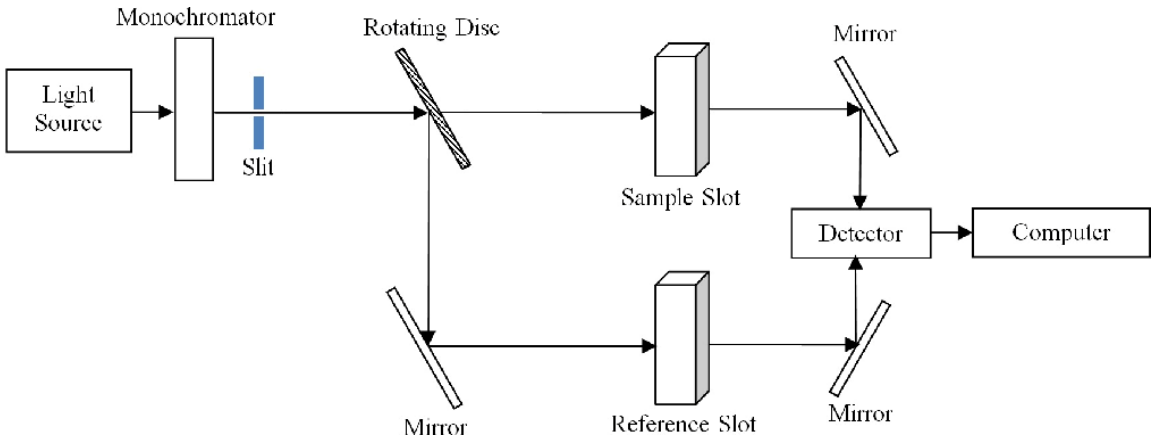

Figure B.8: The schematic of UV−vis−NIR spectroscopy.

B.6 Photoelectron Yield Spectroscopy in Air

Photoelectron Yield Spectroscopy in Air (PYSA)is a technique used to analyze the work function of a surface PESA was carried out using the RKI AC-2 instrument. PYSA data were recorded for pristine and TeNF-doped thin films. Samples were spincoated on quartz substrates at 1500 rpm from 5 g L^{-1} chlorobenzene DPP-DTT solutions doped with the desired concentration of NF. The ionization potential for each sample is presented as an average of five different measurements.

B.7 X-ray Diffraction and Grazing Incidence Wide-Angle X-ray Diffraction (GIWAXS).

X-ray Diffraction (XRD) is the experimental science determining the atomic and molecular structure of a crystal, in which the crystalline structure causes a beam of incident X-rays to diffract into many specific directions. By measuring the angles and intensities of these diffracted beams the crystallographic data is determined. XRD data of this study were collected on a Bruker D8 Phaser instrument using a nickel-filtered Cu Kα (λ = 0.1541 Å) radiation. The spectra of all samples were recorded in the 2θ range of 3−30 degrees.

GIWAXS data was collected on an Anton Paar SAXS point 2.0 system with a Primux 100 micro X-ray source (Cu) and a 2D hybrid photon counting detector. Measurements were conducted on pristine and TeNF-doped DPP-DTT films, which are prepared on the SiO_2 substrate with the same conditions of device fabrication. The coherence length is estimated from $L = 2\pi/\Delta q$, where Δq is the full width at half-maximum of the lamellar peak. Also, d-spacing, along the out-of-plane direction, is calculated using $d = 2\pi/q$, where q is the (100) peak position.

B.9 Impedance Spectroscopy.

Measurements were performed in metal−insulator−semiconductor devices n^{++}-Si/ SiO_2 (200 nm)/ Cytop films (20 nm)/polymer layer (20 nm)/Au. Cytop was spincoated on top of the SiO_2 dielectric layer from a 1:10 diluted solution (CTL-809M in CT-Solv.180.) at 2000 rpm and then annealed at 120 °C for 1 h. The stack of 200 nm SiO_2 and 20 nm CYTOP served as the insulator layer. The polymer layer was spin-coated at 1000 rpm on top of the CYTOP layer from 0.3, and 6 mol % doped DPP-DTT solutions, followed by thermal evaporation of the gold contact. Au and n^{++}-Si contacts were used as the reference/counter and working electrodes, respectively. The impedance spectra were measured using the Biologic SP-300 system in the frequency range between 100 Hz and 3 MHz with a current amplitude signal of 50 mV and various direct current biases ranging from −10 to 10 V. The number of free charge carriers (p) is calculated using the Mott−Schottky method.

List of Publications

First and co-first author publications

1. **Ghamari, P.;** Niazi, M. N.; Perepichka, D. F. Improved environmental and operational stability of polymer field-effect transistors via doping with tetranitrofluorenone. *to be submitted,* 2022.
2. **Ghamari, P.;** Niazi, M. N.; Perepichka, D. F. Controlling Structural and Energetic Disorder in High-Mobility Polymer Semiconductors via Doping with Nitroaromatics, *Chem. Mater.* 2021.
3. Chu, S. Ou P; * Rashid, R.; *** Ghamari, P**.; * Wang, R. Tran, H. Zhao, S. Song, J. Mi, Z. Controllable syngas Generation from Photoelectrochemical CO_2 reduction with Dual cocatalyst, *iSience.* 2020. [* equal contribution]
4. Chu, S.* Ou, P; * **Ghamari, P.; *** Vanka, S.; Zhou, B.; Shih, I.; Song, J.; Mi, Z. Photo electrochemical CO_2 Reduction into Syngas with the Metal/Oxide Interface, *J. Am. Chem. Soc.* 2018. [* equal contribution]

Co- author publication

5. Liu, Y-H.; **Ghamari, P.;** and Perepichka, D. F. High performance Organic Phototransistors based on Acenaphthylenes, *to be submitted,* 2022.
6. Che, Y.; Niazi, M.R.; Chan, Q.; **Ghamari, P**.; Xiao, S.; Izquierdo, R.; Perepichka, D. F. Furan-Based A-D-A Acceptors for Future Organic Photovoltaics, *to be submitted*. 2022.
7. Niazi, M. R.; Hamzehpoor, E.; **Ghamari, P**.; Perepichka, I.F.; Perepichka. D. F. Nitroaromatics as n-type organic semiconductors for field effect transistors, *Chem. Commun.*, 2020.
8. Zhou, B.; Kong, X.; Vanka, S.; Cheng, S.; Chu, S.; **Ghamari, P**.; Wang, Y.; Botton, G.; Cuo, H.; and Mi, Z. GaN:Sn nanoarchitecture integrated on silicon platform for converting CO_2 towards HCOOH by photocatalysis, , *Energy Environ. Sci.*, 2019.
9. Zhou, B.; Kong, X.; Vanka, S.; Chu, S.; **Ghamari, P**.; Wang, Y.; Pant, P.; Shih, I.; Guo, H.; Mi, Z. Gallium, nitride nanowire as a linker of molybdenum sulfides and silicon for Photoelectrocatalytic water splitting. *Nat. Commun.*, 2018.

10. Vanka, S.; Wang, Y.; **Ghamari**, **P**.; Chu, S.; Pandey, A.; Bhattacharya, P.; Shih, I.; Mi. Z.; A High Efficiency Si Photoanode Protected by Few-Layer $MoSe_2$, Sol. *RRL*, 2018.

Conference Presentations

1. **Ghamari, P.**; Niazi, M. N.; Perepichka, D. F. Towards high-performance and stable polymer OFETs using nitroaromatics doping. International Conference on the Science and Technology of Synthetic Metals (ICSM), Glasgow, 2022.
2. **Ghamari, P.**; Niazi, M. N.; Perepichka, D. F. High-Performance Solution-Processed Organic Field-Effect Transistors via Doping with Nitroaromatics, 14th International Symposium on Flexible Organic Electronics (ISFOE21), Greece, 2021.
3. **Ghamari, P.**; Niazi, M. N.; Perepichka, D. F. Nitrofluorene Derivatives as p-Dopants in High-Performance Solution-Processed Polymer Field-Effect Transistors, EMRS Spring meeting, 2021.
4. Low cost Schottky barrier solar cells based on CuO fabricated by sputtering method, **Ghamari, P.;** Raissi, F.; Manavizadeh, N.; International Conference and Exhibition on Solar Energy (ICESE), Iran, 2015.

Bibliography in Alphabetical Order

Abdou, M. S.; Orfino, F. P.; Son, Y.; Holdcroft, S. Interaction of Oxygen with Conjugated Polymers: Charge Transfer Complex Formation with Poly(3-alkylthiophenes). *J. Am. Chem. Soc.* **1997**, *119*, 4518−4524.

Abe, R. Recent Progress on Photocatalytic and Photoelectrochemical Water Splitting under Visible Light Irradiation. *J. Photochem. Photobiol., C* **2010**, *11*, 179−209.

Akamuta, H.; Inokuchi, H.; Matsunaga, Y. Electrical Conductivity of the Perylene–Bromine Complex. *Nature*. **1954**, *173*, 168-169.

Ali, S.; Flores, M. C.; Razzaq, A.; Sorcar, S.; Hiragond, C. B.; Kim, H. R.; Park, Y. H.; Hwang, Y.; Kim, H. S.; Kim, H.; Gong, E. H.; Lee, J.; Kim, D.; In, S. Gas Phase Photocatalytic CO_2 Reduction, "A Brief Overview for Benchmarking. *Catalysts* **2019**, *9*, 727.

Alotaibi, B.; Fan, S.; Wang, D.; Ye, J.; Mi, Z. Wafer-Level Artificial Photosynthesis for CO_2 Reduction into CH4 and CO Using GaN Nanowires. *ACS Catal*. **2015**, *5*, 5342−5348.

AlOtaibi, B.; Kong, X.; Vanka, S.; Woo, S. Y.; Pofelski, A.; Oudjedi, F.; Fan, S.; Kibria, M. G.; Botton, G. A.; Ji, W.; Guo, H.; Mi, Z. Photochemical carbon dioxide reduction on Mg-doped Ga (In) N nanowire arrays under visible light irradiation, *ACS Energy Lett.* **2016**, *1*, 246-252.

Andrei, V.; Reuillard, B.; and Reisner, E. Bias-free solar syngas production by integrating a molecular cobalt catalyst with perovskite-BiVO4 tandems. **2020,** *Nat. Mater*. *19*, 189–194.

Arai, T.; Tajima, S.; Sato, S.; Uemura, K.; Morikawa, T.; Kajino, T, Selective CO_2 conversion to formate in water using a CZTS photocathode modified with a ruthenium complex polymer, *Chem. Commun*. **2011**, *47*, 2664-12666

Arteev, D.S.; Sakharov, A.V.; Zavarin, E.E.; Lundin, W.V.; Smirnov, A.N.; Davydov, V.Y.; Yagovkina, M.A.; Usov, S.O.; Tsatsulnikov, A.F. Investigation of Statistical Broadening in InGaN Alloys. *J. Phys. Conf. Ser*. **2018**, *1135*, 012050

Ausserlechner, S. J.; Gruber, M.; Hetzel, R.; Flesch, H.-G.; Ladinig, L.; Hauser, L.; Haase, A.; Buchner, M.; Resel, R.; Schü rrer, F.; Stadlober, B.; Trimmel, G.; Zojer, K.; Zojer, E. Mechanism of Surface Proton Transfer Doping in Pentacene Based Organic Thin-Film Transistors. *Phys. Status Solidi A.* **2012**, *209*, 181−192.

Babuji, A.; Temiño, I.; Pérez-Rodríguez, A.; Solomeshch, O.; Tessler, N.; Vila, M.; Li, J.; Mas-Torrent, M.; Ocal, C.; Barrena, E. Double Beneficial Role of Fluorinated Fullerene Dopants on Organic Thin-Film Transistors: Structural Stability and Improved Performance. *ACS Appl. Mater. Interfaces* **2020**, *12*, 28416−28425.

Back, J. Y.; Yu, H.; Song, I.; Kang, I.; Ahn, H.; Shin, T. J.; Kwon, S.-K.; Oh, J. H.; Kim, Y.-H. Investigation of Structure−Property Relationships in Diketopyrrolopyrrole-Based Polymer Semiconductors via Side-Chain Engineering. *Chem. Mater*. **2015**, *27*, 1732−1739.

Baeg, K. J.; Bae, G. T.; Noh, Y. Y. Efficient charge injection in p-type polymer field-effect transistors with low-cost molybdenum electrodes through V_2O_5 interlayer. *ACS Appl. Mater. Interfaces*. **2013**, *5*, 5804-5810.

Barf, M.-M.; Benneckendorf, F. S.; Reiser, P.; Bäuerle, R.; Köntges, W.; Müller, L.; Pfannmöller, M.; Beck, S.; Mankel, E.; Freudenberg, J.; et al. Compensation of Oxygen Doping in P-Type Organic Field-Effect Transistors Utilizing Immobilized n-Dopants. *Adv. Mater. Technol.* **2020**, 2000556.

Barra, M.; Girolamo, F. D.; Chiarella, F.; Salluzzo, M.; Chen, Z.; Facchetti, A.; Anderson, L.; Cassinese, A. Transport Property and Charge Trap Comparison for N-Channel Perylene Diimide Transistors with Different Air-Stability. *J. Phys. Chem. C*, **2010**, *114*, 20387−20393.

Barton, E. E.; Rampulla, D. M.; Bocarsly, A. B. Selective solardriven reduction of CO2 to methanol using a catalyzed p-GaP based photoelectrochemical cell. *J. Am. Chem. Soc.* **2008**, *130*, 6342−6344.

Belasco, J.; Mohapatra, S. K.; Zhang, Y.; Barlow, S.; Marder, S. R.; Kahn, A. Molecular Doping and Tuning Threshold Voltage in 6, 13-bis (triisopropylsilylethynyl) Pentacene/Polymer Blend Transistors. *Appl. Phys. Lett*. **2014**, *105*, 063301.

Bell, A. T. Catalytic Synthesis of Hydrocarbons over Group VIII Metals. A Discussion of the Reaction Mechanism. *Catal. Rev*. **1981**, *23*, 203-232.

Bittle, E. G.; Basham, J. I.; Jackson, T. N.; Jurchescu, O. D.; Gundlach, D. J. Mobility overestimation due to gated contacts in organic field-effect transistors. *Nat. Commun.* **2016**, *7*, 10908.

Bobbert, P. A.; Sharma, A.; Mathijssen, S. G. J.; Kemerink, M.; De Leeuw, D. M. Operational Stability of Organic Field-Effect Transistors. *Adv. Mater*. **2012**, *24*, 1146−1158.

Booth, G., Nitro Compounds, Aromatic. In Ullmann's Encyclopedia of Industrial Chemistry, **2000**, *24*, 301-347.

Boufflet, P.; Han, Y.; Fei, Z. P.; Treat, N. D.; Li, R. P.; Smilgies, D.; Stingelin, N.; Anthopoulos, T. D.; Heeney, M. Using Molecular Design to Increase Hole Transport: Backbone Fluorination in the Benchmark Material Poly(2,5-bis(3-alkylthiophen-2-yl)thieno[3,2-b]- thiophene (pBTTT). *Adv. Funct. Mater.* **2015**, *25*, 7038−7048.

Boukhili, W.; Mahdouani, M.; Erouel, M.; Puigdollers, J.; Bourguiga, R. Reversibility of humidity effects in pentacene based organic thin-film transistor: Experimental data and electrical modeling, *Synth. Met.* **2015** ,*199*, 303–309.

Bredas, J. L.; Street, G. B. Polarons, Bipolarons, and Solitons in Conducting Polymers. *Acc. Chem. Res*. **1985**, *18*, 309-315.

Bronstein, H.; Leem, D. S.; Hamilton, R.; Woebkenberg, P.; King, S.; Zhang, W.; Ashraf, R. S.; Heeney, M.; Anthopoulos, T. D.; Mello, J. d.; McCulloch, I. Indacenodithiopheneco-

Benzothiadiazole copolymers for high performance solar cells or transistors via alkyl chain optimization. *Macromolecules* **2011**, *44*, 6649–6652

Brown, A. R.; de Leeuw, D. M.; Havinga, E. E.; Pomp, A. A Universal Relation between Conductivity and Field-Effect Mobility in Doped Amorphous Organic Semiconductors. *Synth. Met.* **1994**, *68*, 65−70.

Bruni, P.; Cardillo, B.; Giorgini, E.; TosI, G.; Bocelli, G.; Cantoni, A. Molecular complexes of hydrazones-VIII. Nitrofluorenes and arylhydrazones. *Spectrochimica Acta*. **1990**, *46*, 389-396.

Brus, V. V.; Proctor, C. M.; Ran, N. A.; Nguyen, T.-Q. Capacitance Spectroscopy for Quantifying Recombination Losses in Nonfullerene Small-Molecule Bulk Heterojunction Solar Cells. *Adv. Energy. Mater.* **2016,** 1502250.

Brütting, W. *Physics of Organic Semiconductors*; WILEY-VCH Verlag: Weinheim, Germany, **2004**.

Campos, A.; Riera-Galindo, S.; Puigdollers, J.; Mas-Torrent, M. Reduction of Charge Traps and Stability Enhancement in Solution Processed Organic Field-effect Transistors Based on a Blended N type Semiconductor. *ACS Appl. Mater. Interfaces.* **2018**, *10*, 15952–15961.

Cappel, U. B.; Daeneke, T.; Bach, U. Oxygen-induced Doping of Spiro-MeOTAD in Solid-state Dye-Sensitized Solar Cells and its Impact on Device Performance. *Nano Lett*. **2012**, *12*, 4925−4931.

Chang, 1. F.; Sun, B. Q.; Breiby, D. W.; Nielsen, M. M.; SolIing, T. I.; Giles, M.; McCulloch, 1.; Sirringhaus, H., Enhanced mobility of poly(3-hexylthiophene) transistors by spin-coating from high-boiling-point solvents. *Chem Mater* **2004**, *16*, 4772-4776.

Chen, H.; Wadsworth, A.; Ma, C.; Nanni, A.; Zhang, W.; Nikolka, M.; Luci, A. M. T.; Perdigao, L. M. A.; Thorley, K. J.; Cendra, C.; Larson, B.; Rumbles, G.; Anthopoulos, T. D.; Salleo, A.; Costantini, G.; Sirringhaus, H.; McCulloch, I. The Effect of Ring Expansion in Thienobenzo[b]indacenodithiophene Polymers for Organic Field-Effect Transistors. *J. Am. Chem. Soc.* **2019**, *141*, 18806-18813.

Chen, H.; Zhang, W.; Li, M.; He, G.; Guo, X. Interface Engineering in Organic Field-Effect Transistors: Principles, Applications, and Perspectives. *Chem. Rev*. **2020**, *120*, 2879−2949.

Chen, M. S.; Lee, O. P.; Niskala, J. R.; Yiu, A. T.; Tassone, C. J.; Schmidt, K.; Beaujuge, P. M.; Onishi, S. S.; Toney, M. F.; Zettl, A.; Frechet, J. M. Enhanced solid-state order and field-effect hole mobility through control of nanoscale polymer aggregation. *J. Am. Chem. Soc.* **2013**, *135*, 19229-19236.

Chen, P. R.; Khetan, A.; Yang, F. K.; Migunov, V.; Weide, P.; Sturmer, S. P.; Guo, P. H.; Kahler, K.; Xia, W.; Mayer, J.; Pitsch, H.; Simon, U.; Muhler, M. Experimental and Theoretical Understanding of Nitrogen-Doping-Induced Strong Metal–Support Interactions in Pd/TiO_2 Catalysts for Nitrobenzene Hydrogenation. *ACS Catal.* **2017**, *7*, 1197.

Chen, Y. W.; Prange, J. D.; Duhnen, S.; Park, Y.; Gunji, M.; Chidsey, C. E. D.; McIntyre, P. C. Atomic layer-deposited tunnel oxide stabilizes silicon photoanodes for water oxidation. *Nat. Mater*. **2011**, *10*, 539-544.

Chen, Y.; Deng, W.; Zhang, X.; Wang, M.; Jie, J. Ambient instability of organic field-effect transistors and its improvement strategies. *J. Appl. Phys*. **2022**, *55*, 053001.

Chiang, C.K.; Fincher Jr, C.R.; Park, Y.W.; Heeger, A.J.; Shirakawa, H.; Louis, E.J.; Gau, S.C.; MacDiarmid, A. G. Electrical conductivity in doped polyacetylene. *Physical review letters*, **1977**, *39*, 1098.

Choi, H. H.; Cho, K.; Frisbie, C. D.; Sirringhaus, H.; Podzorov, V. Critical assessment of charge mobility extraction in FETs. *Nat. Mater*. **2017**, *17*, 2-7.

Choi, H. H.; Paterson, A. F.; Fusella, M. A.; Panidi, J.; Solomeshch, O.; Tessler, N.; Heeney, M.; Cho, K.; Anthopoulos, T. D.; Rand, B. P.; et al. Hall Effect in Polycrystalline Organic Semiconductors: The Effect of Grain Boundaries. *Adv. Funct. Mater*. **2020**, *30*, 1903617.

Choi, S.; Jeong, J. W.; Jo, G.; Ma, B. C.; Chang, M. Conjugated polymer/paraffin blends for organic field-effect transistors with high environmental stability. *Nanoscale* **2019**, *11*, 10004−10016.

Chu, S.; Fan, S.Z.; Wang, Y.J.; Rossouw, D.; Wang, Y.C.; Botton, G.A.; Mi, Z. Tunable syngas production from CO_2 and H_2O in an aqueous photoelectrochemical cell. *Angew. Chem. Int. Ed*. **2016**, *55*, 14260–14264.

Chu, S.; Kong, X.; Vanka, S.; Guo, H.; Mi, Z. Artificial Photosynthesis on III-Nitride Nanowire Arrays. *Semicond. Semimetals* **2017**, *97*, 223−255.

Chu, S.; Ou, P.; Ghamari, P.; Vanka, S.; Zhou, B.; Shih, I.; Song, J.; Mi, Z. Photoelectrochemical CO_2 reduction into syngas with the metal/oxide interface. *J. Am. Chem. Soc*. **2018**, *140*, 7869−7877.

Chu, S.; Ou, P.; Rashid, R. T.; Ghamari, P.; Wang, R.; Tran, H. N.; Zhao, S.; Zhang, H.; Song, J.; Mi, Z. Decoupling Strategy for Enhanced Syngas Generation from Photoelectrochemical CO_2 Reduction. *iScience* **2020**, *23*, 101390.

Chua, L. L.; Zaumseil, J.; Chang, J. F.; Ou, E. C. W.; Ho, P. K. H.; Sirringhaus, H.; Friend, R. H. General observation of n-type field-effect behaviour in organic semiconductors. *Nature* **2005**, *434*, 194-199.

Cicoira, F.; Santato, C. Organic Light Emitting Field Effect Transistors: Advances and Perspectives. *Advanced Functional Materials*. **2007**, *17*, 3421-3434.

Ćirić-Marjanović, G. Recent Advances in Polyaniline Research: Polymerization Mechanisms, Structural Aspects. *Synth. Met.* **2013**, *177*, 1−47.

Colleaux, F.; Ball, J. M.; Wo´bkenberg, P. H.; Hotchkiss, P. J.; Marder, S. R.; Anthopoulos, T. D. Bias-Stress Effects in Organic Field Effect Transistors Based on Self-Assembled Monolayer Nanodielectrics. *Phys. Chem*. **2011**, *13*, 14387−14393

Coppo, P.; Turner, M. L. Cyclopentadithiophene based electroactive materials. *J. Mater. Chem.* **2005**, *15*, 1123–1133.

Coropceanu, V.; Cornil, J.; Filho, D. A.; Olivier, Y.; Silbey, R.; Cornil, J.-L. Charge Transport in Organic Semiconductors. *Chem. Rev.* **2007**, *107*, 926−952.

Dai, A.; Zhou, Y.; Shu, A. L.; Mohapatra, S. K.; Wang, H.; Fuentes-Hernandez, C.; Zhang, Y.; Barlow, S.; Loo, Y. L.; Marder, S. R.; et al. Enhanced Charge-Carrier Injection and Collection via Lamination of Doped Polymer Layers p-Doped with a Solution-Processible Molybdenum Complex. *Adv. Funct. Mater*. **2014**, *24*, 2197−2204.

Deng, J.; Su, Y.; Liu, D.; Yang, P.; Liu, B.; Liu, C. Nanowire Photoelectrochemistry. *Chem. Rev*. **2019**, *119*, 9221−9259.

Desai, M.S., Kandpal, K. and Goswami, R. A Multiple-trapping-and-release transport-based threshold voltage model for oxide thin film transistors. *J. Electron. Mater* **2021**, 50, 4050-4057.

Dimitrakopoulos, C. D.; Malenfant, P. R. L., Organic thin film transistors for large area electronics. *Adv. Mater.* **2002**,*14*, 99-117.

Ding, Z.; Abbas, G.; Assender, H. E.; Morrison, J. J.; Yeates, S. G.; Patchett, E. R.; Taylor, D. M. Effect of Oxygen, Moisture and Illumination on the Stability and Reliability of DNTT OTFTs during Operation and Storage, *ACS Appl. Mater. Interfaces*, **2014**, *6*, 15224–15231.

Dong, H.; Fu, X.; Liu, J.; Wang, Z.; Hu, W. 25th Anniversary Article: Key Points for HighMobility Organic Field-Effect Transistors. *Advanced Materials*. **2013**, *25*, 6158-6182.

Dry, M. E. The Fischer–Tropsch process: 1950–2000. *Catal. Today* **2002**, *71*, 227-241.

DuChene, J. S.; Sweeny, B. C.; Johnston-Peck, A. C.; Su, D.; Stach, E. A.; Wei, W. D., Hot Hole Collection and Photoelectrochemical CO_2 Reduction with Plasmonic Au/p-GaN Photocathodes, Nano Lett. **2018**, 18, 2545-2550.

Duclaux, L. Review of the Doping of Carbon Nanotubes (Multiwalled and Single-walled). *Carbon* **2002**, *40*, 1751−1764.

Ebata, H. et al. Highly Soluble [1]Benzothieno[3,2- b]benzothiophene (BTBT) Derivatives for High-Performance, Solution-Processed Organic Field-Effect Transistors. *J. Am. Chem. Soc.* **2007,** *129*, 15732–15733.

Egginger, M.; Bauer, S.; Schwö diauer, R.; Neugebauer, H.; Sariciftci, N. S. Current versus gate voltage hysteresis in organic field effect transistors, Monatsh. Chem. **2009**, *140*, 735-750.

El-Khatib, N.; Boudjema, B.; Guillaud, G.; Maitrot, M.; Chermette, H. Theoretical and Experimental Doping of Molecular Materials: P and N Doping of Zinc Phthalocyanine. *J. Less-Common Met.* **1988**, *143*, 101−112.

Facchetti, A. Semiconductors for organic transistors. *Materials Today*. **2007**, *10*, 28-37.

Fan, S. Z.; AlOtaibi, B.; Woo, S. Y.; Wang, Y. J.; Botton, G. A.; Mi, Z. High Efficiency Solar-to-Hydrogen Conversion on a Monolithically Integrated InGaN/GaN/Si Adaptive Tunnel Junction Photocathode. *Nano lett*. **2015**, *15*, 2721-2726.

Fediai, A.; Symalla, F.; Friederich, P.; Wenzel, W. Disorder Compensation Controls Doping Efficiency in Organic Semiconductors. *Nat. Commun*. **2019**, *10*, 2−8.

Feng, J.Y.; Huang, H.T.; Yan, S.C.; Luo, W.J.; Yu, T.; Li, Z.S.; and Zou, Z.G. Non-oxide semiconductors for artificial photosynthesis: progress on photoelectrochemical water splitting and carbon dioxide reduction. **2020**, *Nano Today 30*, 100830.

Feng, X.; Jiang, K.; Fan, S.; Kanan, M. W., Grain-boundary-dependent CO_2 electroreduction activity. *J. Am. Chem. Soc.* **2015**, *137*, 4606-4609.

Foit, S. R.; Vinke, I. C.; de Haart, L. G. J.; Eichel, R. A. Power-to-Syngas: An Enabling Technology for the Transition of the Energy System? *Angew. Chem. Int. Ed*. **2017**, *56*, 5402-5411.

Ford, M. J.; Wang, M.; Phan, H.; Nguyen, T.-Q.; Bazan, G. C. Fullerene Additives Convert Ambipolar Transport to p-Type Transport while Improving the Operational Stability of Organic Thin Film Transistors. *Adv. Funct. Mater*. **2016**, *26*, 4472-4480.

Furler, P.; Scheffe, J. R.; Steinfeld, A. Syngas production by simultaneous splitting of H_2O and CO2via ceria redox reactions in a high-temperature solar reactor. *Energy Environ. Sci*. **2012**, *5*, 6098-6103.

Ghamari, P.; Niazi, M. R.; Perepichka, D. F. Controlling Structural and Energetic Disorder in High-Mobility Polymer Semiconductors via Doping with Nitroaromatics. *Chem. Mater.* **2021**, *33*, 2937−2947.

Grundmann, M. *The Physics of Semiconductors: An Introduction Including Nanophysics and Applications*; Springer-Verlag: Berlin, **2010**.

Gu, G.; Kane, M. G.; Doty, J. E.; Firester, A. H. Electron traps and hysteresis in pentacene-based organic thin-film transistors *Appl. Phys. Lett*. **2005**, *87*, 243512.

Guo, S. J.; Zhao, S. Q.; Wu, X. Q.; Li, H.; Zhou, Y. J.; Zhu, C.; Yang, N. J.; Jiang, X.; Gao, J.; Bai, L.; Liu, Y.; Lifshitz, Y.; Lee, S. T.; Kang, Z. H. A Co_3O_4-CDots-C_3N_4 three component electrocatalyst design concept for efficient and tunable CO_2 reduction to syngas. *Nat. Commun*. **2017**, *8*, 1828.

Guo, X.; Guo, D.; Qiu, X.; Chen, L.; Zhu, W. Excellent dispersion and electrocatalytic properties of Pt nanoparticles supported on novel porous anatase TiO_2 nanorods. *J. Power Sources* **2009**, *194*, 281-285.

Habisreutinger, S. N.; Schmidt-Mende, L.; Stolarczyk, J. K. Photocatalytic Reduction of CO_2 on TiO_2 and Other Semiconductors, *Angew. Chem. Int. Ed*. **2013**, *52*, 7372-7408.

Halmann, M. Photoelectrochemical Reduction of Aqueous Carbon-Dioxide on p-Type Gallium-Phosphide in Liquid Junction Solar-Cells. *Nature* **1978**, *275*, 115–116.

Hamzehpoor, E.; Jonderian, A.; McCalla, E., Perepichka, D.F. Synthesis of Boroxine and Dioxaborole Covalent Organic Frameworks via Transesterification and Metathesis of Pinacol Boronates. *J. Am. Chem. Soc*. **2021**, *143*, 13274-13280.

Han, S.; Yu, X.; Shi, W.; Zhuang, X.; Yu, J. Solvent-Dependent Electrical Properties Improvement of Organic Field-Effect Transistor Based on Disordered Conjugated Polymer/Insulator Blends. *Org. Electron*. **2015**, *27*, 160−166.

Han, Y.; Barnes, G.; Lin, Y.-H.; Martin, J.; Al Qaradawi, S. Y.; Anthopoulos, T. D.; Heeney, M. Doping of Large Ionization Potential Indenopyrazine Polymers via Lewis Acid Complexation with Tris(pentafluorophenyl)borane: A Simple Method for Improving the Performance of Organic Thin-Film Transistors. *Chem. Mater*. **2016**, *28*, 8016-8024.

Haneef, H. F.; Zeidell, A. M.; Jurchescu, O. D. Charge carrier traps in organic semiconductors: a review on the underlying physics and impact on electronic devices. *J. Mater. Chem. C*. **2020**, *8*, 759− 787.

Hansen, H. A.; Shi, C.; Lausche, A. C.; Peterson, A. A.; Norskov, J. K. Bifunctional alloys for the electroreduction of CO_2 and CO. *Phys. Chem. Chem. Phys*. **2016**, *18*, 9194-9201.

Hansen, H. A.; Varley, J. B.; Peterson, A. A.; Norskov, J. K. Understanding Trends in the Electrocatalytic Activity of Metals and Enzymes for CO_2 Reduction to CO. *J. Phys. Chem. Lett*. **2013**, *4*, 388-392.

Harada, K.; Werner, A. G.; Pfeiffer, M.; Bloom, C. J.; Elliott, C. M.; Leo, K. Organic Homojunction Diodes with a High Built-in Potential: Interpretation of the Current-Voltage Characteristics by a Generalized Einstein Relation. *Phys. Rev. Lett*. **2005**, *94*, 036601.

He, J.; Janáky, C. Recent Advances in Solar-Driven Carbon Dioxide Conversion: Expectations versus Reality. *ACS Energy Lett*. **2020**, *5*, 1996−2014.

He, R.; Zhang, A.; Ding, Y. L.; Kong, T. Y.; Xiao, Q.; Li, H. L.; Liu, Y.; Zeng, J. Achieving the Widest Range of Syngas Proportions at High Current Density over Cadmium Sulfoselenide Nanorods in CO_2 Electroreduction. *Adv. Mater*. **2018**, *30*, 1705872.

He, Z.; Goulas, J.; Parker, E.; Sun, Y.; Zhou, X.D.; Fei, L. Review on covalent organic frameworks and derivatives for electrochemical and photocatalytic CO_2 reduction, *Catal. Today*. **2022**.

Heimel, G.; Romaner, L.; Zojer, E.; Bredas, J. L. The Interface Energetics of Self-Assembled Monolayers on Metals. *Acc. Chem. Res*. **2008**, *41*, 721–729.

Hein, M. P.; Zakhidov, A. A.; Luessem, B.; Jankowski, J.; Tietze, M. L.; Riede, M. K.; Leo, K. Molecular Doping for Control of Gate Bias Stress in Organic Thin Film Transistors. *Appl. Phys. Lett.* **2014**, *104*, 013507.

Hepel, M.; Kumarihamy, I.; Zhong, C. Nanoporous TiO_2-supported bimetallic catalysts for methanol oxidation in acidic media. *J. Electrochem. Commun*. **2006**, *8*, 1439-1444.

Hernandez, S.; Farkhondehfal, M. A.; Sastre, F.; Makkee, M.; Saracco, G.; Russo, N. Syngas Production from Electrochemical Reduction of CO_2: Current Status and Prospective Implementation. *Green Chem*. **2017**, *19*, 2326−2346

Hinogami, R.; Nakamura, Y.; Yae, S.; Nakato, Y. J. An Approach to Ideal Semiconductor Electrodes for Efficient Photoelectrochemical Reduction of Carbon Dioxide by Modification with Small Metal Particles. *Phys. Chem. B* **1998**, *102*, 974-980.

Hong, D. C.; Tsukakoshi, Y.; Kotani, H.; Ishizuka, T.; Kojima, T. Visible-Light-Driven Photocatalytic CO_2Reduction by a Ni(II) Complex Bearing a Bioinspired Tetradentate Ligand for Selective CO Production. *J. Am. Chem. Soc*. **2017**, *139*, 6538-6541.

Horowitz, G.; Delannoy, P. An analytical model for organic-based thin-film transistors. *J. Appl. Phys*. **1991,** *70*, 469-475.

Hou, J. L.; Kasemann, D.; Widmer, J.; Günther, A. A.; Lüssem, B.; Leo, K. Reduced Contact Resistance in Top-Contact Organic FieldEffect Transistors by Interface Contact Doping. *Appl. Phys. Lett*. **2016**, *108*, 103303.

Hou, J.; Inganas, O.; Friend, R. H.; Gao, F. Organic Solar Cells¨ Based on Non-Fullerene Acceptors. *Nat. Mater*. **2018**, *17*, 119−128.

https://github.com/karlrupp/microprocessor-trend-data. Accessed 5 August 2022.

https://sdgs.un.org/goals. United nations. Accessed 10 August 2022.

https://www.azom.com/article.aspx?ArticleID=9210. Accessed 17 August 2022.

https://www.epa.gov/ghgemissions/overview-greenhouse-gases. U.S. Environmental Protection Agency. Accessed 1 August 2022.

https://www.ibm.com/thought-leadership/innovation-explanations/mukesh-khare-on-smaller-transistors-analytics/ Accessed 1 Jun **2022**.

https://www.samsung.com/ca/smartphones/galaxy-z-flip4/buy/ Accessed 10 August **2022**. https://www.semi.org/en/communities/flextech/what-are-flexible-electronics. 10 August **2022**. https://www.nature.com/articles/d41586-021-00739-z, Accessed 10 August **2022**.

Hu, Y.; Dong, G.; Hu, Y.; Wang, L.; Qiu, Y.; Oxygen effect on the electrical characteristics of pentacene transistors, *J. Phys. D: Appl. Phys*. **2006**, *39*, 4553–4556.

Hu, Y.; Rengert, Z. D.; McDowell, C.; Ford, M. J.; Wang, M.; Karki, A.; Lill, A. T.; Bazan, G. C.; Nguyen, T. Q. Doping Polymer Semiconductors by Organic Salts: Toward High-Performance Solution-Processed Organic Field-Effect Transistors. *ACS. Nano*. **2018**, *12*, 3938-3946.

Hunter, S.; Mottram, A. D.; Anthopoulos, T. D. Temperature and composition-dependent density of states in organic small-molecule/polymer blend transistors. *J. Appl. Phys.* **2016**, *120*, 025502.

Huseynova, G.; Xu, Y.; Nketia Yawson, B.; Shin, E.-Y.; Lee, M. J.; Noh, Y.-Y. P-Type Doped Ambipolar Polymer Transistors by Direct Charge Transfer from a Cationic Organic Dye Pyronin B Ferric Chloride. *Org. Electron.* **2016**, *39*, 229−235.

Inoue, T.; Fujishima, A.; Konishi, S.; Honda, K. Photoelectrocatalytic Reduction of Carbon-Dioxide in Aqueous Suspensions of Semiconductor Powders. *Nature* **1979**, *277*, 637–638.

Iqbal, H. F.; Waldrip, M.; Chen, H.; McCulloch, I. and Jurchescu, O.D., Elucidating the Role of Water-Related Traps in the Operation of Polymer Field-Effect Transistors. *Adv. Electron. Mater.* **2021**, *7*, 2100393.

Jacobs, I. E.; Moule, A. J. Controlling Molecular Doping in Organic Semiconductors. Adv. Mater. 2017, *29*, 1703063.

Janasz, L.; Borkowski, M.; Blom, P. W.; Marszalek, T.; Pisula, W. Organic Semiconductor/Insulator Blends for Elastic Field-Effect Transistors and Sensors. *Adv. Funct. Mater*. **2021**, 2105456.

Jang, J.-W., Cho, S.; Magesh, G.; Jang, Y.J.; Kim, J.Y.; Kim, W.Y.; Seo, J.K.; Kim, S.; Lee, K.-H.; and Lee, J.S. Aqueous-solution route to zinc telluride films for application to CO_2 reduction. *Angew. Chem. Int. Ed.* **2014,** *53*, 5852–5857.

Jang, Y. J.; Jang, J. W.; Lee, J.; Kim, J. H.; Kumagai, H.; Lee, J.; Minegishi, T.; Kubota, J.; Domen, K.; Lee, J. S. Selective CO production by Au coupled ZnTe/ZnO in the photoelectrochemical CO_2 reduction system. *Energy Environ. Sci.* **2015**, *8*, 3597-3604.

Jang, Y. J.; Jeong, I.; Lee, J.; Lee, J.; Ko, M. J.; Lee, J. S. Unbiased sunlight-driven artificial photosynthesis of carbon monoxide from CO_2 using a ZnTe-based photocathode and a perovskite solar cell in tandem. *ACS Nano* **2016**, *10*, 6980−6987.

Jang, Y.J.; Jang, J.W.; Lee, J.; Kim, J.H.; Kumagai, H.; Lee, J.; Minegishi, T.; Kubota, J.; Domen, K.; and Lee, J.S. Selective CO production by Au coupled ZnTe/ZnO in the photoelectrochemical CO_2 reduction system. *Energy Environ. Sci.* **2015,** *8*, 3597–3604.

Jarrett, C. P.; Friend, R. H.; Brown, A. R.; de Leeuw, D. M. Field Effect Measurements in Doped Conjugated Polymer Films: Assessment of Charge Carrier Mobilities. *J. Appl. Phys*. **1995**, *77*, 6289−6294.

Jung, H. S.; Hong, Y. J.; Li, Y.; Cho, J.; Kim, Y. J.; Yi, G. C. Photocatalysis Using GaN Nanowires, *ACS Nano.* **2008**, *2*, 637−642.

Jurchescu, O. D., Baas, J. & Palstra, T. T. M. Effect of impurities on the mobility of single crystal pentacene. *Appl. Phys. Lett*. **2004**, *84*, 3061–3063.

Kamimura, S.; Sasaki, Y.; Kanaya, M.; Tsubota, T.; Ohno, T. Improvement of Selectivity for CO_2 Reduction by Using Cu2ZnSnS4 Electrodes Modified with Different Buffer Layers (CdS and In2S3) under Visible Light Irradiation. *RSC Adv*. **2016**, *6*, 112594−112601.

Kang, I.; Yun, H. J.; Chung, D. S.; Kwon, S. K.; Kim, Y. H. Record high hole mobility in polymer semiconductors via side-chain engineering. *J. Am. Chem. Soc.* **2013**, *135*, 14896-14899.

Kang, K.; Schott, S.; Venkateshvaran, D.; Broch, K.; Schweicher, G.; Harkin, D.; Jellett, C.; Nielsen, C. B.; McCulloch, I.; Sirringhaus, H. Investigation of the Thermoelectric Response in Conducting Polymers Doped by Solid-State Diffusion. *Mater. Today Phys.* **2019**, *8*, 112−122.

Kang, M.; Hwang, H.; Park, W. T.; Khim, D.; Yeo, J. S.; Kim, Y.; Kim, Y. J.; Noh, Y. Y.; Kim, D. Y. Ambipolar Small-Molecule: polymer Blend Semiconductors for Solution-Processable Organic Field-Effect Transistors. *ACS Appl. Mater. Interfaces* **2017**, *9*, 2686−2692

Kang, P.; Chen, Z. F.; Nayak, A.; Zhang, S.; Meyer, T. J. Single catalyst electrocatalytic reduction of CO_2 in water to H_2+CO syngas mixtures with water oxidation to O_2. *Energy Environ. Sci*. **2014**, *7*, 4007-4012.

Kao, C. Y.; Lee, B.; Wielunski, L. S.; Heeney, M.; McCulloch, I.; Garfunkel, E.; Feldman, L. C.; Podzorov, V. Doping of Conjugated Polythiophenes with Alkyl Silanes. *Adv. Funct. Mater.* **2009**, *19*, 1906−1911.

Karatairi, E.; Miller, J. E. Splitting CO_2 to produce syngas and hydrocarbon fuels: PEC and STC. *MRS Bull*. **2017**, *42*, 878-879.

Karpov, Y.; Kiriy, N.; Formanek, P.; Hoffmann, C.; Beryozkina, T.; Hambsch, M.; Al-Hussein, M.; Mannsfeld, S. C. B.; Büchner, B.; Debnath, B.; et al. Sequentially Processed P3HT/CN6-CP •- NBu 4+ Films: Interfacial or Bulk Doping? *Adv. Electron. Mater*. **2020**, *6*, 1901346.

Khodakov, A. Y.; Chu, W.; Fongarland, P. Advances in the Development of Novel Cobalt Fischer−Tropsch Catalysts for Synthesis of Long-Chain Hydrocarbons and Clean Fuels. *Chem. Rev*. **2007**, *107*, 1692-1744.

Kibria, M. G.; Mi, Z. Artificial photosynthesis using metal/ nonmetal-nitride semiconductors: current status, prospects, and challenges. *J. Mater. Chem. A* **2016**, 4, 2801−2820.

Kim, D. H.; Lee, B.; Moon, H.; Kang, H. M.; Jeong, E. J.; Park, J.; Han, K.; Lee, S.; Yoo, B. W.; Koo, B. W.; Kim, J. Y.; Lee, W. H.; Cho, K.; Becerril, H. A.; Bao, Z. Liquid-Crystalline Semiconducting Copolymers with Intramolecular Donor-Acceptor Building Blocks for High-Stability Polymer Transistors, *J. Am. Chem. Soc.* **2009,** *131*, 6124-6132.

Kim, H. J.; Kearney, K. L.; Le, L. H.; Haber, Z. J.; Rockett, A. A.; Rose, M. J. Charge-Transfer through Ultrathin Film TiO_2 on n-Si (111) Photoelectrodes: Experimental and Theoretical

Investigation of Electric Field-Enhanced Transport with a Nonaqueous Redox Couple. *J. Phys. Chem. C.* **2016**, *120*, 25697-25708.

Kim, J.; Kang, M.; Cho, J.; Yu, S. H.; Chung, D. S. Doping-Dedoping Interplay to Realize Patterned/Stacked All-Polymer Optoelectronic Devices. *ACS Appl. Mater. Interfaces*. **2019**, *11*, 18580-18589.

Kim, M.; Ryu, S. U.; Park, S. A.; Choi, K.; Kim, T.; Chung, D.; Park. T. Donor−Acceptor-Conjugated Polymer for High-Performance Organic Field-Effect Transistors: A Progress Report. *Adv. Funct. Mater*. **2019**, *30*, 1904545.

Kim, S. K.; Zhang, Y.-J.; Bergstrom, H.; Michalsky, R.; Peterson, A. Understanding the Low-Overpotential Production of CH4 from CO_2 on Mo_2C Catalysts. *ACS Catal*. **2016**, *6*, 2003-2013.

Kim, Y.; Broch, K.; Lee, W.; Ahn, H.; Lee, J.; Yoo, D.; Kim, J.; Chung, S.; Sirringhaus, H.; Kang, K.; et al. Highly Stable Contact Doping in Organic Field Effect Transistors by Dopant-Blockade Method. *Adv. Funct. Mater*. **2020**, *30*, 2000058.

Kim, Y.; Chung, S.; Cho, K.; Harkin, D.; Hwang, W. T.; Yoo, D.; Kim, J. K.; Lee, W.; Song, Y.; Ahn, H.; Hong, Y.; Sirringhaus, H.; Kang, K.; Lee, T. Enhanced Charge Injection Properties of Organic Field-Effect Transistor by Molecular Implantation Doping. *Adv. Mater*. **2019**, *31*, 1806697.

Kimpel, J.; Michinobu, T. Conjugated Polymers for Functional Applications: Lifetime and Performance of Polymeric Organic Semiconductors in Organic Field-Effect Transistors. *Polym Int.* **2021**, *70*, 367–373.

Kittel, C. *Introduction to Solid State Physics*; John Wiley & Sons: New York, **2005**.

Klauk, H. Organic thin-film transistors. *Chem. Soc. Rev.* **2010**, 39, 2643-2666.

Knopfmacher, O.; Hammock, M. L.; Appleton, A. L.; Schwartz, G.; Mei, J.; Lei, T.; Pei, J.; Bao, Z. Highly stable organic polymer fieldeffect transistor sensor for selective detection in the marine environment. *Nat. Commun.* **2014**, *5*, 2954.

Koezuka, H.; Tsumura, A.; Ando, T. Field-effect transistor with polythiophene thin film. *Synthetic Metals.* **1987**, *18*, 699-704.

Köhler, A.; Bässler, H. *Electronic processes in organic semiconductors: An introduction*. John Wiley & Sons, **2015**.

Kong, Q.; Kim, D.; Liu, C.; Yu, Y.; Su, Y.; Li, Y.; Yang, P. D. Directed Assembly of Nanoparticle Catalysts on Nanowire Photoelectrodes for Photoelectrochemical CO_2 Reduction. *Nano lett.* **2016**, *16*, 5675-5680.

Kristiansen, M.; Smith, P.; Chanzy, H.; Baerlocher, C.; Gramlich, V.; McCusker, L.; Weber, T.; Pattison, P.; Blomenhofer, M.; Schmidt, H.-W. Structural Aspects of 1,3,5-Benzenetrisamides-A New Family of Nucleating Agents. *Cryst. Growth Des*. **2009**, *9*, 2556−2558.

Kudo, A.; Miseki, Y. Heterogeneous Photocatalyst Materials for Water Splitting. *Chem. Soc. Rev*. **2009**, *38*, 253−278.

Kuhl, K. P.; Hatsukade, T.; Cave, E. R.; Abram, D. N.; Kibsgaard, J.; Jaramillo, T. F. Electrocatalytic Conversion of Carbon Dioxide to Methane and Methanol on Transition Metal Surfaces. *J. Am. Chem. Soc*. **2014**, *136*, 14107.

Kumagai, H.; Sahara, G.; Maeda, K.; Higashi, M.; Abe, R.; Ishitani, O., Hybrid photocathode consisting of a CuGaO2 p-type semiconductor and a Ru(II)-Re(I) supramolecular photocatalyst: Non-biased visible-light-driven CO_2 reduction with water oxidation. *Chem. Sci*. **2017**, *8*, 4242.

Kumar, B.; Brian, J. P.; Atla, V.; Kumari, S.; Bertram, K. A.; White, R. T.; Spurgeon, J. M., Controlling the product syngas H_2:CO ratio through pulsed-bias electrochemical reduction of CO_2 on copper. *ACS Catal*. **2016**, *6*, 4739-4745.

Kumar, B.; Kaushik, B. K.; Negi, Y. S. Organic Thin Film Transistors: Structures, Models, Materials, Fabrication, and Applications: A Review. *Polym. Rev*. **2014**, *54*, 33−111

Kumar, B.; Smieja, J. M.; Sasayama, A. F.; Kubiak, C. P. Tunable, light-assisted co-generation of CO and H_2 from CO_2 and H_2O by Re(bipy-tbu)$(CO)_3$Cl and p-Si in non-aqueous medium. *Chem. Commun.* **2012**, *48*, 272-274.

Lamport, Z. A.; Barth, K. J.; Lee, H.; Gann, E.; Engmann, S.; Chen, H.; Guthold, M.; McCulloch, I.; Anthony, J. E.; Richter, L. J.; DeLongchamp, D. M.; Jurchescu, O. D. A simple and robust approach to reducing contact resistance in organic transistors. *Nat Commun*. **2018**, *9*, 5130.

Landers, A. T.; Fields, M.; Torelli, D. A.; Xiao, J.; Hellstern, T. R.; Francis, S. A.; Tsai, C.; Kibsgaard, J.; Lewis, N. S.; Chan, K.; Hahn, C.; Jaramillo, T. F.; The predominance of hydrogen evolution on transition metal sulfides and phosphides under CO_2 reduction conditions: An experimental and theoretical study. *ACS Energy Lett.* **2018**, 3, 1450.

Lee, E. K.; Lee, M. Y.; Park, C. H.; Lee, H. R.; Oh, J. H. Toward Environmentally Robust Organic Electronics: Approaches and Applications. *Adv. Mater.* **2017**, *29*, 1703638.

Lee, H.; Moon, B.; Son, S. Y.; Park, T.; Kang, B.; Cho, K. Charge Trapping in a Low-Crystalline High-Mobility Conjugated Polymer and Its Effects on the Operational Stability of Organic Field-Effect Transistors. *ACS Appl. Mater. Interfaces* **2021**, 13, 16722−16731.

Lee, J. H.; Kattel, S.; Jiang, Z.; Xie, Z.; Yao, S.; Tackett, B. M.; Xu, W.; Marinkovic, N. S.; Chen, J. G., Tuning the activity and selectivity of electroreduction of CO_2 to synthesis gas using bimetallic catalysts. *Nat. Commun.* **2019**, *10*, 3724.

Lee, J. S.; Won, D. I.; Jung, W. J.; Son, H. J.; Pac, C.; Kang, S. O. Controllable Syngas Production by a Dye-Sensitized TiO_2 Hybrid System with ReI and CoIII Catalysts under Visible-Light Irradiation. *Angew. Chem. Int. Ed*. **2017**, *56*, 976-980.

Lee, W. H.; Park, Y. D. Organic Semiconductor/Insulator Polymer Blends for High-Performance Organic Transistors. *Polymers* **2014**, *6*, 1057−1073.

Lei, T.; Cao, Y.; Fan, Y.; Liu, C.-J.; Yuan, S.-C.; Pei, J. High-Performance Air-Stable Organic Field-Effect Transistors: Isoindigo-Based Conjugated Polymers, *J. Am. Chem. Soc.* **2011**, *133*, 6099−6101.

Lei, Y.; Deng, P.; Li, J.; Lin, M.; Zhu, F.; Ng, T. W.; Lee, C. S.; Ong, B. S. Solution-Processed Donor-Acceptor Polymer Nanowire Network Semiconductors for High-Performance Field-Effect Transistors. *Sci. Rep*. **2016**, *6*, 24476.

Leo, K. Organic photovoltaics. *Nature Reviews Materials*, **2016**, *1*, 16056.

Li, A.; Wang, T.; Chang, X.; Zhao, Z. J.; Li, C.; Huang, Z.; Yang, P.; Zhou, G.; Gong, J., Tunable syngas production from photocatalytic CO_2 reduction with mitigated charge recombination driven by spatially separated cocatalysts. *Chem. Sci.* **2018**, *9*, 5334-5340.

Li, C.C.; Wang, T.; Liu, B.; Chen, M.X.; Li, A.; Zhang, G.; Du, M.Y.; Wang, H.; Liu, S.F.; Gong, J.L. Photoelectrochemical CO_2 reduction to adjustable syngas on grain boundary-mediated a-Si/TiO2/Au photocathodes with low onset potentials. *Energy Environ. Sci*. **2019,** *12*, 923–928.

Li, D. W.; Ouyang, S. X.; Xu, H.; Lu, D.; Zhao, M.; Zhang, X. L.; Ye, J. H. Synergistic effect of Au and Rh on SrTiO3 in significantly promoting visible-light-driven syngas production from CO_2 and H_2O. *Chem. Commun*. **2016**, *52*, 5989-5992.

Li, F. F.; Lau, J.; Licht, S., Sungas instead of syngas: Efficient coproduction of CO and H_2 with a single beam of sunlight. *Adv. Sci.* **2015**, *2*, 1500260.

Li, J.; Zhang, G.; Holm, D. M.; Jacobs, I. E.; Yin, B.; Stroeve, P.; Mascal, M.; Moulé, A. J. Introducing Solubility Control for Improved Organic P-Type Dopants. Chemistry of Materials. **2015**, *27*, 5765-5774.

Li, J.; Zhao, Y.; Tan, H. S.; Guo, Y.; Di, C. A.; Yu, G.; Liu, Y.; Lin, M.; Lim, S. H.; Zhou, Y.; Su, H.; Ong, B. S. A stable solution-processed polymer semiconductor with record high-mobility for printed transistors. *Sci. Rep.* **2012**, *2*, 754.

Li, Q. Y.; Wang, K.; Zhang, S. L.; Zhang, M.; Yang, H. J.; Jin, Z. S. Effect of photocatalytic activity of CO oxidation on Pt/TiO_2 by strong interaction between Pt and TiO_2 under oxidizing atmosphere. *J. Mol. Catal. A* ***2006***, *258*, 83-88.

Li, Y. H.; Xing, J.; Chen, Z. J.; Li, Z.; Tian, F.; Zheng, L. R.; Wang, H. F.; Hu, P.; Zhao, H. J.; Yang, H. G. Unidirectional suppression of hydrogen oxidation on oxidized platinum clusters. *Nat. Commun*. **2013**, *4*, 2500.

Li, Y.; Sonar, P.; Murphya, L.; Honga, W. High mobility diketopyrrolopyrrole (DPP)-based organic semiconductor materials for organic thin film transistors and photovoltaics. Energy Environ. Sci. **2013**, *6*, 1684−1710

Lian, S. C.; Kodaimati, M. S.; Weiss, E. A. Photocatalytically Active Superstructures of Quantum Dots and Iron Porphyrins for Reduction of CO_2 to CO in Water. *ACS Nano* **2018**, *12*, 568-575.

Liao, H-H.; Yang, C-M; Liu, C-C; Horng, S-F.; Meng, H.; Shy, J-T. Dynamics and reversibility of oxygen doping and de-doping for conjugated polymer, *J. Appl. Phys.* **2008**, *103*, 104506.

Lim, E.; Peterson, K. A.; Su, G. M.; Chabinyc, M. L. Thermoelectric Properties of Poly(3-Hexylthiophene) (P3HT) Doped with 2,3,5,6-Tetrafluoro-7,7,8,8-Tetracyanoquinodimethane (F4TCNQ) by Vapor-Phase Infiltration. *Chem. Mater*. **2018**, *30*, 998−1010.

Lin, Y. J.; Kapadia, R.; Yang, J. H.; Zheng, M.; Chen, K.; Hettick, M.; Yin, X. T.; Battaglia, C.; Sharp, I. D.; Ager, J. W.; Javey, A. J. Role of TiO_2 Surface Passivation on Improving the Performance of p-InP Photocathodes. *Phys. Chem. C* **2015**, *119*, 2308.

Liu, C.; Dasgupta, N. P.; Yang, P. Semiconductor Nanowires for Artificial Photosynthesis. *Chem. Mater*. **2014**, *26*, 415−422.

Liu, C.; Jang, J.; Xu, Y.; Kim, H.-J.; Khim, D.; Park, W.-T.; Noh, Y.-Y.; Kim, J.-J. Effect of Doping Concentration on Microstructure of Conjugated Polymers and Characteristics in N-Type Polymer Field-Effect Transistors. *Adv. Funct. Mater*. **2015**, *25*, 758-767.

Liu, C.; Li, G.; Di Pietro, R.; Huang, J.; Noh, Y.-Y.; Liu, X.; Minari, T. Device Physics of Contact Issues for the Overestimation and Underestimation of Carrier Mobility in Field-Effect Transistors. *Phys. Rev. Appl*. **2017**, *8*, 034020

Liu, C.; Xu, Y.; Noh, Y. Y. Contact engineering in organic field-effect transistors. *Mater. Today*, **2015**, *18*, 79–96.

Liu, Y.; Nell, B.; Ortstein, K.; Wu, Z.; Karpov, Y.; Beryozkina, T.; Lenk, S.; Kiriy, A.; Leo, K.; Reineke, S. High Electron Affinity Molecular Dopant CN6-CP for Efficient Organic Light-Emitting Diodes. *ACS Appl. Mater. Interfaces* **2019**, *11*, 11660−11666.

Long, D. X.; Choi, E. Y.; Noh, Y. Y. Manganese Oxide Nanoparticle as a New p-Type Dopant for High-Performance Polymer Field-Effect Transistors. *ACS Appl. Mater. Interfaces***. 2017**, *9*, 24763-24770.

Long, J.; Zhang, H.; Ming, J.; Zhao, J.; Gu, Q.; Xu, C.; Ding, Z.; Yuan, R.; Zhang, Z.; Lin, H.; Wang, X. High-rate, tunable syngas production with artificial photosynthetic cells. *Angew. Chem., Int. Ed.* **2019**, *58*, 7718−7722.

Lu, G.; Blakesley, J.; Himmelberger, S.; Pingel, P.; Frisch, J.; Lieberwirth, I.; Salzmann, I.; Oehzelt, M.; Di Pietro, R.; Salleo, A.; et al. Moderate Doping Leads to High Performance of Semiconductor/Insulator Polymer Blend Transistors. *Nat. Commun.* **2013**, 4, 1588.

Lu, X.; Minari, T.; Kumatani, A.; Liu, C.; Tsukagoshi, K. Effect of air exposure on metal/organic interface in organic field-effect transistors, *Appl. Phys. Lett.* **2011**, *98*, 243301.

Luo, C.; Kyaw, A. K.; Perez, L. A.; Patel, S.; Wang, M.; Grimm, B.; Bazan, G. C.; Kramer, E. J.; Heeger, A. J. General strategy for self-assembly of highly oriented nanocrystalline semiconducting polymers with high mobility. *Nano Lett.* **2014**, *14*, 2764−2771.

Luo, H.; Yu, C.; Liu, Z.; Zhang, G.; Geng, H.; Yi, Y.; Broch, K.; Hu, Y.; Sadhanala, A.; Jiang, L.; Qi, P.; Cai, Z.; Sirringhaus, H.; Zhang, D. Remarkable enhancement of charge carrier mobility of conjugated polymer field-effect transistors upon incorporating an ionic additive. *Sci. Adv.* **2016**, *2*, 1600076.

Lüssem, B.; Keum, C. M.; Kasemann, D.; Naab, B.; Bao, Z.; Leo, K. Doped Organic Transistors. *Chem. Rev*. **2016**, *116*, 13714−13751.

Ma, J.; Liu, Z.; Wang, Z.; Yang, Y.; Zhang, G.; Zhang, X.; Zhang, D. Charge Mobility Enhancement for Diketopyrrolopyrrole-Based Conjugated Polymers by Partial Replacement of Branching Alkyl Chains with Linear Ones. Mater. *Chem. Front.* **2017**, 1, 2547−2553.

Ma, L.; Lee, W. H.; Park, Y. D.; Kim, J. S.; Lee, H. S.; Cho, K. High performance polythiophene thin-film transistors doped with very small amounts of an electron acceptor. *Appl. Phys. Lett.* **2008**, *92*, 063310.

Mao, J.; Li, K.; Peng, T. Y. *Catal. Sci. Technol*. **2013**, *3*, 2481− 2498.

Meerheim, R.; Olthof, S.; Hermenau, M.; Scholz, S.; Petrich, A.; Tessler, N.; Solomeshch, O.; Lüssem, B.; Riede, M.; Leo, K. Investigation of C60F36 as Low-Volatility p-Dopant in Organic Optoelectronic Devices. *J. Appl. Phys.* **2011**, *109*, 103102.

Mei, Y.; Diemer, P. J.; Niazi, M. R.; Hallani, R. K.; Jarolimek, K.; Day, C. S.; Risko, C.; Anthony, J. E.; Amassian, A.; Jurchescu, O. D. Crossover from Band-like to Thermally Activated Charge Transport in Organic Transistors Due to Strain-Induced Traps. Proc. Natl. Acad. *Sci. U. S. A.* **2017**, 6739−6748.

Meijer, E. J.; Detcheverry, C.; Baesjou, P. J.; Van Veenendaal, E.; De Leeuw, D. M.; Klapwijk, T. M. Dopant Density Determination in Disordered Organic Field-Effect Transistors. *J. Appl. Phys*. **2003**, *93*, 4831−4835.

Melville, O. A.; Grant, T. M.; Lochhead, K.; King, B.; Ambrose, R.; Rice, N. A.; Boileau, N. T.; Peltekoff, A. J.; Tousignant, M.; Hill, I. G.; et al. Contact Engineering Using Manganese, Chromium, and Bathocuproine in Group 14 Phthalocyanine Organic Thin-Film Transistors. *ACS Appl. Electron. Mater*. **2020**, *2*, 1313−1322.

Mendez, H.; Heimel, G.; Opitz, A.; Sauer, K.; Barkowski, P.; Oehzelt, M.; et al. Doping of Organic Semiconductors: Impact of Dopant Strength and Electronic Coupling. *Angew. Chem., Int. Ed. Engl.* **2013**, *52*, 7751-7755.

Meng, H. F. *Polymer Electronics (Overview of Semiconducting Conjugated Polymers)*, Singapore: Pan Standford Publishing, **2013**.

Meyer, J.; Hamwi, S.; Kröger, M.; Kowalsky, W.; Riedl, T.; Kahn, A. Transition Metal Oxides for Organic Electronics: Energetics, Device Physics and Applications. *Adv. Mater.* **2012**, *24*, 5408−5427.

Meyer, J.; Hamwi, S.; Schmale, S.; Winkler, T.; Johannes, H.-H.; Riedl, T.; Kowalsky, W. A Strategy towards P-Type Doping of Organic Materials with HOMO Levels beyond 6 EV Using Tungsten Oxide. *J. Mater. Chem*. **2009**, *19*, 702−705.

Minari, T.; Miyadera, T.; Tsukagoshi, K.; Aoyagi, Y.; Ito, H. Charge Injection Process in Organic Field-Effect Transistors. *Appl. Phys. Lett*. **2007**, *91*, 053508.

Mishra, A.; Bäuerle, P. Small Molecule Organic Semiconductors on the Move: Promises for Future Solar Energy Technology. *Angew. Chemie Int. Ed*. **2012**, *51*, 2020–2067.

Mistry, H.; Reske, R.; Zeng, Z.; Zhao, Z. J.; Greeley, J.; Strasser, P.; Cuenya, B. R., Exceptional size-dependent activity enhancement in the electroreduction of CO_2 over Au nanoparticles. *J. Am. Chem. Soc.* **2014**, *136*, 16473-16474.

Moore, GE. Cramming more components onto integrated circuits, *Electronics*, **1965**, 86, 114-117.

Müllen, K.; Pisula, W. Donor-Acceptor polymers, *J. Am. Chem. Soc.* **2015**, *137*, 9503-9505.

Mun, J.; Kang, J.; Zheng, Y.; Luo, S.; Wu, H. C.; Matsuhisa, N.; Xu, J.; Wang, G. N.; Yun, Y.; Xue, G.; Tok, J. B.; Bao, Z. Conjugated Carbon Cyclic Nanorings as Additives for Intrinsically Stretchable Semiconducting Polymers. Adv Mater. **2019**, *31*, 1903912.

Mun, J.; Kang, J.; Zheng, Y.; Luo, S.; Wu, Y.; Gong, H.; Lai, J. C.; Wu, H. C.; Xue, G.; Tok, J. B. H.; Bao, Z. F4-TCNQ as an Additive to Impart Stretchable Semiconductors with High Mobility and Stability. *Adv. Electron. Mater*. **2020**, *6*, 2000251

Murawski, C.; Leo, K.; Gather, M. C. Efficiency Roll-Off in Organic Light-Emitting Diodes. *Advanced Materials.* **2013**, *25*, 6801-6827.

Natali, D.; Caironi, M. Charge Injection in Solution-Processed Organic Field-Effect Transistors: Physics, Models and Characterization Methods. *Adv. Mater.* **2012**, *24*, 1357–1387.

Nayak, P. K.; Rosenberg. R; Nehoshtan, L.; Cahen, D. O_2 and organic semiconductors: Electronic effects. *Org. Electron.* **2013**, *14*, 966–972.

Nell, B.; Ortstein, K.; Boltalina, O. V.; Vandewal, K. Influence of Dopant-Host Energy Level Offset on Thermoelectric Properties of Doped Organic Semiconductors. *J. Phys. Chem. C* **2018**, *122*, 11730−11735.

Niazi, M. R.; Hamzehpoor, E.; Ghamari, P.; Perepichka, I. F.; Perepichka, D. F. Nitroaromatics as n-type organic semiconductors for field effect transistors. *Chem. Commun*. **2020**, *56*, 6432-6435.

Nikolka, M., A perspective on overcoming water-related stability challenges in molecular and hybrid semiconductors, *MRS Communications*, **2020**, *10*, 98–111.

Nikolka, M.; Hurhangee, M.; Sadhanala, A.; Chen, H.; McCulloch, I.; Sirringhaus, H. Correlation of Disorder and Charge Transport in a Range of Indacenodithiophene-Based Semiconducting Polymers. *Adv. Electron. Mater*. **2018**, *4*, 1700410.

Nikolka, M.; Nasrallah, I.; Rose, B.; Ravva, M. K.; Broch, K.; Sadhanala, A.; Harkin, D.; Charmet, J.; Hurhangee, M.; Brown, A.; Illig, S.; Too, P.; Jongman, J.; McCulloch, I.; Bredas, J. L.; Sirringhaus, H. High operational and environmental stability of high-mobility conjugated polymer field-effect transistors through the use of molecular additives. *Nat. Mater*. **2017**, *16*, 356-362.

Nikolka, M.; Schweicher, G.; Armitage, J.; Nasrallah, I.; Jellett, C.; Guo, Z.; Hurhangee, M.; Sadhanala, A.; McCulloch, I.; Nielsen, C. B.; Sirringhaus, H. Performance Improvements in Conjugated Polymer Devices by Removal of Water-Induced Traps. *Adv. Mater.* **2018**, *30*, 1801874.

Oh, J. H.; Wei, P.; Bao, Z. Molecular N-Type Doping for AirStable Electron Transport in Vacuum-Processed n-Channel Organic Transistors. *Appl. Phys. Lett*. **2010**, *97*, 243305.

Olah, G. A.; Goeppert, A.; Prakash, G. K. S. Chemical Recycling of Carbon Dioxide to Methanol and Dimethyl Ether: From Greenhouse Gas to Renewable, Environmentally Carbon Neutral Fuels and Synthetic Hydrocarbons. *J. Org. Chem*. **2009**, *74*, 487–498.

Olthof, S.; Mehraeen, S.; Mohapatra, S. K.; Barlow, S.; Coropceanu, V.; Bredas, J. L.; Marder, S. R.; Kahn, A. Ultralow doping in organic semiconductors: evidence of trap filling. *Phys. Rev. Lett.* **2012**, *109*, 176601.

Osaka, I.; Takimiya, K.; McCullough, R. D. Benzobisthiazole-Based Semiconducting Copolymers Showing Excellent Environmental Stability in High-Humidity Air. *Adv. Mater.* **2010**, *22*, 4993−4997.

Osterloh, F. E. Inorganic Nanostructures for Photoelectrochemical and Photocatalytic Water Splitting. *Chem. Soc. Rev.* **2013**, *42*, 2294−2320.

Pang, H.; Masuda, T.; Ye, J. H., Semiconductor-Based Photoelectrochemical Conversion of Carbon Dioxide: Stepping Towards Artificial Photosynthesis. *Chem. Asian J.* **2018**, *13*, 127.

Pang, H.; Yang, G. L.; Li, P.; Huang, H.; Ichihara, F.; Takei, T.; Ye, J. H. Wafer-scale Si nanoconed arrays induced syngas in the photoelectrochemical CO_2 reduction. *Catal. Today* **2020**, *339*, 321−327.

Paniagua, S. A.; Baltazar, J.; Sojoudi, H.; Mohapatra, S. K.; Zhang, S.; Henderson, C. L.; Graham, S.; Barlow, S.; Marder, S. R. Production of Heavily N- and p-Doped CVD Graphene with SolutionProcessed Redox-Active Metal-Organic Species. *Mater. Horiz.* **2014**, *1*, 111−115.

Panidi, J.; Paterson, A. F.; Khim, D.; Fei, Z.; Han, Y.; Tsetseris, L.; Vourlias, G.; Patsalas, P. A.; Heeney, M.; Anthopoulos, T. D. Remarkable Enhancement of the Hole Mobility in Several Organic Small-Molecules, Polymers, and Small-Molecule: Polymer Blend Transistors by Simple Admixing of the Lewis Acid p-Dopant B(C6F5)3. *Adv. Sci*. **2018**, *5*, 1700290.

Park, J. H.; Jung, E. H.; Jung, J. W.; Jo, W. H. A Fluorinated Phenylene Unit as a Building Block for High-Performance n-Type Semiconducting Polymer, *Adv. Mater*. **2013,** 25, 2583.

Park, J. Y.; Baker, L. R.; Somorjai, G. A. Role of Hot Electrons and Metal–Oxide Interfaces in Surface Chemistry and Catalytic Reactions. *Chem. Rev*. **2015**, *115*, 2781.

Park, S.; Kim, S. H.; Choi, H. H.; Kang, B.; Cho, K. Recent Advances in the Bias Stress Stability of Organic Transistors. *Adv. Funct. Mater.* **2019**, *30*, 1904590.

Park, Y. D.; Lim, J. A.; Lee, H. S.; Cho, K. Interface engineering in organic transistors. *Mater. Today.* **2007**, *10*, 46-54.

Paterson, A. F.; Lin, Y.-H.; Mottram, A. D.; Fei, Z.; Niazi, M. R.; Kirmani, A. R.; Amassian, A.; Solomeshch, O.; Tessler, N.; Heeney, M.; Anthopoulos, T. D. The Impact of Molecular p-Doping on Charge Transport in High-Mobility Small-Molecule/Polymer Blend Organic Transistors. *Adv. Electron. Mater.* **2018**, *4*, 1700464.

Paterson, A. F.; Mottram, A. D.; Faber, H.; Niazi, M. R.; Fei, Z.; Heeney, M.; Anthopoulos, T. D. Impact of the Gate Dielectric on Contact Resistance in High-Mobility Organic Transistors. *Adv. Electron. Mater.* **2019**, *5*, 1800723.

Paterson, A. F.; Singh, S.; Fallon, K. J.; Hodsden, T.; Han, Y.; Schroeder, B. C.; Bronstein, H.; Heeney, M.; McCulloch, I.; Anthopoulos, T. D. Recent Progress in High-Mobility Organic Transistors: A Reality Check. *Adv. Mater*. **2018**, *30*, 1801079.

Paterson, A. F.; Treat, N. D.; Zhang, W.; Fei, Z.; Wyatt-Moon, G.; Faber, H.; Vourlias, G.; Patsalas, P. A.; Solomeshch, O.; Tessler, N.; Heeney, M.; Anthopoulos, T. D. Small Molecule/Polymer Blend Organic Transistors with Hole Mobility Exceeding 13 cm (2) V (-1) s (-1). *Adv. Mater.* **2016**, *28*, 7791-7798.

Paterson, A. F.; Tsetseris, L.; Li, R.; Basu, A.; Faber, H.; Emwas, A. H.; Panidi, J.; Fei, Z.; Niazi, M. R.; Anjum, D. H.; Heeney, M.; Anthopoulos, T. D. Addition of the Lewis Acid Zn(C6 F5)2 Enables Organic Transistors with a Maximum Hole Mobility in Excess of 20 cm(2) V(-1) s(-1). *Adv Mater.* **2019**, *31*, 1900871.

Pavelyev, V. G.; Parashchuk, O. D.; Krompiec, M.; Orekhova, T. V.; Perepichka, I. F.; van Loosdrecht, P. H. M.; Paraschuk, D. Y.; Pshenichnikov, M. S. Charge Transfer Dynamics in Donor–Acceptor Complexes between a Conjugated Polymer and Fluorene Acceptors. *J. Phys. Chem. C*. **2014**, *118*, 30291-30301.

Pei, M.; Guo, J.; Zhang, B.; Jiang, S.; Hao, Z.; Xu, X.; Li, Y. Semiconductor/dielectric interface in organic field-effect transistors: charge transport, interfacial effects, and perspectives with 2D molecular crystals. *Adv. Phys. X*. **2020**, 5, 1747945.

Peng, X. Z.; Horowitz, G.; Fichou, D.; Garnier, F. *Appl. Phys. Lett.* **1990**, 57, 2013-2015.

Phan, H.; Ford, M. J.; Lill, A. T.; Wang, M.; Bazan, G. C.; Nguyen, T.-Q. Electrical Double-Slope Nonideality in Organic Field-Effect Transistors. *Adv. Funct. Mater*. **2018,** 28, 1707221.

Phan, H.; Ford, M. J.; Lill, A. T.; Wang, M.; Bazan, G. C.; Nguyen, T.-Q. Improving Electrical Stability and Ideality in Organic Field-Effect Transistors by the Addition of Fullerenes: Understanding the Working Mechanism. *Adv. Funct. Mater*. **2017**, *27*, 1701358.

Phan, H.; Wang, M.; Bazan, G. C.; Nguyen, T. Q. Electrical Instability Induced by Electron Trapping in Low-Bandgap Donor-Acceptor Polymer Field-Effect Transistors. *Adv. Mater*. **2015**, *27*, 7004-7009.

Pingel, P.; Arvind, M.; Kölln, L.; Steyrleuthner, R.; Kraffert, F.; Behrends, J.; Janietz, S.; Neher, D. p-Type Doping of Poly(3-hexylthiophene) with the Strong Lewis Acid Tris (pentafluorophenyl)borane. *Adv. Electron. Mater.* **2016**, *2*, 1600204.

Poverenov, E.; Zamoshchik, N.; Patra, A.; Ridelman, Y.; Bendikov, M. Unusual Doping of Donor-Acceptor-Type Conjugated Polymers Using Lewis Acids. *J. Am. Chem. Soc*. **2014**, *136*, 5138−5149.

Qian, Y.; Zhang, X. W.; Xie, L. H.; Qi, D. P.; Chandran, B. K.; Chen, X. D.; Huang, W. Stretchable Organic Semiconductor Devices. *Adv. Mater.* **2016**, *28*, 9243−9265.

Qiu, J.; Zeng, G. T.; Ha, M. A.; Ge, M. Y.; Lin, Y. J.; Hettick, M.; Hou, B. Y.; Alexandrova, A. N.; Javey, A.; Cronin, S. B. Artificial Photosynthesis on TiO2-Passivated InP Nanopillars. *Nano lett.* **2015**, *15*, 6177-6181.

Qiu, Y.; Wei, P.; Wang, Z.; Lu, W.; Jiang, Y.; Zhang, C.; Qu, Y.; Lu, G. Manipulating Doping of Organic Semiconductors by Reactive Oxygen for Field-Effect Transistors. *Phys. Status Solidi RRL* **2018**, *12*, 1800297.

Quinn, J. T. E.; Zhu, J.; Li, X.; Wang, J.; Li, Y. Recent progress in the development of n-type organic semiconductors for organic field effect transistors. *J. Mater. Chem. C*, **2017**, *5*, 8654−8681.

Rao, H.; Bonin, J.; Robert, M. Visible-light Homogeneous Photocatalytic Conversion of CO_2 into CO in Aqueous Solutions with an Iron Catalyst. *ChemSusChem* **2017**, *10*, 4447.

Reese, C.; Bao, Z. Organic single-crystal field-effect transistors. *Mater. Today*, **2007**, 10, 20-27.

Richards, T. J. & Sirringhaus, H. Analysis of the contact resistance in staggered, top-gate organic field-effect transistors. *J. Appl. Phys*. **2007**, *102*, 94510.

Rienstra-Kiracofe, J. C.; Tschumper, G. S.; Schaefer, H. F.; Nandi, S.; Ellison, G. B. Atomic and Molecular Electron Affinities: Photoelectron Experiments and Theoretical Computations. *Chem. Rev*. **2002**, *102*, 231−282.

Riera-Galindo, S.; Leonardi, F.; Pfattner, R.; Mas-Torrent, M. Organic Semiconductor/Polymer Blend Films for Organic Field Effect Transistors. *Adv. Mater. Technol.* **2019**, *4*, 1900104.

Riordan, M. The Lost History of the Transistor, *IEEE Spectrum*, **2004**, 48-49.

Rivnay, J.; Noriega, R.; Northrup, J. E.; Kline, R. J.; Toney, M. F.; Salleo, A. Structural origin of gap states in semicrystalline polymers and the implications for charge transport. *Phys. Rev. B*. **2011**, *83*, 121306.

Rosen, J.; Hutchings, G. S.; Lu, Q.; Rivera, S.; Zhou, Y.; Vlachos, D. G.; Jiao, F. Mechanistic Insights into the Electrochemical Reduction of CO_2 to CO on Nanostructured Ag Surfaces. *ACS Catal.* **2015**, *5*, 4293.

Ross, M. B.; Dinh, C. T.; Li, Y.; Kim, D.; De Luna, P.; Sargent, E. H.; Yang, P. D., Tunable Cu enrichment enables designer syngas electrosynthesis from CO_2. *J. Am. Chem. Soc*. **2017**, *139*, 9359.

Ross, M. B.; Li, Y.; De Luna, P.; Kim, D.; Sargent, E. H.; Yang, P.; Electrocatalytic rate alignment enhances syngas generation. *Joule* **2019**, *3*, 257.

Rossbauer, S.; Muller, C.; Anthopoulos, TD. Comparative Study of the N-Type Doping Efficiency in Solution-processed Fullerenes and Fullerene Derivatives. *Adv. Funct. Mater*. **2014**; *24*, 7116-7124.

Rosser, T. E.; Windle, C. D.; Reisner, E., Electrocatalytic and solar-driven CO_2 reduction to CO with a molecular manganese catalyst immobilized on mesoporous TiO_2. *Angew. Chem. Int.* Ed. **2016**, *55*, 7388.

Rostrup-Nielsen, J. R. New aspects of syngas production and use. *Catal. Today* **2000**, *63*, 159.

Roy, S. C.; Varghese, O. K.; Paulose, M.; Grimes, C. A. Toward Solar Fuels: Photocatalytic Conversion of Carbon Dioxide to Hydrocarbons. *ACS Nano* **2010**, *4*, 1259−1278.

Roy, S. C.; Varghese, O. K.; Paulose, M.; Grimes, C. A. Toward Solar Fuels: Photocatalytic Conversion of Carbon Dioxide to Hydrocarbons. *ACS Nano* **2010**, *4*, 1259−1278.

Sahara, G.; Abe, R.; Higashi, M.; Morikawa, T.; Maeda, K.; Ueda, Y.; Ishitani, O. Chem. Commun., Photoelectrochemical CO_2 reduction using a Ru(ii)–Re(i) multinuclear metal complex on a p-type semiconducting NiO electrode, *Chem. Commun*. **2015**, *51*, 10722- 10725.

Sahara, G.; Kumagai, H.; Maeda, K.; Kaeffer, N.; Artero, V.; Higashi, M.; Abe, R.; Ishitani, O. J. Photoelectrochemical Reduction of CO_2 Coupled to Water Oxidation Using a Photocathode with a Ru (II)–Re(I) Complex Photocatalyst and a CoOx/TaON Photoanode. *Am. Chem. Soc.* **2016**, *138*, 14152.

Salleo A. Electronic Traps in Organic Semiconductors. *Organic Electronics*: WILEY-VCH Verlag GmbH & Co. **2013**, 341-80.

Saska, J.; Gonel, G.; Bedolla-Valdez, Z. I.; Aronow, S. D.; Shevchenko, N. E.; Dudnik, A. S.; Moulé, A. J.; Mascal, M. A Freely Soluble, High Electron Affinity Molecular Dopant for Solution Processing of Organic Semiconductors. *Chem. Mater*. **2019**, *31*, 1500−1506.

Scaccabarozzi, A. D.; Basu, A.; Anies, F.; Liu, J.; Zapata-Arteaga, O.; Warren, R.; Firdaus, Y.; Nugraha, M. I.; Lin, Y.; Campoy-Quiles, M.; Koch, N.; Muller, C.; Tsetseris, L.; Heeney, M.;

Anthopoulos, T. D. Doping Approaches for Organic Semiconductors. *Chem. Rev*. **2022**, *122*, 4420−4492.

Schmoltner, K.; Schlütter, F.; Kivala, M.; Baumgarten, M.; Winkler, S.; Trattnig, R.; Koch, N.; Klug, A.; List, E. J. W.; Müllen, K. A heterotriangulene polymer for air-stable organic field-effect transistors. *Polym. Chem*. **2013**, *4*, 5337−5344.

Schreier, M.; Curvat, L.; Giordano, F.; Steier, L.; Abate, A.; Zakeeruddin, S. M.; Luo, J.; Mayer, M. T.; Gratzel, M. Efficient photosynthesis of carbon monoxide from CO_2 using perovskite photovoltaics. *Nat. Commun*. **2015**, *6*, 7326.

Schreier, M.; Gao, P.; Mayer, M.T.; Luo, J.S.; Moehl, T.; Nazeeruddin, M.R.; Tilley, S.D.; Gratzel, M. Efficient and selective carbon dioxide reduction on low cost protected Cu2O photocathodes using a molecular catalyst. *Energy Environ. Sci*. **2015,** *8*, 855–861.

Schreier, M.; Luo, J. S.; Gao, P.; Moehl, T.; Mayer, M. T.; Gratzel, M., Covalent Immobilization of a Molecular Catalyst on Cu2O Photocathodes for CO_2 Reduction, *J. Am. Chem. Soc.* **2016**, *138*, 1938-1946.

Schroder, D. K. *Semiconductor Material and Device Characterization*, 3rd ed.; John Wiley & Sons: New York, **2006.**

Sheng, W. C.; Kattel, S.; Yao, S. Y.; Yan, B. H.; Liang, Z. X.; Hawxhurst, C. J.; Wu, Q. Y.; Chen, J. G. G. Electrochemical reduction of CO_2 to synthesis gas with controlled CO/H_2 ratios. *Energy Environ. Sci.* **2017**, *10*, 1180.

Sheraw, C. D., Jackson, T. N., Eaton, D. L. & Anthony, J. E. Functionalized Pentacene Active Layer Organic Thin-Film Transistors. *Adv. Mater.* **2003**, *15*, 2009–2011.

Shi, F.; Baker, L. R.; Hervier, A.; Somorjai, G. A.; Komvopoulos, K. Tuning the Electronic Structure of Titanium Oxide Support to Enhance the Electrochemical Activity of Platinum Nanoparticles. *Nano Lett*. **2013**, *13*, 4469.

Shi, Y.; Zheng, Y.; Wang, J.; Zhao, R.; Wang, T.; Zhao, C.; Chang, K. C.; Meng, H.; Wang, X. Hysteresis-Free, High-Performance Polymer-Dielectric Organic Field-Effect. Transistors Enabled by Supercritical Fluid. *Research.* **2020**, 6587102.

Shockley, William B., John B.; Walter H. B. *Nobel prize in physics 1956-presentation speech*.

Silvi, B.; Savin, A. Classification of chemical bonds based on topological analysis of electron localization functions. *Nature* **1994**, *371*, 683-686.

Singh, C.; Mukhopadhyay, S.; Hod, I. Metal−organic framework derived nanomaterials for electrocatalysis: Recent developments for CO_2 and N_2 reduction. *Nano Convergence* **2021**, *8*, 1-10.

Singh, M. R.; Clark, E. L.; Bell, A. T. Effects of electrolyte, catalyst, and membrane composition and operating conditions on the performance of solar-driven electrochemical reduction of carbon dioxide. *Phys. Chem. Chem. Phys*. **2015**, *17*, 18924-18936.

Sirringhaus, H. 25th Anniversary Article: Organic Field-Effect Transistors: The Path Beyond Amorphous Silicon. *Advanced Materials*. **2014**; *26*, 1319-1335.

Sirringhaus, H. Device Physics of Solution-Processed Organic Field-Effect Transistors. *Adv. Mater*. **2005**, *17*, 2411–2425.

Sirringhaus, H.; Ando, M. Materials Challenges and Applications of Solution-Processed Organic Field-Effect Transistors. *MRS Bull.* **2008**, *33*, 676–682

Sirringhaus, H.; Brown, P. J.; Friend, R. H.; Nielsen, M. M.; Bechgaard, K.; Langeveld-Voss, B. M. W.; Spiering, A. J. H.; Janssen, R. A. J.; Meijer, E. W.; Herwig, P.; de Leeuw, D. M., Two-dimensional charge transport in self-organized, high-mobility conjugated polymers. *Nature* **1999**, *401*, 685-688.

Song, J. T.; Ryoo, H.; Cho, M.; Kim, J.; Kim, J. G.; Chung, S. Y.; Oh, J. Nanoporous Au Thin Films on Si Photoelectrodes for Selective and Efficient Photoelectrochemical CO_2 Reduction. *Adv. Energy Mater*. **2017**, *7*, 1601103.

Sperlich, A.; Kraus, H.; Deibel, C.; Blok, H.; Schmidt, J.; Dyakonov, V. Reversible and irreversible interactions of poly(3-hexylthiophene) with oxygen studied by spin-sensitive methods. J. Phys. Chem. B. **2011**, *115*, 13513-13518.

Stallinga, P. Electronic Transport in Organic Materials: Comparison of Band Theory with Percolation/(Variable Range) Hopping Theory. *Adv. Mater*. **2011**, *23*, 3356- 3362.

Steim, R.; Kogler, F. R.; Brabec, C. J. Interface materials for organic solar cells. J. Mater. Chem. C. ***2010***, *20*, 2499–2512.

Sun, K.; Cheng, T.; Wu, L.; Hu, Y.; Zhou, J.; Maclennan, A.; Jiang, Z.; Gao, Y.; Goddard, W. A., 3rd; Wang, Z., Ultrahigh mass activity for carbon dioxide reduction enabled by gold-iron coreshell nanoparticles. *J. Am. Chem. Soc*. **2017**, *139*, 15608.

Sun, Y.; Lu, X.; Lin, S.; Kettle, J.; Yeates, S. G.; Song, A. Polythiophene-Based Field-Effect Transistors with Enhanced Air Stability. *Org. Electron*. **2010**, *11*, 351−355.

Tada, K.; Harada, H.; Yoshino, K. Field-Effect Mobility of Molecularly Doped Poly(3-Hexylthiophene). *Jpn. J. Appl. Phys*. **1997**, *36*, L718−L720.

Takeda, H.; Ohashi, K.; Sekine, A.; Ishitani, O. Photocatalytic CO_2 Reduction Using Cu(I) Photosensitizers with a Fe(II) Catalyst. J. *Am. Chem. Soc*. **2016**, *138*, 4354.

Tauster, S. J.; Fung, S. C.; Garten, R. L. Strong metal-support interactions. Group 8 noble metals supported on titanium dioxide. *J. Am. Chem. Soc*. **1978**, *100*, 170-175.

Tessler, N.; Preezant, Y.; Rappaport, N.; Roichman, Y. Charge Transport in Disordered Organic Materials and Its Relevance to Thin-Film Devices: A Tutorial Review. *Adv. Mate.* **2009**, *21*, 2741-2761.

Teyssedre, G.; Laurent, C. Charge Transport Modeling in Insulating Polymers: from Molecular to Macroscopic Scale. IEEE Trans. *Dielectr. Electr. Insul*. **2005**, *12*, 857−875.

Tietze, M. L.; Pahner, P.; Schmidt, K.; Leo, K.; Lüssem, B. Doped Organic Semiconductors: Trap-Filling, Impurity Saturation, and Reserve Regimes. *Adv. Funct. Mater*. **2015**, *25*, 2701-2707.

Torralba-Penalver, E.; Luo, Y.; Compain, J. D.; Chardon-Noblat, S.; Fabre, B. Selective Catalytic Electroreduction of CO_2 at Silicon Nanowires (SiNWs) Photocathodes Using Non-Noble Metal-Based Manganese Carbonyl Bipyridyl Molecular Catalysts in Solution and Grafted onto SiNWs. *ACS Catal.* **2015**, *5*, 6138-6147.

Torsi, L.; Magliulo, M.; Manoli, K.; Palazzo, G. Organic field-effect transistor sensors: a tutorial review. *Chem. Soc. Rev*. **2013**, *42*, 8612–8628.

Treat, N. D.; Nekuda Malik, J. A.; Reid, O.; Yu, L.; Shuttle, C. G.; Rumbles, G.; Hawker, C. J.; Chabinyc, M. L.; Smith, P.; Stingelin, N. Microstructure formation in molecular and polymer semiconductors assisted by nucleation agents. *Nat. Mater.* **2013**, *12*, 628-633.

Tseng, H. R.; Phan, H.; Luo, C.; Wang, M.; Perez, L. A.; Patel, S. N.; Ying, L.; Kramer, E. J.; Nguyen, T. Q.; Bazan, G. C.; Heeger, A. J. High-mobility field-effect transistors fabricated with macroscopic aligned semiconducting polymers. *Adv. Mater.* **2014**, *26*, 2993−2998.

Tu, W. G.; Zhou, Y.; Zou, Z. G. Photocatalytic conversion of CO_2 into value-added and renewable fuels. *Adv. Mater*. **2014**, *26*, 4607-4626.

Tumbleston, J. R.; Collins, B. A.; Yang, L.; Stuart, A. C.; Gann, E.; Ma, W.; You, W.; Ade, H. The Influence of Molecular Orientation on Organic Bulk Heterojunction Solar Cells. *Nat. Photonics* **2014**, *8*, 385−391.

Uemura, T.; Rolin, C.; Ke, T. H.; Fesenko, P.; Genoe, J.; Heremans, P.; Takeya, J. On the Extraction of Charge Carrier Mobility in High-Mobility Organic Transistors. *Adv. Mater.* **2016**, *28*, 151-155.

Un, H.; Zheng, Y-Q.; Shi, K.; Wang, J-Y.; Pei, J. Air- and Active Hydrogen-Induced Electron Trapping and Operational Instability in n-Type Polymer Field-Effect Transistors, *Adv. Funct. Mater*. **2017**, *27*, 1605058

Un, H. I.; Wang, J. Y.; Pei, J. Recent Efforts in Understanding and Improving the Nonideal Behaviors of Organic Field-Effect Transistors. *Adv. Sci.* **2019**, 6, 1900375.

Urbain, F.; Tang, P. Y.; Carretero, N. M.; Andreu, T.; Gerling, L. G.; Voz, C.; Arbiol, J.; Morante, J. R., A prototype reactor for highly selective solar-driven CO_2 reduction to synthesis gas using nanosized earth-abundant catalysts and silicon photovoltaics. *Energy Environ. Sci*. **2017**, *10*, 2256.

Van der Staaij, F.M.; Van Keulen, I.M.; Von Hauff, E. Organic Photovoltaics: Where Are We Headed?, *Solar RRL*, **2021**, *5*, 2100167.

Vanka, S.; Arca, E.; Cheng, S.; Sun, K.; Botton, G. A.; Teeter, G.; Mi, Z., High efficiency Si photocathode protected by multifunctional GaN nanostructures. *Nano Lett.* **2018**, *18*, 6530.

Venkateshvaran, D.; Nikolka, M.; Sadhanala, A.; Lemaur, V.; Zelazny, M.; Kepa, M.; Hurhangee, M.; Kronemeijer, A. J.; Pecunia, V.; Nasrallah, I.; et al. Approaching Disorder-Free Transport in HighMobility Conjugated Polymers. *Nature* **2014**, *515*, 384−388.

Vesborg, P. C. K.; Seger, B. Recent progress on advanced design for photoelectrochemical reduction of $CO_2$to fuels. *Chem. Mater*. **2016**, *28*, 8844-8850.

Vezie, M. S.; Few, S.; Meager, I.; Pieridou, G.; Dorling, B.; Ashraf, R. S.; Goni, A. R.; Bronstein, H.; McCulloch, I.; Hayes, S. C.; Campoy-Quiles, M.; Nelson, J. Exploring the origin of high optical absorption in conjugated polymers. *Nat. Mater*. **2016**, *15*, 746-753.

Vidal, A. B.; Feria, L.; Evans, J.; Takahashi, Y.; Liu, P.; Nakamura, K.; Illas, F.; Rodriguez, J. A. CO_2 Activation and Methanol Synthesis on Novel Au/TiC and Cu/TiC Catalysts. *J. Phys. Chem. Lett*. **2012**, *3*, 2275-2280.

Waldrip, M.; Jurchescu, O. D.; Gundlach, D. J.; Bittle, E. G. Contact Resistance in Organic Field-Effect Transistors: Conquering the Barrier. *Adv. Funct. Mater*. **2019,** *30*, 1904576.

Wang, H.; Wang, H.; Wang, Z.; Tang, L.; Zeng, G.; Xu, P.; Chen, M.; Xiong, T.; Zhou, C.; Li, X.; Covalent Organic Framework Photocatalysts: Structures and Applications. *Chem. Soc. Rev.* **2020**, *49*, 4135−4165.

Wang, P.; Wang, S.; Wang, H.; Wu, Z.; Wang, L. Recent Progress on Photo-Electrocatalytic Reduction of Carbon Dioxide. *Part. Part. Syst. Char*. **2018**, 35, 1700371.

Wang, Y.; Fan, S.; AlOtaibi, B.; Wang, Y.; Li, L.; Mi, Z. A monolithically integrated gallium nitride nanowire/silicon solar cell photocathode for selective carbon dioxide reduction to methane. *Chem. - Eur. J.* **2016**, *22*, 8809−8813

Wang, Z. B.; Helander, M. G.; Greiner, M. T.; Qiu, J.; Lu, Z. H. Energy-level alignment and charge injection at metal/C60/organic interfaces. *Appl. Phys. Lett.* **2009**, *95*, 43302.

Wang, Z.; Zhang, L.; Schülli, T. U.; Bai, Y.; Monny, S. A.; Du, A.; Wang, L. Identifying copper vacancies and their role in the CuO based photocathode for water splitting. *Angew. Chem*. **2019**, *131*, 17768−17773.

Waragai, K.; Akimichi, H.; Hotta, S.; Kano, H.; Sakaki, H. Charge transport in thin films of semiconducting oligothiophenes. *Physical Review B.* **1995**, 52, 1786-1792.

Ward, J. W.; Lamport, Z. A.; Jurchescu, O. D. Versatile organic transistors by solution processing. *ChemPhysChem*, **2015**, *16*, 1118–1132.

Waugh, K. C. Methanol Synthesis. *Catal. Today* **1992**, *15*, 5-75.

Wei, L.; Lin, J.; Xie, S.; Ma, W.; Zhang, Q.; Shen, Z.; Wang, Y., Photoelectrocatalytic reduction of CO_2 to syngas over ag nanoparticle modified p-si nanowire arrays. *Nanoscale* **2019**, 11, 12530.

Wenzel, M.; Rihko-Struckmann, L.; Sundmacher, K. Thermodynamic analysis and optimization of RWGS processes for solar syngas production from CO_2. *AIChE J.* **2017**, *63*, 15-22.

White, J. L.; Baruch, M. F.; Pander Iii, J. E.; Hu, Y.; Fortmeyer, I. C.; Park, J. E.; Zhang, T.; Liao, K.; Gu, J.; Yan, Y.; Shaw, T. W.; Abelev, E.; Bocarsly, A. B. Light-Driven Heterogeneous Reduction of Carbon Dioxide: Photocatalysts and Photoelectrodes. *Chem. Rev.* **2015,** *115*, 12888.

Wu, J.; Huang, Y.; Ye, W.; Li, Y. CO_2 Reduction: From the Electrochemical to Photochemical Approach. *Adv. Sci*. **2017**, *4*, 1700194.

Wu, J.; Xie, Y.; Ren, Z.; Du, S.; Meng, H.; Zhao, L.; Wang, X.; Wang, G.; Fu, H. Porous palladium nanomeshes with enhanced electrochemical CO_2-into-syngas conversion over a wider applied potential. *ChemSusChem*, **2019**, 12, 3304−3311.

Xie, S. J.; Zhang, Q. H.; Liu, G. D.; Wang, Y. Photocatalytic and photoelectrocatalytic reduction of CO_2 using heterogeneous catalysts with controlled nanostructures, *Chem. Commun*. **2016**, *52*, 35-59.

Xu, J. Q.; Li, X. D.; Liu, W.; Sun, Y. F.; Ju, Z. Y.; Yao, T.; Wang, C. M.; Ju, H. X.; Zhu, J. F.; Wei, S. Q.; Xie, Y. Carbon Dioxide Electroreduction into Syngas Boosted by a Partially Delocalized Charge in Molybdenum Sulfide Selenide Alloy Monolayers. *Angew Chem. Int. Ed*. **2017**, *56*, 9121-9125.

Xu, Y.; Sun, H.; Liu, A.; Zhu, H. H.; Li, W.; Lin, Y. F.; Noh, Y. Y. Doping: A Key Enabler for Organic Transistors. *Adv. Mater.* **2018**, 30, 1801830.

Xu, Y.; Sun, H.; Shin, E. Y.; Lin, Y. F.; Li, W.; Noh, Y. Y. Planar-Processed Polymer Transistors. *Adv. Mater.* **2016**, *28*, 8531-8537.

Yamashita, Y.; Hinkel, F.; Marszalek, T.; Zajaczkowski, W.; Pisula, W.; Baumgarten, M.; Matsui, H.; Müllen, K.; Takeya, J. Mobility Exceeding 10 $cm^2V^{-1}s^{-1}$ in Donor-Acceptor Polymer Transistors with Band-like Charge Transport. *Chem. Mater.* **2016**, *28*, 420-424.

Yang, C. Guo, C. Shi, D.-K. Wang, T. Zhang, Q. Zhu, Z.-H. Lu, Improving Bias-Stress Stability of p-Type Organic Field-Effect Transistors by Constructing an Electron Injection Barrier at the Drain Electrode/Semiconductor Interfaces, *ACS Appl. Mater. Interfaces*, **2020**,12, 41886-41895.

Yao, Z.-F.; Wang, J.-Y.; Pei, J. Control of π-π Stacking via Crystal Engineering in Organic Conjugated Small Molecule Crystals. *Cryst. Growth Des*. **2018**, *18*, 7−15.

Yee, P. Y.; Scholes, D. T.; Schwartz, B. J.; Tolbert, S. H. DopantInduced Ordering of Amorphous Regions in Regiorandom P3HT. *J. Phys. Chem. Lett*. **2019**, *10*, 4929−4934.

Yoneyama, H.; Sugimura, K.; Kuwabata, S. J. Effects of electrolytes on the photoelectrochemical reduction of carbon dioxide at illuminated p-type cadmium telluride and p-type indium phosphide electrodes in aqueous solutions. *Electroanal. Chem*. **1988**, *249*, 143-153.

Yoon, S. E.; Kang, Y.; Noh, S. Y.; Park, J.; Lee, S. Y.; Park, J.; Lee, D. W.; Whang, D. R.; Kim, T.; Kim, G. H.; Seo, H.; Kim, B. G.; Kim, J. H. High Efficiency Doping of Conjugated Polymer for Investigation of Intercorrelation of Thermoelectric Effects with Electrical and Morphological Properties. *ACS Appl. Mater. Interfaces*, **2020**, *12*, 1151-1158.

Yurash, B.; Cao, D. X.; Brus, V. V.; Leifert, D.; Wang, M.; Dixon, A.; Seifrid, M.; Mansour, A. E.; Lungwitz, D.; Liu, T.; Santiago, P. J.; Graham, K. R.; Koch, N.; Bazan, G. C.; Nguyen, T. Q. Towards understanding the doping mechanism of organic semiconductors by Lewis acids. *Nat. Mater*. **2019**, *18*, 1327-1334.

Zaumseil, J.; Sirringhaus, H. Electron and Ambipolar Transport in Organic FieldEffect Transistors. *Chem. Rev.* **2007**, *107*, 1296–1323.

Zessin, J.; Xu, Z.; Shin, N.; Hambsch, M.; Mannsfeld, S. C. B. Threshold Voltage Control in Organic Field-Effect Transistors by Surface Doping with a Fluorinated Alkylsilane. *ACS Appl. Mater. Interfaces* **2019**, *11*, 2177−2188.

Zhang, F.; Mohammadi, E.; Qu, G.; Dai, X.; Diao, Y. Orientation-Dependent Host-Dopant Interactions for Manipulating Charge Transport in Conjugated Polymers. *Adv. Mater*. **2020**, 32, 2002823.

Zhang, H. W.; Ming, J. T.; Zhao, J. W.; Gu, Q.; Xu, C.; Ding, Z. X.; Yuan, R. S.; Zhang, Z. Z.; Lin, H. X.; Wang, X. X.; Long, J. L., High-rate, tunable syngas production with artificial photosynthetic cells. *Angew. Chem. Int. Ed*. **2019**, *58*, 7718.

Zhang, H.; Li, Y.; Zhang, X.; Zhang, Y.; Zhou, H. Role of interface properties in organic solar cells: from substrate engineering to bulk-heterojunction interfacial morphology. *Mater. Chem. Front*. **2020**, *4*, 2863−2880.

Zhang, H.; Zhu, M.; Schmidt, O.G.; Chen, S.; Zhang, K. Covalent organic frameworks for efficient energy electrocatalysis: rational design and progress. *Adv. Energy Sustainability Res.* **2021**, *2*, 2000090.

Zhang, J.; Geng, B.; Duan, S.; Huang, C.; Xi, Y.; Mu, Q.; Chen, H.; Ren, X.; Hu, W. High-Resolution Organic Field-Effect Transistors Manufactured by Electrohydrodynamic Inkjet Printing of Doped Electrodes. *J. Mater. Chem*. C **2020**, *8*, 15219−15223.

Zhang, N.; Long, R.; Gao, C.; Xiong, Y. *Sci. China Mater*. **2018**, *61*, 771-805.

Zhang, W. M.; Han, Y.; Zhu, X. X.; Fei, Z. P.; Feng, Y.; Treat, N. D.; Faber, H.; Stingelin, N.; McCulloch, I.; Anthopoulos, T. D.; et al. A Novel Alkylated Indacenodithieno[3,2-b] thiophene-Based Polymer for High-Performance Field-Effect Transistors. *Adv. Mater.* **2016**, *28*, 3922−3927.

Zhang, W.; Smith, J.; Watkins, S.E.; Gysel, R.; McGehee, M.; Salleo, A.; Kirkpatrick, J.; Ashraf, S.; Anthopoulos, T;, Heeney, M. and McCulloch, I, ndacenodithiophene semiconducting polymers for high-performance, air-stable transistors. *J. Am. Chem. Soc.* **2010**, *132*, 11437-11439.

Zhang, X.; Bronstein, H.; Kronemeijer, A. J.; Smith, J.; Kim, Y.; Kline, R. J.; Richter, L. J.; Anthopoulos, T. D.; Sirringhaus, H.; Song, K.; Heeney, M.; Zhang, W.; McCulloch, I.; DeLongchamp, D. M. Molecular origin of high field-effect mobility in an indacenodithiophene-benzothiadiazole copolymer. *Nat. Commun.* **2013**, *4*, 2238.

Zhang, Y.; Zhou, H.; Seifter, J.; Ying, L.; Mikhailovsky, A.; Heeger, A. J.; Bazan, G. C.; Nguyen, T.-Q. Molecular doping enhances photoconductivity in polymer bulk heterojunction solar cells, *Adv. Mater.* **2013**, *25*, 7038−7044.

Zhang, Y.-J.; Sethuraman, V.; Michalsky, R.; Peterson, A. A., Competition between CO_2 reduction and H_2 evolution on transition-metal electrocatalysts. *ACS Catal.* **2014**, 4, 3742-3748.

Zhao, X.; Pachfule, P.; Thomas, A. Covalent Organic Frameworks (COFs) for Electrochemical Applications. *Chem. Soc. Rev.* **2021**, *50*, 6871−6913

Zhao, Z.; Yin, Z.; Chen, H.; Zheng, L.; Zhu, C.; Zhang, L.; Tan, S.; Wang, H.; Guo, Y.; Tang, Q.; Liu, Y. High-Performance, Air-Stable Field-Effect Transistors Based on Heteroatom-Substituted Naphthalenediimide-Benzothiadiazole Copolymers Exhibiting Ultrahigh Electron Mobility up to 8.5 cm V (-1) s (-1). *Adv. Mater.* **2017**, *29*, 1602410.

Zhengran, H.; Zhang, Z.; Bi, S.; Chen, J.; Li, D. Conjugated polymer-controlled morphology and charge transport of small-molecule organic semiconductors, *Scientific Reports* 10, **2020**, 1, 1-9.

Zhokhavets, U.; Erb, T.; Gobsch, G.; Al-Ibrahim, M.; Ambacher, O. Relation between absorption and crystallinity of poly(3-hexylthiophene)/fullerene films for plastic solar cells. *Chem. Phys. Lett.* **2006**, *418*, 347-350.

Zhou, B.; Kong, X.; Vanka, S.; Chu, S.; Ghamari, P.; Wang, Y.; Pant, N.; Shih, I.; Guo, H.; Mi, Z., Gallium nitride nanowire as a linker of molybdenum sulfides and silicon for photoelectrocatalytic water splitting. *Nat. Commun.* **2018**, *9*, 3856.

Zhou, Y.; Fuentes-Hernandez, C.; Shim, J.; Meyer, J.; Giordano, A. J.; Li, H.; Winget, P.; Papadopoulos, T.; Cheun, H.; Kim, J.; et al. A Universal Method to Produce Low-Work Function Electrodes for Organic Electronics. *Science* **2012**, *336*, 327−332.

Zhu, H.; Shin, E. S.; Liu, A.; Ji, D.; Xu, Y.; Noh, Y. Y. Printable semiconductors for backplane TFTs of flexible OLED displays. *Adv. Funct. Mater.* **2020**, *30*, 1904588.

Zuo, G.; Li, Z.; Andersson, O.; Abdalla, H.; Wang, E.; Kemerink, M. Molecular Doping and Trap Filling in Organic Semiconductor Host–Guest Systems. *J. Phys. Chem. C.* **2017**, *121*, 7767-7775.

Zuo, G.; Linares, M.; Upreti, T.; Kemerink, M. General rule for the energy of water-induced traps in organic semiconductors. *Nat. Mater.* **2019**, *18*, 588−593.